PhD Thesis

Numerics in fluids and gravitation

Samuel Santos Pérez

Directora: Isabel Cordero Carrión

Programa de Doctorado en Matemáticas
Código de programa: 3138. Regulación: RD 99/2011

Universitat de València

Valencia, Mayo de 2023.

VNIVERSITAT DE VALÈNCIA
Facultat de Ciències Matemàtiques

NUMERICS IN FLUIDS AND GRAVITATION

Memoria presentada por Samuel Santos Pérez, Graduado en Matemáticas y Física; realizada en el Departamento de Matemáticas de la Universitat de València bajo la dirección de Isabel Cordero Carrión, profesora titular de este departamento, con el objetivo de aspirar al Grado de Doctor en Matemáticas.

Valencia, 31 de mayo de 2023

Isabel Cordero Carrión
Directora de la Memoria

Samuel Santos Pérez
Aspirante al Grado de Doctor

DEPARTAMENT DE MATEMÀTIQUES
FACULTAT DE MATEMÀTIQUES
UNIVERSITAT DE VALÈNCIA

Isabel Cordero Carrión
Departamento de Matemáticas
Facultad de Matemáticas, Universidad de Valencia
Dr. Moliner, 50; 46100 Burjassot (Valencia, Spain)
Tel.: (+34) 96 354 3233
Email: isabel.cordero@uv.es

Burjassot, June 2nd, 2023

Favorable report from the thesis director

I declare that this dissertation presented by **Samuel Santos Pérez** entitled *Numerics in fluids and gravitation* has been done under my supervision at the University of Valencia (Spain). I also state that this work corresponds to the thesis project approved by this insitution and it satisfies all the requisites to obtain the degree of Doctor in Mathematics.

Sincerely,

Signed: **Isabel Cordero Carrión**

Contents

Agradecimientos

En primer lugar, tengo que dar las gracias a mi directora Isabel Cordero porque sin ella esta tesis no habría sido posible, y me dio la oportunidad de hacer estancias de investigación increíbles. Gracias a toda la gente del Departamento de Matemáticas por haber hecho más llevadero este periodo difícil que es el doctorado. Tanto a los que me dieron buenos consejos como a aquellos con los que tuve el placer de compartir docencia. Tampoco me puedo olvidar de mis amigos del Departamento de Astrofísica y Astronomía, por esos refrigerios de desconexión en Olegari. Gracias a toda la gente de la ETSE que me ayudó en los primeros pasos en investigación. Ignacio, Pau, Miguel, Dolors, ... Me hicieron sentir parte importante de un grupo humano fantástico.

Gracias a toda la gente del Observatoire de Paris-Meudon que hizo que me sintiera a gusto en mi primera experiencia viviendo en el extranjero, en especial a Jérôme Novak y Gaël Servignat por su calidad humana. Gracias a Michael y Aman porque sin sus amistades mi estancia en el Perimeter Insititute no habría sido la misma. Eternamente agradecido a toda la familia que conocí en el Colegio de España de París. Por hacerme sentir como en casa y por hacerme vivir experiencias inolvidables, que siempre recordaré con emoción. Son demasiados para nombrarlos pero ellos saben muy bien quiénes son.

A todos aquellos miembros de mi familia que confiaron en mí y apoyaron mi decisión de hacer el doctorado. Primos, primas, tíos y tías. En especial, a mi tía Ana. Porque siempre sentí que mis éxitos eran sus éxitos. Y a mi Madre. Por su consuelo en los momentos más críticos. En último lugar, pero no menos importante, quiero dar las gracias a mi familia benidormense. A todos los compañeros y compañeras del Ausias, amigos y amigas, los hermanos y hermanas que elegí. Porque sin duda, forman parte de la persona que soy hoy en día. Por su incondicional apoyo y cariño. Esta tesis es, sin duda, también parte de ellos.

València, 2023 *Samuel*

Resumen

Introducción

En esta tesis encontraremos una extensa variedad de escenarios físicos con aplicación desde las ciencias de la salud hasta la astrofísica. La dinámica de todos ellos vendrá descrita por un sistema de ecuaciones hiperbólico como el siguiente:

$$\frac{\partial U}{\partial t} + \sum_{i=1}^{d} \frac{\partial F^i(U)}{\partial x_i} = r(U), \quad x \in \mathbb{R}^d, \quad t \in \mathbb{R}^+, \tag{1}$$

donde $U = (U_1, \ldots, U_m)^T : \mathbb{R}^d \times \mathbb{R}^+ \longrightarrow \mathbb{R}^m$ es el vector de las variables conservadas y $F^i : \mathbb{R}^m \longrightarrow \mathbb{R}^m$ son los flujos. Este sistema, así escrito, se denomina ley de balance. Si no hay término fuente, $r = 0$, hablamos de ley de conservación. Existen varias estrategias para resolver este tipo de ecuaciones, las cuales dependen del problema a resolver.

Por un lado, abordaremos el tema de la simulación del flujo sanguíneo en la aorta, enmarcado, por supuesto, dentro de la mecánica clásica. Aquí usaremos las Ecuaciones de Navier-Stokes. Nuestro objetivo es conseguir establecer relaciones entre la presión de cizalla arterial y aspectos geométricos de la aorta. Debido a la complejidad de la geometría usaremos el Método de los Volúmenes Finitos.

Por otro lado, nos iremos a situaciones contextualizadas en la Teoría de la Relatividad. Veremos la Ecuación de Euler, deducida de ignorar los efectos de viscosidad en las Ecuaciones de Navier-Stokes, primero en gravedad de Newton y luego en Relatividad General. Hallaremos resultados teóricos sobre estabilidad y curvas características que ayudarán a desarrollar métodos numéricos para su resolución.

Después, resolveremos las Ecuaciones de Einstein, las ecuaciones de la Relatividad General. Usaremos una nueva versión de la llamada Formulación Completamente Ligada (FCF, siglas en inglés) de las mismas. Esto es, una particular descomposición de las Ecuaciones de Einstein, de tal manera que se puedan escribir como una ley de balance para los grados de libertad físicos asociados a la propagación de información (radiación gravitatoria en forma de ondas gravitatorias), acompañado de un sistema de restricciones modeladas por ecuaciones elípticas. El nuevo esquema conservará propiedades matemáticas interesantes similares a las que tenía la versión anterior, como unicidad local y estructura jerárquica, y sumaremos otras ventajas desde el punto de vista de la precisión numérica.

A continuación, trataremos con leyes de balance con términos duros. Estos términos tienen la característica de estar asociados a fenómenos de escalas temporales muy diferentes, y en donde los términos fuente asociados presentan factores que potencialmente pueden ser de varios órdenes de magnitud más grandes que el resto de las fuentes. Para ello, es necesaria la utilización de métodos numéricos implícitos para su integración temporal, o de algún otro tipo de técnica específica para resolver este problema.

Afrontaremos dos contextos con motivación astrofísica: Magnetohidrodinámica Relativista Resistiva e Hidrodinámica Radiativa. En el primer caso, el comportamiento duro se observa en las Ecuaciones de Maxwell cuando la conductividad es alta, y, en el segundo caso, en las ecuaciones del transporte radiativo cuando las opacidades de dispersión y transporte adquieren valores significativos.

Para la resolución numérica de estas ecuaciones con términos duros propondremos un nuevo esquema de integración numérico. Mantendrá las ventajas de los métodos implícitos para el manejo de términos duros, pero además con el coste computacional de un método explícito.

El último proyecto del que hablaremos en esta tesis doctoral no estará relacionado con las leyes de balance. Diseñaremos un algoritmo para llevar a cabo regresión polinómica en varias variables. Lo haremos para resolver un problema que aparece en simulaciones de estrellas de neutrones con ecuaciones de estado realistas para la materia nuclear. Ocurre que los datos tabulados realistas para ecuaciones de estado añaden ruido a las simulaciones de tal manera que éstas pueden volverse inestables. Usaremos un ajuste polinómico multivariable para suavizar estos datos, teniendo en cuenta un polinomio de varias variables de gra-

do determinado en su forma más general.

Dinámica de fluidos computacional

La dinámica de fluidos computacional se encarga de resolver numéricamente las ecuaciones que rigen la evolución de los fluidos, las famosas ecuaciones de Navier-Stokes:

$$\frac{\partial \rho}{\partial t} + \vec{\nabla} \cdot (\rho \boldsymbol{V}) = 0, \tag{2a}$$

$$\frac{\partial (\rho \boldsymbol{V})}{\partial t} + \vec{\nabla} \cdot (\rho \boldsymbol{V} \otimes \boldsymbol{V}) = -\vec{\nabla} p + \vec{\nabla} \cdot \boldsymbol{\Sigma}. \tag{2b}$$

Éstas relacionan la densidad de masa ρ, la velocidad euleriana del fluido $\boldsymbol{V}$ y la presión p. El campo tensorial $\boldsymbol{\Sigma}$ es el tensor de esfuerzos viscosos. Si el fluido es incompresible tenemos que ρ es constante y las ecuaciones se simplifican. En este caso y para fluidos Newtonianos, $\boldsymbol{\Sigma}$ se calcula como

$$\boldsymbol{\Sigma} = \upsilon(\vec{\nabla} \boldsymbol{V} + \vec{\nabla} \boldsymbol{V}^T), \tag{3}$$

con υ una constante característica del fluido llamada viscosidad.

Es habitual tener flujos contenidos en geometrías tubulares donde se tiene una frontera constituida por una entrada, una salida y unas paredes, que engloban la región interior donde se desarrolla el problema. Para la obtención de una solución única de estas ecuaciones es necesario considerar unos datos iniciales en la región interna, y unas condiciones de frontera, tipo Dirichlet o Neumann, en cada uno de los parches (entrada, salida y paredes).

Distinguimos dos tipos de flujo. Por un lado, en un flujo laminar, las líneas de corriente del fluido no se cruzan entre sí mismas y presentan estabilidad. Por otro lado, los flujos turbulentos son caóticos, difusivos (sus perfiles tienden a suavizarse) y presentan una vorticidad, $\boldsymbol{\Omega} = \vec{\nabla} \times \boldsymbol{V}$, variable con escalas temporales y espaciales muy diferentes. La vorticidad es una magnitud que cuantifica la rotación del fluido. Es habitual en estos casos considerar la descomposición de Reynolds en las variables del fluido ϕ, basada en una componente promediada en el tiempo $\bar{\phi}$ y otra fluctuante ϕ'. Aplicando estas descomposiciones acabamos en un nuevo sistema de ecuaciones donde las nuevas variables conservadas serán la velocidad y presión promediadas, $\bar{\boldsymbol{V}}$, $\bar{p}$, y las variables turbulentas

definidas como

$$k := \frac{\overline{\boldsymbol{V'} \cdot \boldsymbol{V'}}}{2}, \quad \epsilon := \frac{1}{2}\frac{\upsilon}{\rho}\overline{(\vec{\nabla}\boldsymbol{V'} + \vec{\nabla}\boldsymbol{V'}^T) : (\vec{\nabla}\boldsymbol{V'} + \vec{\nabla}\boldsymbol{V'}^T)}, \quad \omega := \frac{\epsilon}{C_\upsilon k},$$

donde $\boldsymbol{V'}$ es la componente fluctuante de la velocidad y $C_\upsilon = 0{,}09$ es una constante semiempírica. La operación : representa el doble producto escalar de tensores, $\boldsymbol{A} : \boldsymbol{B} = \sum_{i,j} A_{ij}B_{ij}$. Podemos escoger k y ϵ para cerrar el sistema o k y ω. En el primer caso, tendremos el modelo de turbulencia $k - \epsilon$ y en el segundo caso el modelo $k - \omega$.

Ambos tienen ventajas y desventajas. En el modelo $k - \epsilon$ el flujo interno se calcula con mayor precisión, pero en zonas de altos gradientes de presión (como cerca de las paredes) se tiene el efecto contrario. No obstante, el modelo $k - \omega$ es muy sensible a las condiciones de contorno de la entrada, aunque funciona bien cerca de las paredes. Existe una combinación de ambos modelos llamada SST $k - \omega$, la cual será la elección más adecuada para estudios de la presión de cizalla en la pared.

Los sistemas de leyes de balance descritos serán resueltos numéricamente con el Método de los Volúmenes Finitos, que se adapta bien a geometrías complejas, donde se tienen superficies rugosas, con curvatura y torsión no nulas. Además, por cómo se construyen, tienen la propiedad de cumplir con precisión las leyes de conservación sobre la masa, momento y energía.

El primer paso es cubrir la región interna con poliedros genéricos encajados o volúmenes. La solución numérica estará constituida por los valores de las variables del fluido en los centroides de cada volumen. En segundo lugar, calcularemos la integración del sistema en cada volumen, aplicando el teorema de Gauss en los términos con divergencias. Las aproximaciones numéricas llevadas a cabo al calcular las derivadas y las integraciones constituyen las ecuaciones del método. Por ejemplo, emplear los volúmenes vecinos y la regla de integración del punto medio, nos conduce a ecuaciones algebraicas del tipo:

$$\sum_{i}^{N_m} a_i V_{M_i} + \sum_{j}^{N_c+1} b_j p_{C_j} = c, \tag{4}$$

donde N_m es el número de caras del volumen y N_c el número de volúmenes vecinos. Los coeficientes a_i, b_i, c dependerán de los esquemas empleados en las aproximaciones y la resolución de la malla. Los subíndices M_i y C_i se refieren a los centroides de las caras y los volúmenes

de la malla, respectivamente. En el caso de las Ecuaciones de Navier-Stokes se utiliza el algoritmo iterativo SIMPLE, basado en suponer un valor inicial para la presión p^*, resolver una ecuación algebraica para la velocidad y finalmente obtener unas correcciones p' y $\boldsymbol{V}'$ mediante otras ecuaciones algebraicas.

El paso final para obtener la solución numérica es resolver el conjunto de ecuaciones lineales algebraicas del tipo (4). El número de volúmenes en un problema realista de dinámica de fluidos computacional puede llegar a 10^6, por lo que necesitaremos métodos iterativos como Gauss-Seidel o Jacobi. En la práctica se combinan estos junto con los métodos multimalla, basados en obtener una malla más gruesa a partir de la ya construida y resolver un sistema menor, para luego volver a la malla original. Se ha demostrado que la combinación de cambios de malla junto con métodos iterativos es más eficiente computacionalmente que aplicar solo métodos iterativos (véase [128]).

Simulación del flujo sanguíneo en la aorta

En esta sección aplicaremos todos los detalles introducidos en dinámica de fluidos computacional para el caso del flujo sanguíneo en la aorta, teniendo en mente como motivación las aplicaciones en ciencias de la salud. Tendremos dos objetivos principales.

En primer lugar, queremos establecer relaciones entre aspectos geométricos de la superficie aórtica con valores anómalos de la presión de cizalla en la pared, y que puedan ser responsables de enfermedades cardiovasculares. Para ello es conveniente disponer de una muestra de aortas cuanto más grande mejor. Estas se adquieren por Tomografía Computarizada, por lo que la obtención de una muestra de tal magnitud es complicada. Un algoritmo para generar aortas sintéticas realistas es conveniente. Con este problema en mente, se ha desarrollado un método de reconstrucción a partir de parámetros geométricos clave de aortas reales [108]. Este método permitirá identificar aquellos parámetros sobre la geometría de la superficie aórtica a partir de los cuales poder generar aortas sintéticas. En nuestro primer objetivo, la simulación del flujo

sanguíneo se llevará a cabo en la aorta real y la aorta reconstruida para validar este método de reconstrucción; en el sentido de ver si los perfiles de presión y flujo son reproducidos fielmente en las aortas reconstruidas.

En segundo lugar, queremos ver la forma en la que afectan las condiciones de frontera en la entrada de la aorta a los perfiles de la presión de cizalla, con el objetivo de simular el efecto de varias válvulas aórticas, naturales y protésicas.

Usaremos el modelo descrito por las Ecuaciones de Navier-Stokes (2) para la validación del método de reconstrucción y el modelo SST $k-\omega$ para el análisis de válvula aórtica, considerando en todos los casos un flujo incompresible y estacionario. Este esquema supone una primera aproximación, y en futuros trabajos se tendrá en cuenta el ciclo cardíaco completo. Las condiciones de contorno tratarán de reproducir aquellas del flujo sanguíneo en la fase de sístole, cuando la velocidad de entrada es máxima.

Para las simulaciones usaremos un resolvedor de Volúmenes Finitos llamado OpenFOAM. Esta herramienta permitirá cubrir con una malla la región aórtica, seleccionar el modelo y las condiciones de contorno, así como diferentes parámetros de la resolución numérica. En concreto, partiremos de una malla preliminar de hexaedros regulares de 2 mm de lado, a partir de la cual aplicaremos un proceso de refinamiento. Se aplicará el algoritmo SIMPLE y se usará un método multimalla geométrico junto con el método iterativo de Gauss-Seidel para resolver las ecuaciones lineales de la discretización.

Para validar el método de reconstrucción se ha usado un perfil parabólico para el flujo sanguíneo en la entrada. Además, en el proceso de refinamiento, hemos reducido la resolución espacial gradualmente desde la zona interna de la aorta hasta alcanzar 0.1 mm en la pared aórtica. Se han utilizado hasta 8 aortas con las que se han comparado líneas de corrientes y perfiles de presión de cizalla arterial en la aorta real y reconstruida. En la Figura 1 se muestran los perfiles de presión de cizalla en el caso de dos aortas. En general, se puede apreciar como los patrones de la versión reconstruida se tienen también en la original.

Una mejora del método de reconstrucción, añadiendo más parámetros geométricos característicos, ayudará al objetivo de final de establecer relaciones entre geometría y perfiles de presión de cizalla con métodos de Aprendizaje de Máquina (Machine Learning en inglés).

A continuación, describimos el análisis realizado sobre la influencia

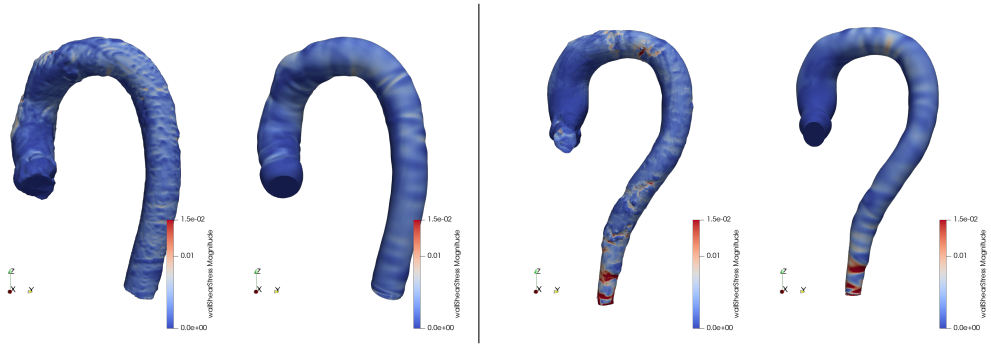

Figura 1: Resultados de los perfiles WSS generados a partir de simulaciones, comparando la aorta original (izquierda) y la aorta reconstruida (derecha). Se muestran las aortas de dos pacientes diferentes.

de la válvula aórtica con los valores de presión de cizalla. Se han usado condiciones de contorno en la entrada reproduciendo una válvula sana tricúspide y dos protésicas (válvula bidisco y disco pivotante). En este caso, la resolución espacial alcanzada en la pared ha sido de 50 μm.

Para el análisis se ha establecido un valor crítico de presión de cizalla de 0.5 Pa, por debajo del cual hay riesgo de arteriosclerosis, ver [83]. Nos hemos centrado en la aorta ascendente, la primera parte de la aorta donde los resultados son más fiables. Después, la geometría ha sido simplificada considerablemente, eliminando ramificaciones importantes.

Atendiendo a los resultados obtenidos, el comportamiento general es que la válvula tricúspide proporciona una zona de riesgo menor que con las válvulas protésicas. Por otro lado, la válvula bidisco induce una zona de riesgo mayor que con la válvula de disco pivotante.

Relatividad y gravitación

A partir de ahora dejaremos de lado la mecánica clásica y todos los proyectos estarán enmarcados en la Teoría de la Relatividad. En ausencia de gravitación, cuando las velocidades están cerca de la velocidad de la luz c, la teoría del espacio y el tiempo es la de la Relatividad Especial. La medición de tiempos y distancias se basa en el tensor métrico de Minkowski, el cual en componentes cartesianas se escribe como

$$\eta_{\alpha\beta} = \text{diag}(-1, 1, 1, 1). \tag{5}$$

Este tensor métrico induce un producto escalar en el espacio afín formado por los puntos que designan los eventos del espacio-tiempo.

Por otro lado, la teoría aceptada del espacio-tiempo en presencia de gravedad es la Relatividad General. A partir del Principio de Equivalencia de Einstein se deduce que gravedad y curvatura del espacio-tiempo, entendido como una variedad diferencial pseudoriemaniana de 4 dimensiones, son lo mismo. El tensor métrico $g_{\alpha\beta}$ se obtiene de resolver las Ecuaciones de Einstein:

$$R_{\alpha\beta} - \frac{1}{2} g_{\alpha\beta} R = \frac{8\pi G}{c^4} T_{\alpha\beta}, \tag{6}$$

donde $R = R^{\alpha}{}_{\alpha}$, $R_{\alpha\beta} = R^{\gamma}{}_{\alpha\gamma\beta}$, $R^{\gamma}{}_{\alpha\delta\beta}$ es el tensor de Riemann, G es la constante de la gravitación universal y $T_{\alpha\beta}$ es el tensor energía-momento. El tensor de Riemann contiene toda la información de la curvatura del espacio-tiempo y se calcula a partir de derivadas segundas de la métrica. El tensor energía-momento proporciona una descripción completa de la densidad de energía, momento y tensiones de la materia presente en el entorno estudiado.

Las Ecuaciones de Einstein tienen solución analítica en muy pocas situaciones, en la mayoría de las ocasiones en condiciones de alto grado de simetría. Por ejemplo, en simetría esférica y vacío, tenemos la solución de Schwarzschild, cuyo tensor métrico está definido por el elemento de línea

$$ds^2 = -\left(1 - \frac{R_S}{r}\right) d(ct)^2 + \left(1 - \frac{R_S}{r}\right)^{-1} dr^2 + r^2(d\theta^2 + \sin^2\theta d\phi^2), \tag{7}$$

donde $R_S = GM/c^2$ es el radio de Schwarzschild. Aquí, tenemos una singularidad coordenada en el horizonte de sucesos $r = R_S$, que se puede evitar con un cambio de coordenadas, y otra singularidad de curvatura en $r = 0$. Otras soluciones analíticas en simetría axial son las del espacio-tiempo de Kerr.

En la mayoría de las situaciones astrofísicas relevantes, las Ecuaciones de Einstein deben resolverse numéricamente. Para ello, es conveniente expresarlas como un problema de Cauchy, o en este caso, como un sistema de leyes de balance con condiciones iniciales y de contorno. A continuación, explicaremos brevemente el procedimiento para tal cometido.

En primer lugar, se utiliza una foliación del espacio-tiempo por hipersuperficies espaciales, definidas a partir de la fijación de una coordenada temporal t. A partir de aquí, la proyección de las Ecuaciones de Einstein sobre cada hipersuperficie generará un conjunto de ecuaciones elípticas, en donde no aparecen derivadas temporales, y las proyecciones que involucran la dirección normal a las hipersuperficies generará un sistema de ecuaciones hiperbólicas. Al final, la métrica del espacio-tiempo se podrá expresar como

$$ds^2 = -(N^2 - \beta^i\beta_i)dt^2 + 2\beta_i dx^i dt + \gamma_{ij}dx^i dx^j, \tag{8}$$

donde $N := \sqrt{-1/(\nabla_\mu t\, \nabla^\mu t)}$ es la función lapso, ∇ la conexión de Levi-Civita, $\boldsymbol{\beta} = \boldsymbol{\partial}_t - N\boldsymbol{n}$ es el vector desplazamiento, $\boldsymbol{n}$ es el vector unitario normal a las hipersuperficies y γ_{ij} la métrica espacial de cada hipersuperficie. La primera expresión de las Ecuaciones de Einstein separando espacio y tiempo fue el sistema 3+1 [77, 46, 7, 135]. Este tiene dos ecuaciones de evolución

$$\partial_t K_{ij} = -D_i D_j N + N(\bar{R}_{ij} + KK_{ij} - 2K_{ik}K^k_{\ j}) - 4\pi N(\gamma_{ij}(S-E) - 2S_{ij}) + \mathcal{L}_{\boldsymbol{\beta}}K_{ij}, \tag{9}$$

$$\partial_t \gamma_{ij} = -2NK_{ij} + \mathcal{L}_{\boldsymbol{\beta}}\gamma_{ij}, \tag{10}$$

y dos ecuaciones de ligadura o restricciones

$$\bar{R} + K^2 - K_{ij}K^{ij} - 16\pi E = 0, \tag{11}$$

$$D_j K^j_{\ i} - D_i K - 8\pi p_i = 0, \tag{12}$$

donde $\mathcal{L}_{\boldsymbol{\beta}}$ es la derivada de Lie respecto de $\boldsymbol{\beta}$, K_{ij} es la curvatura extrínseca de cada hipersuperficie, $K = \gamma^{ij}K_{ij}$, $S = S^\mu_{\ \mu}$, con $S_{\mu\nu} = \gamma^\rho_{\ \mu}\gamma^\sigma_{\ \nu}T_{\rho\sigma}$, $E = n^\mu n^\nu T_{\mu\nu}$ y $p^i = -\gamma^{i\mu}n^\nu T_{\mu\nu}$. Se ha usado $c = G = 1$. Las ecuaciones de ligadura deben cumplirse en cada hipersuperficie.

En la práctica, los esquemas de resolución numérica se dividen entre los que resuelven las ligaduras solo inicialmente, llamados esquemas evolutivos, y los que las resuelven cada cierto número de pasos de tiempo, llamados esquemas ligados. Se puede demostrar que si las ligaduras se satisfacen inicialmente de manera analítica, también lo harán en posteriores hipersuperficies. Pese a esto, las ligaduras pueden no cumplirse numéricamente.

Para acabar esta sección, remarcamos el hecho de que el sistema 3+1 es débilmente hiperbólico y se deberán introducir transformaciones adicionales de las ecuaciones para obtener un sistema fuertemente hiperbólico que nos garantice la estabilidad de las simulaciones numéricas.

Ecuación de Euler con gravedad

En esta sección estudiaremos la Ecuación de Euler en presencia de gravedad en simetría esférica. Lo haremos desde el punto de vista clásico, en gravedad de Newton, y desde la Relatividad General.

En su versión clásica se obtiene de la Ecuación (2b) imponiendo $\mathbf{\Sigma} = 0$, y si queremos añadir interacción gravitatoria introduciríamos el término fuente $-\rho\vec{\nabla}\Phi$, con Φ el potencial gravitatorio de Newton. Consideremos un fluido auto-gravitante formando un objeto compacto esférico de radio R. Sea, además, un fluido politrópico cumpliendo la ecuación de estado $p = \kappa\rho^{\Gamma_1}$. Hemos deducido que las velocidades características del sistema en la superficie son

$$\lambda_\pm = \pm\frac{\sqrt{\Gamma_1\kappa}}{R}(\rho_s)^{\frac{\Gamma_1-1}{2}}, \tag{13}$$

donde ρ_s es la densidad en la superficie. Normalmente, esta densidad es cero o muy baja, lo cual vendría a indicar que las curvas características se mantienen en la superficie, donde el sistema es linealmente degenerado. Desde el punto de vista de la resolución numérica del sistema nos evitaría tener que imponer una condición de contorno en esta región.

Pasemos a Relatividad General. Esta vez consideraremos un fluido en un espacio-tiempo de Schwarzschild. La Ecuación de Euler en su versión relativista se obtiene de imponer la conservación de energía y momento $\nabla_\alpha T^{\alpha\beta} = 0$, siendo

$$T^{\alpha\beta} = (\mu + p)v^\alpha v^\beta + pg^{\alpha\beta},$$

el tensor energía-momento de un fluido perfecto, con μ la densidad de energía, p la presión y v^β la cuadrivelocidad del fluido. Asumiremos que la descripción del fluido se completa con una ecuación de estado $p = p(\mu)$.

En [73] se usan coordenadas de Schwarzschild (7) para estudiar esta ecuación, aunque, como hemos visto, este sistema de coordenadas tiene una singularidad en el horizonte de sucesos $r = R_S$. Haciendo la transformación de la coordenada temporal

$$cT = ct + 2R_S\left\{\sqrt{\frac{r}{R_S}} + \frac{1}{2}\log\left(\frac{\sqrt{r/R_S}-1}{\sqrt{r/R_S}+1}\right)\right\}, \tag{14}$$

nos deshacemos de este problema, y las nuevas coordenadas se denominan de Gullstrand-Painlevé. La Ecuación de Euler se puede escribir

como una ley de balance cuyas soluciones estacionarias son

$$r^2(1-B\gamma)(\mu+p)\frac{\gamma-B}{1-\gamma^2}=C_0, \tag{15a}$$

$$\log(1-B\gamma)-\frac{1}{2}\log(1-\gamma^2)+l(\mu)=D_0, \tag{15b}$$

con $B=\sqrt{R_S/r}$, $\gamma=v^1/v^0+B$, $l(\mu)$ es una primitiva de $p'(\mu)/(\mu+p(\mu))$ y C_0, D_0 son constantes que dependen de condiciones de contorno. Se puede demostrar que no existen soluciones estacionarias salientes de la región de agujero negro $r<R_S$ y que las curvas entrantes atraviesan el horizonte de sucesos. La obtención de estas soluciones permite el desarrollo de métodos bien balanceados [22] para la Ecuación de Euler relativista en coordenadas de Gullstrand-Painlevé de manera análoga a cómo se hizo en [72] en coordenadas de Schwarzschild.

Formulación completamente ligada de las Ecuaciones de Einstein

En esta sección extendemos la formulación FCF de las Ecuaciones de Einstein presentada en [31]. Esta se basa en hacer una transformación conforme de la métrica espacial γ_{ij} y una descomposición de la curvatura extrínseca K_{ij} en parte con y sin traza. Trataremos con las nuevas variables ψ, $\tilde{\gamma}_{ij}$ y A_{ij}, definidas como

$$\psi:=\left(\frac{\gamma}{f}\right)^{1/12},\quad \tilde{\gamma}_{ij}:=\psi^{-4}\gamma_{ij},\quad A_{ij}:=K_{ij}-\frac{1}{3}K\gamma_{ij}, \tag{16}$$

donde $\gamma=\det\gamma_{ij}$ y $f=\det f_{ij}$, con f_{ij} una métrica plana de fondo independiente del tiempo. Notemos que $\tilde{\gamma}=\det\tilde{\gamma}_{ij}=f$. A partir de la métrica plana definimos el tensor

$$h^{ij}=\tilde{\gamma}^{ij}-f^{ij}. \tag{17}$$

Usaremos las condiciones gauge $K=0$ y $\mathcal{D}_k\tilde{\gamma}^{kj}=0$. A continuación, definimos $\hat{A}^{ij}:=\psi^{-10}A^{ij}$ y consideramos su descomposición en parte longitudinal y transversal, basada en la introducción de un nuevo campo vectorial X^i,

$$\hat{A}^{ij}=(LX)^{ij}+\hat{A}^{ij}_{TT}, \tag{18}$$

donde L es el operador lineal diferencial de Killing. Por razones de precisión numérica introduciremos el campo vectorial

$$V^i = 2N\psi^{-6}X^i - \beta^i, \tag{19}$$

y cerraremos el sistema con la inclusión de la variable auxiliar $\dot{X}^i = \partial_t X^i$. Al final, el nuevo sistema estará formado por dos ecuaciones de evolución hiperbólicas para h^{ij} y $\hat{A}^{ij}_{TT}$,

$$\begin{aligned}\partial_t h^{ij} &= \beta^k\mathcal{D}_k h^{ij} - h^{ik}\mathcal{D}_k\beta^j - h^{kj}\mathcal{D}_k\beta^i + \frac{2}{3}h^{ij}\mathcal{D}_k\beta^k + 2N\psi^{-6}\hat{A}^{ij}_{TT} + (LV)^{ij} \\ &\quad -X^j\mathcal{D}^i(2N\psi^{-6}) - X^i\mathcal{D}^j(2N\psi^{-6}) + \frac{2}{3}f^{ij}X^k\mathcal{D}_k(2N\psi^{-6}).\end{aligned} \tag{20}$$

$$\begin{aligned}\partial_t\hat{A}^{ij}_{TT} &= \beta^k\mathcal{D}_k\hat{A}^{ij} - \hat{A}^{kj}\mathcal{D}_k\beta^i - \hat{A}^{ik}\mathcal{D}_k\beta^j + \frac{5}{3}\hat{A}^{ij}\mathcal{D}_k\beta^k + 2N\psi^{-6}\tilde{\gamma}_{kl}\hat{A}^{ik}\hat{A}^{jl} \\ &\quad +\frac{3}{4}N\psi^{-6}\tilde{\gamma}^{ij}\tilde{\gamma}_{lk}\tilde{\gamma}_{nm}\hat{A}^{km}\hat{A}^{ln} + N\psi^2\tilde{R}^{ij}_* - \frac{1}{4}N\psi^2\tilde{R}\tilde{\gamma}^{ij} \\ &\quad +\frac{1}{2}(\tilde{\gamma}^{kl}\mathcal{D}_k h^{ij} - \tilde{\gamma}^{ik}\mathcal{D}_k h^{lj} - \tilde{\gamma}^{kj}\mathcal{D}_k h^{il})\mathcal{D}_l(N\psi^2) \\ &\quad +4\psi^{-1}\tilde{\gamma}^{ik}\tilde{\gamma}^{jl}\mathcal{D}_k\psi\mathcal{D}_l(N\psi^2) + 4\psi^{-1}\tilde{\gamma}^{ik}\tilde{\gamma}^{jl}\mathcal{D}_l\psi\mathcal{D}_k(N\psi^2) - 2\psi^{-1}\tilde{\gamma}^{ij}\tilde{\gamma}^{kl}\mathcal{D}_k\psi\mathcal{D}_l(N\psi^2) \\ &\quad +\frac{N\psi^2}{2}\tilde{\gamma}^{kl}\mathcal{D}_k\left(\mathcal{D}_l h^{ij}\right) - 8N\tilde{\gamma}^{ik}\tilde{\gamma}^{jl}\mathcal{D}_l\psi\mathcal{D}_k\psi + 2N\tilde{\gamma}^{ij}\tilde{\gamma}^{kl}\mathcal{D}_k\psi\mathcal{D}_l\psi - \tilde{\gamma}^{ik}\tilde{\gamma}^{jl}\mathcal{D}_k\mathcal{D}_l(N\psi^2) \\ &\quad -(L\dot{X})^{ij} - 8\pi N\psi^{10}S^{ij} + 4\pi NS^*\tilde{\gamma}^{ij},\end{aligned} \tag{21}$$

y ecuaciones de ligadura elípticas para X^i, ψ, $N\psi^2$, V^i, $\dot{X}^i$. El sector de evolución del nuevo sistema será fuertemente hiperbólico, el sector elíptico tendrá unicidad local y se podrá resolver de forma jerárquica, propiedades ya presentes en su anterior versión. En este nuevo esquema resolveremos, además, las ecuaciones para las variables V^i, $(N\psi^2-1)$ y $\hat{A}^{ij}_{TT}$, cuya expansión postnewtoniana es de orden $\mathcal{O}(c^{-5})$, $\mathcal{O}(c^{-4})$ y $\mathcal{O}(c^{-5})$, respectivamente, en contraposición con las de las variables β^i, $(N\psi-1)$ y $\hat{A}^{ij}$, cuya expansión es de orden $\mathcal{O}(c^{-3})$, $\mathcal{O}(c^{-2})$ y $\mathcal{O}(c^{-3})$, respectivamente.

Como primer test de la nueva formulación se ha escogido un modelo de estrella de neutrones en rotación, considerando un espacio-tiempo estacionario. Las dos ecuaciones de evolución se transforman en una ecuación elíptica para h^{ij} y otra algebraica para $\hat{A}^{ij}_{TT}$. Mostramos algunos resultados en la Figura 2, donde vemos que las nuevas variables introducidas V^i y $(N\psi^2-1)$ tienen órdenes de magnitud hasta dos veces por debajo de las anteriores β^i, X^i, $(N-1)$ y $(\psi-1)$.

En la resolución de h^{ij} no se han impuesto directamente las condiciones $\mathcal{D}_k\tilde{\gamma}^{kj}=0$ y $\tilde{\gamma}=f$. En el primer caso, un análisis numérico determinó que es necesaria una estrategia de resolución de h^{ij} donde se tenga en

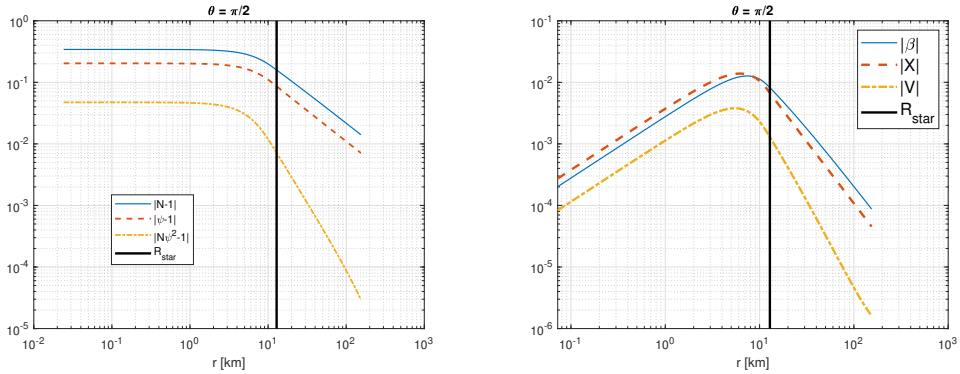

Figura 2: Perfiles radiales en $\theta = \pi/2$ en escala log-log. La línea vertical continua indica el radio de la estrella. Izquierda: $(N-1)$ (línea azul continua), $(\psi-1)$ (línea roja discontinua) y $(N\psi^2-1)$ (línea amarilla punteada-discontinua). Derecha: β^i (línea azul continua), X^i (línea roja discontinua) y V^i (línea amarilla punteada-discontinua).

cuenta esta condición. Aun así, al alejarse del centro de la estrella obtenemos un error relativo de menos del 10 % cuando comparamos la divergencia $\mathcal{D}_k\tilde{\gamma}^{kj}$ con la mayor de las derivadas involucradas. En cuanto a la condición del determinante, obtenemos que se satisface al nivel del error numérico.

Se planea aplicar el nuevo sistema en simulaciones numéricas de escenarios astrofísicos más complejos y dinámicos, y extraer la correspondiente radiación gravitatoria del sistema. Esta reformulación también puede usarse para calcular datos iniciales mediante diferencias finitas más allá de la condición de métrica espacial conformemente plana. Otra potencial aplicación de este trabajo es usar una versión simplificada del esquema en el contexto de simulaciones cosmológicas, considerando únicamente los términos principales en la expansión postnewtoniana.

Ecuaciones de la magnetohidrodinámica relativista con resistividad

En esta sección explicaremos los resultados del artículo publicado [29], donde se tratan las ecuaciones de la Magnetohidrodinámica Relativista con Resistividad. Por un lado, tenemos el sector de la electrodinámica, que determina la evolución del campo magnético $\boldsymbol{B}$ y eléctrico $\boldsymbol{E}$, y por otro el sector de la hidrodinámica, involucrando densidad de masa,

energía y presión. La ecuación de evolución del campo eléctrico $\boldsymbol{E}$ tiene un término potencialmente duro debido a que la conductividad σ puede ser alta o muy alta. En trabajos anteriores como [37] y [96] se han usado métodos Implícitos-Explícitos (IMEX) de Runge-Kutta para la integración temporal de estas ecuaciones, los cuales tratan el comportamiento duro en leyes de balance obteniendo simulaciones estables. Aquí usaremos un método alternativo que conservará las propiedades de estabilidad y tendrá un coste computacional similar al de un método explícito.

Usaremos $c = \epsilon_0 = \mu_0 = 1$, donde ϵ_0, μ_0 son, respectivamente, la permitividad y la permeabilidad del vacío. El sistema de ecuaciones de evolución tiene la forma

$$\partial_t E^j = S_E^j - \sigma\,\Gamma\left(E^j + (\boldsymbol{V}\times\boldsymbol{B})^j - (V_l E^l)V^j\right), \tag{22}$$

$$\partial_t B^j = S_B^j, \tag{23}$$

$$\partial_t Y = S_Y, \tag{24}$$

donde V^i es la velocidad del fluido, $\Gamma = (1-V^2)^{-1/2}$ es el factor de Lorentz e Y representa el resto de variables, incluyendo las variables conservadas del sector de la hidrodinámica y la densidad de carga. Los términos etiquetados con S son términos fuente a tratar de forma explícita en la resolución numérica.

El nuevo esquema para la integración temporal se basará en lo siguiente. Sea el sistema de leyes de balance

$$\partial_t U + \partial_i F^i(U) = S(U),$$

donde U es el vector de variables conservadas. Supongamos que la fuente se puede separar en un término de magnitud controlada S_E y otro potencialmente duro σS_I tal que $S(U) = S_E(U) + \sigma S_I(U)$. Un método IMEX evaluaría de forma implícita todo el término $\sigma S_I(U)$. Supongamos que podemos escribir $S_I^i(U) = H^i + \sum_{j=1}^n G_j^i(U)\,U^j$, donde H^i no depende de las variables conservadas. Nuestro nuevo enfoque consistirá en evaluar implícitamente solo las variables conservadas U^i que multiplican a los factores $G_j^i(U)$, y el resto de cantidades se evaluarán explícitamente. Nos referiremos a esta nueva estrategia como método Runge- Kutta Mínimamente Implícito (MIRK, por sus siglas en inglés).

Con esto, la ecuación del método a primer orden para (22) se puede escribir como:

$$E^i|_{n+1} = E^i|_n + \frac{\Delta t}{1+\Delta t\,\bar\sigma|_n}\left(S_E^i|_n + \bar\sigma|_n\,E^l|_n(V^i|_n V_l|_n - \delta_l^i) - \bar\sigma|_n(\boldsymbol{V}|_n\times\boldsymbol{B}|_{n+1})^i\right). \tag{25}$$

Tiene la misma forma que la de un método explícito de primer orden con un paso de tiempo efectivo $\Delta t/(1+\Delta t\,\bar{\sigma}|_n)$, donde $\bar{\sigma} = \Gamma\sigma$. Hemos escogido los valores de los coeficientes del método de tal manera que se preserve la estabilidad y se reproduzcan correctamente los comportamientos ondulatorios y de la magnetohidrodinámica ideal o también límite duro ($\sigma \to \infty$). De manera análoga, podemos hallar las ecuaciones del método a segundo orden obteniendo unas expresiones que recuerdan a las de un método explícito de segundo orden con un tiempo efectivo.

Se han llevado a cabo simulaciones para poner a prueba el método en dos tests simples en una dimensión espacial. El primero es el llamado test de la corriente auto-similar donde no hay evolución de la parte hidrodinámica, y el segundo es el de las ondas Alfven polarizadas circularmente. En este último es necesaria la evolución del sector hidrodinámico y es necesaria una recuperación de variables primitivas. No obstante, esta recuperación se ha realizado de manera directa gracias a las evaluaciones explícitas en el término duro. Se han completado simulaciones estables y realizado análisis de convergencia en todos los test a primer y segundo orden.

Ecuaciones del transporte radiativo

La interacción entre neutrinos y materia juega un papel determinante en las simulaciones de explosiones de supernova [88, 89] y colapso de binarias de estrellas de neutrones [104]. Esta interacción debe tener en cuenta las ecuaciones de la Hidrodinámica Radiativa; esto es, la evolución de las ecuaciones del sector hidrodinámico acopladas con las ecuaciones de transporte radiativo de neutrinos. Estas últimas se obtienen al resolver la Ecuación de Boltzmann para la función de distribución de las partículas radiativas, los neutrinos en nuestro caso. La función de distribución depende del tiempo, la posición y el momento de las partículas, dificultando la resolución directa de la Ecuación de Boltzmann.

El Método de los Momentos es una estrategia para resolver la Ecuación de Boltzmann basada en la definición de nuevas variables construidas a partir de integrales de la función de distribución en el espacio de momentos. Dentro de cada integral, la función de distribución es multiplicada por productos tensoriales del vector unitario $\boldsymbol{N} = \boldsymbol{K}/K$, con $\boldsymbol{K}$

el vector de onda, indicando la dirección de propagación de la radiación. El número de veces n que se multiplica tensorialmente $\boldsymbol{N}$ por sí mismo determina el orden n de la nueva variable, designada momento de orden n. La idea del método consiste en truncar la serie de momentos a cierto orden n y determinar los de orden superior a partir de relaciones algebraicas. De esta manera queda definida la familia de métodos M_n. Más detalles pueden consultarse en [63].

En los métodos M_1 se consideran como variables la densidad de energía radiativa E y la densidad de momento F^i, y constituyen un buen compromiso entre coste y precisión para resolver la Ecuación de Boltzmann. Así pues, las ecuaciones del transporte radiativo en la clausura M_1 tienen la forma

$$\partial_t E = S_E + c\,\kappa_a(E_{\rm eq} - E), \tag{26a}$$

$$\partial_t F^i = S_F^i - c\,\kappa_{\rm tra} F^i, \tag{26b}$$

donde κ_a, $\kappa_{\rm tra}$ son las opacidades de absorción y de transporte, respectivamente, $E_{\rm eq}$ es una densidad de energía de equilibrio y los términos con S son términos fuente de magnitud controlada. Las opacidades son escalares que pueden alcanzar valores altos o muy altos, haciendo que el sistema anterior tenga un comportamiento duro. Por tanto, el método MIRK explicado en la sección anterior es de vital importancia. Métodos IMEX se han usado recientemente para integrar temporalmente estas ecuaciones [57]. Aquí, aplicaremos el método MIRK para la resolución numérica del sistema (26) en simulaciones de colapso de supernova. Usaremos la misma estrategia que en [63] para el tratamiento numérico del resto de variables involucradas.

De la misma manera que en la sección anterior, podemos hacer un análisis lineal de estabilidad y en límite duro $\kappa_a, \kappa_{\rm tra} \to \infty$ para fijar los coeficientes del método. Igualmente, las evaluaciones explícitas nos permiten escribir las ecuaciones del método en una forma que recuerde a las de un método explícito. A primer orden se pueden escribir como

$$E^{n+1} = E^n + \frac{\Delta t}{1 + \Delta t\,\kappa^n}\left(S_E^n + \kappa^n(E_{\rm eq}^n - E^n)\right), \tag{27a}$$

$$(F^i)^{n+1} = (F^i)^n + \frac{\Delta t}{1 + \Delta t\,\kappa'^n}\left((S_F^i)^n - \kappa'^n (F^i)^n\right), \tag{27b}$$

donde $\kappa = c\kappa_a$ y $\kappa' = c\kappa_{\rm tra}$. Efectivamente, el esquema es similar al de un método explícito con un paso de tiempo efectivo $\Delta t/(1 + \Delta t\,\kappa^n)$ en (27a) y $\Delta t/(1 + \Delta t\,\kappa'^n)$ en (27b). De la misma forma, a segundo orden, podemos

obtener expresiones parecidas a las de un método explícito.

En todos los casos se han obtenido regiones de estabilidad para los coeficientes haciendo un análisis lineal. Con el método MIRK de primer y segundo orden hemos sido capaces de realizar simulaciones estables de colapso de supernova usando valores de los coeficientes dentro de estas regiones de estabilidad. Por otro lado, otras elecciones han producido simulaciones estables pero convergentes hacia valores de las variables incorrectos en el límite duro, y otras simulaciones han sido inestables en el régimen duro. Encontramos una relación directa entre la clasificación de cada caso y nuestro análisis teórico.

Ecuaciones de estado realista para materia nuclear

Se ha visto que los datos tabulados de ecuaciones de estado realista para materia nuclear pueden provocar que simulaciones con estrellas de neutrones sean inestables. Esto es debido a que estos datos, calculados a partir de física nuclear y de partículas, tienen demasiado ruido. Por tanto, es conveniente una estrategia para suavizarlos.

En esta sección describiremos brevemente un algoritmo desarrollado para llevar a cabo regresión polinómica en varias variables. Dicha regresión nos ayudará al suavizado de los datos anteriores. En general, las ecuaciones de estado realistas para materia nuclear dependen de tres variables independientes. En las tablas de la base CompOSE [1] se usan densidad del número bariónico n_b, fracción del número de electrones Y_e y temperatura T. El ajuste se realizará sobre el índice adiabático, a partir del cual se pueden hallar el resto de variables termodinámicas. Todos los cálculos se han realizado con la librería LORENE [2], que utiliza expansiones espectrales para las funciones en términos de los polinomios de Chebyshev.

En una variable, el método de mínimos cuadrados se puede usar para ajustar los n datos $(\boldsymbol{x}, \boldsymbol{y}) = (x_i, y_i)_{i=1}^{i=n}$ al polinomio de grado N

$$p_N(x) = a_0 + a_1 x + ...a_N x^N. \tag{28}$$

Para ello es útil la matriz de Vandermonde $A_{ij}^x = (x_i)^j$, a partir de la

cual se pueden hallar los coeficientes $\boldsymbol{a} = (a_j)_{j=0}^{j=N}$ mediante la operación $\boldsymbol{a} = \boldsymbol{\beta}\alpha^{-1}$, donde $\boldsymbol{\beta} = \boldsymbol{y}A^x$ y $\alpha = (A^x)^T A^x$. A continuación describiremos un algoritmo para ajustar por el método de mínimos cuadrados los datos $(\boldsymbol{x}, \boldsymbol{y}, \boldsymbol{z}) = (x_i, y_i, z_i)_{i=1}^{i=n}$ al polinomio más general que depende de dos variables

$$\begin{aligned} p_N(x,y) =& a_0 + a_1 x + a_2 x^2 + ... + a_N x^N + a_{N+1} y + a_{N+2} xy + ... \\ &+ a_{k(i,j)} x^i y^j + ... + a_M y^N, \end{aligned} \tag{29}$$

donde $M = (N+2)(N+1)/2$. El procedimiento es similar al caso de una variable; solo que construiremos una matriz de Vandermonde generalizada A^{xy} a partir de la cual, mediante expresiones análogas a las anteriores, hallaremos los coeficientes $\boldsymbol{a} = (a_j)_{j=0}^{j=M}$. La matriz A^{xy} se construirá a partir de las matrices de Vandermonde para los datos $\boldsymbol{x}$, A^x, e $\boldsymbol{y}$, A^y, mediante la expresión

$$A^{xy}_{ij} = A^x_{im_j} A^y_{il_j} \tag{30}$$

donde l_j es el único entero cumpliendo $f_N(l_j - 1) < j \leq f_N(l_j)$, con

$$f_N(l_j) := \binom{N+2}{N} - \binom{N-l_j+2}{N-l_j}, \tag{31}$$

y $m_j = j \mod f_N(l_j - 1)$, asignando $j \mod 0 := j$. El proceso también se ha extendido a tres variables construyendo una matriz A^{xyz}_{ij} a partir de las tres matrices de Vandormonde de cada una de las variables independientes. Esta estrategia ha permitido la obtención de datos suaves realistas de ecuaciones de estado para simulaciones de estrellas de neutrones.

Conclusiones y trabajo futuro

En primer lugar, hemos usado simulaciones del flujo sanguíneo en la aorta para validar el método de reconstrucción presentado en [108], el cual se espera mejorar en el futuro para que sea capaz de reproducir la morfología de la aorta de forma más precisa. Por ejemplo, teniendo en cuenta los senos de Valsalva o las arterias supraórticas. El objetivo es identificar qué parámetros de la geometría son claves para la generación de aortas sintéticas. Finalmente, esperamos que la generación de aortas sintéticas nos provea de una muestra grande y realista para llevar a cabo simulación del flujo sanguíneo, con el objetivo de establecer relaciones

entre aspectos geométricos y valores anómalos de la presión de cizalla. Por otro lado, hemos hecho un estudio preliminar de la influencia de tipo de válvula aórtica en los valores de la presión de cizalla, obteniendo que la válvula tricúspide era la que proporcionaba valores más sanos. Todas las simulaciones se han hecho en flujo estacionario como primera aproximación. Esperamos que la simulación transitoria teniendo en cuenta todo el ciclo cardíaco y la interacción fluido-estructura nos aporte resultados más realistas, así como calcular otras magnitudes dependientes del tiempo de interés médico.

Posteriormente, estudiamos la Ecuación de Euler con gravedad, primero de forma clásica y después relativista, en simetría esférica. En el estudio clásico, hicimos un estudio a primer orden expandiendo la solución en torno a un valor fijo, viendo que el sistema era linealmente degenerado en la superficie, es decir, la superficie es una discontinuidad de contacto. Por otro lado, analizamos la versión en Relatividad General en un espacio-tiempo de Schwarzschild y en coordenadas de Gullstrand-Painlevé. Escribimos la ecuación como una ley de balance y hallamos las soluciones estacionarias. La obtención de estas soluciones estacionarias permitirá el desarrollo de métodos bien balanceados [22] para la resolución numérica de la ecuación en ausencia de estacionariedad, de manera análoga a como se hizo en [72] en coordenadas de Schwarzschild, teniendo en cuenta que en este caso el dominio $0 < r < \infty$ está disponible.

Ampliamos la formulación FCF de las Ecuaciones de Einstein [31] introduciendo las variables V^i y $\dot{X}^i$. La nueva versión conserva las buenas propiedades de unicidad local y estructura jerárquica y posee ventajas de precisión numérica. Hemos realizado las primeras pruebas preliminares con una estrella de neutrones en rotación. Calculamos los datos iniciales resolviendo numéricamente el nuevo sector elíptico. Está previsto para el futuro aplicar la nueva formulación a escenarios astrofísicos más complejos y contextos cosmológicos.

A continuación, hemos introducido el método Runge-Kutta Mínimamente Implícito (MIRK, de sus siglas en inglés) para leyes de balance con términos potencialmente duros. En este nuevo enfoque solo las variables conservadas son evaluadas implícitamente de forma mínima en el término duro. Esto permitió que las ecuaciones del método hayan podido escribirse de manera similar a las de un método explícito. Por tanto, preservamos las buenas propiedades de los métodos implícitos manejando términos duros con un coste computacional propio de un método explíci-

to. Aplicamos el método en dos test simples de la Magnetohidrodinámica Relativista Resistiva (corriente auto-similar y ondas Alfven) y las ecuaciones del Transporte Radiativo de neutrinos en simulaciones de colapso de supernova. En todos los casos se obtuvieron simulaciones estables aplicando el método MIRK a primer y segundo orden.

Otras aplicaciones de esta nueva estrategia son posibles en otras leyes de balance con términos duros como en Electrodinámica libre de fuerzas [82], gases enrarecidos [66] y ecuaciones de aguas poco profundas [66]. Además, puede ser interesante una combinación con métodos bien balanceados [22] para recuperar soluciones cerca de una solución estacionaria.

El último trabajo del que hablamos en este manuscrito era sobre regresión polinómica en varias variables con el que objetivo de suavizar datos tabulados de la base CompOSE [1] para modelizar ecuaciones de estado realistas para materia nuclear. Desarrollamos un algoritmo para llevar a cabo dicha tarea teniendo en cuenta la expresión más general de un polinomio con dos y tres variables independientes. Planeamos para el futuro acoplar estos ajustes con simulaciones con estrellas de neutrones con la librería LORENE [2]. Esta librería se basa en métodos espectrales, donde cada variable se trata como una expansión truncada en polinomios de Chebyshev $T_i(x)$. Un proyecto futuro es implementar expansiones de funciones de varias variables (x_j) en términos de productos de polinomios de Chebyshev $\prod_j T_{i_j}(x_j)$. Esto ayudaría a tratar de forma analítica las variables termodinámicas calculadas a partir del ajuste polinómico en varias variables.

Abstract

In this work we face hyperbolic and elliptic systems of partial differential equations with applications from health sciences to astrophysics. Some will be framed in the context of classical mechanics and other in the Theory of Relativity.

Concerning the classical sector we will solve Navier-Stokes Equations to model the blood flow in aorta trying to get some relations between geometrical features and physiological magnitudes of interest. We will also discuss the Euler Equation from both Newtonian and general relativistic approach. We will derive some theoretical results with applications in the development of numerical methods for this balance law.

We will propose an improved version of a Fully Constrained Formulation of the Einstein Equations. It will preserve the local uniqueness from previous versions and posses accuracy improvements with the introduction of new variables. Some preliminary test will be carried out.

On the other hand, we will introduce a new numerical method to perform the time integration of stiff balance laws. The new approach present stability properties of implicit methods dealing with stiffness but with a computation cost similar to that of an explicit method. First tests in the context of Resistive Relativistic Magnetohydrodynamics and Radiation Hydrodynamics were performed.

We will finish with a new algorithm to polynomial regression in several variables with applications in simulations of neutron stars.

1

Introduction

1.1 Motivation

Throughout the manuscript we will encounter an academically broad set of physical scenarios with motivations from health sciences to astrophysics. Some come from classical mechanics and other will be framed in the Theory of Relativity. Either classical or relativistic its dynamics will be model by a hyperbolic system of partial differential equations of the form

$$\partial_t U + \sum_{i=1}^{d} \partial_i F^i(U) = r(U), \quad x \in \mathbb{R}^d, \quad t \in \mathbb{R}^+, \tag{1.1}$$

where $U = (U_1, \ldots, U_m)^T : \mathbb{R}^d \times \mathbb{R}^+ \longrightarrow \mathbb{R}^m$ is the vector of conserved variables and the functions $F^i : \mathbb{R}^m \longrightarrow \mathbb{R}^m$, are called fluxes. We will say that a system like (1.1) is a balance law, and when $r = 0$ we will refer to it as a conservation law. Many strategies are available to tackle each problem and we will choose the most suitable one in each case.

On the one hand, a classical fluid mechanics scenario will be studied: blood flow in aorta. It has been proved that a hemodynamic flow dependent quantity, called wall shear stress, is related to the genesis of many cardiovascular diseases, see [83]. It is known that anomalous values of this magnitude in the aorta can induce atherosclerosis, that at the same time produces stenosis, a shrinking of the arteries. Computational Fluid Dynamics is believed to help in the task to establish the genesis of such undesired values. The equations involved in this context are the Navier-Stokes Equations in its classical form.

On the other hand, we will study the dynamical behaviour of a fluid in astrophysical scenarios from a fundamental point of view. Viscous effects will be neglected, so we work with the Euler Equation. First, a self-gravity fluid is considered, which constitutes the model of a star. Then, a fluid moving in a black hole environment is addressed. In order to get some insight about the numerical resolution of theses systems is important to have information about the characteristic curves and the stationary solutions. Classical and modern gravity approaches are considered.

General Relativity is the accepted theory to describe gravitation. It is ruled by the Einstein Equations, a highly non-linear and coupled system of partial differential equations. Relevant astrophysical scenarios require the numerical resolution of these equations, and to do so, a formulation of the Einstein Equations as a Cauchy problem is convenient. The area that encompass all the aspects involved in the numerical resolution of the Einstein Equations is called Numerical Relativity. Some advances from the accuracy point of view in this topic will be exposed here.

Another contexts where we will be interested in are astrophysical environments with a stiff behaviour. Stiffness arise in some conservation laws when one of the source terms becomes much higher than the rest. Electrodynamics with interacting media can become stiff when the conductivity of the media is high. This is the case in accretion disks, active galactic nuclei, relativistic jets, quasars, or compact objects. Here, the electromagnetic field interacts with a charged fluid which at the same time is relativistic. The topic that addresses this kind of phenomena is called Resistive Relativistic Magnetohydrodynamics.

Another scenario where we find stiff conservation laws is core-collapse supernovae, where neutrino radiation interact with nuclear matter. Radiation Hydrodynamics is the area that describes such scenario. Here,

the stiff behaviour is determined by the scattering and transport opacities present in the Radiation Transport equations for neutrinos.

Implicit methods are necessary in conservation laws with stiff terms. One example are the Implicit-Explicit Runge-Kutta Methods. It turns out that the management of the stiff terms in systems that model relevant astrophysical scenarios is a very time-consuming process, and it is the main contributor to burden the numerical resolution.

We will also address a numerical issue that arise in the context of realistic equations of state for nuclear matter. It has been seen that tabulated data from particle and nuclear physics to model the nuclear matter present in neutron stars are too noisy to be used in numerical simulations. A smoother strategy is convenient, and here, we will choose polynomial regression of these data. Realistic equations of state depend on three independent thermodynamic variables in general. Then, a strategy to carry out polynomial regression in several variables is needed.

1.2 Previous work

We outline different studies about the contexts previously described.

Many studies about blood flow with health purposes have been published, see [61, 21] as examples. Different type of vessels and models have been used with different health goals. The work [21] includes an analysis of the wall shear stress values in aorta. A complete study of the blood flow in arteries requires Fluid Structure Interaction models [122, 131]. These models describe the interaction between the fluid and the walls of the recipient it flows through. But only a few groups have started applying Machine Learning techniques to relate geometrical aspects of aorta with blood flood behaviour. The work [76] has provided good results in this goal but with a high simplification of the geometry involved. A strategy that encompasses realistic descriptions of the aorta geometry and realistic models for the blood flow is believed to improve such studies.

The Euler Equation in presence of gravity was studied in the works

[73, 72] with the aim of the development of well-balanced methods. Stability analysis and derivation of stationary solutions were performed in spherical symmetry and in Schwarzschild coordinates. However, these coordinates precise a particular treatment of the event horizon in the presence of a black hole. This technical issue constrains the spatial domain not to cover the desired spatial region.

Concerning Numerical Relativity, several studies have been carried out since the 40s. The first ones [77, 46, 7, 135] rewrote the Einstein Equations splitting space and time in the so-called 3+1 system. They split in a set of hyperbolic equations (evolution equations) and elliptic equations (constraint equations). Strong hyperbolic formulations are necessary to carry out numerical simulations. Some examples are the BSSNOK (see [13, 90, 117]) or the Fully Constrained Formalism (FCF) [18] formulations. The first is framed in the so-called free evolution schemes, where the constraints are solved only initially and then monitored to check the accuracy of the numerical solution through the evolution. The latter is framed in the so-called constrained schemes, where the constraints are solved every certain number of time steps. We will focus on constrained schemes. Here, some numerical simulations have been performed using the Conformal Flatness Condition [31], which assumes that the metric is conformally flat, and other works using the FCF for solving a stationary spacetime [79] or dealing with dynamical spacetimes [27].

Conservation laws with stiff terms have been addressed with the employment of implicit schemes in many works. Examples with the Resistive Relativistic Magnetohydrodynamics equations can be found in [67, 37, 96], to cite a few ones. In [67] the ideal Magnetohydrodynamic equations were tackled with Godunov schemes. In [37, 96] Implicit-Explicit Runge-Kutta methods were employed for the time integration. In Radiation Hydrodynamics also implicit methods have been used in [92, 70, 62] to treat Radiation Transport sector to model neutrino-matter interactions.

Polynomial regression in several variables has been possible by means of the Kronecker product of Vandermonde matrices, see [35] for an example. This provides an easy extension of the method of least squares for the polynomial regression in one variable. The expression of the polynomial fitted is not the most general one though, as it does not contain all possible monomials.

1.3 Scope of the work

Simulations of blood flow in aorta are to be carried out to validate the reconstruction method [108] which supposes the first steps of a generating method of synthetic aortas. This method will allow applying Machine Learning techniques to relate geometrical aspects of aortas and anomalous behaviour of walls shear stress values. We also perform a preliminary analysis about the dependence of the wall shear stress values with different inlet boundary conditions reproducing different types of aortic valves. The complexity of the geometry involved will take us to the employment of the Finite Volume Method.

We will write the general relativistic Euler Equation in Gullstrand-Painlevé coordinates. Doing so, the spatial domain without including the central curvature singularity will be available, as the coordinate singularity of the event horizon will have been removed. We will establish some stability results and the stationary solutions in the new coordinates, which will ease the development of well-balanced methods for the Euler Equation in this context.

Moreover, we will propose a modification of the FCF equations. The system will present local uniqueness, a hierarchical structure and some accuracy improvements with respect to previous formulation. The numerical implementation of the formulation was completed and some preliminary tests concerning a rotating neutron star were carried out.

We also present a new numerical integration scheme to conservation laws with stiff terms, the so-called Minimally Implicit Runge-Kutta (MIRK) methods. Our new approach will keep the good properties of implicit methods but with a much smaller computational cost. In our opinion, this method will be very useful in many astrophysical contexts where stiff behaviours arise. In this work, we will apply it to the two aforementioned scenarios: the Resistive Relativistic Magnetohydrodynamics equations and the Radiation Transport equations for neutrino dynamics.

Finally, we will explain a strategy to numerically treat realistic equations of state for nuclear matter present in neutron stars. An algorithm

to apply polynomial regression in several variables will be outlined. The strategy followed will be different from the one using Kronecker products in the sense that we will consider the most generic form of the polynomial.

1.4 Organization of the manuscript

The manuscrpt is organized as follows:

In the Chapter 2 we will introduce basic concepts about Computational Fluid Dynamics, including Navier-Stokes Equations, the concept of turbulence and different turbulent models. The Finite Volume Method will also be briefly described. All these concepts are applied in the Chapter 3 where we face the simulation of blood flow in aorta. The physical model to describe the scenario will be detailed and we will also outline basic features about OpenFOAM, the Finite Volume solver used. There, results about the validation of the reconstruction method and a wall shear stress analysis is performed. With these chapters we finish with classical mechanics and we start addressing problems contextualized in the Theory of Relativity.

In the Chapter 4 we overview some basic ideas about Special Relativity and General Relativity. We will present the equations describing fluid dynamics and electrodynamics in its relativistic version and some analytical solutions of the Einstein Equations. We will also introduce foliations of spacetime and the 3+1 decomposition of Einstein Equations, commonly used in Numerical Relativity. In the Chapter 5 we will study the Euler Equations with gravity. Firstly, in the context of Newtonian gravity and, secondly, in General Relativity. In the Chapter 6 we present a reformulation of the FCF of the Einstein Equations and we will use it to numerically solve a stationary spacetime.

On the other hand, in the Chapters 7 and 8 we will apply the MIRK methods to integrate the evolution equations of the Resistive Relativistic Magnetohydrodynamics and the Radiation Transport, respectively. In the first case, we will present the self-similar current sheet and the Cir-

cular Polarized Alfven Waves tests. In the second case, we will deal with the transport equations for neutrino radiation in the M_1 closure.

Finally, in the Chapter 9 we will describe the numerical problem that arises in the context of simulations with neutron stars when realistic equations of state are used. There, we will show the proposed algorithm to carry out polynomial regression in several variables using the most general expression of the polynomial.

We summarize the whole work in the Chapter 10, where some conclusions and perspectives are mentioned.

1.5 Notations and conventions

We will follow the next notations and conventions:

- Greek indices (μ, ν, α, β, ...) are used for the four-vectors and four-tensors and run from 0 to 3.
- Latin indices (i, j, k, l, ...) are used for the spatial vectors and tensors and run from 1 to 3.
- We use Einstein's summation convention over repeated indices.
- The abbreviations $\partial_t = \frac{\partial}{\partial t}$ and $\partial_\alpha = \frac{\partial}{\partial x^\alpha}$ will be followed.
- The four-vector fields will be denoted by bold lowercase letters, meanwhile three-vector fields in bold uppercase letters.
- All components of the vectors in some basis are written with the indices placed above, for instance $\boldsymbol{v} = v^\alpha \boldsymbol{e}_\alpha$.
- The metric tensor $g_{\alpha\beta}$ of a vector space is used to lower the upper (contravariant) indices of vectors and tensors, while the inverse of the metric tensor, denoted $g^{\alpha\beta}$, raise the lower (covariant) indices.

2

Overview about Computation Fluid Dynamics

In this Chapter we introduce the Navier-Stokes Equations. They are a system of partial differential equations to describe the fluid dynamics in classical mechanics. We will define concepts as wall shear stress or turbulence that will be used in the Chapter 3 where we address the blood flow problem in aorta. There exist several formulations of the Navier-Stokes Equations that fit worse or better depending on the type of fluid flow. For instance, a turbulent model will be useful in turbulent flows. They are also used in complex scenarios with complex geometries, where a numerical method is to be applied. The area concerning the numerical resolution of fluid problems is called Computational Fluid Dynamics (CFD). The Finite Volume Method (FVM) is one the most widely used to solve the Navier-Stokes Equations and we will briefly illustrate the main concepts of it. Moreover, other numerical aspects and strategies will be outlined. All the figures have been generated by the author of this manuscript using LaTeXDraw.

2.1 Navier-Stokes Equations

The Navier-Stokes Equations are a set of partial differential equations that describe the dynamics of a fluid. They are used to model a wide range of fluid flow phenomena, included in health sciences, aerodynamics, meteorology, and oceanography. The equations involve fluid variables such as pressure, density, velocity or temperature. Several references [71, 128, 33] show a vast description of the Navier-Stokes Equations in all these areas. They embrace three blocks, each one coming from mass, momentum and energy conservation, respectively. Throughout this text we will not need the energy equation and the first two blocks, leaving aside gravity, take the form:

$$\partial_t \rho + \vec{\nabla} \cdot (\rho \boldsymbol{V}) = 0, \tag{2.1a}$$

$$\partial_t (\rho \boldsymbol{V}) + \vec{\nabla} \cdot (\rho \boldsymbol{V} \otimes \boldsymbol{V}) = -\vec{\nabla} p + \vec{\nabla} \cdot \boldsymbol{\Sigma}, \tag{2.1b}$$

where ρ is the density of the fluid, $\boldsymbol{V}$ is the Eulerian velocity and p the pressure. The sign $\otimes$ stands for the tensor product and $\boldsymbol{\Sigma}$ is the viscous stress tensor field. If viscous stresses are neglected ($\boldsymbol{\Sigma} \to 0$) the Equation (2.1b) is called Euler Equation. Usually, one needs two constitutive equations to close the system: an equation of state $p = p(\rho)$ and another one for $\boldsymbol{\Sigma}$.

In compressible flows, there are few well-established theoretical results for determining the permissible boundary conditions. Consequently, CFD practice often relies on physical arguments and the success of its simulations. Our focus is on tubular problems, which involve a boundary constituted by an inlet, outlet and wall, as it is illustrated in the Figure 2.1. The inlet is the patch through which the fluid flows into the enclosed volume, and the outlet patch through which the fluid exits. The remaining portions of the boundary are referred to as walls. Let $\mathcal{V}$ be the domain of the tubular volume in $\mathbb{R}^3$, where our mechanical fluid problem takes place, and $\partial\mathcal{V}$ its boundary. Then $\partial\mathcal{V} = \Gamma_{\text{in}} \cup \Gamma_{\text{out}} \cup \Gamma_{\text{wall}}$ is the partition of the boundary in the inlet, outlet and wall, respectively. The most

used type of boundary conditions [128] are the following ones:

$$\begin{cases} \rho(x,0) = f_\rho(x) \\ \boldsymbol{V}(x,0) = \boldsymbol{f}_V(x) \end{cases} \quad \text{if } x \in \mathcal{V}$$

$$\begin{cases} \rho(x,t) = g_\rho(x) \\ \boldsymbol{V}(x,t) = \boldsymbol{g}_V(x) \end{cases} \quad \text{if } x \in \Gamma_{\text{in}} \tag{2.2}$$

$$\boldsymbol{V}(x) = \boldsymbol{c} \quad \text{if } x \in \Gamma_{\text{wall}}$$

$$\begin{cases} p(x,t) = g_p(x) \\ \partial V_n / \partial n(x) = 0 \end{cases} \quad \text{if } x \in \Gamma_{\text{out}}$$

where letters f and g stand for functions, either scalar or vector, $\boldsymbol{c}$ is a constant vector and the n-direction is the the normal direction to the corresponding point in the boundary. The boundary condition for the velocity in the outlet is referred as fully-developed flow condition and if $\boldsymbol{c} = 0$ we speak of non-slip condition.

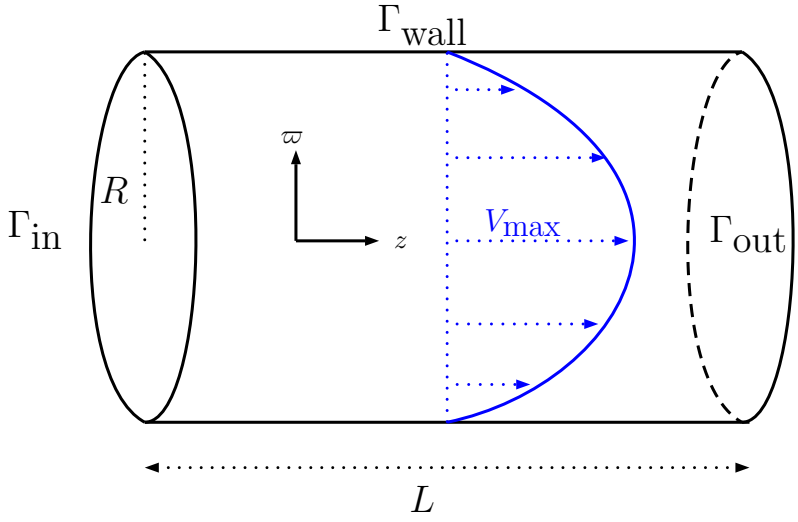

Figure 2.1: Poiseuille flow in a tubular surface.

From now on, we restrict ourselves to incompressible flows. In incompressible flows the density ρ is a constant. Then, a equation of state for p is no longer needed. On the other hand, we will take into account the Stokes's constitutive equation for $\boldsymbol{\Sigma}$ in the case of incompressible flows:

$$\boldsymbol{\Sigma} = \upsilon(\vec{\nabla}\boldsymbol{V} + \vec{\nabla}\boldsymbol{V}^T), \tag{2.3}$$

where υ is a constant called viscosity. Fluids that accomplish this law are called **Newtonian fluids**. Therefore, the incompressible Navier-Stokes Equations read

$$\vec{\nabla} \cdot \boldsymbol{V} = 0, \tag{2.4a}$$

$$\partial_t \boldsymbol{V} + \boldsymbol{V} \cdot \vec{\nabla} \boldsymbol{V} = -\frac{1}{\rho} \vec{\nabla} p + \nu \vec{\nabla}^2 \boldsymbol{V}, \tag{2.4b}$$

where we have defined the kinematic viscosity $\nu = \upsilon/\rho$. If all variables are time-independent we have a steady-state flow. Boundary conditions in incompressible flows can be the same as the ones in (2.2) but just ignoring ρ.

We are now in position to give a mathematical definition of wall shear stress, denoted τ_{w}. Consider a fluid flowing in contact with some surface $\mathcal{S}$. Be $x \in \mathcal{S}$, **the wall shear stress** (WSS) in that point is

$$\tau_{\mathrm{w}} := -\boldsymbol{\Sigma}(x)(\boldsymbol{N}, \boldsymbol{T}). \tag{2.5}$$

Let us explain this formula. $\boldsymbol{\Sigma}$ is a 2-tensor field, so the evaluation in x gives a tensor, the shear stress tensor, that acts over the vector $\boldsymbol{N}$ and $\boldsymbol{T}$. $\boldsymbol{N}$ is the normal vector to the surface in x, and $\boldsymbol{T}$ is the tangential vector to the surface in x defined as

$$\boldsymbol{T} = \lim_{y \to x} \frac{\boldsymbol{V}}{\|\boldsymbol{V}\|}(y),$$

when the limit exists. This definition only makes sense when the vectors $\boldsymbol{N}$ and $\boldsymbol{T}$ can be defined unequivocally, at least near the surface.

To give some insight, we take a simple case: Poiseuille flow (see Figure 2.1). This is an incompressible viscous fluid flowing through a finite cylindrical pipe induced by a pressure difference Δp between the ends. Let us suppose cylindrical coordinates (ϖ, ϕ, z) and the axis of the pipe aligned with z axis. A simple analytical solution can be found for the velocity:

$$V^z = \frac{\Delta p}{4 \upsilon L}(R^2 - \varpi^2), \tag{2.6}$$

with R the radius of the pipe and L the length. The flow is unidirectional in the z direction, so $\boldsymbol{T} = \boldsymbol{e}_z$, and $\boldsymbol{N} = \boldsymbol{e}_\varpi$. The only non-zero components of $\boldsymbol{\Sigma}$ are $\Sigma_{rz} = \Sigma_{zr} = \upsilon \partial V_z / \partial \varpi$, which is a definition used in many manuals of fluid mechanics for the WSS. Poiseuille walls shear stress rests:

$$\tau_{\mathrm{w}}^{\mathrm{P}} = -\upsilon \frac{\partial V^z}{\partial \varpi} = \frac{\Delta p \, R}{2 \, L} = \frac{2 \, \upsilon \, V_{\max}}{R}, \tag{2.7}$$

where $V_{\max} = \dfrac{\Delta p R^2}{4\upsilon L}$ is the maximum velocity of the fluid, at the center of the pipe.

2.2 Turbulence

In this Section we define the concept of turbulent flow, following the steps of [71]. Let us assume that we have a steady solution $(p_0, \boldsymbol{V_0})$ of the incompressible Navier-Stokes Equations (2.4), this is $\partial_t \boldsymbol{V_0} = 0$, and we superpose a perturbation $(\delta p, \boldsymbol{\delta V})$. Then, $\boldsymbol{V} = \boldsymbol{V_0} + \boldsymbol{\delta V}$ and $p = p_0 + \delta p$ must satisfy (2.4). Substituting $\boldsymbol{V}$ and p, and keeping first order terms in $\boldsymbol{\delta V}$ and δp, we end up with the equation

$$\begin{aligned} \vec{\nabla} \cdot \boldsymbol{\delta V} &= 0, \\ \partial_t \boldsymbol{\delta V} + \boldsymbol{V_0} \cdot \vec{\nabla} \boldsymbol{\delta V} &= -\frac{1}{\rho} \vec{\nabla} \delta p + \nu \vec{\nabla}^2 \boldsymbol{\delta V}. \end{aligned} \tag{2.8}$$

Let us consider the scenario of a flow across a cylinder of diameter D. If the flow velocity is U far away form the cylinder, we define the **Reynolds number** as $Re = UD/\nu$. After a stability analysis of the Equation (2.8), it is found that a critical Reynolds number, denoted as $\bar{Re}$, exists at which the perturbation $\boldsymbol{\delta V}$ begins to grow exponentially for $Re > \bar{Re}$, and remains bounded for $Re < \bar{Re}$. Theoretically, one can determine $\bar{Re} \sim 10$. However, it is important to note that the critical Reynolds number is not a universal constant, as it varies depending on the type of flow. For example, in plane Poiseuille flow (flow between two fixed planes), the critical Reynolds number is approximately 6000, as confirmed experimentally. To define the critical Reynolds number in this scenario, we use the expression $Re = U(h/2)/\nu$, where U is the maximum velocity and $(h/2)$ is half of the distance between the two planes. In cylindrical Poiseuille flow the definition is similar. We will consider blood flow in aorta in the Chapter 3, so we deal with a tubular geometry with torsion and non-constant section. This complex geometry makes the stability analysis theoretically difficult. Here, it makes sense to define the Reynolds number as

$$Re = \frac{\bar{V} R}{\nu},$$

where $\bar{V}$ is a mean velocity in the center line, and R a mean radius of the aortic section. We observe values of $Re \sim 10^4$, so according to the two previous analysis in simple cases, one would think that we are in the instability region. It turns out that WSS is inversely proportional to the Reynolds number; see (2.7) for the case of Poiseuille flow. More information on this phenomenon can be found in the reference [71].

Flows that satisfy $Re < \bar{Re}$ are said to be **laminar flows**, where the streamlines of the fluid particles does not cross each other; on the contrary **turbulent flows** satisfy $Re > \bar{Re}$. Blood flow in aorta is one of the latter in most of the cases. Notice that the Euler Equation, i.e. inviscid flow, is recovered in the limit $Re \to \infty$.

Laminar flows are stable, while turbulent flows are chaotic, diffusive, and characterized by vorticity fluctuations across a wide range of time and length scales. The vorticity is defined as $\boldsymbol{\Omega} = \vec{\nabla} \times \boldsymbol{V}$ and quantifies the rotation of the fluid. The numerical resolution of the Navier-Stokes Equations for turbulent flows is computationally demanding, requiring a small time step and a extremely fine mesh. This approach is known as Direct Numerical Simulation (DNS). To reduce computational cost, statistical techniques can be used to simplify the resolution of turbulent flows. These techniques take into account the time-dependent nature of turbulence and its wide range of time scales, approximating random fluctuations through statistical averaging. These methods are computationally less intensive than DNS.

The most widely used method for addressing turbulent flow problems is the Reynolds Averaged Navier-Stokes (RANS) approach, which uses statistical averaging in time. This method involves decomposing the flow variables into a time-mean value component and a fluctuating component. If ϕ is any fluid variable, this decomposition reads

$$\phi = \bar{\phi} + \phi',$$

where ϕ' is the fluctuating component and

$$\bar{\phi}(x,t) = \lim_{T\to\infty} \frac{1}{T} \int_t^{t+T} \phi(x,t')dt',$$

is the time-averaged variable. Making this decomposition for all variables in the Equations (2.4), and time-averaging the resulting equations we get the **RANS equations**:

$$\begin{aligned} \vec{\nabla} \cdot \bar{\boldsymbol{V}} &= 0, \\ \partial_t \bar{\boldsymbol{V}} + \bar{\boldsymbol{V}} \cdot \vec{\nabla} \bar{V} &= -\frac{1}{\rho} \vec{\nabla} \bar{p} + \nu \vec{\nabla}^2 \bar{\boldsymbol{V}} + \frac{1}{\rho} \vec{\nabla} \cdot \boldsymbol{\Sigma'}, \end{aligned} \tag{2.9}$$

where $\bar{\boldsymbol{V}}$ and $\bar{p}$ are the averaged velocity and pressure, respectively, and

$$\boldsymbol{\Sigma'} := \rho\overline{\boldsymbol{V'} \otimes \boldsymbol{V'}}$$

is the Reynolds stress tensor field, where $\boldsymbol{V'}$ is the fluctuating component of the velocity. The bar notation denotes time-average. Note that the concept of steady is different when dealing with time-averaged variables. $\bar{\boldsymbol{V}}$ may not depend on time while $\boldsymbol{V}$ does. We will talk about turbulent steady-state flow when the time-averaged variables are non-dependant on time.

The inclusion of unknown stresses, which are the components of the Reynolds stress tensor, indicates that the system is not closed. One approach to do so is trying to use the original Navier-Stokes Equations but there are some problems involving stability issues [33]. A better approach is modeling $\boldsymbol{\Sigma'}$ by the so-called Boussinesq hypothesis, which reads:

$$\boldsymbol{\Sigma'} = \upsilon_t \left(\vec{\nabla}\bar{\boldsymbol{V}} + \vec{\nabla}\bar{\boldsymbol{V}}^T\right) - \frac{2}{3}\rho k\boldsymbol{I},$$

where we have introduced the turbulent viscosity υ_t, $\boldsymbol{I}$ is the identity tensor and we have defined the turbulent kinetic energy

$$k := \frac{\overline{\boldsymbol{V'} \cdot \boldsymbol{V'}}}{2}.$$

Boussinesq hypothesis tries to resemble Stoke's law for Newtonian fluids and the reasons of its particular form are motivated in the reference [128]. Notice that, with this closure, the Reynolds stress tensor term adds an extra advection and diffusive term, not present in the original Navier-Stokes Equations (2.1). From now, several strategies are possible to close the system. We will see some of them in next subsections.

2.2.1 $k - \epsilon$ turbulence model

In this model, turbulence is stored in the variables k and ϵ, the kinetic energy and the rate of dissipation of kinetic energy, respectively. This last magnitude is computed as:

$$\epsilon = \frac{1}{2}\frac{\upsilon}{\rho}\overline{(\vec{\nabla}\boldsymbol{V'} + \vec{\nabla}\boldsymbol{V'}^T) : (\vec{\nabla}\boldsymbol{V'} + \vec{\nabla}\boldsymbol{V'}^T)},$$

where : stands for the double scalar product for tensors, $\boldsymbol{A} : \boldsymbol{B} = \sum_{i,j} A_{ij}B_{ij}$. By using these two variables, the turbulent viscosity can be modeled as $\upsilon_t = \rho C_\upsilon k^2/\epsilon$. The system is closed with the inclusion of two evolution equations for the newly introduced turbulent variables. These equations are obtained after an algebraic exercise using the original Navier-Stokes Equations and the RANS equations, more details can be consulted in [128]. They take the form

$$\partial_t k + \bar{\boldsymbol{V}} \cdot \vec{\nabla} k = \frac{1}{\rho}\vec{\nabla} \cdot \left(\upsilon_k \vec{\nabla} k\right) + \frac{\upsilon_t}{\rho}\left(\boldsymbol{\Sigma'} : \vec{\nabla}\bar{\boldsymbol{V}}\right) - \epsilon, \tag{2.10}$$

$$\partial_t \epsilon + \bar{\boldsymbol{V}} \cdot \vec{\nabla} \epsilon = \frac{1}{\rho}\vec{\nabla} \cdot \left(\upsilon_\epsilon \vec{\nabla} \epsilon\right) + C_{\epsilon 1}\frac{\epsilon}{\rho k}\left(\boldsymbol{\Sigma'} : \vec{\nabla}\bar{\boldsymbol{V}}\right) - C_{\epsilon 2}\frac{\epsilon^2}{k}, \tag{2.11}$$

where $\upsilon_k = \upsilon + \upsilon_t/\sigma_k$ and $\upsilon_\epsilon = \upsilon + \upsilon_t/\sigma_\epsilon$ are effective viscosities, and $C_\upsilon = 0.09$, $C_{\epsilon 1} = 1.44$,$C_{\epsilon 2} = 1.92$, $\sigma_k = 1.0$ and $\sigma_\epsilon = 1.3$ are constants whose values have been established experimentally [128].

2.2.2 $k - \omega$ turbulence model

Another strategy is the $k - \omega$ model. Here we replace ϵ by a new variable denoted ω that is the rate at which turbulence kinetic energy is converted into internal thermal energy per unit volume and time, defined as

$$\omega = \frac{\epsilon}{C_\upsilon k},$$

for which an equation can be derived from (2.11). The new set of equations for the turbulent variables rest

$$\partial_t k + \bar{\boldsymbol{V}} \cdot \vec{\nabla} k = \frac{1}{\rho}\vec{\nabla} \cdot \left(\upsilon_k \vec{\nabla} k\right) + \frac{\upsilon_t}{\rho}\left(\Sigma' : \vec{\nabla}\bar{\boldsymbol{V}}\right) - C_k k\omega, \tag{2.12}$$

$$\partial_t \omega + \bar{\boldsymbol{V}} \cdot \vec{\nabla} \omega = \frac{1}{\rho}\vec{\nabla} \cdot \left(\upsilon_\omega \vec{\nabla} \omega\right) + C_{\omega 1}\frac{\omega}{\rho k}\left(\Sigma' : \vec{\nabla}\bar{\boldsymbol{V}}\right) - C_{\omega 2}\omega^2, \tag{2.13}$$

where $\upsilon_\omega = \upsilon + \upsilon_t/\sigma_\omega$ is an effective viscosity, and $C_k = 0.09$, $C_{\omega 1} = 5/9$, $C_{\omega 2} = 0.075$, $\sigma_k = 2.0$ and $\sigma_\omega = 2.0$ are empirical constants .

The $k-\omega$ model has the advantage of being more precise near the walls than $k-\epsilon$ model, meanwhile the latter is more precise in the free stream. There exist a model that combine both features and it is called Shear Stress Transport (SST) $k-\omega$ model. Some details about how the model is built can be found in [33]; due to its length, we do not include a detailed derivation of the method. Roughly speaking, it mixes both models through blending functions, which somehow activates one model or the other depending on the region.

Sometimes the quantity we are interested in can be equally obtained from the averaged variables, and here is where turbulent models become appealing, as they are computationally cheaper than DNS. It turns out that this is the case of the WSS. The turbulent kinetic energy k decays to zero as one approaches the wall, see [123]. Then, the fluctuating component of the velocity goes to zero, and the WSS is the same either computed with the viscous stress tensor or the time-averaged one.

2.3 Finite Volume Method

The Finite Volume Method (FVM) will be used to numerically solve the balance laws of the Chapter 3. It has a high flexibility as far as the discretization of the equations is concerned and it is suitable for solving flows in complex geometries, as it is the case of airflow around an airplane wing, analysing the aerodynamics of car body or blood flow in aorta. Another interesting characteristic of the FVM is that it mirrors physical properties of the problem modeled: it is based on the fulfillment of the integral form of the balance laws, volume per volume. All these features make the FVM very appealing in CFD. Vast descriptions of this methods can be found in [33] and [128]. Here, we just summarize the main ideas.

2.3.1 Equations of the method

Let us consider a balance law of a scalar field ϕ of the form:

$$\partial_t(\rho\phi) + \vec{\nabla}\cdot(\rho\boldsymbol{V}\phi) = \vec{\nabla}\cdot(\upsilon\vec{\nabla}\phi) + S, \tag{2.14}$$

where ρ is the mass density, $\boldsymbol{V}$ the velocity, υ a diffusion coefficient and S is a source term. The first and second terms in the left-hand side are called transient and advection terms, respectively, meanwhile the first term in the right-hand side is called diffusion term. The scalar field ϕ represents any fluid scalar variable as temperature, pressure or a component of the velocity. For the sake of simplicity the method is explained in 2-dimensional geometries. The extension to 3 dimensions can be developed easily.

Let us suppose we want to solve the Equation (2.14) in the region $\mathcal{V}$ shown in the Figure 2.2 given some boundary conditions defined on the boundary $\partial\mathcal{V}$. We have distinguished three patches at the boundary: a solid line Γ_{wall}, a dotted line Γ_{in} and a dashed line Γ_{out} in such a way $\partial V = \Gamma_{\text{in}} \bigcup \Gamma_{\text{wall}} \bigcup \Gamma_{\text{out}}$.

Before applying the FVM, we need to mesh the region with polygons, as shown in the Figure 2.2, in the case of two dimensions, or polyhedra in 3 dimensions. One can guess that the more density of polygons there is, the more exact will be the numerical solution of (2.14). For instance, the region closer to Γ_{in} will provide better results than the one close to Γ_{out}. As the polygons or polyhedra do not need to be regular or have a fixed number of vertices, the mesh can have a high flexibility and be well-adapted to the geometry of the problem. Once we have fixed the mesh there comes the discretization procedure that will end with the equations of the FVM. We refer to each polygon of the Figure 2.2 as *element* or *volume*. Let N be the total number of elements in the mesh. A numerical solution for ϕ of (2.14) will be a set of values $\{\phi_i\}_{i=1}^{i=N}$ that try to approximate ϕ at the centroids of the elements. The first step is integrating numerically the whole Equation (2.14) in each volume, and then in time from t to $t+\Delta t$, once we have fixed a time step Δt:

$$\begin{aligned}\int_t^{t+\Delta t}\int_{\mathcal{V}} \partial_t(\rho\phi)d\mathcal{V}dt + \int_t^{t+\Delta t}\int_{\mathcal{V}} \vec{\nabla}\cdot(\rho\boldsymbol{V}\phi)d\mathcal{V}dt = \\ \int_t^{t+\Delta t}\int_{\mathcal{V}} \vec{\nabla}\cdot(\upsilon\vec{\nabla}\phi)d\mathcal{V}dt + \int_t^{t+\Delta t}\int_{\mathcal{V}} Sd\mathcal{V}dt,\end{aligned} \tag{2.15}$$

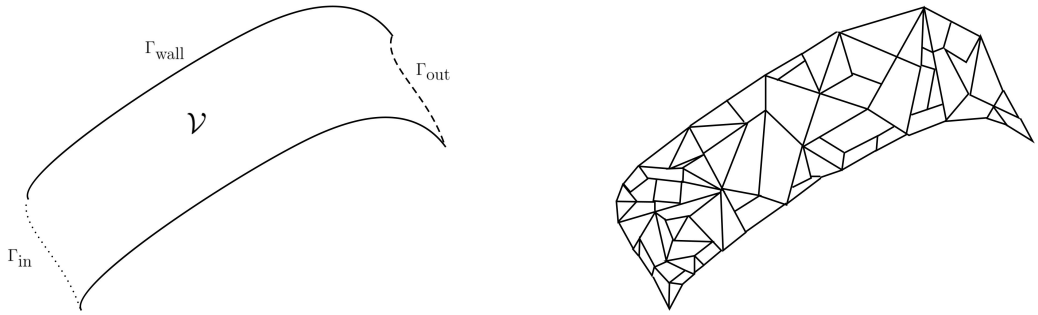

Figure 2.2: Example of region $\mathcal{V}$ (left) where a FVM is to be applied and the same region after being meshed (right).

where $\mathcal{V}$ is the region occupied by a specific element. We focus our attention on a specific element whose centroid point is P (see Figure 2.3), but the same procedure applies to all elements. The strategy applied carrying out these integrations characterizes the first step of the discretization of (2.14).

The volume integration of the transient and source term is done directly applying a numerical integration rule. Using the value of the integrand in the centroid of the element provides a second order approximation in the same way mid-point rule does [33]. Doing so, these integrals rest:

$$\int_{\mathcal{V}_P} \partial_t(\rho\phi)d\mathcal{V} \approx \partial_t(\rho_P\phi_P)\ \mathcal{V}_P, \tag{2.16}$$

$$\int_{\mathcal{V}_P} SdV \approx S_P\mathcal{V}_P. \tag{2.17}$$

$\mathcal{V}_P$ is the volume of the element we are focused on. Of course, increasing the number of points used inside $\mathcal{V}_P$ to approximate these integrals improves the accuracy of the approximation. Advection and diffusion terms integrals are computed using Gauss theorem:

$$\int_{\mathcal{V}_P} \vec{\nabla}\cdot(\rho\boldsymbol{V}\phi)d\mathcal{V} = \int_{\partial\mathcal{V}_P} \rho\boldsymbol{V}\phi\cdot d\boldsymbol{\mathcal{S}} = \sum_{i=1}^{N_e}\int_{\mathcal{A}_i} \rho\boldsymbol{V}\phi\cdot d\boldsymbol{\mathcal{S}}, \tag{2.18}$$

$$\int_{\mathcal{V}_P} \vec{\nabla}\cdot(\upsilon\vec{\nabla}\phi)d\mathcal{V} = \int_{\partial\mathcal{V}_P} \upsilon\vec{\nabla}\phi\cdot d\boldsymbol{\mathcal{S}} = \sum_{i=1}^{N_e}\int_{\mathcal{A}_i} \upsilon\vec{\nabla}\phi\cdot d\boldsymbol{\mathcal{S}}. \tag{2.19}$$

In the last equality it has been taken into account that the element P has N_e edges (faces in 3 dimensions) $\mathcal{A}_i$ with $i = 1, ..., N_e$. In the Figure

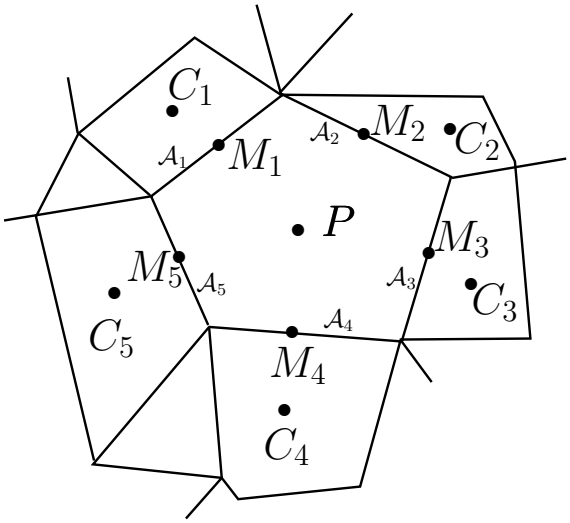

Figure 2.3: Application of the first discretization of a conservation law in a selected volume.

2.3 we have $N_e = 5$. Again, using the centroid M_i of each edge provides a second order approximation for each surface (line) integral:

$$\int_{\mathcal{A}_i} \rho \boldsymbol{V} \phi \cdot d\boldsymbol{\mathcal{S}} \approx (\rho \boldsymbol{V} \phi \cdot \boldsymbol{N}_i)|_{M_i} \mathcal{A}_i, \tag{2.20}$$

$$\int_{\mathcal{A}_i} \upsilon \vec{\nabla} \phi \cdot d\boldsymbol{\mathcal{S}} \approx \left(\upsilon \vec{\nabla} \phi \cdot \boldsymbol{N}_i\right)\Big|_{M_i} \mathcal{A}_i, \tag{2.21}$$

where $\boldsymbol{N}_i$ stands for the unit vector normal to the edge A_i and pointing outwards the element P. Expressions (2.20) and (2.21) represent the fluxes of the vector fields $\rho \boldsymbol{V} \phi$ and $\upsilon \vec{\nabla} \phi$, respectively. Now, considering a fixed mesh in time, the integral of the transient term reads

$$\int_t^{t+\Delta t} \int_{\mathcal{V}} \partial_t(\rho\phi) d\mathcal{V} dt \approx (\rho_P^* \phi_P^* - \rho_P \phi_P)\mathcal{V}_P, \tag{2.22}$$

where the asterisk stands for an evaluation of a function in time $t + \Delta t$, $f^* = f(t + \Delta t)$, and no asterisk means evaluation at t. Concerning the other terms we have to make a choice for the time integral. Usually, implicit and explicit evaluations are taken. For instance, in the case of the source term, the approximation of the integral would rest

$$\int_t^{t+\Delta t} \int_{\mathcal{V}} S d\mathcal{V} dt \approx \left(f_{\mathrm{s}} S_P^* - (1 - f_{\mathrm{s}}) S_P\right)\mathcal{V}_P \Delta t, \tag{2.23}$$

where a choice for f_s has to be made. The source term is said to evolve explicitly in the method for $f_\mathrm{s} = 0$ and implicitly for $f_\mathrm{s} = 1$. The same applies for the advection and diffusion terms. Finally, the equation of the FVM will result after substituting the former approximations of the integrals:

$$\begin{aligned}(\rho_P^*\phi_P^* - \rho_P\phi_P)\mathcal{V}_P + \sum_i \big(f_\mathrm{a}\,(\rho\boldsymbol{V}\phi\cdot\boldsymbol{n}_i)^*|_{M_i} + (1-f_\mathrm{a})\,(\rho\boldsymbol{V}\phi\cdot\boldsymbol{n}_i)|_{M_i}\big)\mathcal{A}_i \\ - \sum_i \big(f_\mathrm{d}\left(\upsilon\vec{\nabla}\phi\cdot\boldsymbol{n}_i\right)^*\Big|_{M_i} + (1-f_\mathrm{d})\left(\upsilon\vec{\nabla}\phi\cdot\boldsymbol{n}_i\right)\Big|_{M_i}\big)\mathcal{A}_i \\ = \big(f_\mathrm{s}S_P^* - (1-f_\mathrm{s})S_P\big)\mathcal{V}_P\Delta t.\end{aligned} \tag{2.24}$$

In addition to fix the coefficients f_a, f_d and f_s, we need to settle how to manage the value of the variables at M_i. This is because, as stated, the unknowns to be determined are the values of the variables at the centroids of the elements. In the case of known variables this is not a very complicated problem, but regarding the variable under resolution ϕ, it is an issue. The main idea is taking the variable in the centroids of that elements surrounding the corresponding edge. We will do that for the values of ϕ in the edges but also for the derivatives. In the case of the Figure 2.3, a simple choice is

$$\phi_{M_i} = a_i\phi_{C_i} + b_i\phi_P, \tag{2.25}$$

$$\partial_j\phi|_{M_i} = c_i\phi_{C_i} + d_i\phi_P. \tag{2.26}$$

Coefficients a_i, b_i, c_i and d_i must be such that the fluxes between the elements of the mesh are consistent. This is, the flux entering a specific element through a specific face from another element must be the same than the outgoing flux through that face. A possible choice in (2.25) is $a_i = 1$, $b_i = 0$ if the velocity points to C_i in M_i and $a_i = 0$ and $b_i = 1$ if it is the other way around. This is the so-called **upwind scheme**.

If an edge point M belongs to a boundary patch Γ, we have additional information because of the boundary conditions. For instance, if a Dirichlet boundary condition is settled,

$$\phi(x) = f(x), \quad x \in \Gamma,$$

we just assign $\phi_M = f(M)$. However, when this type of condition is provided the values of the derivative in the edge points are to be assigned as in (2.26). It goes the other way around in the case of a Neumann

boundary condition. In that case, we know the derivative and we need a strategy to assign a value to ϕ_M.

The procedure was explained focusing our attention to one volume. Similar equations are to be derived for all volumes to finally get N algebraic linear equations with N variables. Realistic CFD scenarios require an order of 10^5-10^6 volumes, so a strategy will be needed to solve such a huge system. We will turn to this matter.

2.3.2 Case of Navier-Stokes equations

The equation (2.14) becomes the component i of the momentum conservation equation (2.1b) if one substitutes ϕ by V^i and $S = \partial p/\partial x^i$. In principle, the content of the last Subsection is valid to apply it to Navier-Stokes equations, but sometimes not directly.

When one deals with compressible flows, we normally have an equation of state that relates density ρ and pressure p. Then, the mass conservation equation (2.1a) becomes an evolution equation for ρ and the momentum conservation equation (2.1b) constitutes an evolution equation for the velocity $\boldsymbol{V}$. Finally, p comes from the equation of state.

It turns out that incompressible flows are more complicated to solve numerically than compressible flows. In incompressible flows the value of ρ is known and one demands an equation for p. Let us suppose steady flow to clarify the next explanation. If we discretize (2.4) we end up with a linear system of equations of the form

$$\begin{pmatrix} \boldsymbol{F} & \boldsymbol{B}^T \\ \boldsymbol{B} & \boldsymbol{0} \end{pmatrix} \begin{pmatrix} \bar{\boldsymbol{U}} \\ \bar{\boldsymbol{p}} \end{pmatrix} = \begin{pmatrix} \boldsymbol{0} \\ \boldsymbol{0} \end{pmatrix} \tag{2.27}$$

where $\bar{\boldsymbol{p}}$ and $\bar{\boldsymbol{U}}$ are the arrays forming the numerical solution of pressure and velocity, respectively. $\boldsymbol{F}$ and $\boldsymbol{B}$ are known matrices. The last equation exhibits a zero diagonal block in the system, meaning that it cannot support being solved through iterative methods. As a result, an equation for pressure must be obtained.

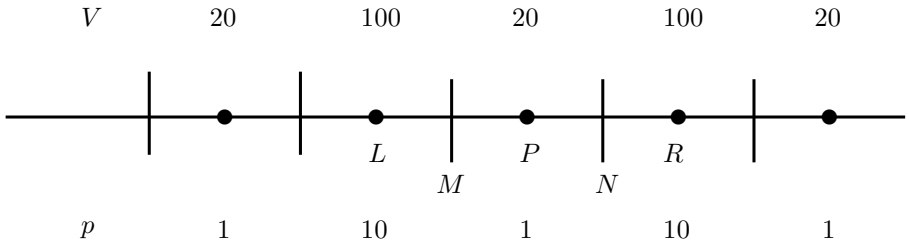

Figure 2.4: Oscillations of V and p to illustrate the checkerboard problem.

Checkerboard problem

Besides, there is an extra problem with the discretization of (2.4). To address this clearer let us consider the one dimensional version of the Navier-Stokes Equations to be solved numerically in a Cartesian grid, equally spaced. We add artificially an extra dimension, one cell wide, such that the surface integral makes sense. The physical dimension is x and the artificial one y. Let us consider the approximations of the integrals for the velocity $V = V^x$ and pressure p. We focus on the element P of the Figure 2.4 and make the assignment

$$V_M = \frac{V_L + V_P}{2}, \quad V_N = \frac{V_R + V_P}{2}, \tag{2.28}$$

$$p_M = \frac{p_L + p_P}{2}, \quad p_N = \frac{p_R + p_P}{2}, \tag{2.29}$$

which is perfectly valid given the symmetry of the situation. Now, suppose, that some oscillations arise in such a way we have the exaggerated behaviour shown in the Figure 2.4, where p oscillates between 1 and 10 from cell to cell and V from 20 to 100. Then, the integrals rest:

$$\int_{\mathcal{V}_P} \frac{dV}{dx} d\mathcal{V} = \int_{\partial\mathcal{V}_P} V d\mathcal{S} \approx (V_M - V_N)\Delta y = \frac{V_L - V_R}{2}\Delta y = 0, \tag{2.30}$$

$$\int_{\mathcal{V}_P} \frac{dp}{dx} d\mathcal{V} = \int_{\partial\mathcal{V}_P} p d\mathcal{S} \approx (p_M - p_N)\Delta y = \frac{p_L - p_R}{2}\Delta y = 0 \tag{2.31}$$

So, we observe that the continuity equation is satisfied automatically and no pressure gradient is observed. This non-physical behaviour also arises in more dimensions, but it is harder to visualize.

Staggered grid and SIMPLE algorithm

One strategy that solves the Checkerboard problem is to consider the mid points of the edges as members of the grid, forming the so-called Staggered grid. But only the velocity is taken in those new points. The remaining variables are still in the centroid points, the original grid.

In the end, the integration of the momentum conservation equation (taking a component) of an element will rest

$$\sum_{i}^{N_e} a_i V_{M_i} + \sum_{j}^{N_c} b_j p_{C_j} = c, \tag{2.32}$$

where M_i refers to the N_e mid points of edges surrounding the element, C_j to the N_c centroids around the element and a_i, b_i, c are constants that depend on the scheme of the discretization process and the mesh resolution.

Let us guess a preliminary value for the pressure and denote it p^*. Then, the velocity that comes from the Equation (2.32) with this pressure does not satisfy the mass conservation equation. Let us call this velocity $\boldsymbol{V}^*$. Of course, p and $\boldsymbol{V}$ precise a correction such that they satisfy both Navier-Stokes Equations (2.4). Let us denote these corrections p' and $\boldsymbol{V}'$ such that

$$p = p^* + p', \quad \boldsymbol{V} = \boldsymbol{V}^* + \boldsymbol{V}'.$$

Both corrected and asterisk variables satisfy the Equation (2.32). Using this, we derive an equation for the corrected components of the form

$$\sum_{i}^{N_e} a_i V'_{M_i} + \sum_{j}^{N_c} b_j p'_{C_j} = 0. \tag{2.33}$$

Now, by considering that $\boldsymbol{V}$ fulfills the mass conservation equation and making use of the Equation (2.33), we derive another equation for pressure correction:

$$\sum_{j}^{N_c} c_j p'_{C_j} = b, \tag{2.34}$$

where the coefficients c_j depend on grid parameters and $\boldsymbol{V}^*$.

The strategy to get velocity and pressure is based in the previous equations and it is called Semi-Implicit Method for Pressure Linked Equations (SIMPLE), proposed by Patankar and Spalding [98]. It consists in the following steps:

1. Guess a value for the pressure p^*.
2. Solve the Equations (2.32) with the asterisk pressure p^* to get an asterisk velocity $\boldsymbol{V}^*$
3. Solve the Equations (2.34) to get the pressure correction p', and then the corrected pressure $p = p^* + p'$.
4. Solve the Equations (2.33) to get the velocity correction $\boldsymbol{V}'$, and then the corrected velocity $\boldsymbol{V} = \boldsymbol{V}^* + \boldsymbol{V}'$.
5. Go back to step 2 replacing p^* by p.

The algorithm is repeated until mass conservation is fulfilled up to some level of tolerance ϵ.

2.3.3 Solving discretized equations

In the previous analysis we focused on one unique element, but the same applies to each element of the mesh of our geometry. Then, having a set of linear algebraic equations presumptively large.

Usual methods

There are many techniques to solve the algebraic linear equations that come up when discretizing partial differential equations. Normally, one have the same number of equations than variables and it is fully determined. In matrix form they are written as

$$\boldsymbol{A}\boldsymbol{x} = \boldsymbol{b},$$

where $\boldsymbol{x}$ is the numerical solution. Let N be the dimension of the system. We distinguish two principal blocks of solvers: direct methods and iterative methods. Examples of the first kind are Cramer's rule or Gaussian elimination which need around N^3 operations. However, in iterative methods as Gauss-Seidel or Jacobi methods only around N operations per iteration are needed. N can reach values around 10^6 in realistic CFD problems. So, as human lives and computational storage is limited, iterative methods are not only appealing but necessary. The intention of

this manuscript is not to give a extended description of these methods and we address the reader to specialized books [33, 128] on this subject.

Multigrid methods

Among iterative methods multigrid methods are widely used in CFD. They analyze the CFD problem using multiple grids that are coarser than the original, and in each one a selected iterative method proceeds. The convergence rate is significantly improved when using this technique compared to using the iterative method alone. The reasons of this fact are explained hereunder.

Suppose we want to solve the algebraic linear equation

$$\boldsymbol{A^h x^h = b^h}$$

that comes from the discretization of a conservation law, and denote h as the spatial resolution of a simple Cartesian equally-spaced grid, established to solve the CFD problem. After n iterations of a selected iterative method we get an approximation of $\boldsymbol{x}^h$, called $\boldsymbol{y}^h$. Let us call the error of the approximation by $\boldsymbol{e}^h = \boldsymbol{x}^h - \boldsymbol{y}^h$. It turns out that purely iterative methods are sensitive to errors that vary with a scale of h or below, and they reduce them. This type of errors are called high frequency errors. On the contrary, they have difficulties to reduce low frequency errors, whose values vary with a scale higher than h, i.e. they are barely noted from one volume to the next one.

Multigrid methods consist in creating one or several coarser grids from the original one, so the low frequency errors are perceived as high frequency errors by the selected iterative method. The algebraic linear equations are transferred to the new grid with some technique, that has to be established, giving another system

$$\boldsymbol{A^{h'} x^{h'} = b^{h'}},$$

with $h' > h$. Applying the iterative method to the new system will reduce the high frequency component of the error $\boldsymbol{e}^{h'}$. Finally we go back to the the original and finest grid with some other technique. The iterations made in coarser grids are usually much less costly than in the finest, in such a way the total path is worthwhile. Improvements of one order of magnitude in the number of iterations to reach the same accuracy are observed when comparing multigrid methods and Gauss-Seidel method

alone [128].

A simple case of grid formation is to join every pair of volumes to form a unique one, coarsening the scale of the grid from h to $h' = 2h$. Then, the simplest multigrid method with these two grids proceeds as follows.

- First, we get an approximation in the finest grid with an iterative method, $\boldsymbol{y^h}$. The high frequency part of $\boldsymbol{e^h}$ is then reduced.
- Secondly, we transfer the system to the coarse grid, where we use the iterative method again to reduce the low frequency errors, which in the new grid are high frequency.
- Then, we carry the system back to the original grid in such a way the initial approximation is corrected
- A few final iterations may be convenient to minimize possible errors in the grid tour. When an iterative method proceed in this way it is called smoother, which makes sense as it tries to shrink potential spikes that can appear in the error.

These steps are repeated in cycle until getting the desired accuracy.

The technique followed when transferring the system between meshes can be based in geometric arguments. In that case, the multigrid method is said to be a **geometric multigrid method**. On the other hand, if we just use the coefficients of the original system to form the new one (without taking care of geometrical aspects) we say that it is an **algebraic multigrid method**. The latter ones are more suitable when the complexity of the mesh is high but we may lose some insight about what is going on geometrically.

Other strategies with more grids and paths are possible. The one described is called V-cycle because we "go down" to the coarser grid and then "go up" to the original one. Other strategies are W-cycles, in which we deal with three grids: first going down two steps; second, going up one step and to go down again, to finally go up two steps.

Note that multigrid methods are much more complex than using a single iterative method, but once they are implemented, the convergence velocity is higher. Here, we described the method briefly, and further details can be consulted in [128].

To end this section, we mention a useful tool to solve linear systems: **Preconditioners**. A preconditioner is an invertible matrix M such that the system

$$\boldsymbol{M}^{-1}\boldsymbol{A}\boldsymbol{x} = \boldsymbol{M}^{-1}\boldsymbol{b}$$

has a higher rate of convergence than the original when applying the corresponding iterative solver. The matrix product of the preconditioner and $\boldsymbol{A}$ should be cheap not to increase much the computational cost. In the previous equation M was a left preconditioner, but left or central preconditioners are also possible.

2.4 Final remarks

We have introduced important concepts and tools to be applied in the Chapter 3. We began introducing the Navier-Stokes Equations and defined the WSS and the concept of turbulence. Different turbulent models of the Navier-Stokes Equations were described. These are computationally cheaper than applying DNS in turbulent flows, which are very frequent in nature.

All these systems of partial differential equations precise a numerical method in realistic flows. Therefore, we also outlined the main ideas of the FVM which are very useful for conservation and balance laws in complex geometries. Moreover, the SIMPLE algorithm was exposed which is needed for incompressible Navier-Stokes equations. We finalized the Chapter by briefly presenting the different techniques to solve the linear algebraic equation that arise when partial differential equations are discretized. Therein, we justified that multigrid methods seemed to be a suitable choice which combined iterative methods with a coarsening process of the mesh.

3

Blood flow in aorta

In this Chapter we face the numerical resolution of a classical fluid dynamics problem: blood flow in aorta. The partial differential equations that model this scenario are the Navier-Stokes Equations (2.1). Although the equations are very well known and can be solved analytically in many situations, the complexity of the geometry here demands the employment of advanced numerical tools. We will use the FVM to solve the Navier-Stokes Equations inside the aorta artery. Many applications can be derived from blood flow simulation in health sciences. In particular, some physiological quantities are only measurable by numerical simulation due to the high difficulty of doing it by clinical diagnosis.

We are specially interested in the computation of the WSS (2.5). The ultimate goal is relating geometrical aspects of the aorta with potential developments of cardiovascular diseases derived from anomalous values of WSS. To do so, it is very convenient having a big sample of realistic aortas, but in practice, the availability of such a sample can be complicated. However, the creation of realistic synthetic aortas can easily increase the sample. For this purpose, a reconstruction algorithm has been developed in the group CoMMLAB from Universitat de Valencia [108], which allows us to identify key geometrical parameters. In this Chapter, we will carry out CFD simulations of blood flow in aorta with

the intention of giving credit to the reconstruction algorithm. Besides, we will make a preliminary analysis about which type of aorta valve is more appropriate to soften the anomalous behaviour of the blood flow. Moreover, we will properly choose a turbulence model to carry out the numerical simulations. Some results herein have been published in [107] and [110].

3.1 The cardiovascular system

Cardiovascular diseases are the most common cause of death in the world, see [91, 42, 40]. The work described in this Chapter aims to study a physiological quantity that is related with diseases such atherosclerosis, stenosis and aneurysm in aorta: the WSS, defined in (2.5), which is the tangential component of the stress at the aortic wall.

First, let us introduce some basics about aorta anatomy, illustrated in the Figure 3.1. The blood penetrates from the heart through the aortic valve where we find the sinus of Valsalva, three bulges at the beginning of the aorta. Right there the aorta ramifies in the coronary arteries. We continue through the ascendant aorta, the aortic arch and the descendant aorta. These three parts constitute the thoracic aorta. At the aortic arch three more ramifications are present, the supra-aortic arteries. After thoracic aorta comes the abdominal aorta with much more ramifications supplying blood to the lower body.

The aim of this work is relating geometrical properties of aortas with patterns of WSS. And if some anomalous value is found, determining what possible prosthetic aortic valves can remedy such a behaviour. Measuring WSS in a patient with medical tests is extremely difficult, because it depends on the velocity of blood point to point, which at the same time is vaguely determined by 4D medical visualization techniques [21]. This kind of measures are called *in vivo*. A better strategy is carrying out simulations of blood flow in a scanned aorta from a patient, and then, compute the WSS from the numerical solution of the flow, This is a *in silico* measurement. The Figure 3.2 shows a summarized scheme of the *in silico* process.

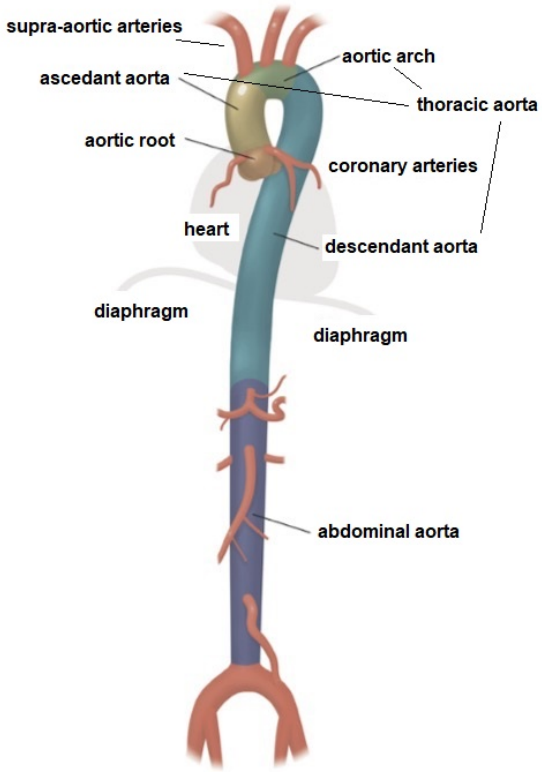

Figure 3.1: Aorta picture, from Cirugía Cardiaca Madrid

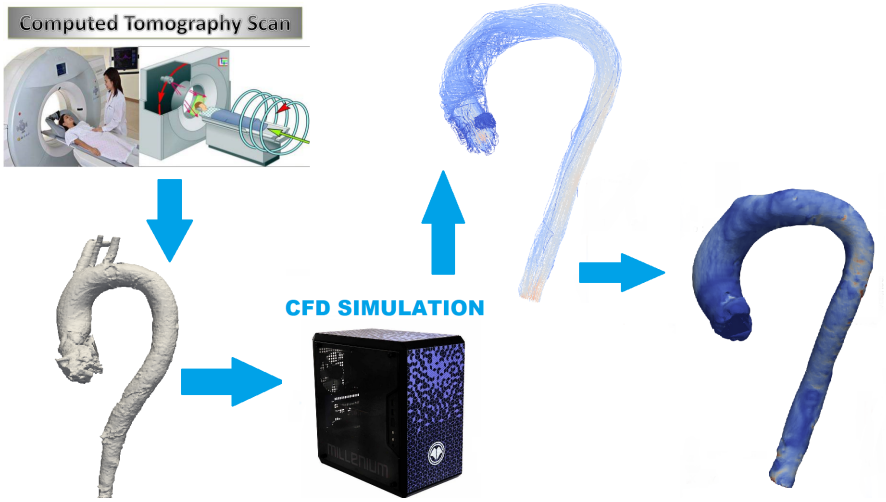

Figure 3.2: Scheme of an *in silico* measurement of the WSS in the aorta of a patient.

In this context, our aim is to solve the Navier-Stokes Equations with boundary conditions, which will model blood flow in aorta. In order to establish proper boundary conditions one needs data about how the blood gets in the aorta through the aortic valve from the heart. Some good references about the physics of the cardiovascular system are [39, 20]. The cardiac cycle has two principal phases: diastole and systole. In the latter the aortic valve opens letting the blood to come in. In systole, blood flow reaches maximum values, so we will focus our attention in this phase. We have two main purposes: validate the reconstruction method mentioned and determine how different aortic valves affect WSS profiles. For the former, simulations in both real aorta and reconstructed one are to be carried out, and in the latter, we will vary boundary conditions in order to reproduce the effect of different type of valves (natural and prosthetic). On the other hand, blood flow in aorta develop a turbulent behaviour, with twists and many length scales. For an accurate estimation of WSS, the use of a turbulence model can be of great relevance. Then, we also present a study to compare the estimations of fluid variables with three different turbulence models. We will use the Finite Volume solver OpenFOAM to carry out the CFD simulations

3.2 Computational fluid dynamics for blood flow in aorta

In this Section we will detail the main features of the model taken to describe the blood flow in the aorta.

3.2.1 Aorta geometry

Real aorta geometries are obtained by Computed Tomography scans realized by collaborators in Hospital Universitari i Politècnic La Fe of Valencia. Some manipulations are needed to clean the aorta surface in order to make it suitable for CFD simulation. With Blender we eliminate

Figure 3.3: Aorta scan with Computed Tomography (left), after processing (center) and reconstructed (right).

some calcifications that do not correspond to the aorta surface and, for the sake of simplicity, we are removing the supra-aortic arteries. We also define three different patches in the aorta surface, which are the inlet Γ_{in}, the wall Γ_{wall} and the outlet Γ_{out}. The reconstruction method is applied to the aorta after this process. It consists in a parametrization of the tubular surface with elliptical cross sections for the aorta:

$$\boldsymbol{x}(s,\theta) = \boldsymbol{\alpha}(s) + \boldsymbol{a}(s)\cos(\theta) + \boldsymbol{b}(s)\sin(\theta).$$

The centerline $\boldsymbol{\alpha}(s)$ and ellipses semi-axis $\boldsymbol{a}(s), \boldsymbol{b}(s)$ are obtained through our reconstruction algorithm. Then, B-splines are used to get continuous functions that reshape the ellipses in such a way reconstructed sections reproduce the originals. More details can be found in [108]. In the Figure 3.3 we show examples of real aorta, as it is obtained from the scan, a processed aorta and a reconstructed aorta.

3.2.2

Blood flow model

Blood flow can be approximated by a Newtonian fluid in certain situations [61]. Fortunately, ours is one of those thanks to the wide Section of the aorta. See [20] to consult the models used in other type of vessels. As approximation, we consider steady-state flow as if peak systolic cardiovascular conditions remained constant, when flow and arterial pressure are maximum. We know that our results will not be exact but at least we expect that some reasonable conclusions can be made in that instant of maximum arterial stress. Then, our model will be the steady-state incompressible Navier-Stokes equations:

$$\vec{\nabla} \cdot \boldsymbol{V} = 0, \tag{3.1a}$$

$$\boldsymbol{V} \cdot \vec{\nabla} \boldsymbol{V} = -\frac{1}{\rho} \vec{\nabla} p + \nu \vec{\nabla}^2 \boldsymbol{V}. \tag{3.1b}$$

We set the kinematic viscosity of the blood to $\nu = 3.37 \cdot 10^{-6}$ m^2/s as [21]. We will impose boundary condition according to the expressions (2.2) which, at the same time, will try to resemble the peak systolic cardiovascular phase. For syntax reasons, the pre-established OpenFoam parameter files demands to settle a boundary condition to each patch and for all variables, even it is not necessary, as it happens with the pressure at the inlet. Normally, in pipe-like problems one either establishes boundary conditions over pressure values and velocity derivatives or only to the velocity values. If one settles in the same patch conditions fixing values to both variables, OpenFOAM will report a message and the simulation will stop; it assumes that we have made a mistake and that conditions over velocity derivatives are required instead. at the inlet, values for the velocity are settled modeling the blood entry. Then a condition over the values of the pressure is not allowed by the software in this patch. Nonetheless, a boundary condition for the pressure is still needed by OpenFOAM. Then, we will use a condition over pressure

derivative. In the end, the following boundary conditions are applied:

$$\begin{cases} \nabla p(x) = 0 \\ \boldsymbol{V}(x) = \boldsymbol{f}(x) \end{cases} \quad \text{if } x \in \Gamma_{\text{in}}$$

$$\begin{cases} \nabla p(x) = 0 \\ \boldsymbol{V}(x) = 0 \end{cases} \quad \text{if } x \in \Gamma_{\text{wall}} \tag{3.2}$$

$$\begin{cases} p(x) = 0 \\ \nabla \boldsymbol{V}(x) = 0 \end{cases} \quad \text{if } x \in \Gamma_{\text{out}}$$

This is in agreement with the boundary conditions (2.2) expect for the fact that there, we had an outlet condition over $\partial V^n/\partial n$ and here, we have it over $\nabla \boldsymbol{V}$. It turns out that there is not much difference, as we explain now. Consider two orthonormal tangential directions, $\boldsymbol{T}_1$ and $\boldsymbol{T}_2$, and another one perpendicular $\boldsymbol{N}$ to the outlet. The 2-tensor field $\vec{\nabla}\boldsymbol{V}$ has the following components:

$$\vec{\nabla}\boldsymbol{V} = \begin{pmatrix} \partial V^n/\partial n & \partial V^{t_i}/\partial n \\ \partial V^n/\partial t_j & \partial V^{t_i}/\partial t_j \end{pmatrix}.$$

In fully-developed flows $V^{t_i} = 0$ is satisfied by definition. So, at the outlet the unique difference between the boundary conditions in (2.2) and (3.2) is that $\partial V^n/\partial t_i = 0$ is imposed in the second. This condition would be incompatible with the wall non-slip condition $\boldsymbol{V} = 0$. Nonetheless, at the beginning of each simulation OpenFOAM does a few iterations to get a preliminary smooth flow such that the condition $\partial V^n/\partial t_i = 0$ is not strictly satisfied near the wall. Then, $\partial V^n/\partial n = 0$ is the one really imposed, as it was stated in (2.2). The reason having $\nabla \boldsymbol{V} = 0$ is because, doing so, we have a friendly implementation of boundary conditions in OpenFOAM which provide good results.

We want to impose the most realistic boundary conditions. An approach to reality will be a parabolic profile of the flow at the inlet, as it is illustrated in the Figure 3.4. We make this description with an aorta with elliptic section for simplicity, but it can be easily extended to more general sections. In the Figure, we plot the modulus of the velocity respect the position in the elliptic section. In particular we have imposed the expression

$$\boldsymbol{V} = V_c \left(\frac{x^2}{a^2} + \frac{y^2}{b^2} \right) \boldsymbol{N}, \tag{3.3}$$

where (x, y) are the coordinates in the basis formed by the unit vectors along the axis of the ellipse, V_c is the velocity in the center, a and b the semi-axis longitude and $\boldsymbol{N}$ the unit vector normal to the inlet.

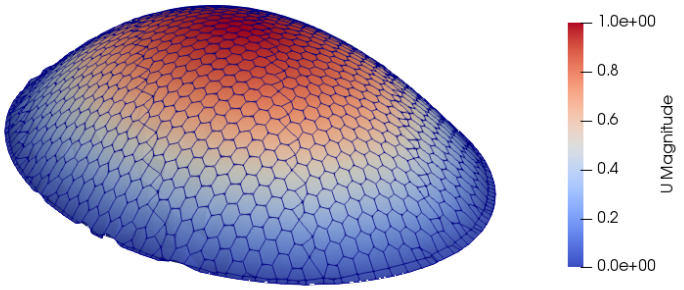

Figure 3.4: Vertical profile of some of the inlet boundary conditions considered. The maximum velocity is $V_c = 1$ m/s.

This type of boundary condition is used in the validation of the reconstruction algorithm. On the other hand, we know now that a healthy aortic valve section is more similar to the tricuspid valve [58]. In fact, it seems that a plateau function at the inlet, instead of the parabolic profile, is more realistic. We will take this into account in the analysis of aortic valves. We will carry out simulations with inlet boundary conditions reproducing the tricuspid valve and two more profiles that try to resemble the effect of two types of artificial valves: Meditronic valve [36] and St. Jude Medical valve [84]. The three profiles are shown in the Figure 3.5. Artificial valves try to treat cardiovascular diseases. We will compute the effect of these in the WSS of an aorta with stenosis, a cardiovascular disease that consists in a shrinking of the aorta walls.

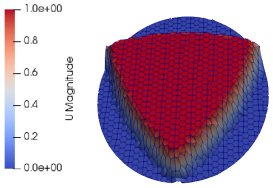

(a) Natural healthy valve.

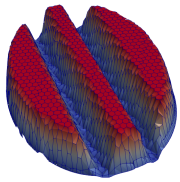

(b) Artificial bileaflet valve.

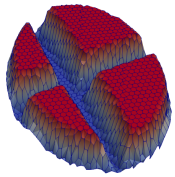

(c) Artificial tilting disk valve.

Figure 3.5: Vertical profile of some of the inlet boundary conditions considered. The maximum velocity is 1 m/s.

Turbulent models

We know that the Reynolds number in the aorta can reach values around 10^4. Then, a turbulent model to describe blood flow may be more appropriate against DNS with the pure Navier-Stokes Equations. We use the three models described in the Section 2.2 in its steady-state version: $k-\epsilon$, $k-\omega$ and SST $k-\omega$ models. When a turbulent model has been selected, additional boundary conditions must be settled. We will make use of some analytical functions called wall functions. In the closest region to the wall, also called boundary layer, some time-averaged and turbulent variables can be approximated analytically by means of the wall functions. Some of them are pre-established in OpenFOAM and other CFD solvers.

The boundary conditions to be applied over the new turbulent variables are shown in (3.4). We use the reference [80] to get the wall function ω_{wall} and other conditions over k and ω. Meanwhile we have used [53] to settle boundary conditions to ϵ.

$$\begin{cases} \epsilon(x) = 2 \\ k(x) = 10^{-6} \\ \omega(x) = 1 \end{cases} \quad \text{if } x \in \Gamma_{\text{in}}$$

$$\begin{cases} \nabla\epsilon(x) = \mathbf{0} \\ k(x) = 10^{-10} \\ \omega(x) = \omega_{\text{wall}}(x) \end{cases} \quad \text{if } x \in \Gamma_{\text{wall}} \tag{3.4}$$

$$\begin{cases} \nabla\epsilon(x) = \mathbf{0} \\ \nabla k(x) = \mathbf{0} \\ \nabla\omega(x) = \mathbf{0} \end{cases} \quad \text{if } x \in \Gamma_{\text{out}}$$

3.2.3 Finite Volume Method solver: OpenFOAM

We employ the CFD solver OpenFoam which is an open source C++ object-oriented library. This software applies the FVM to the balance laws introduced and it has tools to process and mesh the geometry where the fluid problem takes place. The structure of the principal directo-

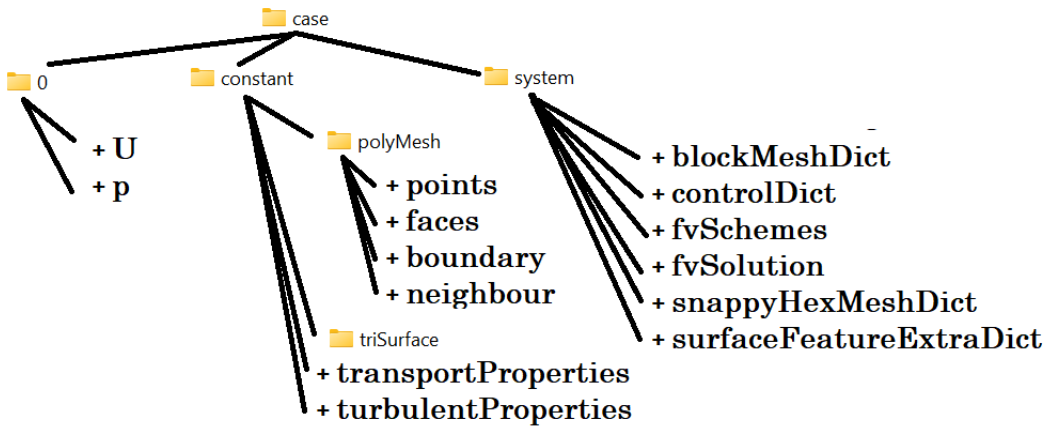

Figure 3.6: Scheme of the file structure of OpenFOAM.

ries and files is shown in the Figure 3.6. The main directory contains all the information about mechanical fluid problem and the numerical resolution. We distinguish files that define the geometry and meshing properties, and files that characterize the CFD resolution.

The volume of the aorta will be determined by a tringulated surface which constitutes the aorta boundary. The information about the surface is carried in a STL file, format used to describe the surface of a three-dimensional object. It sets the triangles that constitutes the surface by giving a structured list of all the vertices. This file is provided by our collaborators from the Hospital Universitari i Politècnic La Fe. The three principal patches of the surface (inlet, outlet and wall) are tagged inside the file, and its structure is shown in the Figure A.1.

Meshing

The mesh where the CFD simulation will take place consists in staked polyhedra (volumes). The meshing process from the triangulated surface is divided in three steps, each one carried out by a specific utility in OpenFOAM.

The first one is the `blockMesh` utility, which defines a preliminary mesh with regular hexaedra. The second one is called `surfaceFeature-Extract`, which extract geometrical information about points, edges and faces from our STL file. Basically, it marks those pair of faces of the boundary for which the angle formed by their normal vectors exceed a

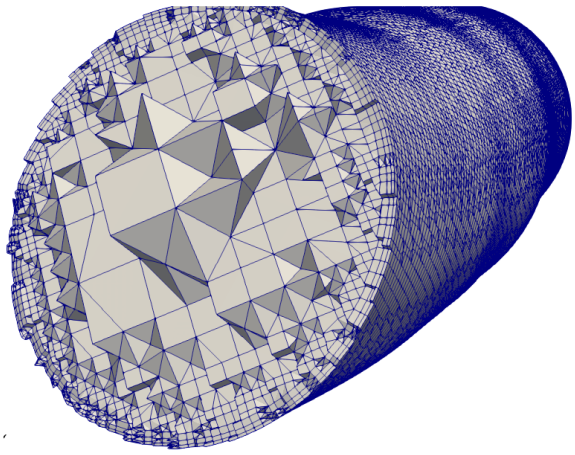

Figure 3.7: A close-up of the mesh used for simulation. The resolution at the wall is 1mm.

determined value. Then, it stores information about the roughness of the surface. The last utility is called `snappyHexMesh`, which carries the process of refinement and addition of layers near the boundaries.

The refinement process consists in the increment of the spatial resolution as one gets closer to the boundaries. For us, a refinement level is the number of times we split the polyhedra close to the wall with respect its resolution in the coarser region of the mesh. For instance a level 1 of refinement means improving the spatial resolution a factor 2 with respect the coarser region, and a level 2 to improve it a factor 4. In the Figure 3.7 we show an example of a mesh used in aorta with a refinement level of 2. Notice that three sizes are present for the polyhedra. On the other hand, the layer addition process shrinks the mesh after the refinement to add extra polyhedra becoming gradually thinner as approaching the wall. In the Figure 3.7 3 layers have been incorporated. All this features can be settled in a parameter file, shown in A.2.

Our focus is on the WSS, which is related to the velocity variation in the normal direction to the wall. Then, the refinement and layer addition processes will be essential.

After the meshing processes, the mesh is stored in three principal files containing the vertices, faces and patches. The first is called `points` and is read by the next one, `faces`, which at the same time is read by the latter, `boundary`. The structure of these files can be seen in the Figures A.3, A.4 and A.5.

Fluid properties

Properties about the fluid are settled in the file `transportProperties`. There, we establish the kinematic viscosity ν and whether the fluid is Newtonian or precise other constitutive relation.

On the other hand, if we want to apply some turbulence model, we have to specify it in the file `turbulenceProperties` (see A.6). One can set the keyword `laminar`, which means that no turbulence model is going to be applied, i.e. DNS. There are several turbulence models available.

Initial and boundary conditions

Boundary conditions and initial conditions are settled inside the directory `case/0` (see Figure 3.6). Particularly, there exist one file per variable to set these conditions.

For syntax reasons one always need to settle initial conditions, even if we are in steady-state flow. Concerning boundary conditions, we are applying the ones shown in (3.2). The file that settles these conditions for the pressure is shown in the Figure A.7. Besides, we show in the Figures A.8 and A.9 examples to settle a uniform and non-uniform boundary condition for the velocity at the inlet. In the last case we have used a parabolic profile as the one in the Figure 3.4.

There is no tool in OpenFOAM to apply a determined function as boundary condition. Therefore, we have drawn a script in Python that does this task. We do not show the details of this script but the structure is presented as pseudo-code in the Box 3.1.

The main steps are the following. First, we read the files that contain information about the location of the inlet faces. With this we are able to compute the centroid of each face, where the velocity is settled by our FVM. Then, we read some parameters from the reconstruction process about the inlet: normal vector, center point and two semi-axis (the ellipse axis if a reconstruction method by ellipses has been used). If the reconstruction takes into account a more general closed curve, we can always obtain the ellipse that better reproduces the curve. Once we have these data we can compute the elliptic coordinates of each face centroid to compute the velocity of that point with the parabolic profile formula (3.3). Then, an array with these velocities is created in agreement with the sorting of the inlet faces by OpenFOAM. Finally, we can rewrite the file `case/0/U` with these values of the velocity in the correct syntax.

```
read points
read faces
read boundary
compute centroid_faces_inlet
read normal_vector
read center_inlet
read semi_axis
for each c ∈ centroid_faces_inlet
      compute elliptic_coordinates
      compute velocity_vector
      append velocity_vector to velocities_array
end
for each v ∈ velocities_array
      write v to case/0/U
end
```

Box 3.1: Pseudo-code of the scrip to settle a parabolic profile for the velocity as boundary condition at the inlet.

When a turbulent model is selected additional boundary conditions must be set, as in (3.4). There is no much mystery here once we have explained how to do it for pressure and velocity. However, we show an illustrative example with k in the Figure A.10, where we have used a wall function for k.

Numerical resolution issues

Now, we explain the parameter files that control the numerical solution: `controlDict`, `fvSchemes` and `fvSolution`. In the first one, several balance laws and algorithms of resolution can be established. In the example shown in the Figure A.11, the keyword `simpleFoam` has been set, which is an application for incompressible steady-state flows using SIMPLE algorithm. Here, we can also fix the time step, which is meaningless in this case.

In `fvSchemes` the discretization strategy for the transient term, gradients, divergences and laplacians is settled (see Figure A.12). Finally, in `fvSolution` we put parameters concerning the SIMPLE algorithm and iterative solvers for the algebraic linear systems that come from the discretization process (see Figure A.13). There, a geometric multigrid method called `faceAreaPair` has been set.

The simulation is an iterative process. The solution of each iteration of the SIMPLE algorithm is stored in directories. When a transient model is applied the directories correspond to a specific time. WSS is computed in a post process, after the numerical simulation, and it is also stored in these directories.

3.3 Results

In the previous Sections we have introduced the tools to apply the FVM to solve numerically the Navier-Stokes Equations in aorta.

The simulations have a twofold goal. One is based in geometrical aspects. In this work we have a sample of aortas from Computerized Tomography with aortic stenosis to which we apply the designed reconstruction method to be validated here with CFD.

The other goal is the determination of how inlet conditions affect the shear stress in a non-desirable manner and put some redress. We know that low values of WSS are related to atherosclerosis [83]. To do so, we first need to determine what model is more appropriate to this task. We test a model based on the Navier-Stokes Equations (DNS), and also $k-\epsilon$, $k-\omega$ and SST $k-\omega$ models of turbulence. Once we have chosen our model we will study the influence of three types of aortic valves: a healthy valve and two prosthetic valves.

With the meshing tools of OpenFOAM, we build a preliminary mesh of cubes of 2 mm, followed of a refinement process and finally adding some additional layers to increase further the spatial resolution near the wall. We will specify the maximum resolution in each problem.

In all simulations a linear Gauss finite volume discretization is employed for the balance laws, and we will combine a geometric multigrid method with the Gauss-Seidel method as smoother. All this in the context of the SIMPLE algorithm.

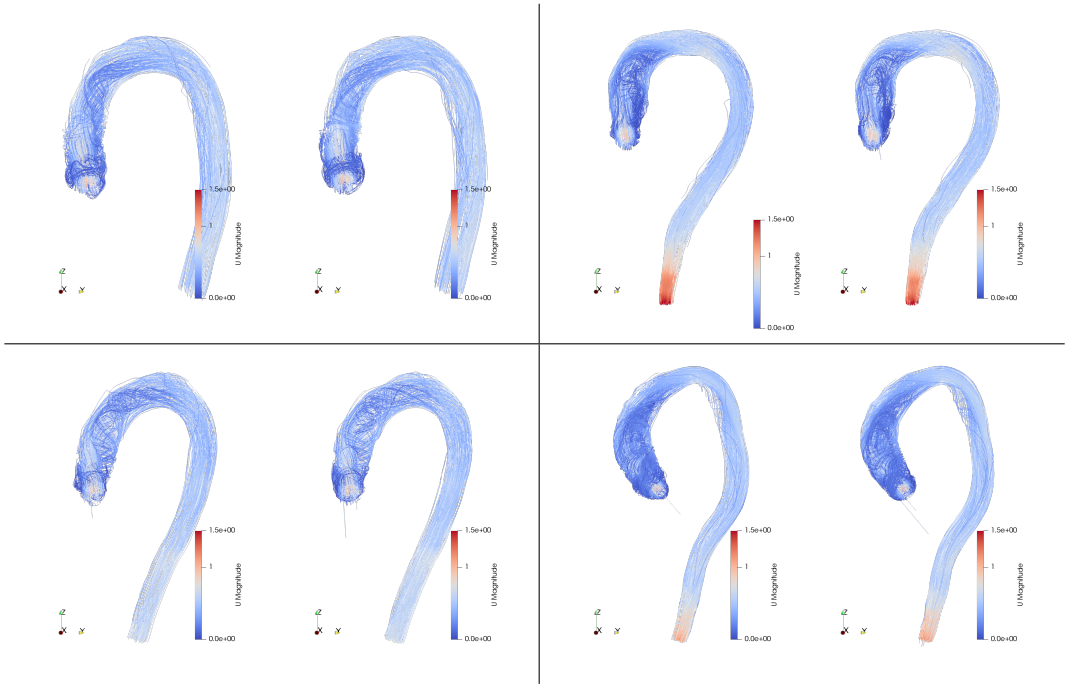

Figure 3.8: Results of the streamlines from simulations with the original aorta (left) and reconstructed aorta (right). Four different aorta patients are shown.

3.3.1 Validation of the reconstruction algorithm

In this Subsection we work with a mesh of volumes where a refinement level of 2 has been applied. We also use 3 additional layers becoming thinner and thinner until reaching a spatial resolution of 0.1 mm at the aortic wall. The boundary conditions applied are the ones in (3.2) with a parabolic profile for the inlet. DNS is to be applied in this part.

The following results show the differences between the original geometries and the reconstructed ones. We present four streamlines comparisons between original aorta (left) and reconstructed one (right) in the Figure 3.8. And in the Figure 3.9 we show four WSS comparisons between original aorta (left) and reconstructed one (right).

Even though the results are very preliminary, the most noticeable macroscopic WSS patterns that appear on the original aorta mesh are

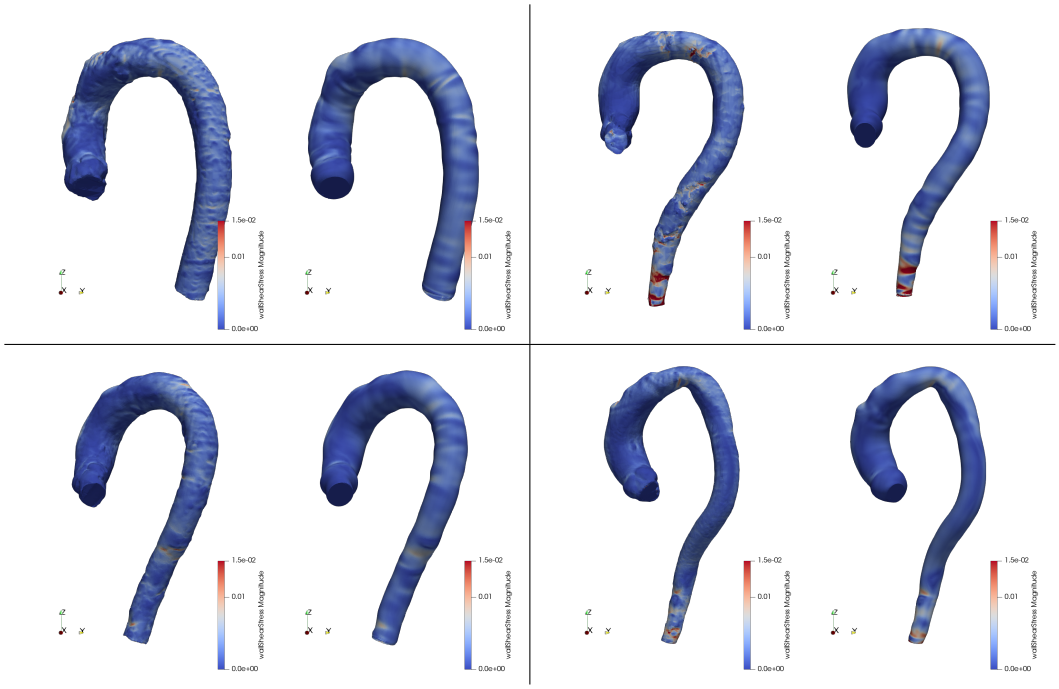

Figure 3.9: Results of the WSS profiles from simulations with the original aorta (left) and reconstructed aorta (right). Four different aorta patients are shown.

reproduced when using the reconstructed surface. This might indicate that the proposed characterization would be able to store geometric information relevant to reproduce WSS profiles.

The proposed characterization of the geometry offers a low-dimensional representation of the aorta that can be used as a characteristic vector for statistical or Machine Learning analyses. By means of Statistical Shape Modelling, a large dataset of aorta geometries can be generated to run simulations and characterize different WSS profiles from the geometry. Compared to other dimensional reduction techniques, such as Principal Component Analysis or Neural Network approaches [76], our approach is based on geometry and, thus, characteristics are more meaningful even from a clinical point of view.

3.3.2 WSS analysis

Now, we focus our attention on one specific thoracic aorta and its values of WSS. Particularly, we know that low values are related to atherosclerosis [83]. We first need to determine what model is more appropriate to this task. Once we have chosen the model, we will study the influence of three types of aortic valves: a healthy valve and two prosthetic valves.

Our purposes have a health motivation here, so the choice of the mesh plays a crucial role. A mesh independence analysis in this context (see [106]) has determined that a level 5 of refinement plus an addition of 15 thinner and thinner layers is good enough to get stabilized WSS profiles. We will work with a mesh of 8.6 millions of volumes with maximum spatial resolution of 50 μm at the aortic wall. The mesh used is shown in the Figure 3.10.

Boundary conditions for pressure and velocity are the same of those in the Subsection 3.3.1, expect for the velocity inlet conditions where we apply those shown in the Figure 3.5. We use DNS and three RANS models ($k-\epsilon$, $k-\omega$ and SST $k-\omega$) for the simulations. Boundary conditions over the new turbulent variables are shown in (3.4).

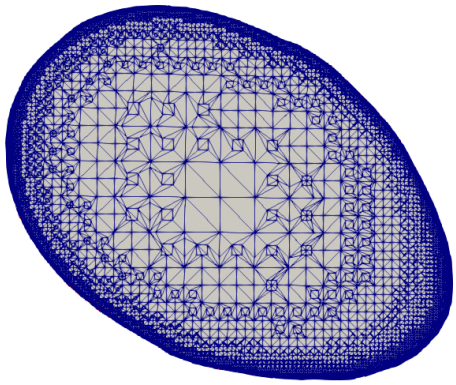

Figure 3.10: Aorta section showing the ultimate mesh used for the WSS analysis.

CFD model

First of all, we are determining which one is the most suitable model for simulation. To do so we are using a healthy valve profile for the inlet boundary condition. In the Figure 3.11 we show some simulations using DNS, $k-\epsilon$ and $k-\omega$ models. The first row present streamlines and the second one WSS profiles.

We described in the Subsection 2.2 the main features of $k-\epsilon$ and $k-\omega$ turbulent models. The most remarkable result is the high values of WSS provided by the $k-\epsilon$ in the descending aorta. Since this model does not properly compute turbulence in regions with large pressure gradients (such as the boundary layer) and strong accelerations (when the aortic duct narrows), this model can be assumed to provide a poor approximation. On the other hand, we know that the $k-\omega$ model is sensitive to boundary conditions of the turbulent variables at the inlet free stream, which does not happen with the $k-\epsilon$ model. This explains the distinct behaviour of streamlines computed with $k-\omega$ model in the cavity of the aorta.

One would expect that the SST $k-\omega$ model, which combines good features of both model, will work better. In the Figure 3.12 simulations with this turbulence model can be found for three inlet boundary conditions, each one reproducing the behaviour of a type of aortic valve. Focusing in the healthy valve, the cavity flow computed with this model looks like the one computed with $k-\epsilon$ model, which is most reliable in this region,

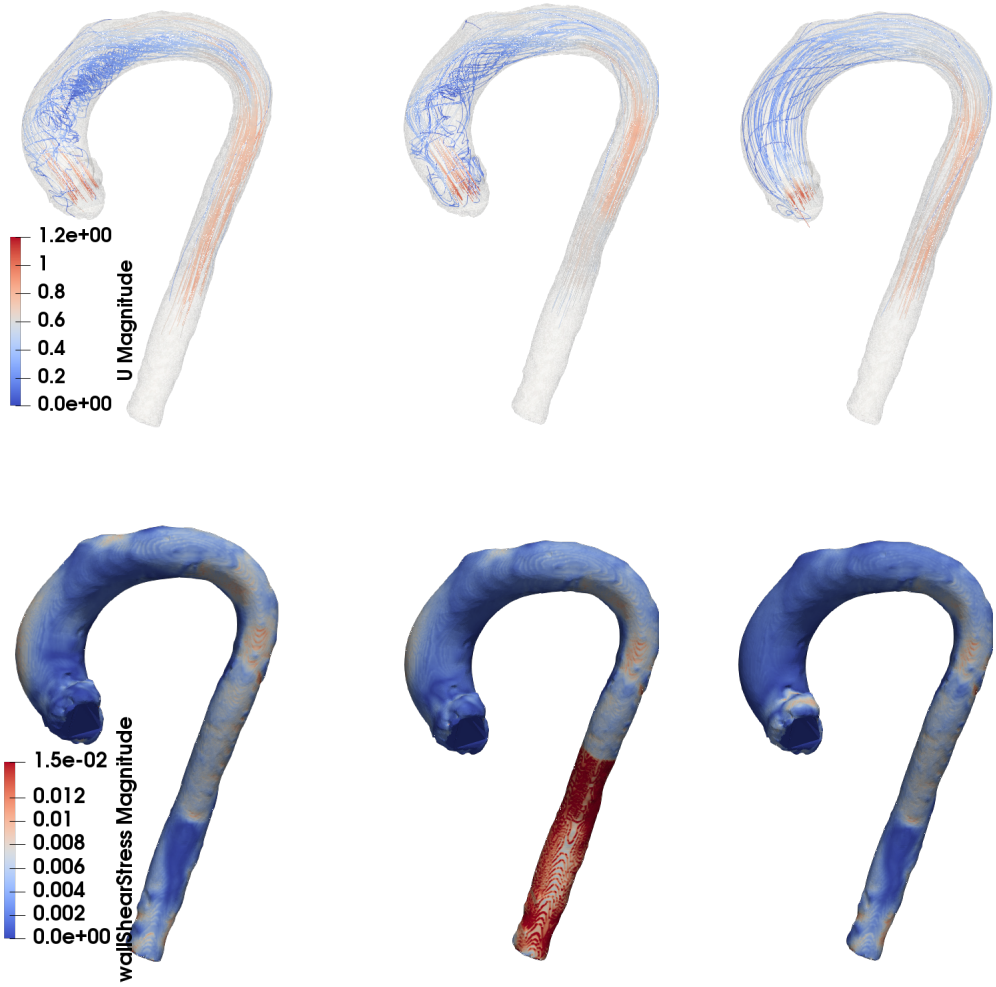

(a) DNS model and healthy valve.

(b) $k-\epsilon$ model and healthy valve.

(c) $k-\omega$ model and healthy valve.

Figure 3.11: Streamlines (above) and τ_w/ρ profiles (below) obtained with different turbulence models. All units in the SI.

and the WSS profile has more resemblance with the one computed with $k-\omega$ model, the one that behaves better near the wall. Performing a DNS seems in good agreement with SST $k-\omega$ model. Nevertheless k is an essential parameter in the study of diseases like stenosis or coarctation. Besides a turbulent model is more efficient computationally in certain contexts (see Section 2.2). Then, we claim that the SST $k-\omega$ model is

more suitable for the task addressed here.

(a) SST $k-\omega$ model and healthy valve.

(b) SST $k-\omega$ model and bileaflet valve.

(c) SST $k-\omega$ model and tilting disk valve.

Figure 3.12: Streamlines (above) and τ_w/ρ profiles (below) obtained with different turbulence models. All units in the SI.

Influence on the type of valve

Now, we focus on the profiles of the Figure 3.12 to analyse the influence of the inlet boundary condition, trying to extract some conclusions about aortic valves. Streamlines obtained in ascending aorta with the three types of valve are trustable when comparing with experimental and theoretical works [54, 133]. Regarding the effect of the valve type, it clearly affects the WSS profile. We consider a critical value of 0.5 Pa under which there is risk of atherosclerosis appearance, see [83]. The Figure 3.13 shows a detailed analysis of the influence of valve on the WSS values. We analyze 7 sections along the aorta, S_i for $1 \leq i \leq 7$. S_1, S_2 and S_3 are placed in the ascending aorta where the results are more trustworthy. We can see that in the case of the bileaflet valve almost 16% of S_1 is in risk, the highest value of the analysis, meanwhile 10% with the tilting disk valve and 2% with the healthy valve. In S_2 there is no region in risk for any valve and in S_3 we have 6%, 5% and 4% for the healthy, bileaflet and tilting disk valve, respectively.

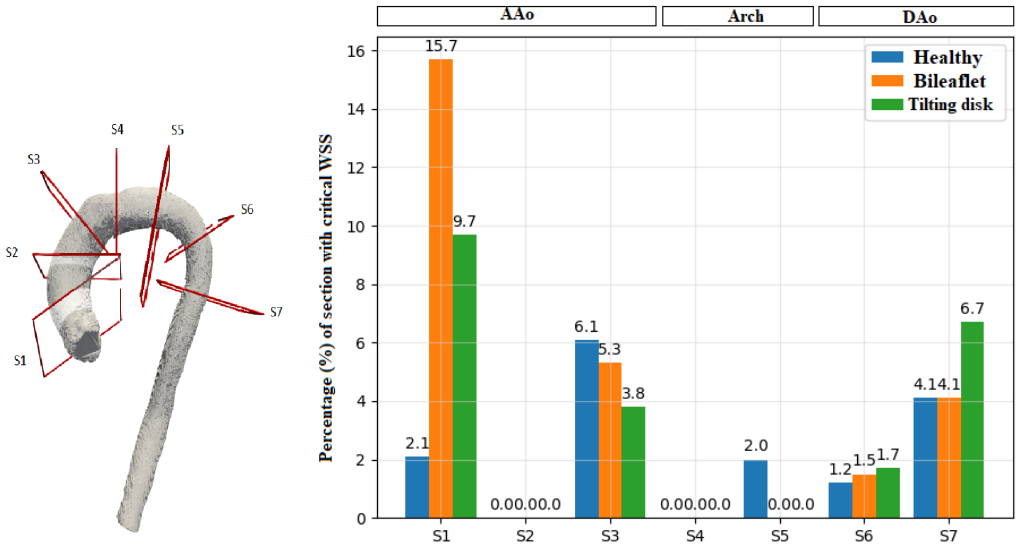

Figure 3.13: Location of the selected aortic sections for the WSS analysis (left) and histograms showing, for each section and for the three valves studied, the percentage of points with ananomalous values of WSS (right).

Sections S_4 and S_5 are placed at the aortic arch where we have suppressed the supraortic arteries. These arteries suppose the 30% of the entire flow. Besides, in this region the geometry is highly modified be-

cause of this. Then, the results in this zone are to be ignored. Similarly, the values on the descending aorta are not trustable. Although the geometry is not altered there, the lack of flow may be determinant in this analysis. Nonetheless, we observe in an increase of the risk region with artificial valves.

3.4 Final remarks

The reconstruction method for aorta geometries has been capable to capture the general behaviour of WSS patterns. However, it is still at an early stage and requires further improvement. First of all, there are some free parameters, such as the number of elliptic cross sections, or the degrees of freedom of the centerline that need to be fixed to have an standard characterization. The proper selection of these and other parameters needs to be done using a larger sample of aortas to determine which are more discriminant of the intra-population variations. The method, in its current form, does not reconstruct the sinuses of Valsalva and is not able to build the main aorta branches. Using a centerline extraction that is able to reproduce branching would enable this feature. The location and orientation of these branches should also be considered as relevant features.

On the other hand, we concluded that the SST $k-\omega$ model was the most reliable in WSS studies as it posses the good properties from both $k-\epsilon$ and $k-\omega$. Besides, it calculates the turbulent kinetic energy k, which is important in the study of cardiovascular diseases and it is computationally cheaper than applying DNS.

Concerning the study of WSS values and aortic valves, we have observed the following: the inlet boundary conditions that model the two prosthetic valves contribute, in general, to increase the region with risky WSS values. The bileaflet valve does it in a minor level than the tilting disk valve in the ascending aorta. According to this we affirm that human biology has made a good work and whenever a prosthetic valve is needed we will support the bileaflet valve above the tilting disk one.

Of course, this is a very preliminary analysis. Future studies must

include the addition of the supraortic arteries. Besides, transitory simulations, to take into account the whole cardiac cycle, are needed. By doing so, we will be able to compute other hemodynamic variables of interest as OSI or TAWSS [131]. Also a fluid-structure interaction should be considered to get a complete study of genesis of cardiovascular diseases.

4

Overview about Relativity and Gravitation

The forecoming chapters will be framed in the Theory of Relativity either with or without gravitation. Then, we include here an introductory chapter to establish the basic concepts and notions about this theory. The contents herein are a summary of the references [102, 125, 51, 50, 130]. The Theory of Relativity supposes a change of paradigm in the notion of space and time. The time will no longer be an absolute quantity in which every observer or detector agrees, but it becomes an observer dependent quantity, as it will be space. We begin introducing the theory of Special Relativity and then extend it to General Relativity, a theory to describe gravitation, based on the Einstein Equations. We will continue describing some analytical solutions of the Einstein Equations and finish with a section about Numerical Relativity, where the equations are rewritten to make them suitable for numerical simulations.

4.1 Special Relativity

Special Relativity was published by Einstein in 1905. It is framed in the context of non-accelerated observers and in the absence of gravity, which will be addressed the next section. The theory is supported by two initial postulates which involve the notion of inertial (non-accelerated) observer. We will assume both of them as true over the manuscript. They are called **Einstein Postulates** and read as follows:

1. Any inertial observer perceives the same laws of physics.

2. The speed of light in vacuum detected by any inertial observer has always the same value.

The constant value of the speed of light will be denoted c from now on. As noticed both postulates involve important symmetry arguments. The second has an interesting causality motivation. Einstein realized that should this not be case, some inertial observers would detected the effect before the cause. And this could not happen for him. Many experiments have checked the constant value of the speed of light. The most famous is the Michelson-Morley experiment. The established value is $c = 299.792.458$ m/s

4.1.1 New description of space and time

Let us consider an inertial observer O. Any event will be tag by four quantities (t, x, y, z) by O, which are referred as coordinates measured by O. The first one will be the time and the latter three the spatial position as perceived by O, in Cartesian coordinates. Let us consider two events labeled by the coordinates (t_1, x_1, y_1, z_1) and (t_2, x_2, y_2, z_2). $\Delta t = t_2 - t_1$ is the lapse of time measured by O between the events. Now, we define the spacetime interval of the two events as the quantity

$$\Delta s^2 := -(c\Delta t)^2 + \Delta x^2 + \Delta y^2 + \Delta z^2. \tag{4.1}$$

Suppose there exist another inertial observer O' moving at constant speed V with respect O. The constant value of the speed of light implies that the new observer O' will measure another set of coordinates for both events. If O' moves alongside the x-direction of O, their coordinates are related by the expressions

$$ct' = \Gamma(ct - Vx/c), \quad x' = \Gamma(x - Vt), \quad y' = y, \quad z' = z. \tag{4.2}$$

where $\Gamma = (1 - V^2/c^2)^{-1/2}$ is the Lorentz factor, to be properly defined later. It turns out that the spacetime interval (4.1) is preserved when the coordinates are substituted by the ones detected by O'. Hence, discovering that it is a conserved quantity, no matter the inertial observer who is taking measures. We say that the coordinate change (4.2) is a **Lorentz transformation**. So, the spacetime interval is preserved by these transformations. In this manner, we have found an absolute (non-observer-dependant) quantity which allow us to define the following metric of spacetime in Cartesian components:

$$\eta_{\alpha\beta} = \text{diag}(-1, 1, 1, 1), \tag{4.3}$$

to be applied over the affine space M constituted by the set of points of all events. In other words, the vectors of this affine space are endowed with the scalar product

$$\langle \boldsymbol{v}, \boldsymbol{u} \rangle = \eta_{\alpha\beta} v^\alpha u^\beta. \tag{4.4}$$

We also write $\langle \boldsymbol{v}, \boldsymbol{u} \rangle = v_\alpha u^\alpha$, with $v_\alpha = \eta_{\alpha\beta} v^\alpha$. Of course, the scalar product (4.4) is a Lorentz invariant. The affine space M is dimension 4 and endowed with the metric (4.3) is called Minkowski spacetime or flat spacetime. As seen, the signature of the metric is $(1, 3)$, so it is a Lorentzian metric.

The interval expressed in differential form takes the form

$$ds^2 = \eta_{\alpha\beta} dx^\alpha dx^\beta. \tag{4.5}$$

We denote $x^0 = c\,t$ as a rescaled time coordinate and x^i are the spatial Cartesian coordinates. The differential expression of the spacetime interval (4.5) in some coordinates will be a regular form for presenting the metric of the spacetime in those coordinates.

If two event satisfy that $\Delta s^2 < 0$ they are said to have a timelike separation. For those events there exists an inertial observer for which $\Delta l = \Delta x^2 + \Delta y^2 + \Delta z^2 = 0$ and we define the proper time as the measured by this observer,

$$\tau := \sqrt{-\Delta s^2}/c. \tag{4.6}$$

Similarly, the vectors for which $v_\alpha v^\alpha < 0$ are called timelike vectors. On the other hand, those events with $\Delta s^2 > 0$ are said to have a spatial separation. There exists an inertial observer for which both events occur at the same time. The length measured by this observer between both events is called proper length, $l := \Delta s^2$, and a vector such that $v_\alpha v^\alpha > 0$ is called spacelike vector. Finally, if $\Delta s^2 = 0$ both events are said to be connected by a null separation and a vector such that $v_\alpha v^\alpha = 0$ is called null vector.

A curve of spacetime $\mathcal{C}$ can be described by four functions $x^\alpha(\lambda)$, for which each value of the parameter λ give the spacetime coordinates of the particle with respect some inertial observer. We say that a curve is timelike, spacelike or null if its tangent vector has the same character. A timelike curve can be parametrized by the proper time τ, a more convenient choice as it is Lorentz invariant. Then, the four-velocity of a timelike curve is defined as

$$v^\alpha := \frac{1}{c}\frac{dx^\alpha}{d\tau}. \tag{4.7}$$

Notice that the components of the four-velocity do not have physical dimensions. One can easily show that $v_\alpha v^\alpha = -1$. We define the four-acceleration of the curve as

$$a^\alpha := \frac{1}{c}\frac{dv^\alpha}{d\tau}. \tag{4.8}$$

It can be checked that this is a spacelike vector.

Despite the fact that the notion of observer can be intuitively realized as a person with some kind device to take measures, some books make a rigorous mathematical definition. We say that a set of four vector fields $(\boldsymbol{e}_\alpha)$ is a **local frame** if it is a right-handed orthonormal basis of M for all point $p \in M$ and each element $\boldsymbol{e}_\alpha$ is differentiable. A local frame is said to be alongside a timelike curve $\mathcal{C}$ if it satisfies $\boldsymbol{e}_0(p(\lambda)) = \boldsymbol{v}$ (the four-velocity of the curve), where $p(\lambda) \in \mathcal{C}$. Then, an observer is defined as the set of a timelike curve and local frame alongside this curve. Moreover, an inertial observer is defined such that it satisfies

$$\frac{e_\alpha(\lambda)}{d\lambda} = 0,$$

so they always move in straight lines.

4.1.2 Kinematics of a particle

Let us consider the movement of a particle. The trajectory of the particle will be a curve described by some coordinates (x^α) according to an inertial observer. Suppose that the trajectory of the particle is a timelike curve of spacetime. Particles that follow spacelike trajectories are called tachyons, and its existence would provoke some causality issues. Choose the proper time τ as a parameter of the timelike curve. It can be seen as the time measured by a clock attached to the particle. Be $\boldsymbol{v}$ the four-velocity of the particle and let us call $V^i = dx^i/dt$ the usual velocity of classical mechanics. Then, the four-velocity can be express as

$$v^\alpha = \Gamma(1,\, V^i/c), \tag{4.9}$$

where we have defined the Lorentz factor of the particle as

$$\Gamma := \frac{dt}{d\tau}. \tag{4.10}$$

One can easily show the following formula

$$\Gamma = \frac{1}{\sqrt{1-(V/c)^2}}. \tag{4.11}$$

with $V = \sqrt{(V^x)^2 + (V^y)^2 + (V^z)^2}$. The four-momentum of a particle of mass m is defined as

$$p^\alpha := m v^\alpha. \tag{4.12}$$

It satisfies

$$p_\alpha p^\alpha = -m^2. \tag{4.13}$$

The component p^0 have a significance relevance. If we expand in Taylor expansion up to V^2 we get

$$c^2\, p^0 = mc^2 + \frac{1}{2} m V^2 + ... \tag{4.14}$$

The first term mc^2 in the righthand side is called rest energy of the particle, and in the second one we recognize the kinetic energy of classical mechanics. Then, we define the energy of the particle ε as $c^2\, p^0$ and the following expressions hold

$$p^\alpha = (\varepsilon/c^2,\, P^i/c), \qquad \varepsilon = \Gamma m c^2, \tag{4.15}$$

where we have defined the momentum of the particle $P^i = \Gamma\, m\, V^i$, which is the one perceived by the inertial observer.

Particles that follow null trajectories travel at the speed of light. Indeed

$$ds^2 = -c^2dt^2 + dl^2 = 0 \implies c = dl/dt = V \tag{4.16}$$

Thus, they cannot be parametrized by the proper time τ, as $d\tau = -ds^2/c = 0$. Let us consider a parameter λ realized as the quotient τ/m if the particle moved close but strictly below c and had mass m. The four-momentum of the particle is defined as

$$p^\alpha = \frac{dx^\alpha}{d\lambda}. \tag{4.17}$$

This expression resembles that for the timelike particle (4.12). Then, as it follows a null curve, it satisfies

$$p_\alpha p^\alpha = 0, \tag{4.18}$$

from which, according to (4.13), we affirm that the particle must have zero mass $m = 0$.

Particles moving at the speed of light are massless. According to Planck's formula massless particles have energy $\varepsilon = hf$, with f the associated frequency by quantum physics and h the Planck constant. It is often to write the four-momentum of a massless particle as

$$p^\alpha = (\hbar\omega/c^2,\, \hbar K^i/c), \qquad \omega = cK \tag{4.19}$$

where $\omega = f/2\pi$, $\hbar = h/2\pi$, K^i is the wave vector and K its modulus. The wave vector determines the direction of propagation and is also identified with the (three) momentum of the massless particle.

4.1.3 Hydrodynamics

In classical fluid dynamics, the matter an momentum conservation lead the to the Navier-Stokes Equations or the Euler Equation in the absence of viscous stresses. They involve quantities as mass density or momentum. In Special Relativity mass, momentum and energy are

observer dependant magnitudes. Then, it will be very convenient to write conservation laws in a non observer dependant form.

Let us define the matter density ρ and the internal energy density ϵ of the fluid as those quantities that would measure an observer moving with the fluid particles. This type of observer is called comoving observer. The total energy density is $\mu = \rho c^2 + \epsilon$. Now, for our purposes, we define the matter-current four-vector j^α such that:

- j^0 is the matter density,
- cj^k is the matter flux in the x^k-direction,

measured by an inertial observer. We consider now the four-velocity v^α of the fluid. The following relation can be demonstrated:

$$j^\alpha = \rho v^\alpha. \tag{4.20}$$

and the matter conservation can be described by the expression

$$\partial_\alpha j^\alpha = 0. \tag{4.21}$$

It also can be expressed as

$$\frac{d\rho}{d\tau} + \rho \partial_\alpha v^\alpha = 0, \tag{4.22}$$

where $d\rho/d\tau = v^\alpha \partial_\alpha \rho$. This equation is the generalization of the mass conservation equation (2.1a) to Special Relativity.

Conservation of energy and momentum can be written in a similar form with the help of the energy-momentum tensor. The energy-momentum tensor is a (2,0)-tensor $T^{\alpha\beta}$ defined such that

- T^{00} is the energy density,
- cT^{0j} is the energy flux in the x^j-direction,
- $c^{-1}T^{j0}$ is the j-component of momentum density,
- T^{jk} is the j-momentum flux in the x^k-direction, specifically T^{jk} is the pressure in the x^j-direction,

all quantities measured by the inertial observer. Energy and momentum conservation can be written as

$$\partial_\alpha T^{\alpha\beta} = 0. \tag{4.23}$$

Let us take a perfect fluid model. This type of fluid is characterized by not accounting for viscous effects or shear stresses. Its energy-momentum tensor is

$$T^{\alpha\beta} = (\mu + p)v^\alpha v^\beta + p\eta^{\alpha\beta}. \tag{4.24}$$

If we develop the expression (4.23) and project it over the direction of v^α we obtain the conservation equation for the energy:

$$\frac{d\mu}{d\tau} + (\mu + p)\partial_\alpha v^\alpha = 0 \tag{4.25}$$

On the other hand, the orthogonal part to v^α leads to the momentum conservation equation

$$(\mu + p)\frac{dv^\alpha}{d\tau} + (\eta^{\alpha\beta} + v^\alpha v^\beta)\partial_\beta p = 0. \tag{4.26}$$

which is the relativistic version of the Equation (2.1b) without viscosity, i.e. it is the relativistic Euler Equation. The classical version is recovered in the limit $c \to \infty$, or put in another way, when the velocities are much smaller than c.

4.1.4 Electrodynamics

Electric $\boldsymbol{E}$ and magnetic $\boldsymbol{B}$ fields are observer dependant magnitudes too. The equations describing its dynamics are the so-known Maxwell Equations

$$\begin{aligned} \nabla \times \boldsymbol{E} &= -\frac{\partial \boldsymbol{B}}{\partial t}, & \nabla \cdot \boldsymbol{E} &= \frac{q}{\varepsilon_0}, \\ \nabla \times \boldsymbol{B} &= \mu_0 \boldsymbol{J} + \mu_0 \varepsilon_0 \frac{\partial \boldsymbol{E}}{\partial t}, & \nabla \cdot \boldsymbol{B} &= 0, \end{aligned} \tag{4.27}$$

where ε_0 is the permitivity of vacuum, μ_0 the permeability of vacuum, q the charge density and $\boldsymbol{J}$ the charge-current density. When the charged matter is moving in vacuum, we simply have $\boldsymbol{J} = q\boldsymbol{V}$ with $\boldsymbol{V}$ the velocity of the charged particles.

Wave solutions of the Maxwell Equations are called electromagnetic waves and are a description of the wavelike behaviour of light. It turns out that its propagation speed in vacuum is equal to $(\varepsilon_0\mu_0)^{-1/2}$ which must coincide with c.

A spacetime observer independent form can be derived for Maxwell Equations. For this task we define the electromagnetic tensor field $F^{\alpha\beta}$ which is defined such that $F^{\alpha\beta} = -F^{\beta\alpha}$, $F^{0j} = E^j/c$ and $F^{ij} = \epsilon^{ijk}B_k$, where ϵ^{ijk} is the totally antisymmetric spatial Levi-Civita symbol. We define too a charge-current density four-vector

$$k^\alpha = qv^\alpha \tag{4.28}$$

where q is the charge density measured by an observer attached to the charged particle element. It has an analogous interpretation to the matter current four-vector j^α: k^0 is the charge density and k^j the charge flux density in the x^j-direction as perceived by an inertial observer. Then, the Maxwell Equations can be cast as

$$\partial_\beta F^{\alpha\beta} = \mu_0 k^\alpha, \qquad \partial_\beta F^{*\alpha\beta} = 0. \tag{4.29}$$

where $F^{*\alpha\beta} = (1/2)\epsilon^{\alpha\beta\gamma\delta}F_{\gamma\delta}$ is the dual electromagnetic tensor, with $\epsilon^{\alpha\beta\gamma\delta}$ the totally antisymmetric spacetime Levi-Civita symbol. The antisymmetry of the electromagnetic tensor enforces $\partial_\alpha\partial_\beta F^{\alpha\beta} = 0$ which translates in

$$\partial_\alpha(qv^\alpha) = 0, \tag{4.30}$$

finding the charge conservation equation.

We know that the electromagnetic field carries energy, momentum and stresses. The latter two are represented by the Poynting vector and the Maxwell stress tensor. This is compatible with the following definition for the energy-momentum tensor of the electromagnetic field:

$$T^{\alpha\beta} = \frac{1}{\mu_0}\left(F^{\alpha\gamma}F^{\beta}{}_{\gamma} - \frac{1}{4}\eta^{\alpha\beta}F_{\gamma\delta}F^{\gamma\delta}\right). \tag{4.31}$$

In this case, a conservation law for energy and momentum similar to the one found for a perfect fluid does not exits. Indeed,

$$\partial_\beta T^{\alpha\beta} = -F^{\alpha}{}_{\gamma}\, k^\gamma. \tag{4.32}$$

This makes sense as the electromagnetic field exerts forces and interchanges energy with charged particles. Precisely, the spatial components of (4.32) are related to the Lorentz force. On the other hand, an isolated system constituted by a fluid interacting with the electromagnetic fields must preserve energy and momentum. In that case, the

energy-momentum tensor of the whole system include both fluid and electromagnetic contributions $T^{\alpha\beta}_{\text{total}} = T^{\alpha\beta}_{\text{fluid}} + T^{\alpha\beta}_{\text{EM}}$, and it will satisfy

$$\partial_\alpha T^{\alpha\beta}_{\text{total}} = 0. \tag{4.33}$$

Taking the model of perfect fluid, this relation drives to

$$(\mu + p)\frac{dv^\alpha}{d\tau} + (\eta^{\alpha\beta} + v^\alpha v^\beta)\partial_\beta p + c^2 q F^\alpha{}_\beta\, v^\beta, \tag{4.34}$$

which we call relativistic magnetohydrodynamic Euler Equation.

Ohm's law

When the charged matter is moving in the interior of some material we have to add a contribution to the charge-current density $\boldsymbol{J}$. According to Ohm's law, in the comoving frame, this contribution reads

$$\boldsymbol{J} = \sigma \boldsymbol{E} \tag{4.35}$$

where σ is the conductivity of the material. The quantity $\eta = 1/\sigma$ is referred as resistivity. Notice that $\boldsymbol{J}$ is an observer dependant magnitude. It can be shown (see [120]) that in a general inertial frame the expression transforms into

$$\boldsymbol{J} = \Gamma q \boldsymbol{V} + \sigma\Gamma\left(\boldsymbol{E} + \boldsymbol{V}\times\boldsymbol{B} + (\boldsymbol{E}\cdot\boldsymbol{V})\boldsymbol{V}\right). \tag{4.36}$$

The expression of the charge-current density four-vector takes the form

$$k^\alpha = q v^\alpha + \sigma F^\alpha{}_\beta\, v^\beta. \tag{4.37}$$

When Ohm's law is taken into account we talk about Resistive Relativistic Magnetohydrodynamics. On the other hand, ideal magnetohydrodynamics is the limit $\sigma \to \infty$ or $\eta \to 0$. In that case, the electromagnetic field satisfy the next relations

$$\boldsymbol{E} = -\boldsymbol{V}\times\boldsymbol{B}, \tag{4.38}$$

$$\frac{\partial \boldsymbol{B}}{\partial t} = \nabla\times(\boldsymbol{V}\times\boldsymbol{B}). \tag{4.39}$$

So the electric field is derived from an algebraic equation. The limit $\sigma \to \infty$ is a particular case of a more general behaviour that arise in the area of partial differential equation. Consider a balance law with a source term. When a term inside the source is associated to phenomena of very different temporal scales, and where the source terms associated to them show factors which can potentially be several orders of magnitude higher than the others source terms, the balance law is said to be stiff, and those terms are refereed to stiff terms.

4.2 General Relativity

General Relativity is the theory of gravitation Einstein developed in 1915 [38]. It is written in the language of differential geometry. Then, some aspects about it will be outlined, although we will assume that some semantics of this area are previously known.

4.2.1 Differential geometry

The spacetime is defined as a four-dimensional differential manifold $\mathcal{M}$ endowed with a Lorentzian metric $\boldsymbol{g}$. The pair $(\mathcal{M}, \boldsymbol{g})$ is called pseudo-Riemannian manifold. We denote ∇ an affine connection on $\mathcal{M}$. Be $\boldsymbol{u}$ and $\boldsymbol{v}$ two vector fields, we denote the covariant derivative of $\boldsymbol{v}$ respect to $\boldsymbol{u}$ as $\nabla_{\boldsymbol{u}}\boldsymbol{v}$.

A set of vector fields $(\boldsymbol{e}_\alpha)$ in M is said to be a local frame if the conditions established in the previous Section for a local frame are satisfied for all $p \in M$ in the tangent space $\mathcal{T}_p(\mathcal{M})$. The connection coefficients $\Gamma^\mu{}_{\alpha\beta}$ associated with ∇ are defined as the scalar fields such that

$$\nabla_{\boldsymbol{e}_\beta}\boldsymbol{e}_\alpha = \Gamma^\mu{}_{\alpha\beta}\boldsymbol{e}_\mu. \tag{4.40}$$

An affine connection is said to be torsion-free if for any scalar field f, the bilinear form $\nabla\nabla f$ is symmetric. The Levi-Civita connection is the unique torsion-free affine connection satisfying $\nabla\boldsymbol{g} = 0$. In that case the connection coefficients are called Christoffel coefficients. Consider some coordinates (x^α) and the associated coordinate basis $(\boldsymbol{e}_\alpha) = (\partial_\alpha)$. In that case, the Christoffel coefficients are computed as

$$\Gamma^\mu{}_{\alpha\beta} = \frac{1}{2}g^{\mu\lambda}\left(\partial_\alpha g_{\lambda\beta} + \partial_\beta g_{\lambda\alpha} - \partial_\lambda g_{\alpha\beta}\right), \tag{4.41}$$

where $g^{\mu\nu}$ is defined as the inverse of the metric $g_{\mu\nu}$, i.e. $g^{\mu\lambda}g_{\lambda\nu} = \delta^\mu{}_\nu$, where $\delta^\mu{}_\nu$ is the Kronecker delta. The tensor indexes are raised and lowered with $g^{\mu\nu}$ and $g_{\mu\nu}$.

Given a vector field $\boldsymbol{v}$, we define $(1,1)-$tensor $\nabla \boldsymbol{v}$ such that component by component in the coordinate basis is expressed as:

$$\nabla_\mu v^\nu = \partial_\mu v^\nu + \Gamma^\nu{}_{\mu\lambda} v^\lambda. \tag{4.42}$$

Check [50] for more details. This definition can be generalized to any tensor field $\boldsymbol{T}$:

$$\begin{aligned} \nabla_\mu T^{\mu_1 \dots \mu_k}{}_{\nu_1 \dots \nu_l} = \partial_\mu T^{\mu_1 \dots \mu_k}{}_{\nu_1 \dots \nu_l} + \sum_{i=1}^{k} \Gamma^{\mu_i}{}_{\lambda\mu} T^{\mu_1 \dots \overset{i}{\downarrow} \dots \mu_k}{}_{\nu_1 \dots \nu_l} \\ - \sum_{j=1}^{l} \Gamma^{\lambda}{}_{\nu_j \mu} T^{\mu_1 \dots \mu_k}{}_{\nu_1 \dots \underset{j}{\uparrow} \dots \nu_l}. \end{aligned} \tag{4.43}$$

4.2.2 Curvature

General Relativity is lean on the Einstein's equivalence principle, which can be formulated as follows:

It is impossible to detect the presence of gravity within the boundaries of a small enough free-falling laboratory in a gravitational field.

This idea, along with the mental experiment of bend of light in an accelerated frame, drove Einstein to connect gravity with the curvature of the spacetime. Curvature manifests itself when a vector field $\boldsymbol{v}$ is parallely transported from one point to another through different curves. In an euclidean space, a parallelly transported vector field does not depend on the curve it is transported through. But when curvature is present this is no longer the case. This mismatch is captured in the lack of commutativity of two successive covariant derivatives over a vector field. It can be demonstrated that the tensor field $(\nabla_\alpha \nabla_\beta - \nabla_\beta \nabla_\alpha) v^\mu$ evaluated at $p \in \mathcal{M}$ not only is distinct from zero in general but it uniquely depends on the values of the vector $v^\mu(p)$ [130]. This defines the components of the Riemann tensor field $\boldsymbol{R}$:

$$(\nabla_\alpha \nabla_\beta - \nabla_\beta \nabla_\alpha) v^\mu = R^\mu{}_{\nu\alpha\beta} v^\nu. \tag{4.44}$$

The relation can be extended to any tensor field:

$$(\nabla_\alpha\nabla_\beta - \nabla_\beta\nabla_\alpha)T^{\mu_1\dots\mu_k}{}_{\nu_1\dots\nu_l} = \sum_{i=1}^{k} R^{\mu_i}{}_{\lambda\alpha\beta}T^{\mu_1\dots\overset{i}{\downarrow}\lambda\dots\mu_k}{}_{\nu_1\dots\nu_l} - \sum_{j=1}^{l} R^{\lambda}{}_{\nu_j\alpha\beta}T^{\mu_1\dots\mu_k}{}_{\nu_1\dots\underset{j}{\uparrow}\lambda\dots\nu_l}\,. \tag{4.45}$$

The Riemann tensor can be expressed in terms of the Christoffel coefficients:

$$R^{\mu}{}_{\nu\alpha\beta} = \partial_\alpha\Gamma^{\mu}{}_{\nu\beta} - \partial_\beta\Gamma^{\mu}{}_{\nu\alpha} + \Gamma^{\mu}{}_{\lambda\alpha}\Gamma^{\lambda}{}_{\nu\beta} - \Gamma^{\mu}{}_{\lambda\beta}\Gamma^{\lambda}{}_{\nu\alpha}. \tag{4.46}$$

A spacetime is said to be flat or has no curvature when $R^{\mu}{}_{\nu\alpha\beta} = 0$. Then, if no curvature is present the operator $\nabla\nabla$ is always commutative and General Relativity reduces to Special Relativity. When the Christoffel coefficients are zero the spacetime is flat, but the reciprocal is not true. They may not the be zero in a flat spacetime, a reason that can come from the complexity of the charts used to cover the full spacetime. The Riemann tensor encodes the full information about geometry of spacetime and it is a measurable quantity (see [130] for some techniques). One can easily check the following symmetries of the Riemann tensor:

$$R_{\mu\nu(\alpha\beta)} = R_{(\mu\nu)\alpha\beta} = R_{\mu[\nu\alpha\beta]} = 0, \qquad R_{\mu\nu\alpha\beta} = R_{\alpha\beta\mu\nu}, \tag{4.47}$$

where the indices between parenthesis mean to apply the action of antisymmetry $A_{(\alpha\beta)} = A_{\alpha\beta} - A_{\beta\alpha}$, and the indices between brackets mean the action of symmetry $A_{[\alpha\beta]} = A_{\alpha\beta} + A_{\beta\alpha}$.

4.2.3 Geodesics

The timelike, spacelike and null character of a vector field or a curve is defined as in Special Relativity but considering the metric tensor $g_{\alpha\beta}$. The proper time is also defined equivalently,

$$\tau := \int \sqrt{-ds^2}/c = \int \sqrt{-g_{\alpha\beta}dx^\alpha dx^\beta}/c. \tag{4.48}$$

In a flat spacetime the curves with zero four-acceleration are timelike straight lines. The four-acceleration in flat spacetime was defined in

(4.8). The generalized four-acceleration of a particle, with four-velocity field $\boldsymbol{v}$, in a curved spacetime is

$$\boldsymbol{a} := \frac{D\boldsymbol{v}}{d\tau} := \nabla_{\boldsymbol{v}}\boldsymbol{v}. \tag{4.49}$$

And the generalization of a straight line will be the curve satisfying $\boldsymbol{a} = 0$. Such a curve is called geodesic. Choosing some coordinates x^α, a curve is a geodesic if the equation

$$\frac{d^2x^\alpha}{d\tau^2} + \Gamma^\alpha{}_{\beta\gamma}\frac{dx^\beta}{d\tau}\frac{dx^\gamma}{d\tau} = 0 \tag{4.50}$$

holds. The last equation is called geodesic equation. If gravity and geometry are the same, it turns out that the curves of the free-falling particles in a gravitational field are identified with the geodesics of the spacetime.

4.2.4 Recovery of Newtonian gravity

For instance, in Newtonian gravity spacetime is flat and the classical acceleration of a particle is $(\vec{\nabla}\Phi)$, where Φ is the Newtonian potential satisfying the elliptic equation

$$\vec{\nabla}^2\Phi = 4\pi G\rho \tag{4.51}$$

where ρ is the matter density and G the universal constant of gravitation. The equation of motion for a particle in a gravitational field is

$$\frac{dV^i}{d\tau} = -\partial_i\Phi,$$

which can also be written as

$$\frac{d^2x^0}{d\tau^2} = 0, \qquad \frac{d^2x^i}{d\tau^2} + \frac{\partial\Phi}{\partial x^i}\left(\frac{dx^0}{d\tau}\right)^2 = 0. \tag{4.52}$$

The change of paradigm of the equivalence principle says that this has to be the geodesic equation of a free particle in a curved spacetime. Comparing the Equations (4.50) and (4.52) one can get the Christoffel coefficients of a Newtonian-curved spacetime:

$$\Gamma^i{}_{00} = \frac{1}{c^2}\frac{\partial\Phi}{\partial x^i}, \qquad \Gamma^\alpha{}_{\beta\gamma} = 0 \ \text{ otherwise.} \tag{4.53}$$

From the last expressions we get the Riemann tensor easily:

$$R^{i}{}_{0j0} = -R^{i}{}_{00j} = \frac{1}{c^2}\frac{\partial^2\Phi}{\partial x^i \partial x^j}, \qquad R^{\mu}{}_{\nu\alpha\beta} = 0 \text{ otherwise.} \tag{4.54}$$

Now we define the Ricci tensor in terms of contractions of the Riemann tensor as $R_{\mu\nu} = R^{\alpha}{}_{\mu\alpha\nu}$, and the scalar curvature as $R = R^{\mu}{}_{\mu}$. In Newtonian-curved spacetime only the component R_{00} is distinct to zero and the following relation holds:

$$R_{00} = \frac{4\pi G}{c^2}\rho. \tag{4.55}$$

This can be viewed as a partial differential equation to determine the metric tensor. A solution expressed in Cartesian coordinates is

$$ds^2 = g_{\mu\nu}dx^\mu dx^\nu = -\left(1 + \frac{2\Phi}{c^2}\right)d(ct)^2 + \delta_{ij}dx^i dx^j. \tag{4.56}$$

This metric tensor encompass all phenomena in Newtonian gravity.

4.2.5 Einstein Equations

The metric tensor (4.56) does not predict the bending of light or the correct measure of the precession rate of the perihelion of Mercury. What is the equation that accurately describes the relationship between the distribution of matter and spacetime? Einstein was influenced by the Mach's principle, which asserts that the geometry of spacetime is determined by the distribution of matter of the universe.

Consider the energy-momentum tensor of a perfect fluid (4.24) without pressure, $T^{\alpha\beta} = \mu\, v^\alpha v^\beta$. The classical limit is recover if $c \to \infty$. In that case, T^{00}, $T_{00} \to \rho c^2$ as long as $\rho c^2 \gg \epsilon$. Then, in view of the Equation (4.55), one could think that

$$R_{\mu\nu} = \frac{4\pi G}{c^4}T_{\mu\nu}, \tag{4.57}$$

is the correct equation to describe gravity. In fact, this equation was postulated by Einstein. Now, remember that energy and momentum conservation is expressed through the Equation (4.23) in Special Relativity. If

gravity is the same as curvature of spacetime, the partial derivative in the energy-momentum conservation equation must be changed by the Levi-Civita connection, getting

$$\nabla_\alpha T^{\alpha\beta} = 0. \tag{4.58}$$

This fact would imply that $\nabla_\mu R^{\mu\nu} = 0$, according to (4.57). Should this be the case, the relation $\nabla_\mu R = 0$ is obtained, and hence $\nabla_\mu T = 0$, a huge and poor realistic constrain for the matter. If we instead introduce the Einstein tensor

$$G_{\mu\nu} := R_{\mu\nu} - \frac{1}{2} g_{\mu\nu} R \tag{4.59}$$

there is no longer conflicts with conservation laws. Then, we end up with the equation

$$G_{\mu\nu} = \frac{8\pi G}{c^4} T_{\mu\nu}, \tag{4.60}$$

which are the Einstein Equations, and they are the correct description of gravity we were looking for: the General Relativity equations. The Einstein Equations are a system of ten coupled second order non-linear partial differential equations. The symmetries of the Riemann tensor leave only six independent components, which leave us the freedom to choose four extra condition, called gauge conditions. This refers to the ability to select a system of coordinates.

4.3 Solutions of the Einstein Equations

The Einstein Equations are solvable analytically only in high-symmetry scenarios. In the following we will show solutions in spherical and axial symmetry.

4.3.1 Spherical symmetry

A famous solution of the Einstein Equations is the one found by Karl Schwarzschild to describe the exterior region of a compact spherical dis-

tribution of matter. This region is called Schwarzschild spacetime and it is described by the following metric tensor:

$$ds^2 = -\left(1 - \frac{R_S}{r}\right) d(ct)^2 + \left(1 - \frac{R_S}{r}\right)^{-1} dr^2 + r^2(d\theta^2 + \sin^2\theta d\phi^2), \quad (4.61)$$

where $R_S = 2GM/c^2$ is the Schwarzschild radius and M is identified by the mass of a spherically symmetric central body. The coordinates used to express the metric tensor field (4.61) are called Schwarzschild coordinates, and they are well adapted to the symmetry of the problem. In the spatial infinity $r \to \infty$ Minkowski spacetime is recovered and the spatial coordinates are the usual spherical coordinates. If the matter distribution is concentrated below $r = R_S$, we call black hole region the one for which $r < R_S$. Birkhoff's theorem [15] establishes that, up to a potential coordinate transformation, the spacetime in the empty area outside of a spherically symmetric object is equivalent to a portion of the Schwarzschild spacetime.

Schwarzschild coordinates have the advantage to ease calculations finding a solution of the Einstein Equations. However, one can see that they are bad behaved at $r = R_S$, the event horizon, which translates in a freezing of the coordinate time as a particle approaches this point. To illustrate this, consider a falling particle approaching $r = R_S$ and following the curve

$$\frac{dr}{dt} = -V\left(1 - \frac{R_S}{r}\right), \quad (4.62)$$

where V is a constant and can be proven to be the velocity measured by a static observer, with spatial coordinates constant. This curve is not a geodesic of this spacetime but this choice makes calculations simpler. Let us suppose that the particle departs from $r_0 > R_S$ at $t = 0$. Then, the curve of the particle is

$$r - r_0 + R_S \log\left(\frac{r - R_S}{r_0 - R_S}\right) = -Vt, \quad (4.63)$$

We see that the particle $r \to R_S$ when $\to \infty$. The proper time measured by the static observer of the travel from $r_0 = r(0)$ to $r = r(t)$ is

$$\tau = \int_0^t d\tau = \int_0^t \sqrt{-ds^2}/c = \int_0^t \sqrt{1 - \frac{R_S}{r_O}} dt, \quad (4.64)$$

where r_O is the fixed radial position of the observer. Then, $\lim_{r \to R_S} \tau = \infty$. So according to the static observer the particle never touches the event

horizon. The particle would have been a falling timelike geodesic if V in (4.62) had been changed by

$$V(r) = c\left(\frac{\frac{R_S}{r} - \frac{R_S}{r_0} + \left(\frac{U}{c}\right)^2\left(1 - \frac{R_S}{r}\right)}{1 - \frac{R_S}{r_0}}\right)^{1/2},$$

with U the velocity at $r_0 > R_S$ [119]. Supposing that it departs at zero velocity from the spatial infinity, it rests $V(r) = c\sqrt{R_S/r}$. In any case, the time measured by the static observer would have been infinity with trickier computations.

We can show that this problem is an issue derived from Schwarzschild coordinates: it is a coordinate singularity. Let us make a change $t \to T$ in the coordinate time:

$$cT = ct + 2R_S\left(\sqrt{\frac{r}{R_S}} + \frac{1}{2}\log\left(\frac{\sqrt{r/R_S} - 1}{\sqrt{r/R_S} + 1}\right)\right]. \tag{4.65}$$

The tensor metric in these new coordinates takes the form

$$ds^2 = -d(cT)^2 + \left(dr + \sqrt{\frac{R_S}{r}}d(cT)\right)^2 + r^2(d\theta^2 + \sin^2\theta d\phi^2). \tag{4.66}$$

The new coordinates are called Gullstrand-Painlevé and they have not any singularity at $r = R$. Suppose a particle following the curve

$$\frac{dr}{dT} = -c\sqrt{\frac{R_S}{r}}. \tag{4.67}$$

Notice that it becomes greater than c when the event horizon is crossed. This is not in disagreement with the theory of Relativity, or has any causality issues, because is not a velocity measured by an inertial observer. Notice that the static observer is not inertial.

One can easily see that the newly introduced coordinate time T is the proper time associated with the observer (4.67). If $r = r_0$ is the position at $T = 0$, one can easily integrate and have an explicit expression for the curve:

$$\frac{2}{3}\left(r_0\sqrt{\frac{r_0}{R_S}} - r\sqrt{\frac{r}{R_S}}\right) = cT. \tag{4.68}$$

Then, if $r_0 > R_S$, the particle can cross the event horizon in a finite time. It is not hard to see that the previous curve is a timelike geodesic. We

have found that T is well-behaved at $r = R_S$, which definitely proves that t is bad-behaved if we check (4.65).

On the other hand, the point $r = 0$ is also reached in a finite time. This is a real singularity that cannot be avoided. This type of singularities have been studied since the publication of the General Relativity during many years. Oppenheimer and Snyder in 1939 [94] proved that, indeed, there exists a solution of the Einstein Equations in which a spherical symmetric stellar collapse is continued indefinitely, when the mass of the object is big enough. Certainly, once a specific radius is reached, the gravitational quantum effects would come into play, thus requiring a more comprehensive examination of the scenario. To get more insight about the phenomena of singularities we address the reader to the Penrose's article [99], merit to the Physics Nobel Prize in 2020.

4.3.2 Axial symmetry

For completeness reasons we give another example of solution of the Einstein Equations that gets rid of spherical symmetry and goes to the next step: axial symmetry. The spacetime here described is referred as Kerr spacetime. The contents presented in this Subsection are a summary of the reference [129]. This spacetime can be described by the Kerr coordinates, for which the metric tensor reads:

$$\begin{aligned} ds^2 = &-\left(1 - \frac{R_S\, r}{r^2 + a^2\cos^2\theta}\right)\left(d(cu) + a\sin^2\theta d\varphi\right)^2 \\ &+2\left(d(cu) + a\sin^2\theta d\varphi\right)\left(dr + a\sin^2\theta d\varphi\right) \\ &+\left(r^2 + a^2\cos^2\theta\right)\left(d\theta^2 + \sin^2 d\varphi^2\right), \end{aligned} \tag{4.69}$$

where R_S is the Schwarzschild radius, previously defined. M can be identified with the mass of a rotational object with constant angular momentum $J = Ma$. Unfortunately there not exists any Birkhoff's theorem in axial symmetry. The best we can do is stating that a in the outer region of an axisymmetric object the spacetime approaches the Kerr spacetime asymptotically, as one gets closer to spatial infinity.

Kerr coordinates have curvature singularity at the region

$$r^2 + a^2\cos^2\theta = 0 \iff r = 0 \ \wedge \ \theta = \frac{\pi}{2}. \tag{4.70}$$

It turns out that this does not correspond to a point but to a ring around the equator. It is referred as ring singularity. In Kerr coordinates we do not have any other singularity, nor curvature-like nor coordinate, but the metric have many off-diagonal terms, which can make computations tedious.

It may be convenient to work with another set of coordinates. By the coordinate transformation $u \to t$, $\varphi \to \phi$ defined by

$$u = t + r + R_S \int \frac{r\,dr}{r^2 - R_S r + a^2}, \quad \varphi = -\phi - a \int \frac{dr}{r^2 - R_S r + a^2}, \tag{4.71}$$

we get the so-called Boyer-Lindquist coordinates, for which the metric tensor reads:

$$\begin{aligned} ds^2 = &- \left(1 - \frac{R_S\, r}{r^2 + a^2 \cos^2\theta}\right) d(ct)^2 - 2\left(\frac{R_S\, r\, a \sin^2\theta}{r^2 + a^2\cos^2\theta}\right) d(ct) d\phi \\ &+ \left(\frac{r^2 + a^2\cos^2\theta}{r^2 + a^2 - R_S r}\right) dr^2 + \left(r^2 + a^2\cos^2\theta\right) d\theta^2 \\ &+ \left(r^2 + a^2 + \frac{R_S\, r\, a^2 \sin^2\theta}{r^2 + a^2\cos^2\theta}\right) \sin^2\theta\, d\phi^2, \end{aligned} \tag{4.72}$$

where there is only one off-diagonal component. In the limit $r \to \infty$ we recover Minkowski spacetime and the spatial coordinates become the usual spherical coordinates. We also get a richer description of the spacetime. The ring singularity holds in the same region, since r and θ have not been changed. However, due to the change of coordinates, we find two coordinate singularities: an outer and an inner event horizon, with equations given by

$$r_\pm = \frac{R_S}{2} \pm \sqrt{\left(\frac{R_S}{2}\right)^2 - a^2}. \tag{4.73}$$

In the case of $a = 0$, the previous expression degenerates to, on one hand, the event horizon and, on the other hand, the central curvature singularity of the Schwarzschild spacetime. We find also another type of surfaces called stationary limit surfaces. We find an outer and inner stationary limit surface described by the equations

$$r_\pm^{\text{SL}} = \frac{R_S}{2} \pm \sqrt{\left(\frac{R_S}{2}\right)^2 - a^2\cos^2\theta}. \tag{4.74}$$

In the region between these two surfaces is impossible for any particle to stand still. We see that

$$r_+^{\text{SL}} \geq r_+ \geq r_- \geq r_-^{\text{SL}}. \tag{4.75}$$

The region between the outer stationary limit surface and the outer event horizon is called ergosphere and it is characterized by the fact that any particle cannot stand still, although they can reach spatial infinity. More features about the behaviour of this spacetime can be found in [129].

4.4 Numerical relativity

In most of the real astrophysical scenarios Einstein Equations must be solved numerically. Hence, it is convenient to express the system of partial differential equations as Cauchy problem, a problem with initial and boundary condition. To do so, one option is to split time and space in what is called the 3+1 formalism. In this Section we summarize the decomposition of the Einstein Equations in the 3+1 formalism. In this Section we will summarize the contents of the references [14, 50, 5]. We will use geometric units, $c = G = 1$.

4.4.1 Foliations

Let us introduce a scalar function t to determine a foliation of the spacetime by hypersurfaces Σ_t. This is

$$\Sigma_t = \{p \in M \text{ such that } t(p) \text{ is constant } \}. \tag{4.76}$$

The hypersurfaces are said to be spacelike if the vector $\nabla^\mu t$ is timelike. Let us assume this is the case. We define the 1-form $\Omega_\mu = \nabla_\mu t$ and we define the scalar function

$$N := \sqrt{\frac{-1}{\Omega_\mu \Omega^\mu}} \tag{4.77}$$

The function N is known as lapse function and allows us to define the unit normal vector to the hypersurfaces:

$$n^\mu = -N g^{\mu\nu} \Omega_\nu. \tag{4.78}$$

We can easily check $n_\alpha n^\alpha = -1$. The spatial projector is

$$\gamma^\mu_{\ \nu} = \delta^\mu_{\ \nu} + n^\mu n_\nu, \tag{4.79}$$

and the temporal projector

$$N^\mu_{\ \nu} = -n^\mu n_\nu. \tag{4.80}$$

Both operators are orthogonal, $\gamma^\mu_{\ \lambda} N^\lambda_{\ \nu} = 0$. The spatial and temporal projectors allows one to project components of tensor fields onto the hypersurfaces and the normal direction $\boldsymbol{n}$, respectively. For instance, the spatial metric induced in each hypersurface is

$$\gamma_{\mu\nu} := \gamma^\mu_{\ \lambda}\gamma^\nu_{\ \kappa} g_{\lambda\kappa} = g_{\mu\nu} + n_\mu n_\nu. \tag{4.81}$$

We define the inverse space metric $\gamma^{\mu\nu}$ by requiring $\gamma_{\mu\lambda}\gamma^{\lambda\nu} = \delta_\mu^{\ \nu}$. The spatial covariant derivative will be $D_\mu = \gamma^\nu_{\ \mu}\nabla_\nu$, which is compatible with the spatial metric, $D_\mu \gamma_{\nu\rho} = 0$. The Christoffel coefficients associated with D in the coordinate basis $(\boldsymbol{e}_i) = (\partial_i)$ in the hypersurfaces will be

$$\bar{\Gamma}^\rho_{\ \mu\nu} = \frac{1}{2}\gamma^{\rho\sigma}\left(\partial_\nu \gamma_{\sigma\mu} + \partial_\mu \gamma_{\sigma\nu} - \partial_\sigma \gamma_{\mu\nu}\right), \tag{4.82}$$

where the bar designates the fact that they are quantities defined in the spatial hypersurfaces. The spatial Riemann tensor will be:

$$\bar{R}^\mu_{\ \nu\rho\sigma} = \partial_\rho \bar{\Gamma}^\mu_{\ \nu\sigma} - \partial_\sigma \bar{\Gamma}^\mu_{\ \nu\rho} + \bar{\Gamma}^\lambda_{\ \nu\sigma}\bar{\Gamma}^\mu_{\ \lambda\rho} - \bar{\Gamma}^\lambda_{\ \nu\rho}\bar{\Gamma}^\mu_{\ \lambda\sigma}. \tag{4.83}$$

As we will see below, in the Equation (4.89), the information lost when going from $R^\mu_{\ \nu\rho\sigma}$ to $\bar{R}^\mu_{\ \nu\rho\sigma}$ is contained in the extrinsic curvature tensor of the hypersurface, which can be computed as:

$$K_{\mu\nu} = -\frac{1}{2}\mathcal{L}_{\boldsymbol{n}}\gamma_{\mu\nu}, \tag{4.84}$$

being $\mathcal{L}_{\boldsymbol{n}}$ the Lie derivative with respect the vector field $\boldsymbol{n}$. But the vector field $\boldsymbol{n}$ is not the natural evolution vector field orthogonal to the hypersurfaces because is not dual to Ω_μ. However, the vector field $\boldsymbol{m} := N\boldsymbol{n}$ which is dual to Ω_μ, $m^\mu \Omega_\mu = 1$, plays that role. Let us suppose we have chosen some coordinates (x^i) in each hypersurface and consider the coordinate basis $(\boldsymbol{\partial}_\alpha)$ associated to the coordinates (t, x^i). The vector field $\boldsymbol{t} := \boldsymbol{\partial}_t$ also plays the role of evolution vector as it is dual to Ω_μ by definition. Nonetheless, $\boldsymbol{t}$ is tangent to the curves that preserve the spatial coordinates (x^i) as we move through the hypersurfaces of the foliation. The difference between both vectors is called shift vector,

$$\boldsymbol{\beta} := \boldsymbol{t} - \boldsymbol{m} \tag{4.85}$$

It follows that $N\mathcal{L}_{\boldsymbol{n}} = \mathcal{L}_{\boldsymbol{t}} - \mathcal{L}_{\boldsymbol{\beta}}$. In the coordinate basis the Lie derivative along $\boldsymbol{t}$ is the partial derivative, $\mathcal{L}_{\boldsymbol{t}} = \partial_t$, β^μ has only spatial components, $\beta^\mu = (0, \beta^i)$ and n_μ has only temporal component, so that:

$$n^\mu = \frac{1}{N}(1, -\beta^i), \qquad n_\mu = (-N, 0, 0, 0). \tag{4.86}$$

The metric of spacetime can be written as

$$ds^2 = -(N^2 - \beta^i\beta_i)dt^2 + 2\beta_i dx^i dt + \gamma_{ij}dx^i dx^j. \tag{4.87}$$

As $\boldsymbol{n}$ and $\boldsymbol{t}$ are timelike vectors fields can be associated to observers. The one associated with $\boldsymbol{n}$ is called Eulerian observer and the other one follow the curves that preserve the spatial coordinates, so we will call it static observer. Attending to the expression (4.87) and the Figure 4.1, we make the following interpretations:

- The lapse function N is the proportionality factor between the lapse of proper time of the Eulerian observer and the static observer.
- The shift vector $\boldsymbol{\beta}$ can be regarded as the relative velocity between the Eulerian observer and the static observer,
- The 3-metric γ_{ij} measures distances between points on each hypersurface.

For asymptotically flat spacetimes, we have

$$N \to 1, \quad \beta \to 0, \tag{4.88}$$

at spatial infinity.

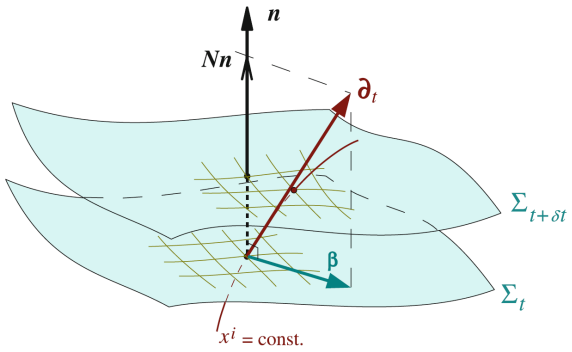

Figure 4.1: Interpretation of t^μ, β^μ and n^μ between two neighbouring hypersurfaces Σ_1 y Σ_2, taken from [50].

4.4.2 3+1 decomposition

Now, we already have all the ingredients to decompose the Einstein Equations in the 3+1 formalism, introduced by the work [7]. For this purpose, we will have to use the Gauss-Codazzi equations, which are obtained by projecting all the indices of the Riemann tensor onto the hypersurfaces:

$$\gamma^{\alpha}_{\mu}\gamma^{\beta}_{\nu}\gamma^{\delta}_{\rho}\gamma^{\gamma}_{\sigma}R_{\alpha\beta\delta\gamma} = \bar{R}_{\mu\nu\rho\sigma} + K_{\mu\sigma}K_{\nu\rho} - K_{\mu\sigma}K_{\nu\rho}. \tag{4.89}$$

The Codazzi-Minardi equations, which are obtained by making three spatial projections and one temporal projection, will also be used:

$$\gamma^{\alpha}_{\mu}\gamma^{\beta}_{\nu}\gamma^{\delta}_{\rho}n^{\gamma}R_{\alpha\beta\delta\gamma} = D_{\nu}K_{\mu\rho} - D_{\mu}K_{\nu\rho}. \tag{4.90}$$

Finally, by making two spatial and two temporal projections we obtain the Ricci equations:

$$\frac{1}{N}\left(\frac{\partial K_{\mu\nu}}{\partial t} - \mathcal{L}_{\boldsymbol{\beta}}K_{\mu\nu}\right) = n^{\rho}n^{\sigma}\gamma^{\alpha}_{\mu}\gamma^{\beta}_{\nu}R_{\beta\rho\alpha\sigma} - \frac{1}{N}D_{\mu}D_{\nu}N - K^{\rho}_{\nu}K_{\mu\rho}. \tag{4.91}$$

Following this procedure we can arrive at the 3+1 decomposition of the Einstein Equations. Notice that the spatial tensors, the ones defined in the spacelike hypersurfaces, must cancel when contracted with the normal vector $\boldsymbol{n}$. Now, looking at the above equations, we can deduce that any contravariant component with index 0 in a spatial tensor must cancel. The 3+1 system split in two evolution equations

$$\partial_t K_{ij} = -D_iD_jN + N(\bar{R}_{ij} + KK_{ij} - 2K_{ik}K^k_j) - 4\pi N(\gamma_{ij}(S-E) - 2S_{ij}) + \mathcal{L}_{\boldsymbol{\beta}}K_{ij}, \tag{4.92}$$

$$\partial_t \gamma_{ij} = -2NK_{ij} + \mathcal{L}_{\boldsymbol{\beta}}\gamma_{ij}, \tag{4.93}$$

and two constraint equations

$$\mathcal{H} = \bar{R} + K^2 - K_{ij}K^{ij} - 16\pi E = 0, \tag{4.94}$$

$$\mathcal{M}^i = D_jK^j_i - D_iK - 8\pi p_i = 0, \tag{4.95}$$

where $K = \gamma^{ij}K_{ij}$ is the trace of the extrinsic curvature, $S = S^{\mu}_{\mu}$ (with $S_{\mu\nu} = \gamma^{\rho}_{\mu}\gamma^{\sigma}_{\nu}T_{\rho\sigma}$), $E = n^{\mu}n^{\nu}T_{\mu\nu}$ and $p^i = -\gamma^{i\mu}n^{\nu}T_{\mu\nu}$. The Equations (4.94) and (4.95) are known as Hamiltonian and momentum constraint equations, respectively, and are elliptic equations. They are equations that do not involve time derivatives and must be satisfied on a each spacelike

hypersurface. Note that $\bar{R}_{ij}$ is a spatial tensor only with spatial derivatives of the space metric. In summary, the 3+1 system has 12 evolution equations (6 corresponding to the space metric and 6 to the extrinsic curvature) and 4 constraint equations. Notice that the evolution equations (4.92) and (4.93) do not allow any set of initial conditions, but only those that preserve the constraint equations. These initial conditions are referred as initial data.

Well-posedness behaviour of the 3+1 system

The 3+1 system is not suitable for numerical treatment, since it is a weakly hyperbolic system, and therefore constitutes an ill-posed Cauchy problem. A physical theory must be predictive, and this requires a well-posed Cauchy problem. We now proceed to define the concept of hyperbolicity more formally. Let be the system:

$$\partial_t u + M^i \partial_i u = s(u), \tag{4.96}$$

where u denotes the set of variables, M^i matrices $n \times n$ (where n is the number of variables and $i = 1, 2, 3$) and $s(u)$ is a vector of dimension n containing source terms and no temporal or spatial derivatives of u. Let us construct too the matrix $P = M^i n_i$, being n_i any 1-form. Thus, we will say that the system is:

- Strongly hyperbolic: when P has real eigenvalues and a complete set of eigenvectors for all n_i.
- Weakly hyperbolic: when P has real eigenvalues but does not have a complete set of eigenvectors.
- Symmetric hyperbolic: when P can be a symmetric matrix independently of n_i. They are automatically strongly hyperbolic

Strongly hyperbolic Cauchy problems are well-posed, which means that the solutions depend continuously on the initial data, or, in other words, that small changes in the initial data correspond to small changes in the solutions. We can improve the stability of a weakly hyperbolic, i.e. numerically unstable system (such as the 3+1 system), by introducing new evolution variables defined from the previous ones, in order to make the system strongly hyperbolic.

Free evolution and constrained schemes

There are the two main schemes followed in Numerical Relativity to solve the systems of partial differential equations. We have already seen that the system of equations splits into evolution and constraint equations.

If we solve the constraint equations in an initial hypersurface Σ_0, they are theoretically satisfied in all next hypersurfaces Σ_t, $t > 0$. Then, another strategy is to solve the constraint equations only initially. These are the **free evolution schemes**. One of the most used evolution schemes in Numerical Relativity is the BSSNOK formalism [13, 90, 117]. Despite the fact that in an evolution scheme the constraint equations are not solved in practice, they are monitored to verify that the constraints $\mathcal{H} \simeq \mathcal{M}^i < \epsilon \ll 1$. BSSNOK formulation is a standard 3+1 formulation in Numerical Relativity. Stable numerical simulations have been possible in systems with intense gravity, neutron stars [41] and black holes [126].

On the other hand, we say that a **constrained formalism** is being applied if all constraint equations are solved in each time step of the numerical resolution. The formulations described hereinafter are in the set of the constrained formalisms.

Conformal decomposition

The next decompositions and definitions are motivated by previous works and ideas, clearly summarized in [50], and lead to strong hyperbolic systems. First, we introduce a time independent flat background metric f_{ij}, which coincides with γ_{ij} at spatial infinity, and the following conformal decomposition of the spatial metric:

$$\gamma_{ij} = \psi^4 \tilde{\gamma}_{ij}. \tag{4.97}$$

$\tilde{\gamma}_{ij}$ is the conformal metric and the scalar $\psi := (\gamma/f)^{1/12}$ is the conformal factor, where $\gamma = \det \gamma_{ij}$ and $f = \det f_{ij}$. Defining the conformal metric in this way, it is a tensor field and

$$\det(\tilde{\gamma}_{ij}) = f. \tag{4.98}$$

We define the inverse spatial conformal metric $\tilde{\gamma}^{ij}$ by requiring that

$$\tilde{\gamma}_{ik}\tilde{\gamma}^{kj} = \delta_i^{\ j}, \tag{4.99}$$

which is equivalent to

$$\gamma^{ij} = \psi^{-4}\tilde{\gamma}^{ij}. \tag{4.100}$$

The affine connections associated with $\tilde{\gamma}_{ij}$ and f_{ij} are denoted $\tilde{D}$ and $\mathcal{D}$, respectively. For asymptotically flat spacetimes, we have $\psi \to 1$ at spatial infinity. We define the tensor A^{ij} as the traceless part of $K^{ij} = \gamma^{ik}\gamma^{jl}K_{kl}$:

$$A^{ij} = K^{ij} - \frac{1}{3}K\gamma^{ij}. \tag{4.101}$$

The next step is introducing a conformal decomposition of the extrinsic curvature,

$$A^{ij} = \psi^{10}\hat{A}^{ij}. \tag{4.102}$$

Then, we end up with the following system of evolution equations

$$\left(\frac{\partial}{\partial t} - \mathcal{L}_{\boldsymbol{\beta}}\right)\psi = \frac{\psi}{6}\left(\tilde{D}_i\beta^i - NK\right), \tag{4.103}$$

$$\left(\frac{\partial}{\partial t} - \mathcal{L}_{\boldsymbol{\beta}}\right)\tilde{\gamma}_{ij} = -2N\psi^{-6}\hat{A}_{ij} - \frac{2}{3}\tilde{D}_k\beta^k\tilde{\gamma}_{ij}, \tag{4.104}$$

$$\left(\frac{\partial}{\partial t} - \mathcal{L}_{\boldsymbol{\beta}}\right)K = -\psi^{-4}\left(\tilde{D}_i\tilde{D}^iN + 2\tilde{D}_i\log\psi\tilde{D}^iN\right) + N\left(4\pi(E+S) + \psi^{-12}\hat{A}_{ij}\hat{A}^{ij} + \frac{K^2}{3}\right) \tag{4.105}$$

$$\begin{aligned}\left(\frac{\partial}{\partial t} - \mathcal{L}_{\boldsymbol{\beta}}\right)\hat{A}_{ij} = {}& \frac{1}{3}\tilde{D}_k\beta^k\hat{A}_{ij} + N\left[-2\psi^{-6}\tilde{\gamma}^{kl}\hat{A}_{ik}\hat{A}_{jl} - 8\pi\psi^6\left(\psi^{-4}S_{ij} - \frac{S}{3}\tilde{\gamma}_{ij}\right)\right] \\ & +\psi^2\left\{-\tilde{D}_i\tilde{D}_jN + 2\tilde{D}_i\log\psi\tilde{D}_jN + 2\tilde{D}_k\log\psi\tilde{D}_iN\right. \\ & +\frac{1}{3}\left(\tilde{D}_k\tilde{D}^kN - 4\tilde{D}_k\log\psi\tilde{D}^kN\right)\tilde{\gamma}_{ij} \\ & +N\left[\tilde{R}_{ij} - \frac{1}{3}\tilde{R}\tilde{\gamma}_{ij} - 2\tilde{D}_i\tilde{D}_j\log\psi + 4\tilde{D}_i\log\psi\tilde{D}_j\log\psi\right. \\ & \left.\left.\frac{2}{3}\left(\tilde{D}_k\tilde{D}^k\log\psi - 2\tilde{D}_k\log\psi\tilde{D}^k\log\psi\right)\tilde{\gamma}_{ij}\right]\right\},\end{aligned} \tag{4.106}$$

together with the following set of two constraint equations

$$\tilde{D}_i\tilde{D}^i\psi - \frac{1}{8}\tilde{R}\psi + \frac{1}{8}\psi^{-7}\hat{A}_{ij}\hat{A}^{ij}\left(2\pi E - \frac{K^2}{12}\right)\psi^5 = 0, \tag{4.107}$$

$$\tilde{D}_j\hat{A}^{ij} - \frac{2}{3}\psi^6\tilde{D}^iK = 8\pi\psi^{10}p^i, \tag{4.108}$$

where

$$\tilde{R} = \frac{1}{4}\tilde{\gamma}^{kl}\mathcal{D}_k\tilde{\gamma}^{mn}\mathcal{D}_l\tilde{\gamma}_{mn} - \frac{1}{2}\tilde{\gamma}^{kl}\mathcal{D}_k\tilde{\gamma}^{mn}D_n\tilde{\gamma}_{ml}.$$

This system (4.104)-(4.108) is the one presented in [50] with slight modifications. We will refer to the previous system as conformal system. A frequent approximation to the conformal system is the so-called Conformally Flat Condition (CFC), which considers $\tilde{\gamma}_{ij} = f_{ij}$. CFC is an exact condition in spherical symmetry. Besides, it can be a good approximation in cases where the deviation from spherical symmetry is not significant (even if the curvature is not negligible).

Local uniqueness

It turns out that the uniqueness of the solution of the conformal system is not guaranteed. Indeed, suppose an elliptic equation for u of the form

$$\Delta u + hu^p = g, \tag{4.109}$$

where h and g are function not dependant on u and p is a constant. There is a maximum principle that guarantees the uniqueness of the previous equation provided the sign of p is different from the sign of h. Attending to (4.107) this condition is not satisfied. In practice, it is observed the transition to non physical solution when compactness is high enough [31]. However, with the introduction of the rescaled variables:

$$E^* = \psi^6 E, \tag{4.110}$$

$$S^* = \psi^6 S, \tag{4.111}$$

$$(S^*)_i = \psi^6 S_i, \tag{4.112}$$

we solve the problem of the sign in such a way the stated maximum principle can be applied. The conformal decomposition $A^{ij} = \psi^{10}\hat{A}^{ij}$ is also key in this issue.

4.4.3 Fully Constrained Formalism

The following considerations will lead us to the so-called Fully Constrained Formalism (FCF) [18, 31]. Let us change the connection of the conformal space metric $\tilde{D}$ by the connection of the flat metric $\mathcal{D}$. They

are related by the formula:

$$\begin{aligned}\tilde{D}_k T^{i_1\dots i_k}{}_{j_1\dots j_l} =& \mathcal{D}_k T^{i_1\dots i_k}{}_{j_1\dots j_l} + \sum_{m=1}^{p} \Delta^{i_m}{}_{lk} T^{i_1\dots \overset{m}{\underset{\downarrow}{l}} \dots i_k}{}_{j_1\dots j_l} \\ & - \sum_{n=1}^{q} \Delta^{l}{}_{j_n k} T^{i_1\dots i_k}{}_{j_1\dots \underset{\uparrow}{k} \dots j_l}\,,\end{aligned} \tag{4.113}$$

where we have introduced the (1,2)-tensor field

$$\Delta^k{}_{ik} = \frac{1}{2}\tilde{\gamma}^{kl}\left(\mathcal{D}_i\tilde{\gamma}_{lj} + \mathcal{D}_j\tilde{\gamma}_{il} - \mathcal{D}_l\tilde{\gamma}_{ij}\right). \tag{4.114}$$

If we call $\tilde{\Gamma}^k{}_{ik}$ and $\bar{\Gamma}^k{}_{ik}$ the Christoffel coefficients of $\tilde{D}$ and $\mathcal{D}$, respectively, then, the relation $\Delta^k{}_{ik} = \tilde{\Gamma}^k{}_{ik} - \bar{\Gamma}^k{}_{ik}$ is satisfied.

To solve the system we further decompose the conformal traceless part of extrinsic curvature $\hat{A}^{ij}$ such that

$$\hat{A}^{ij} = \hat{A}^{ij}_{TT} + (LX)^{ij}, \tag{4.115}$$

where $\hat{A}^{ij}_{TT}$ is traceless and tranverse with respect f_{ij}, i.e.

$$\mathcal{D}_j \hat{A}^{ij}_{TT} = 0. \tag{4.116}$$

$(LX)^{ij}$ is the flat Killing operator associated with f_{ij},

$$(LX)^{ij} = \mathcal{D}^i X^j + \mathcal{D}^j X^i - \frac{2}{3} f^{ij}\mathcal{D}_k X^k. \tag{4.117}$$

The condition $\mathcal{D}_i \hat{A}^{ij}_{TT} = 0$, up to boundary conditions, determines X^i. At spatial infinity, we will consider $\hat{A}^{ij}_{TT} \to 0$. $(LX)^{ij}$ and $\hat{A}^{ij}_{TT}$ are called, respectively, longitudinal and transverse part of $\hat{A}^{ij}$. This strategy was inspired by the decomposition done in [134] which is called the conformal transverse traceless (CTT) method. The tensor $\hat{A}^{ij}_{TT}$ is to be determined by an evolution equation, while X^i by a constraint equation.

We also introduce the tensor

$$h^{ij} = \tilde{\gamma}^{ij} - f^{ij}. \tag{4.118}$$

For asymptotically flat spacetimes we have

$$h^{ij} \to 0, \quad A^{ij} \to 0, \tag{4.119}$$

at spatial infinity. There remains to choose the 4 gauge conditions, that permit the Einstein Equations, to close the system. We are using $K = 0$,

which is called maximal slicing, and the generalized Dirac gauge condition:

$$\mathcal{D}_i\tilde{\gamma}^{ij} = 0. \tag{4.120}$$

The name Dirac gauge comes from its resemblance to the Dirac gauge of electrodynamics. We called this formulation the FCF of the Einstein Equations.

Finally, we have the evolution equations:

$$\partial_t h^{ij} = \beta^k\mathcal{D}_k h^{ij} + 2N\psi^{-6}\hat{A}^{ij}_{TT} + 2N\psi^{-6}(LX)^{ij} - \tilde{\gamma}^{ik}\mathcal{D}_k\beta^j - \tilde{\gamma}^{kj}\mathcal{D}_k\beta^i + \frac{2}{3}\tilde{\gamma}^{ij}\mathcal{D}_k\beta^k, \tag{4.121}$$

$$\begin{aligned}\partial_t\hat{A}^{ij} = {}& \mathcal{D}_k\left(\beta^k\hat{A}^{ij}\right) - \hat{A}^{kj}\mathcal{D}_k\beta^i - \hat{A}^{ik}\mathcal{D}_k\beta^j + \frac{2}{3}\hat{A}^{ij}\mathcal{D}_k\beta^k + 2N\psi^{-6}\tilde{\gamma}_{kl}\hat{A}^{ik}\hat{A}^{jl} + N\psi^2\tilde{R}^{ij}_* \\ & + \mathcal{D}_k\left(\frac{N\psi^2}{2}\right)\tilde{\gamma}^{kl}\mathcal{D}_l h^{ij} + \frac{N\psi^2}{2}\tilde{\gamma}^{kl}\mathcal{D}_k\left(\mathcal{D}_l h^{ij}\right) \\ & + 4\psi(\tilde{\gamma}^{ik}\tilde{\gamma}^{jl}\mathcal{D}_k\psi\mathcal{D}_l N + \tilde{\gamma}^{ik}\tilde{\gamma}^{jl}\mathcal{D}_k N\mathcal{D}_l\psi) + 8N\tilde{\gamma}^{ik}\tilde{\gamma}^{jl}\mathcal{D}_k\psi\mathcal{D}_l\psi \\ & - \frac{1}{3}\left(N(\psi^2\tilde{R} + 8\tilde{\gamma}^{kl}\mathcal{D}_k\psi\mathcal{D}_l\psi) + 8\psi\tilde{\gamma}^{kl}\mathcal{D}_k\psi\mathcal{D}_l N\right)\tilde{\gamma}^{ij} - \frac{1}{2}(\tilde{\gamma}^{ik}\mathcal{D}_k h^{lj} + \tilde{\gamma}^{kj}\mathcal{D}_k h^{il})\mathcal{D}_l(N\psi^2) \\ & - \tilde{\gamma}^{ik}\tilde{\gamma}^{jl}\mathcal{D}_k\mathcal{D}_l(N\psi^2) + \frac{1}{3}\tilde{\gamma}^{ij}\tilde{\gamma}^{kl}\mathcal{D}_k\mathcal{D}_l(N\psi^2) - 8\pi N\psi^6\left(\psi^4 S^{ij} - \frac{S\tilde{\gamma}^{ij}}{3}\right).\end{aligned} \tag{4.122}$$

where

$$\begin{aligned}\tilde{R}^{ij}_* = {}& \frac{1}{4}\tilde{\gamma}^{ik}\tilde{\gamma}^{jl}\mathcal{D}_k h^{mn}\mathcal{D}_l\tilde{\gamma}_{mn} \\ & + \frac{1}{2}\left(-\mathcal{D}_l h^{ik}\mathcal{D}_k h^{jl} - \tilde{\gamma}_{kl}\tilde{\gamma}^{mn}\mathcal{D}_m h^{ik}\mathcal{D}_n h^{jl} + \tilde{\gamma}_{nl}\mathcal{D}_k h^{mn}(\tilde{\gamma}^{ik}\mathcal{D}_m h^{jl} + \tilde{\gamma}^{jk}\mathcal{D}_m h^{il})\right).\end{aligned} \tag{4.123}$$

And we add the following constraint equations:

$$\begin{aligned}\Delta X^i + \frac{1}{3}\mathcal{D}^i\mathcal{D}_j X^j = {}& -\tilde{\gamma}^{im}\left(\mathcal{D}_k\tilde{\gamma}_{ml} - \frac{1}{2}\mathcal{D}_m\tilde{\gamma}_{kl}\right)\left(\mathcal{D}^k X^l + \mathcal{D}^l X^k - \frac{2}{3}f^{kl}\mathcal{D}_p X^p\right) \\ & + 8\pi\tilde{\gamma}^{ij}(S^*)_j - \tilde{\gamma}^{im}\left(\mathcal{D}_k\tilde{\gamma}_{ml} - \frac{1}{2}\mathcal{D}_m\tilde{\gamma}_{kl}\right)\hat{A}^{kl}_{TT},\end{aligned} \tag{4.124}$$

$$\tilde{\gamma}^{kl}\mathcal{D}_k\mathcal{D}_l\psi = -2\pi\psi^{-1}E^* - \frac{1}{8}\psi^{-7}\tilde{\gamma}_{il}\tilde{\gamma}_{jm}\hat{A}^{lm}\hat{A}^{ij} + \frac{1}{8}\psi\tilde{R}, \tag{4.125}$$

$$\tilde{\gamma}^{kl}\mathcal{D}_k\mathcal{D}_l(N\psi) = N\psi\left(2\pi\psi^{-2}(E^* + 2S^*) + \frac{7}{8}\psi^{-8}\tilde{\gamma}_{il}\tilde{\gamma}_{jm}\hat{A}^{lm}\hat{A}^{ij} + \frac{1}{8}\tilde{R}\right), \tag{4.126}$$

$$\Delta\beta^i + \frac{1}{3}\mathcal{D}^i\mathcal{D}_j\beta^j = 16\pi N\psi^{-6}\tilde{\gamma}^{ij}(S^*)_j - h^{kl}\mathcal{D}_k\mathcal{D}_l\beta^i - \frac{1}{3}h^{ik}\mathcal{D}_k\mathcal{D}_j\beta^j + \hat{A}^{ij}\mathcal{D}_j(2N\psi^{-6}) \\ -N\psi^{-6}\tilde{\gamma}^{im}(\mathcal{D}_k\tilde{\gamma}_{ml} + \mathcal{D}_l\tilde{\gamma}_{km} - \mathcal{D}_m\tilde{\gamma}_{kl})\left((LX)^{kl} + \hat{A}^{kl}_{TT}\right). \tag{4.127}$$

The hyperbolic sector (4.121)-(4.122) has been proven to be strongly hyperbolic when ∂_t is timelike [25]. The whole system (4.121)-(4.127) is the one shown in [31] with slight modifications. There, numerical simulations were carried out using the CFC (i.e., $h^{ij} = 0$), which in the improved formulation is referred as xCFC. They demonstrate that in this approximation $\hat{A}^{ij}_{TT} = 0$ can be considered. The uniqueness problem, observed in the original conformal formulation (4.104)-(4.108) with the CFC approximation, is not present anymore in the xCFC formulation, for which the CTT decomposition is fundamental. In the 6.5, the second source term has the correct sign thanks to the decompositions (4.102) and (4.115), from which it follows that $\hat{A}^{ij} = (LX)^{ij}$ is known as X^i is previously solved.

4.5 Final remarks

In this Chapter we outlined the basic concepts of Special Relativity and General Relativity with the aim to give some background for the forecoming chapters. The contents about relativistic hydrodynamics will be used constantly and systems with spherical and axial symmetries will be considered. The Resistive Relativistic Magntetohydrodynamic equations will be addressed in the Chapter 7 and numerically integrated with a new scheme.

We paid attention in the derivation of the system (4.121)-(4.127), to be used in the Chapter 6. The main advantage of a FCF formulation is that the constraint equations are satisfied numerically in every time step by definition. Therefore, long term simulations are likely to be safer in these formalism. This formulation will be extended to a version with some accuracy improvements. It will also be solved numerically in the context of a stationary spacetime.

5

Euler Equation with gravity

The main goal of this Chapter is to study the Euler Equation in presence of gravity. This equation, in its classical version, is derived from the Navier-Stokes Equations neglecting viscous stresses. In its relativistic version is obtained from the energy-momentum conservation equation considering the energy-momentum tensor of a perfect fluid. We study here two scenarios in spherical symmetry. One classical and another relativistic. The first one will be a self-gravity Newtonian star, meanwhile the second one will be a perfect fluid in the Schwarzschild spacetime. We get the Riemann invariants and the wave speeds for both systems.

In the first case, we write the Euler Equation in its classical version adding an extra source term accounting for the Newtonian potential. A study of the characteristic curves is to be carried out, which was useful to the work [114].

In the second case, we describe the general relativistic Euler Equation. We will write it as a balance law and derive its stationary solutions in the Gullstrand-Painlevé coordinates. This work tries to complete the articles [73] and [72] where Schwarzschild coordinates were used. The

stationary solutions derived will permit to develop well-balance methods in the way it was done in [72]. Well-balanced methods for balanced laws [22] are proven to be very powerful when stationary solutions exists. They are able to numerically recover these solutions, or their behaviour when a perturbation is applied, with more precision than other schemes that treat the fluxes differently. To develop these methods is very convenient to have analytical expressions of the stationary solutions of the system of partial differential equations under resolution, or at least a numerical solution of it.

5.1 Euler Equation in Newtonian gravity

For the gravity sector, in classical mechanics, we just have to solve an elliptic equation for the Newtonian potential Φ:

$$\vec{\nabla}^2\Phi = 4\pi G\rho, \tag{5.1}$$

with G the universal constant of gravitation.

In Newtonian gravity, the Euler Equation have the form

$$\frac{\partial(\rho\boldsymbol{V})}{\partial t} + \nabla\cdot(\rho\boldsymbol{V}\otimes\boldsymbol{V}) = -\nabla p - \rho\nabla\Phi. \tag{5.2}$$

It is basically the Equation (2.1b) neglecting the viscosity effects and adding the Newtonian term. It has to be solved along the matter conservation equation

$$\frac{\partial\rho}{\partial t} + \nabla\cdot(\rho\boldsymbol{V}) = 0. \tag{5.3}$$

From now on we, restrict ourselves to spherical symmetry and suppose that the fluid is forming a compact object of tilting radius $R(t)$. The velocity field is radial, $\boldsymbol{V} = V\boldsymbol{e}_r$, and all variables depend on one spatial coordinate, the radial coordinate r. In order to have coordinates well adapted to the problem, we make a change of the spatial coordinate from r to $\xi = r/R(t)$. In the new coordinates, our set of hyperbolic equations can be written as

$$\frac{\partial\rho}{\partial t} - \frac{1}{R}(R'\xi - V^r)\frac{\partial\rho}{\partial\xi} + \frac{\rho}{R}\frac{\partial V^r}{\partial\xi} = -\frac{2}{R\xi}\rho V^r, \tag{5.4}$$

$$\frac{\partial V^r}{\partial t} + \frac{\Gamma_1\kappa}{R}\rho^{\Gamma_1-2}\frac{\partial\rho}{\partial\xi} - \frac{1}{R}(R'\xi - V^r)\frac{\partial V^r}{\partial\xi} = -\frac{1}{R}\frac{\partial\Phi}{\partial\xi}, \tag{5.5}$$

where $R'(t) = \partial_t R$, or

$$\frac{\partial u}{\partial t} + A\frac{\partial u}{\partial \xi} = f, \tag{5.6}$$

where

$$u = \begin{pmatrix} \rho \\ V^r \end{pmatrix}, \quad A = \frac{1}{R}\begin{pmatrix} -(R'\xi - V^r) & \rho \\ \Gamma_1\kappa\rho^{\Gamma_1 - 2} & -(R'\xi - V^r) \end{pmatrix}, \quad f = -\frac{1}{R}\begin{pmatrix} \frac{2}{\xi}\rho V^r \\ \frac{\partial \Phi}{\partial \xi} \end{pmatrix}, \tag{5.7}$$

and a polytropic equation of state $p = \kappa\rho^{\Gamma_1}$ has been taken into account, with κ and $\Gamma_1 > 1$ constants. See [114] for more details about the derivation of these equations. The eigenvectors and eigenvalues, respectively, are given by the following expressions (derived by the author of this manuscript in [114]):

$$r_\pm = \begin{pmatrix} 1 \\ \pm\sqrt{\Gamma_1\kappa}\rho^{\frac{\Gamma_1 - 3}{2}} \end{pmatrix}, \qquad \lambda_\pm = \frac{1}{R}\left[(V^r - R'\xi) \pm \sqrt{\Gamma_1\kappa}\rho^{\frac{\Gamma_1 - 1}{2}}\right]. \tag{5.8}$$

At the radius of the star, $r = R(t)$ or equivalently $\xi = 1$,

$$\lambda_\pm(t, 1) = \pm\frac{\sqrt{\Gamma_1\kappa}}{R}(\rho_s)^{\frac{\Gamma_1 - 1}{2}}, \tag{5.9}$$

where it has been used $R' = V^r(\xi = 1)$ and $\rho_s = \rho(1)$ denotes the density at the surface. ρ_s is usually close to zero, so we expect $\lambda_\pm$ to be also close to zero at the surface. Let us perform a stability analysis by considering the homogeneous system $\partial_t u + A\,\partial_\xi u = 0$, with A fixed at $(t_0, \xi_0 = 1)$. The system can written in diagonal form as

$$\frac{\partial w}{\partial t} + \Lambda\frac{\partial w}{\partial \xi} = 0, \tag{5.10}$$

where $w = M^{-1}u = (w_-\ w_+)^T$, $\Lambda = \text{diag}(\lambda_-,\ \lambda_+)$, and

$$M = (r_-\ r_+) = \begin{pmatrix} 1 & 1 \\ -\sqrt{\Gamma_1\kappa}\rho^{\frac{\Gamma_1 - 3}{2}} & \sqrt{\Gamma_1\kappa}\rho^{\frac{\Gamma_1 - 3}{2}} \end{pmatrix}. \tag{5.11}$$

Then, the system decouples into

$$\frac{\partial w_\pm}{\partial t} + \lambda_\pm\frac{\partial w_\pm}{\partial \xi} = 0, \tag{5.12}$$

with

$$w_\pm = \frac{1}{2}\left(\rho \pm \frac{1}{\sqrt{\Gamma_1\kappa}}\rho^{-\frac{\Gamma_1 - 3}{2}}V^r\right). \tag{5.13}$$

Each equation in (5.12) is a constant coefficient linear advection equation. The scalar functions $w_\pm$ are called Riemann invariants and are constant along the characteristic curves $\xi = \xi_0 + \lambda_\pm t$. We also refer to $\lambda_\pm$ as wave speeds. The solutions of the system are derived from the initial conditions:

$$w_\pm(\xi, t) = w_\pm(\xi - \lambda_\pm t,\, 0). \tag{5.14}$$

And the solution to the original system is finally recovered via (5.11) and can be expressed as

$$u(t, \xi) = w_-(\xi - \lambda_- t,\, 0) r_- + w_+(\xi - \lambda_+ t,\, 0) r_+ \tag{5.15}$$

where by assumption $r_\pm$ are constant. We have seen that at the surface of the star both $\lambda_\pm$ approach zero, which means that small disturbances applied at the surface propagate very slowly. Of course, A is not really constant, but we would have arrived to the same conclusion if an expansion around a constant value $\bar{u}$ were possible. For instance, if

$$u(\xi, t) = \bar{u} + \epsilon u^{(1)}(t, \xi) + \epsilon^2 u^{(2)}(t, \xi) + \dots, \tag{5.16}$$

with $\epsilon \leq 1$, we find that $u^{(1)}(t, \xi)$ satisfies

$$\frac{\partial u^{(1)}}{\partial t} + A(\bar{u}) \frac{\partial u^{(1)}}{\partial \xi} = 0, \tag{5.17}$$

with $A(\bar{u})$ constant and the same conclusions would have been derived for $u^{(1)}(t, \xi)$.

According to [75, 73] the system is said **strictly hyperbolic** if the wave speeds are all real and distinct. According to (5.9) this is indeed the case as the density ρ is always positive. Moreover, we say that the system is **genuinely non-linear** if all waves speeds are monotonic. This is a required statement in rarefaction waves. Also, the system is **linearly degenerate** if all wave speeds are constant. Linear degeneracy is linked with contact discontinuities, points where a jump in the density exists but the velocity is kept continuous. We address the reader to the reference [75] for further details. If the density at the surface is zero, $\rho_s = 0$, our system is linearly degenerate and the surface is a contact discontinuity.

5.2 Euler Equation in Schwarzschild spacetime

Now we consider the Euler Equation in a curved, fixed spacetime, coupled to the matter conservation equation. The equation (4.22) corresponds to the matter conservation in Special Relativity; its generalization in General Relativity is given by:

$$\frac{d\rho}{d\tau} + \rho \nabla \cdot \boldsymbol{v} = 0, \tag{5.18}$$

where $d\rho/d\tau = \boldsymbol{v} \cdot \nabla\rho$, and $\boldsymbol{v}$ is the Eulerian four-velocity of the fluid. We have just changed the usual partial derivative by the Levi-Civita connection. The generalization of the energy and momentum conservation equations in Special Relativity, (4.25) and (4.26), are given by:

$$\frac{d\mu}{d\tau} + (\mu + p)\nabla \cdot \boldsymbol{v} = 0, \tag{5.19}$$

$$(\mu + p)\frac{D\boldsymbol{v}}{d\tau} + (\boldsymbol{g} + \boldsymbol{v} \otimes \boldsymbol{v}) \cdot \nabla p = 0, \tag{5.20}$$

where $D\boldsymbol{v}/d\tau = \boldsymbol{v} \cdot \nabla\boldsymbol{v}$. The Equation (5.20) is the version of the Euler Equation in a curved spacetime. In this Section we will restrict the spacetime metric to the Schwarzschild one, which was introduced in the Subsection 4.3.1. The Gullstrand-Painlevé coordinates will be used.

5.2.1 Balance law equation

The generalized Euler Equation has an interesting resemblance to its classical version. However, it is also interesting to consider the equations derived from the direct use of the energy-momentum conservation equations, $\nabla_\alpha T^{\alpha\beta} = 0$ (see (4.43)). This approach is followed in [73] considering Schwarzschild coordinates and spherical flow. Nevertheless, these coordinates have a singularity at the horizon, which is not physical. To avoid any issue, it is important to refrain from including this region in our numerical domain and imposing boundary conditions in its vicinity.

The problem is directly removed when the Gullstrand-Painlevé coordinates are used (see (4.66)). Here, we derive equivalent equations in these coordinates. To use the expression (4.43), some Christoffel coefficients are needed. They can be easily computed from the Equation (4.41). We list those that are not zero:

$$\begin{aligned}
&\Gamma^0{}_{00} = \frac{R_S}{2r^2}\sqrt{\frac{R_S}{r}}, && \Gamma^0{}_{10} = \frac{R_S}{2r^2}, && \Gamma^0{}_{11} = \frac{1}{2r}\sqrt{\frac{R_S}{r}},\\
&\Gamma^0{}_{22} = -r\sqrt{\frac{R}{r}}, && \Gamma^1{}_{00} = \frac{R_S}{2r^2}\left(1-\frac{R_S}{r}\right), && \Gamma^1{}_{01} = -\frac{R_S}{2r^2}\sqrt{\frac{R_S}{r}},\\
&\Gamma^1{}_{11} = -\frac{R_S}{2r^2}, && \Gamma^1{}_{22} = R_S - r, && \Gamma^1{}_{33} = (R_S - r)\sin^2\theta,\\
&\Gamma^2{}_{12} = \Gamma^3{}_{13} = \frac{1}{r}, && \Gamma^2{}_{33} = -\sin\theta\cos\theta, && \Gamma^3{}_{23} = \cot\theta.
\end{aligned} \tag{5.21}$$

We have bypassed those that can be derived from the symmetry $\Gamma^{\mu}{}_{\alpha\beta} = \Gamma^{\mu}{}_{\beta\alpha}$. Now, we can write expression (4.43) with the energy-momentum tensor of a perfect fluid (4.24). We assume spherical flow, as in [73], i.e.,

$$\boldsymbol{v} = \boldsymbol{v}(T, r) = (v^0(T, r),\, v^1(T, r), 0, 0),$$

where T and r are time and radial coordinates in Gullstrand-Painlevé coordinates (see Subsection 4.3.1). Let us denote $x^0 = cT$ and $x^1 = r$. Then, we get two equations, which read as:

$$\begin{aligned}
&\frac{\partial}{\partial x^0}\left(r^2(\mu+p)v^0v^0 - r^2p\right) + \frac{\partial}{\partial x^1}\left(r^2(\mu+p)v^0v^1 + r^2Bp\right)\\
&\quad + \frac{rB}{2}\left((\mu+p)(v^0v^0-1) - 3p\right) = 0,\\
&\frac{\partial}{\partial x^0}\left(r^2(\mu+p)v^0v^1 + r^2Bp\right) + \frac{\partial}{\partial x^1}\left(r^2(\mu+p)v^1v^1 + r^2Dp\right)\\
&\quad + \frac{R_S}{2}(\mu+p) + (R_S - 2r)p = 0,
\end{aligned} \tag{5.22}$$

where $B = \sqrt{R_S/r}$ and $D = 1 - R_S/r$. As the four-velocity is normalized by definition, $g_{\alpha\beta}v^\alpha v^\beta = -1$, only one of the two non-zero components of $\boldsymbol{v}$ is independent. Besides, an equation of state $p = p(\mu)$ is still needed. In the end, there are two equations and two independent variables (as it should be). Let us introduce the effective velocity,

$$v := \frac{c}{B}\frac{v^1}{v^0}. \tag{5.23}$$

Then, using the normalization condition, the following relations hold:

$$(v^0)^2 = \frac{r\,c^2}{rc^2 - R_S(v+c)^2}, \qquad (v^1)^2 = \frac{R_S\,v^2}{rc^2 - R_S(v+c)^2}, \\ Bv^0v^1 = \frac{R_S\,vc}{rc^2 - R_S(v+c)^2}. \tag{5.24}$$

Finally, the previous system can be rewritten is a a more compact way:

$$\frac{\partial}{\partial x^0}\left[r^2\left((\mu+p)\frac{r}{d} - p\right)\right] + \frac{\partial}{\partial x^1}\left[r^2 B\left((\mu+p)u\frac{r}{d} + p\right)\right] \\ + \frac{rB}{2}\left((\mu+p)(1+u)^2\frac{R_S}{d} - 3p\right) = 0, \tag{5.25a}$$

$$\frac{\partial}{\partial x^0}\left[r^2 B\left((\mu+p)u\frac{r}{d} + p\right)\right] + \frac{\partial}{\partial x^1}\left[r^2\left((\mu+p)u^2\frac{R}{d} + Dp\right)\right] \\ + \frac{R_S}{2}(\mu+p) + (R_S - 2r)p = 0, \tag{5.25b}$$

where $u = v/c$ is a dimensionless velocity and $d = r - R_S(u+1)^2$ is an effective distance. Let us introduce the variable $\gamma = B(u+1)$. With this choice we get expressions aesthetically similar of those in [73], where Schwarzschild coordinates are used. We can present them as the following system of nonlinear balance law:

$$\partial_0 V + \partial_1 F(V,\, r) = S(V,\, r), \tag{5.26a}$$

where

$$(1-\gamma^2)V = \begin{pmatrix} \mu + p\gamma^2 \\ (\mu+p)\,\gamma - B\left(\mu + p\gamma^2\right) \end{pmatrix}, \tag{5.26b}$$

$$(1-\gamma^2)F = \begin{pmatrix} (\mu+p)\,\gamma - B\left(\mu + p\gamma^2\right) \\ \left(\mu\gamma^2 + p\right) - 2B\,(\mu+p)\,\gamma + B^2\left(\mu + p\gamma^2\right) \end{pmatrix}, \tag{5.26c}$$

$$(1-\gamma^2)S = \begin{pmatrix} -\frac{2}{r}\,(\mu+p)\,\gamma + \frac{2B}{r}\,(\mu + p\gamma^2) - \frac{B}{2r}\,\left((\mu+4p)\gamma^2 - 3p\right) \\ -\frac{2}{r}\,(\mu\gamma^2 + p) + \frac{2B}{r}\,(\mu+p)\,\gamma - \frac{2B^2}{r}\,(\mu + p\gamma^2) - \frac{B^2}{2r}(1-\gamma^2)\mu - \frac{3B^2-4}{2r}(1-\gamma^2)p \end{pmatrix}. \tag{5.26d}$$

It has been assumed that we can get expressions of the primitive variables (μ, γ) in terms of the conservative ones $V = (V^0, V^1)$, that is $\mu = \mu(V)$ and $\gamma = \gamma(V)$. For instance, if the sound speed is constant, say k, one

has the equation of state $p = k^2\mu$. In that case, the following relations hold

$$\gamma = \frac{(1+k^2) - \sqrt{(1+k^2)^2 - 4k^2\left(B + \frac{V^1}{V^0}\right)}}{2k^2\left(B + \frac{V^1}{V^0}\right)}, \qquad \mu = V^0\left(\frac{1-\gamma^2}{1+k^2\gamma^2}\right). \quad (5.27)$$

The Equations (1.3d) in [73], which are the analogous ones to (5.27), can be recovered imposing $B = 0$. This makes sense since Schwarzschild and Gullstrand-Painlevé coordinates converge to Minkowski flat spacetime at spatial infinity ($r \to \infty$).

5.2.2 Well-podness behaviour

We are now determining the necessary and sufficient conditions that ensure hyperbolicity and genuine non-linearity properties of the system (5.26). Let us consider its homogeneous part, $\partial_0 V + \partial_1 F(V, r_0) = 0$, where the flux F is evaluated at a fixed radius r_0. The system can be written in terms of the Riemannn invariants and waves speeds:

$$\partial_0 w_\pm + \lambda_\pm(w_\pm, r_0)\partial_1 w_\pm = 0. \quad (5.28)$$

Considering the first Lemma of [73], we can proceed by following the outlined steps of its proof to compute the Riemann invariants and the wave speeds, respectively, as:

$$w_\pm = \frac{1}{2}\log\left(\frac{1+\gamma}{1-\gamma}\right) \pm \int_1^\mu \frac{\sqrt{p'(x)}}{x + p(x)}dx, \quad (5.29)$$

$$\lambda_\pm = \frac{\gamma \pm \sqrt{p'(\mu)}}{1 \pm \sqrt{p'(\mu)}\gamma} - B, \quad (5.30)$$

where $p'(\mu)$ denotes the derivative of the pressure p with respect to μ. Again, the results in Schwarzschild coordinates are similar by using the effective velocity γ, and they coincide at spatial infinity.

Attending to (5.30), our system is: strictly hyperbolic if and only if $p'(\mu) > 0,\ \forall\, \mu$; genuinely non-linear if and only if

$$2p'(1-p') + p''(\mu + p) > 0,\ \forall\, \rho; \tag{5.31}$$

and linearly degenerate if and only if the sign $>$ in previous inequality is replaced by an equal sign. This result is the same as using Schwarzschild coordinates (at it should be) and the proof is actually similar to the one presented in the first Proposition of [73]. The difference is that in the Gullstrand-Painlevé coordinates we do not need to restrict our spatial domain to $r > R_S$.

5.2.3 Stationary solutions

We are deriving the stationary solutions $\mu = \mu(r)$ and $\gamma = \gamma(r)$ of the Equations (5.26), for specified conditions at some $r = r_0$. There are significant differences in the derivation of these solutions with respect to the ones obtained using Schwarzschild coordinates.

Lemma. *If $\mu = \mu(r)$ and $\gamma = \gamma(r)$ are solutions to the system*

$$\frac{dF(\mu,\gamma,r)}{dr} = S(\mu,\gamma,r), \tag{5.32a}$$

$$\mu(r_0) = \mu_0, \qquad \gamma(r_0) = \gamma_0, \tag{5.32b}$$

the following relations hold:

$$r^2(1-B\gamma)(\mu+p)\frac{\gamma - B}{1-\gamma^2} = C_0, \tag{5.33a}$$

$$\log(1-B\gamma) - \frac{1}{2}\log(1-\gamma^2) + l(\mu) = D_0, \tag{5.33b}$$

where $l(\mu)$ is a primitive of $\frac{p'(\mu)}{\mu+p(\mu)}$ and C_0, D_0 are constants satisfying

$$C_0 = r_0^2(1-B_0\gamma_0)(\mu_0 + p(\mu_0))\frac{\gamma_0 - B_0}{1-\gamma_0^2}, \tag{5.34a}$$

$$D_0 = \log(1-B_0\gamma_0) - \frac{1}{2}\log(1-\gamma_0^2) + l(\mu_0), \tag{5.34b}$$

where $B_0 = \sqrt{R/r_0}$.

Proof. The system (5.32a) can be written as

$$\frac{d(r^2F^0)}{dr} = -\frac{rB}{2}\left((\mu+p)\frac{\gamma^2}{1-\gamma^2} - 3p\right), \tag{5.35a}$$

$$\frac{d(r^2F^1)}{dr} = -\frac{R}{2}(\mu+p) + r(D+1)p, \tag{5.35b}$$

where

$$F^0 = (\mu+p)\frac{(\gamma-B)}{1-\gamma^2} + Bp, \tag{5.36a}$$

$$F^1 = (\mu+p)\frac{(\gamma-B)^2}{1-\gamma^2} + Dp. \tag{5.36b}$$

We see that $F^1 = (F^0 - Bp)(\gamma - B) + Dp$. Making use of this relation in the Equation (5.35b), one can get that

$$(\mu+p)\frac{(\gamma-B)}{1-\gamma^2}\frac{d\gamma}{dr} + (1-B\gamma)\frac{dp}{dr} + \frac{B\gamma}{2r}(\mu+p) = 0. \tag{5.37}$$

Since $-\frac{dB}{dr} = \frac{B}{2r}$, introducing the variable $\chi = B\gamma$,

$$\frac{d\chi}{dr} - B\frac{d\gamma}{dr} = \gamma\frac{dB}{dr} = -\frac{B\gamma}{2r}. \tag{5.38}$$

Taking this relation into account in (5.37), and dividing by $(\mu+p)(1-\chi)$, we get

$$\frac{\gamma}{1-\gamma^2}\frac{d\gamma}{dr} + \frac{1}{\mu+p}\frac{dp}{dr} - \frac{1}{1-\chi}\frac{d\chi}{dr} = 0, \tag{5.39}$$

which can be integrated and (5.33b) is obtained. On the other hand, using the Equations (5.35a) and (5.37), one can see that

$$\frac{d}{dr}\left(r^2(1-B\gamma)(\mu+p)\frac{\gamma-B}{1-\gamma^2}\right) = 0. \tag{5.40}$$

Therefore, the Equation (5.33a) can be also obtained. □

As an example let us compute some solutions for an equation of state $p(\mu) = k^2\mu$, with k a constant value. We have already stated that k plays the role of the speed of sound. The stationary solution to (5.32a), attending to the previous Lemma, can be rewritten in the following form:

$$r^2\frac{\left(1-\gamma^2\right)^{\frac{1-k^2}{2k^2}}(\gamma-B)}{(1-B\gamma)^{1/k^2}} = C_1, \qquad r^2\left(\frac{\gamma-B}{1-\gamma^2}\right)\mu = C_2, \tag{5.41}$$

where the constants C_1, C_2 depend on r_0, μ_0 and γ_0. From the definition $\gamma = B(u+1)$, we can derive the corresponding expression for u. In the Figure 5.1 we show some solutions $u(r/R)$ for different values of the constant C_1. This figure is similar to the one obtained in [72] when $r \to \infty$. Note that γ does not play the role of any physical speed particle, but it is an effective Eulerian velocity. We can check that at the event horizon the Eulerian effective velocity u is zero or negative, and the radial component of the fluid velocity is zero or points towards the center of the black hole, respectively.

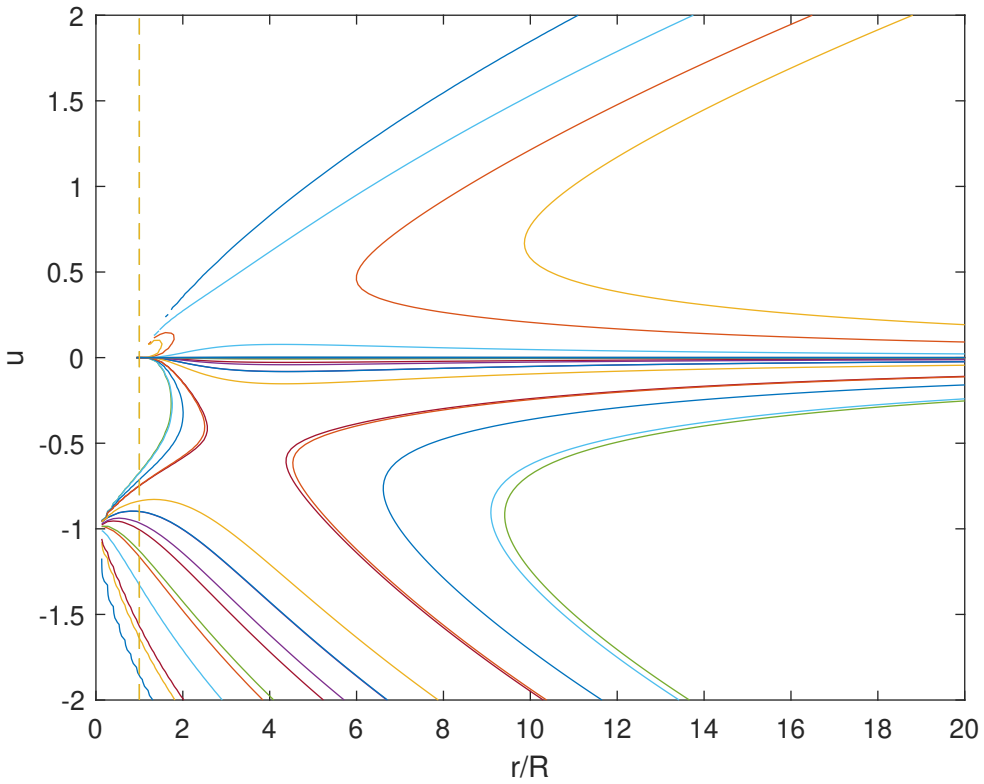

Figure 5.1: Function $u(r/R)$ associated to stationary solutions of the Euler Equation in spherical symmetry using Gullstrand-Painlevé coordinates. Different colors refer to different values of the constant C_1.

5.3 Final remarks

In the first Section of this Chapter, we have considered the Euler Equation in Newtonian gravity and made an analysis of the characteristic curves. This was useful to go to the next step, where General Relativity was considered, studying the problem of a perfect fluid moving in a fixed Schwarzschild spacetime. To do so we have considered the general relativistic Euler Equation in the Gullstrand-Painlevé coordinates. The resulting system allows the fluid to cross the event horizon $r = R_S$ with different negative values for the radial component of the velocity. Then, using these coordinates we do not need to restrict our spatial domain to the region $r > R_S$ as in Schwarzschild coordinates, the ones used in [73] to address the same problem. Gullstrand-Painlevé coordinates do not have any coordinate singularity but have the drawback of making computations trickier. We studied the hyperbolic behaviour of the system and we obtained its stationary solutions. The availability of these solutions make possible the development of well-balanced methods as the ones given in [72], where the authors considered the Schwarzschild coordinates. The main advantage of using now the Gullstrand- Painlevé coordinates is that we can consider the whole domain $0 < r < \infty$.

6

Reformulation of the Fully Constrained Formalism

The modeling of relevant astrophysical and cosmological scenarios often requires the numerical solution of the Einstein Equations. It is important having a diversity in our numerical simulations to compare numerical results, and different gauge choices can be more appropriate. In this Chapter we focus on the Fully Constrained Formulation (FCF) of the Einstein Equations [18, 32], which was introduced in the Chapter 4. Along these lines [132, 23, 112, 56] have proposed waveless constrained approximations to the full Einstein equations, while [19] derived a fourth-order post-Newtonian approximation to the system. We will propose a reformulation of the equations by adding two new variables to make explicitly visible a post-Newtonian hierarchical structure of the equations and, at the same time, preserving the good properties of the formulation, such as local uniqueness of the elliptic sector [31]. In the case of long-term numerical simulations (i.e., in supernovae explosions [124] or cosmological applications, this scheme or part of it can be very useful to get accurately enough numerical simulations, while re-

ducing the computational cost. We will derive stationary initial data of a rotating neutron star without assuming a conformally flat spatial metric (CFC) [56, 132] to show the potential of this new reformulation. We also make a comparison between our solution with the new reformulation of the FCF equations and a spacetime assuming a CFC. CFC scheme can be derived from FCF by neglecting the FCF hyperbolic sector; this comparison confirms the accuracy improvement in the proposed reformulation of the FCF equations.

We will assume geometrized units, in which $c = G = 1$.

6.1 Motivation

Astrophysical scenarios containing compact objects are modeled by complex spacetimes which require, in general, to solve the Einstein Equations numerically [5, 74, 116]. This is also true in the case of complex cosmological models [49, 81]. The gravitational radiation emitted by these scenarios encode some of their physical properties. The accurate extraction of the gravitational radiation both from our numerical simulations and from the experimental measurements is crucial to determine the physical properties of the corresponding scenario. In the last decade numerous gravitational wave detections were observed by the LIGO-Virgo-KAGRA Collaborations [24]; all the detected signals were generated by binary systems of compact objects. In particular, the observation of the first binary neutron star system detected with gravitational waves together with the associated electromagnetic counterparts [4] marks a new era of multi-messenger astronomy, including the gravitational waves in the different, complementary, key channels to observe these scenarios. The fourth observing run, O4, has just started, and numerical simulations with more accuracy will be required in the near future to extract new gravitational wave signals from the next observing runs data.

6.2 Reformulation of the equations

Many of the manipulations in this Section have in mind the post-Newtonian expansions (PNEs) of the variables we are considering. This means to expand variables in powers of $1/c$, valid in the approximation of weak gravity and small velocities of the sources. Post-Newtonian hydrodynamics has been considered by a number of authors in the past [17, 8, 11]. To the leading order, the PNE of the metric variables we are manipulating can be deduced from [17], and are listed below:

$$N = 1 - \frac{\Phi}{c^2} + \mathcal{O}\left(\frac{1}{c^4}\right), \quad \psi = 1 + \frac{\Phi}{2c^2} + \mathcal{O}\left(\frac{1}{c^4}\right), \quad N\psi^2 = 1 + \mathcal{O}\left(\frac{1}{c^4}\right),$$
$$\beta^i = \mathcal{O}\left(\frac{1}{c^3}\right), \quad h^{ij} = \mathcal{O}\left(\frac{1}{c^4}\right),$$
$$\hat{A}^{ij} = \mathcal{O}\left(\frac{1}{c^3}\right), \quad X^i = \mathcal{O}\left(\frac{1}{c^3}\right), \quad \hat{A}^{ij}_{TT} = \mathcal{O}\left(\frac{1}{c^5}\right),$$

where Φ is the Newtonian potential.

We introduce now a new vector field, with the goal of simplifying at least part of our equations:

$$V^i = 2N\psi^{-6}X^i - \beta^i. \tag{6.1}$$

The post-Newtonian order of this vector is $V^i = \mathcal{O}(c^{-5})$. This order is justified below in the text. Once X^i, ψ, N and V^i are known, the shift vector β^i can be computed directly from the previous definition for V^i. The equation most positively affected by this new auxiliary variable is the evolution equation for the h^{ij} tensor, which, in terms of the new variables, reads:

$$\begin{aligned}\partial_t h^{ij} = {} & \beta^k \mathcal{D}_k h^{ij} - h^{ik}\mathcal{D}_k\beta^j - h^{kj}\mathcal{D}_k\beta^i + \frac{2}{3}h^{ij}\mathcal{D}_k\beta^k + 2N\psi^{-6}\hat{A}^{ij}_{TT} + (LV)^{ij} \\ & - X^j\mathcal{D}^i(2N\psi^{-6}) - X^i\mathcal{D}^j(2N\psi^{-6}) + \frac{2}{3}f^{ij}X^k\mathcal{D}_k(2N\psi^{-6}).\end{aligned} \tag{6.2}$$

It turns out that, after the introduction of V^i, this equation has been slightly simplified and, more importantly, has balanced post-Newtonian orders in both sides of the equation, which are now both $\mathcal{O}(c^{-5})$. The

previous version of this Equation (4.121) had $\mathcal{O}(c^{-5})$ at the left hand side while $\mathcal{O}(c^{-3})$ at the right hand side. Of course, in the previous version, terms of order $\mathcal{O}(c^{-3})$ must cancel out theoretically to become $\mathcal{O}(c^{-5})$, but this may not happen always numerically. With the introduction of the vector V^i we avoid this potential numerical issue.

Let us focus now on the other evolution equation for $\hat{A}^{ij}$ (4.122). Instead of $\hat{A}^{ij}$, we propose explicitly working with the variables X^i and $\hat{A}^{ij}_{TT}$. Remind that $\hat{A}^{ij}$ is $\mathcal{O}(c^{-3})$, while $\hat{A}^{ij}_{TT}$ is $\mathcal{O}(c^{-5})$ in post-Newtonian order. The main reason of taking into account $\hat{A}^{ij}_{TT}$ is to solve the spacetime metric more accurately in those cases or regions where the post-Newtonian approximation is valid. In other cases, our reformulation is just a change of variables with no additional effects. The resulting evolution equation for $\hat{A}^{ij}_{TT}$ reads:

$$\begin{aligned}
\partial_t \hat{A}^{ij}_{TT} &= \beta^k \mathcal{D}_k \hat{A}^{ij} - \hat{A}^{kj}\mathcal{D}_k\beta^i - \hat{A}^{ik}\mathcal{D}_k\beta^j + \frac{5}{3}\hat{A}^{ij}\mathcal{D}_k\beta^k + 2N\psi^{-6}\tilde{\gamma}_{kl}\hat{A}^{ik}\hat{A}^{jl} \\
&+\frac{3}{4}N\psi^{-6}\tilde{\gamma}^{ij}\tilde{\gamma}_{lk}\tilde{\gamma}_{nm}\hat{A}^{km}\hat{A}^{ln} + N\psi^2\tilde{R}^{ij}_* - \frac{1}{4}N\psi^2\tilde{R}\tilde{\gamma}^{ij} \\
&+\frac{1}{2}(\tilde{\gamma}^{kl}\mathcal{D}_k h^{ij} - \tilde{\gamma}^{ik}\mathcal{D}_k h^{lj} - \tilde{\gamma}^{kj}\mathcal{D}_k h^{il})\mathcal{D}_l(N\psi^2) \\
&+4\psi^{-1}\tilde{\gamma}^{ik}\tilde{\gamma}^{jl}\mathcal{D}_k\psi\mathcal{D}_l(N\psi^2) + 4\psi^{-1}\tilde{\gamma}^{ik}\tilde{\gamma}^{jl}\mathcal{D}_l\psi\mathcal{D}_k(N\psi^2) - 2\psi^{-1}\tilde{\gamma}^{ij}\tilde{\gamma}^{kl}\mathcal{D}_k\psi\mathcal{D}_l(N\psi^2) \\
&+\frac{N\psi^2}{2}\tilde{\gamma}^{kl}\mathcal{D}_k\left(\mathcal{D}_l h^{ij}\right) - 8N\tilde{\gamma}^{ik}\tilde{\gamma}^{jl}\mathcal{D}_l\psi\mathcal{D}_k\psi + 2N\tilde{\gamma}^{ij}\tilde{\gamma}^{kl}\mathcal{D}_k\psi\mathcal{D}_l\psi - \tilde{\gamma}^{ik}\tilde{\gamma}^{jl}\mathcal{D}_k\mathcal{D}_l(N\psi^2) \\
&-(L\dot{X})^{ij} - 8\pi N\psi^{10}S^{ij} + 4\pi N S^*\tilde{\gamma}^{ij}, \qquad (6.3)
\end{aligned}$$

where $\dot{X}^i = \partial_t X^i$. The left hand side of the Equation (6.3) has order $\mathcal{O}(c^{-6})$, while the terms of the last two lines of the right hand side of this equation have order $\mathcal{O}(c^{-4})$. This new expression reduces significantly the number of terms that should cancel with respect to previous versions. Correcting the post-Newtonian order of these terms is a possibility that will be considered in the future. However, it will not be easy in general since it contains terms including matter variables. We note that for this equation there is no need to introduce V^i since in does not modify the post-Newtonian order of the different terms.

The elliptic equations we are going to consider are the ones from the Chapter 4, see (4.124)-(4.127), with some modifications and simplifications due to the use of the vector field V^i, as well as an additional elliptic equation for the new variable V^i instead of the elliptic equation for the shift vector β^i, and another additional elliptic equation for the variable $\dot{X}^i$ to close the system. The whole elliptic sector is presented below, where the post-Newtonian order of the corresponding expressions is placed at the end of each equation, which is, at the same time, the order of the variable under resolution:

$$\Delta X^i + \frac{1}{3}\mathcal{D}^i\mathcal{D}_j X^j = -\tilde{\gamma}^{im}\left(\mathcal{D}_k\tilde{\gamma}_{ml} - \frac{1}{2}\mathcal{D}_m\tilde{\gamma}_{kl}\right)\hat{A}^{kl} + 8\pi\tilde{\gamma}^{ij}(S^*)_j = \mathcal{O}\left(\frac{1}{c^3}\right); \qquad (6.4)$$

$$\tilde{\gamma}^{kl}\mathcal{D}_k\mathcal{D}_l\psi = -2\pi\psi^{-1}E^* - \frac{1}{8}\psi^{-7}\tilde{\gamma}_{il}\tilde{\gamma}_{jm}\hat{A}^{lm}\hat{A}^{ij} + \frac{1}{8}\psi\tilde{R} = \mathcal{O}\left(\frac{1}{c^2}\right); \tag{6.5}$$

$$\begin{aligned}\tilde{\gamma}^{ik}\mathcal{D}_i\mathcal{D}_k(N\psi^2) &= 2\psi^{-1}\tilde{\gamma}^{ik}\mathcal{D}_k\psi\mathcal{D}_i(N\psi^2) - 2\psi^{-2}(N\psi^2)\tilde{\gamma}^{ik}\mathcal{D}_k\psi\mathcal{D}_i\psi + \frac{1}{4}(N\psi^2)\tilde{R} \\ &\quad + \frac{3}{4}\psi^{-8}(N\psi^2)\tilde{\gamma}_{il}\tilde{\gamma}_{jm}\hat{A}^{lm}\hat{A}^{ij} + 4\pi\psi^{-2}(N\psi^2)S^* = \mathcal{O}\left(\frac{1}{c^4}\right);\end{aligned} \tag{6.6}$$

$$\begin{aligned}\Delta V^i + \frac{1}{3}\mathcal{D}^i\mathcal{D}_jV^j &= -h^{kj}\mathcal{D}_k\mathcal{D}_jV^i - \frac{1}{3}h^{ik}\mathcal{D}_k\mathcal{D}_jV^j + 2N\psi^{-6}\left(h^{kj}\mathcal{D}_k\mathcal{D}_jX^i + \frac{1}{3}h^{ik}\mathcal{D}_k\mathcal{D}_jX^j\right) \\ &\quad + \tilde{\gamma}^{kj}X^i\mathcal{D}_k\mathcal{D}_j(2N\psi^{-6}) + \frac{1}{3}\tilde{\gamma}^{ik}X^j\mathcal{D}_k\mathcal{D}_j(2N\psi^{-6}) \\ &\quad + \mathcal{D}_k(2N\psi^{-6})\left(2\tilde{\gamma}^{kj}\mathcal{D}_jX^i + \frac{1}{3}\tilde{\gamma}^{ik}\mathcal{D}_jX^j + \frac{1}{3}\tilde{\gamma}^{ij}\mathcal{D}_jX^k - \hat{A}^{ik}\right) = \mathcal{O}\left(\frac{1}{c^5}\right);\end{aligned} \tag{6.7}$$

$$\begin{aligned}\Delta\dot{X}^j + \frac{1}{3}\mathcal{D}^j\mathcal{D}_i\dot{X}^i &= \beta^k\mathcal{D}_i\mathcal{D}_k\hat{A}^{ij} - \mathcal{D}_i\hat{A}^{ik}\mathcal{D}_k\beta^j - \hat{A}^{ik}\mathcal{D}_i\mathcal{D}_k\beta^j + \frac{2}{3}\hat{A}^{ij}\mathcal{D}_i\mathcal{D}_k\beta^k + \frac{5}{3}\mathcal{D}_i\hat{A}^{ij}\mathcal{D}_k\beta^k \\ &\quad - \frac{1}{2}N\psi^{-6}\tilde{\gamma}^{jl}\mathcal{D}_l\left(\tilde{\gamma}_{in}\tilde{\gamma}_{km}\hat{A}^{nm}\hat{A}^{ik}\right) - \psi^{-8}\tilde{\gamma}^{jl}\tilde{\gamma}_{in}\tilde{\gamma}_{km}\hat{A}^{nm}\hat{A}^{ik}\mathcal{D}_l(N\psi^2) \\ &\quad + 8\psi^{-7}N\tilde{\gamma}^{jl}\tilde{\gamma}_{in}\tilde{\gamma}_{km}\hat{A}^{nm}\hat{A}^{ik}\mathcal{D}_l\psi \\ &\quad + 2N\psi^{-6}\mathcal{D}_i(\tilde{\gamma}_{kl}\hat{A}^{ik}\hat{A}^{jl}) - 16\psi^{-7}N\tilde{\gamma}_{kl}\hat{A}^{ik}\hat{A}^{jl}\mathcal{D}_l\psi + 2\psi^{-8}\tilde{\gamma}_{kl}\hat{A}^{ik}\hat{A}^{jl}\mathcal{D}_l(N\psi^2) \\ &\quad - \frac{1}{2}\mathcal{D}_i(N\psi^2)\mathcal{D}_lh^{ik}\mathcal{D}_kh^{jl} - \frac{1}{6}\tilde{\gamma}^{kj}\mathcal{D}_kh^{il}\mathcal{D}_i\mathcal{D}_l(N\psi^2) - \tilde{\gamma}^{ik}\mathcal{D}_ih^{jl}\mathcal{D}_k\mathcal{D}_l(N\psi^2) \\ &\quad - 8N\tilde{\gamma}^{ik}\mathcal{D}_ih^{jl}\mathcal{D}_k\psi\mathcal{D}_l\psi + 4N\tilde{\gamma}^{jl}\mathcal{D}_lh^{ik}\mathcal{D}_i\psi\mathcal{D}_k\psi \\ &\quad + 4\psi^{-1}\tilde{\gamma}^{ik}\mathcal{D}_ih^{jl}\left(\mathcal{D}_l(N\psi^2)\mathcal{D}_k\psi + \mathcal{D}_k(N\psi^2)\mathcal{D}_l\psi\right) \\ &\quad - 4\psi^{-1}\tilde{\gamma}^{jl}\mathcal{D}_lh^{ik}\mathcal{D}_i(N\psi^2)\mathcal{D}_k\psi + \tilde{R}^{ij}_{**}\mathcal{D}_i(N\psi^2) + N\psi^2\mathcal{D}_i\tilde{R}^{ij}_{**} - \frac{1}{2}N\psi^2\tilde{\gamma}^{ij}\mathcal{D}_i\tilde{R} \\ &\quad - 8\pi\psi^{-2}E^*\tilde{\gamma}^{jl}\mathcal{D}_l(N\psi^2) + 16\pi\psi^{-1}NE^*\tilde{\gamma}^{jl}\mathcal{D}_l\psi + 16\pi\psi^{-1}NS^*\tilde{\gamma}^{jl}D_l\psi \\ &\quad - 8\pi N\psi^{10}\mathcal{D}_iS^{ij} - 8\pi\psi^8S^{ij}\mathcal{D}_i(N\psi^2) - 64\pi\psi^9NS^{ij}\mathcal{D}_i\psi = \mathcal{O}\left(\frac{1}{c^4}\right),\end{aligned} \tag{6.8}$$

where

$$\begin{aligned}\tilde{R}^{ij}_{**} &= \frac{1}{2}\left(-\tilde{\gamma}_{kl}\tilde{\gamma}^{mn}\mathcal{D}_mh^{ik}\mathcal{D}_nh^{jl} + \tilde{\gamma}_{nl}\mathcal{D}_kh^{mn}(\tilde{\gamma}^{ik}\mathcal{D}_mh^{jl} + \tilde{\gamma}^{jk}\mathcal{D}_mh^{il})\right) \\ &\quad + \frac{1}{4}\tilde{\gamma}^{ik}\tilde{\gamma}^{jl}\mathcal{D}_kh^{mn}\mathcal{D}_l\tilde{\gamma}_{mn}.\end{aligned} \tag{6.9}$$

We can check that the hyperbolic and elliptic sectors can be solved hierarchically (as previously). Indeed, given the hydrodynamical variables E^*, S^*, S^*_j, S^{ij}, we have the hierarchical structure of Table 6.1 with equations including terms with progressively post-Newtonian orders. Note that $\tilde{\gamma}^{ij} = f^{ij} + h^{ij}$, with f^{ij} a flat, fixed and known background metric.

Variable under resolution	Computed from Equation	PNE
h^{ij}	(6.2)	$\mathcal{O}(c^{-4})$
$\hat{A}^{ij}_{TT}$	(6.3)	$\mathcal{O}(c^{-5})$
$X^i(h^{ij}, \hat{A}^{ij}_{TT}, S^*_j)$	(6.4)	$\mathcal{O}(c^{-3})$
$\hat{A}^{ij}(X^i, \hat{A}^{ij}_{TT})$	(4.115)	$\mathcal{O}(c^{-3})$
$\psi(h^{ij}, \hat{A}^{ij}, E^*)$	(6.5)	$1+\mathcal{O}(c^{-2})$
$(N\psi^2)(h^{ij}, \hat{A}^{ij}, \psi, S^*)$	(6.6)	$1+\mathcal{O}(c^{-4})$
$N(\psi, N\psi^2)$	–	$1+\mathcal{O}(c^{-2})$
$V^i(h^{ij}, \hat{A}^{ij}, X^i, \psi, N)$	(6.7)	$\mathcal{O}(c^{-5})$
$\beta^i(X^i, \psi, N, V^i)$	(6.1)	$\mathcal{O}(c^{-3})$
$\dot{X}^i(h^{ij}, \hat{A}^{ij}, X^i, \psi, N, \beta^i, E^*, S^*, S^{ij})$	(6.8)	$\mathcal{O}(c^{-4})$

Table 6.1: Hierarchical structure of resolution for the hyperbolic and elliptic sectors of the reformulated FCF.

Note that in the Equation (6.6) we solve $N\psi^2$, with post-Newtonian order $\mathcal{O}(c^{-4})$, instead of N or $N\psi$, of order $\mathcal{O}(c^{-2})$. However, there may be additional numerical errors due to the presence of the first derivative of $(N\psi^2)$ in the right hand side of the Equation (6.6). This was not the case in the elliptic equation for $(N\psi)$ stated in the Equation (4.126). So we will keep in mind potential numerical advantages when solving $(N\psi)$ instead of $(N\psi^2)$.

In the next Section we compute the stationary initial data associated to the spacetime geometry of a rotating neutron star as an illustrative numerical application of the proposed reformulation of the FCF.

6.3 Computation of stationary spacetime initial data

6.3.1 Initial set-up

As a numerical test we use a rotating neutron star composed of a perfect fluid with polytropic equation of state $p = C\rho^{\Gamma}$, where p is the pressure, $\Gamma = 2$ and $C = 145731$ (cgs units, $K = 100$ in geometrized units). Considering a central density $\rho_c = 7.91 \cdot 10^{14}$ g/cm^3 and a rotation frequency $f = 550$ Hz, we obtain a neutron star with equatorial radius $R_{\rm eq} = 12.86$ km and polar radius $R_{\rm p} = 11.20$ km, and gravitational mass $M = 1.487\, M_{\odot}$. Hydrodynamical and spacetime metric variables are computed with the code `rotstar_dirac` [79] based on the C++ library LORENE [2]. This code employs the same gauge we use here, i.e., maximal slicing and Dirac gauge (4.120). This allows us to use the hydrodynamical quantities to compute the spacetime metric variables with our reformulation. In addition, the spacetime metric variables from LORENE can be used to check the numerical results from our approach. For this compact object, spacetime is stationary and we can adapt the coordinate time t to this stationarity, setting the derivatives with respect to t in the Equations (6.2) and (6.3) to zero. Moreover, this spacetime is axisymmetric and we can also adapt spherical type coordinates r and θ (2-dimensional problem). The rotation axis is fixed at $\theta = 0$. Orthornormal spherical components are used for all vector and tensor fields in the numerical implementation of the formulation, but we change to orthonormal cylindrical components at the time of the numerical resolution because is a simpler strategy for this scenario.

We are going to use a finite-difference grid, with equally spaced cells in the radial and angular directions. The numerical grid has $n_r = 3200$ points in the radial coordinate r and $n_\theta = 64$ points in polar angle θ, where

$$r_1 = \frac{\Delta r}{2},\ r_{n_r} = 12R_{\rm eq} - \frac{\Delta r}{2},\ \theta_1 = \frac{\Delta\theta}{2},\ \theta_{n_\theta} = \pi - \frac{\Delta\theta}{2},$$

being $\Delta r = 12R_{\rm eq}/n_r \approx 48$ m and $\Delta\theta = \pi/n_\theta \approx 0.05$ the radial and angular

cell sizes, respectively. This grid covers the spacetime up to 12 times the radius of the star with more than 260 radial points inside the star at the equator.

We use ghosts cells to compute the discretization of the spatial derivatives close to the numerical grid boundaries, keeping the same radial and angular cell sizes. The values of the numerical solution in the ghost cells for the different variables take into account the theoretical behaviour of these variables close to the boundaries. If u_{ij} denotes the numerical solution of the variable u, where i and j indexes refer to the radial and angular cells, respectively, then its values in the ghost cells are given by:

$$u_{(1-l)j} = \pm u_{lj}, \tag{6.10}$$

$$u_{i(1-l)} = \pm u_{il}, \quad u_{i(n_\theta+l)} = \pm u_{i(n_\theta-l+1)}, \tag{6.11}$$

where l denotes the number of ghost cells in the corresponding direction, the positive sign denotes symmetric boundary conditions and the negative sign denotes antisymmetric boundary conditions. We are going to follow the symmetries used in [12]. Since we will need to solve some elliptic equations in orthonormal cylindrical components, we also need to consider symmetries in this new basis. Taking into account the transformations from spherical to cylindrical components, we will follow the prescription of Table 6.2.

		Center	Axis	Equator
Vectors X^i, V^i and $\dot{X}^i$	ϖ	-	-	+
	z	+	+	-
	φ	-	-	+
Tensor h^{ij}	$\varpi\varpi$	+	+	+
	zz	+	+	+
	$\varphi\varphi$	+	+	+
	ϖz	-	-	-
	$\varpi\varphi$	+	+	+
	$z\varphi$	-	-	-

Table 6.2: Parity conditions for cylindrical orthonormal components of vectors and tensors as implemented in the resolution of some elliptic equations. Components of vectors X^i, V^i and $\dot{X}^i$, and tensor h^{ij} have to be multiplied with the corresponding sign when they are copied into ghost zones.

At the outer boundary we impose a Robin condition, assuming $u = u_0 + M/r^n$ for a generic variable u, which is equivalent to impose $u \to u_0$

at spatial infinity ($r \to \infty$) and $\partial_r u = -n\,(u-u_0)/r$, so only the values n and u_0 need to be specified. The values in the ghost cells of the outer boundary $u_{(n_r+l)j}$ are set such that this behaviour is reproduced. We consider $n = 1$ for scalar fields and $n = 2$ for vector fields. We will also need to solve an elliptic equation for the tensor h^{ij} using orthonormal cylindrical components; in this case, $n = 3$ will be used for the diagonal components and $n = 4$ for the non-diagonal non-zero component $h^{\varpi z}$. This is the case when we solve stationary initial data for a rotating neutron star in the Dirac gauge. In dynamical spacetimes, we must set $n = 1$ for the h^{ij} components in general.

All discretizations of the spatial differential operators are second-order and we use the LAPACK library to invert the Laplacian operators in the resolution of the elliptic equations. In some equations the variable under resolution appears outside the main Laplacian operator in the source term; in this case we apply a fix-point iterative method with a relaxation factor. Each loop finishes when the mean difference between two successive iterations is smaller than a given tolerance ϵ,

$$\sum_{i=1}^{n_r}\sum_{j=1}^{n_\theta}\frac{|u_{ij}^{k+1}-u_{ij}^{k}|}{n_r n_\theta} < \epsilon,$$

where k denotes the corresponding iteration and (i,j) refers to a generic point of the numerical mesh. For all variables we use $\epsilon = 10^{-6}$.

6.3.2 Vector and tensor Poisson-like equations

In those cases where we solve a vector or tensor Poisson-like equation, we make a transformation to the orthonormal cylindrical coordinates because there are more components decoupled with respect to the orthonormal spherical one. The vector Poisson-like equations we need to solve have the following form:

$$\Delta v^i + \lambda\, f^{ij}\mathcal{D}_j\mathcal{D}_k v^k = R^i. \tag{6.12}$$

where $\Delta = \mathcal{D}_k\mathcal{D}^k$, R^i is a general source term which does not depend on the unknown vector v^i and λ is a constant. The first step of the general procedure for solving the Equation (6.12) follows the strategy used in

[52, 18]. It considers the divergence of the previous equation to derive

$$\Delta\phi = \frac{\mathcal{D}_i R^i}{1+\lambda}, \tag{6.13}$$

with $\phi = \mathcal{D}_k v^k$. We solve this scalar Poisson equation and get ϕ. The second step is to solve v^i via the following equation (equivalent to the original one):

$$\Delta v^i = R^i - \lambda\, f^{ij}\mathcal{D}_j\phi. \tag{6.14}$$

In orthonormal cylindrical coordinates $\{\varpi, \phi, z\}$ and in axisymmetry, all components decouple in the following way:

$$(\Delta v)^{\varpi} = \Delta v^{\varpi} - \frac{v^{\varpi}}{\varpi^2} = R^{\varpi} - \lambda\,\mathcal{D}^{\varpi}\phi, \tag{6.15}$$

$$(\Delta v)^{\phi} = \Delta v^{\phi} - \frac{v^{\phi}}{\varpi^2} = R^{\phi}, \tag{6.16}$$

$$(\Delta v)^{z} = \Delta v^{z} = R^{z} - \lambda\,\mathcal{D}^{z}\phi. \tag{6.17}$$

The left hand side of these equations is discretized applying second-order finite differences, leading to a linear operator, which we invert using LAPACK subroutines, as previously mentioned.

On the other hand, as we are imposing stationarity for the computation of stationary initial data, from the Equation (6.3), we end up with a tensor Poisson-like equation for h^{ij} of the following form:

$$(\Delta h)^{ij} = R^{ij}, \tag{6.18}$$

where R^{ij} is a general source term which does not depend on the unknown tensor h^{ij}. Besides, in axisymmetry, we can set coordinates in such a way that $h^{r\phi} = h^{\theta\phi} = 0$. It turns out that in orthonormal cylindrical coordinates not all the non-zero components of h^{ij} ($h^{\varpi\varpi}$, h^{zz}, $h^{\varpi z}$ and $h^{\phi\phi}$) are fully decoupled, even if axisymmetry is imposed:

$$(\Delta h)^{\varpi\varpi} = \Delta h^{\varpi\varpi} - \frac{2}{\varpi^2}\left(h^{\varpi\varpi} - h^{\phi\phi}\right), \tag{6.19}$$

$$(\Delta h)^{\phi\phi} = \Delta h^{\phi\phi} + \frac{2}{\varpi^2}\left(h^{\varpi\varpi} - h^{\phi\phi}\right), \tag{6.20}$$

$$(\Delta h)^{zz} = \Delta h^{zz}, \tag{6.21}$$

$$(\Delta h)^{\varpi z} = \Delta h^{\varpi z} - \frac{h^{\varpi z}}{\varpi^2}. \tag{6.22}$$

The equations for h^{zz} and $h^{\varpi z}$ are fully decoupled from the rest ones. If we define the auxiliary variables

$$C_1 = h^{\varpi\varpi} + h^{\phi\phi},\ C_2 = h^{\varpi\varpi} - h^{\phi\phi}, \tag{6.23}$$

then we can derive the following decoupled elliptic equations:

$$\Delta C_1 = R^{\varpi\varpi} + R^{\phi\phi}, \tag{6.24}$$

$$\Delta C_2 - \frac{4}{\varpi^2} C_2 = R^{\varpi\varpi} - R^{\phi\phi}. \tag{6.25}$$

Once C_1 and C_2 are solved, we can easily get $h^{\varpi\varpi}$ and $h^{\phi\phi}$.

We will use this strategy to solve the whole system of elliptic equations.

6.3.3 Code

We are using a Fortran based code to solve the previous system. The structure of scripts is divided in the following modules or directories:

`common` `elliptic` `fcf_ellitpic` `fcf_hyperbolic`

In the module `common` we define some subroutines to compute changes of coordinates and tensor calculations. Inside `elliptic` the subroutines to solve all the types of elliptic equations are programmed. We also set the boundary conditions according to the type of variable. Here, we use the library LAPACK to finally solve the algebraic linear equations coming from the discretization of the differential operators by the finite differences. The module `fcf_ellitpic` contains the definition of the source terms of all elliptic equations of the formulation. The computation of all first and second order covariant derivatives of all vector and tensor fields is carried out by subroutines built inside this directory. Finally, in `fcf_hyperbolic` we set the numerical integration of the hyperbolic sector of the formulation.

6.3.4 Comparison with results in the xCFC formulation

In this Subsection we set $h^{ij} = 0$, so we can compare our results with the ones obtained with the xCFC formulation [31] (without the introduc-

tion of the auxiliary variables V^i and $\dot{X}^i$). The xCFC formulation can be seen as an approximation to the FCF, except in the spherically symmetric case, where this formulation is exact (see [28]). Then, we will compare the numerical solution of the Equations (6.4)–(6.8) imposing $h^{ij} = 0$ to the resulting one using the original xCFC formulation. Actually, it is convenient to solve an elliptic equation for $(N\psi^2 - 1)$ instead of $N\psi^2$, due to the fact that $(N\psi^2 - 1)$ is $\mathcal{O}(c^{-4})$ in PNE. Therefore, the elliptic equations for X^i and ψ are the same as in the xCFC case, and the main differences are that in our proposal we compute N from the elliptic equation for $(N\psi^2 - 1)$, derived from the Equation (6.6), the shift vector is obtained once V^i is known, and the elliptic equation for $\dot{X}^i$ was not considered in the xCFC formulation.

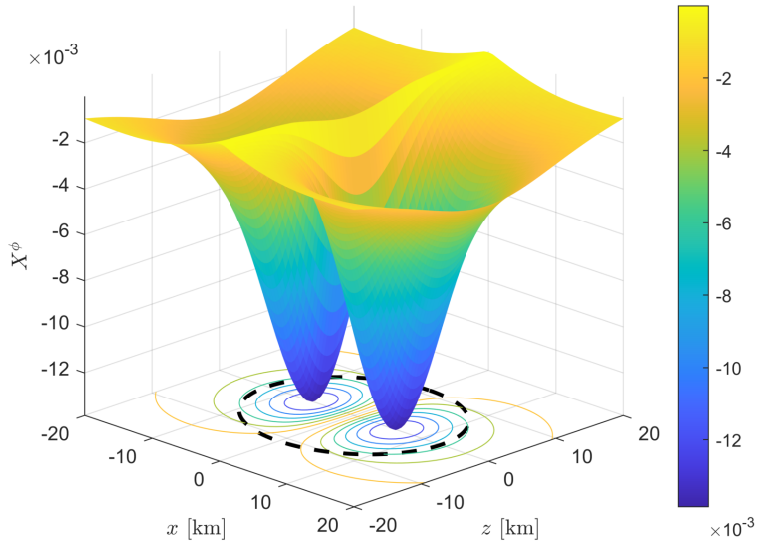

Figure 6.1: Profile of X^ϕ in the meridional plane. A contour plot is also displayed. The location of the surface of the star is denoted with a dashed black line. The rotation axis is placed at $\theta = 0$ (axis in the meridional plane determined by $x = 0$ in Cartesian coordinates).

The profile for X^ϕ in the meridional plane is shown in the Figure 6.1. This is the only non-zero component of the vector field X^i in orthonormal spherical components when axisymmetry is imposed. Contours of the profile are also displayed. The location of the surface of the star is also included in the contours with a dashed black line.

In the Figure 6.2 we show the profiles of the numerical solutions of

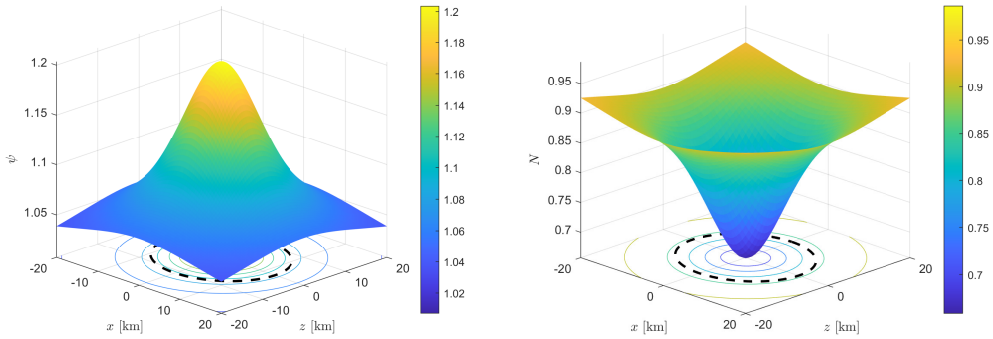

Figure 6.2: Profiles of ψ (left) and N (right) in the meridional plane. A contour plot is also displayed. The location of the surface of the star is denoted with dashed black lines. The rotation axis is placed at $\theta = 0$.

the variables ψ and N. To get N, we use the numerical solutions of the elliptic equations for $(N\psi^2 - 1)$ and ψ. In the Figure 6.3 we check that the radial profile of $(N\psi^2 - 1) \sim \mathcal{O}(c^{-4})$ decreases much faster than $(N - 1) \sim \mathcal{O}(c^{-2})$ and $(\psi - 1) \sim \mathcal{O}(c^{-2})$; for example, at $r = 10^2$, $(N\psi^2 - 1)$ is 100 times smaller than the other two quantities.

In the Figure 6.4 we display the profiles of the only two non-zero components of the conformal traceless extrinsic curvature, $\hat{A}^{r\phi}$ and $\hat{A}^{\theta\phi}$, where $\hat{A}^{ij} = (LX)^{ij}$, since we are considering $h^{ij} = 0$ in the Equation (4.115).

The figure 6.5 shows the numerical solution of the new introduced vector field V^i. The shift vector β^i, directly computed from V^i, is displayed in the Figure 6.6. For these vector fields only the angular components V^ϕ and β^ϕ are non-zero. $V^i \sim \mathcal{O}(c^{-5})$, while $X^i \sim \mathcal{O}(c^{-3})$ and $\beta^i \sim \mathcal{O}(c^{-3})$. Radial profiles of these quantities are displayed on the left of the Figure 6.7. When we compare β^i computed through the xCFC formulation, β^i_{xCFC}, to that computed with our new approach, the difference is very small (i.e., around 10^{-6} at most) and increases with r, as it can be observed on the right of the Figure 6.7, where the radial profiles of this difference in absolute value at $\theta = 0, \pi/4, \pi/2$ are displayed. This small difference may be related to the fact that we are solving $V^i \sim \mathcal{O}(c^{-5})$ (with an elliptic equation with source terms of the same post-Newtonian orders), and then we compute β^i from V^i; this strategy may be more accurate for larger radial values with respect to the direct computation of β^i_{xCFC}.

Concerning the vector field $\dot{X}^i$, we know that it must be zero theoretically as ∂_t is a Killing vector if the full metric is solved ($h^{ij} = 0$ is not

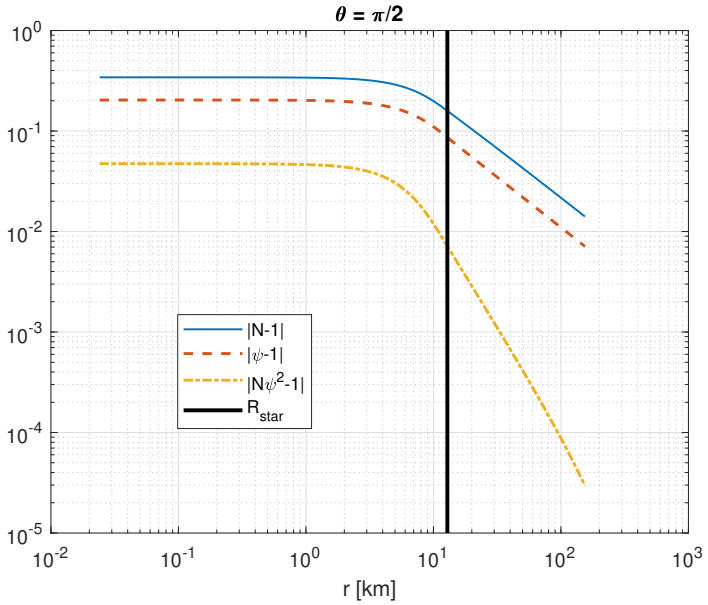

Figure 6.3: Radial profiles of $(N-1)$ (solid blue line), $(\psi-1)$ (dashed red line), and $(N\psi^2-1)$ (dash-dotted yellow line) in log-log scale at $\theta=\pi/2$ are plotted. The vertical solid black line denotes the radius of the star.

imposed). However, we can solve the Equation (6.8) imposing $h^{ij}=0$ as an experiment; the expected error should be of the order of the tensor $h^{ij}=\mathcal{O}(c^{-4})$ that we are neglecting. In fact, we obtain a maximum absolute value for $\dot{X}^i$ of order 10^{-5} km^{-1}, which can be justified taking into account that X^i reaches a maximum absolute value of order 10^{-2}, the characteristic distance of the system is $R\sim 10$ km, and an underestimated approximation of the characteristic time of the system $T\sim R$ (geometrized units) can be considered, so one would roughly expect $\dot{X}^i\sim X^i/T\sim 10^{-3}$, 2 orders of magnitude above the maximum value obtained for $\dot{X}^i$. The variables are solved with a tolerance of 10^{-6}, so the non-zero value obtained for $\dot{X}^i$ might be just numerical error.

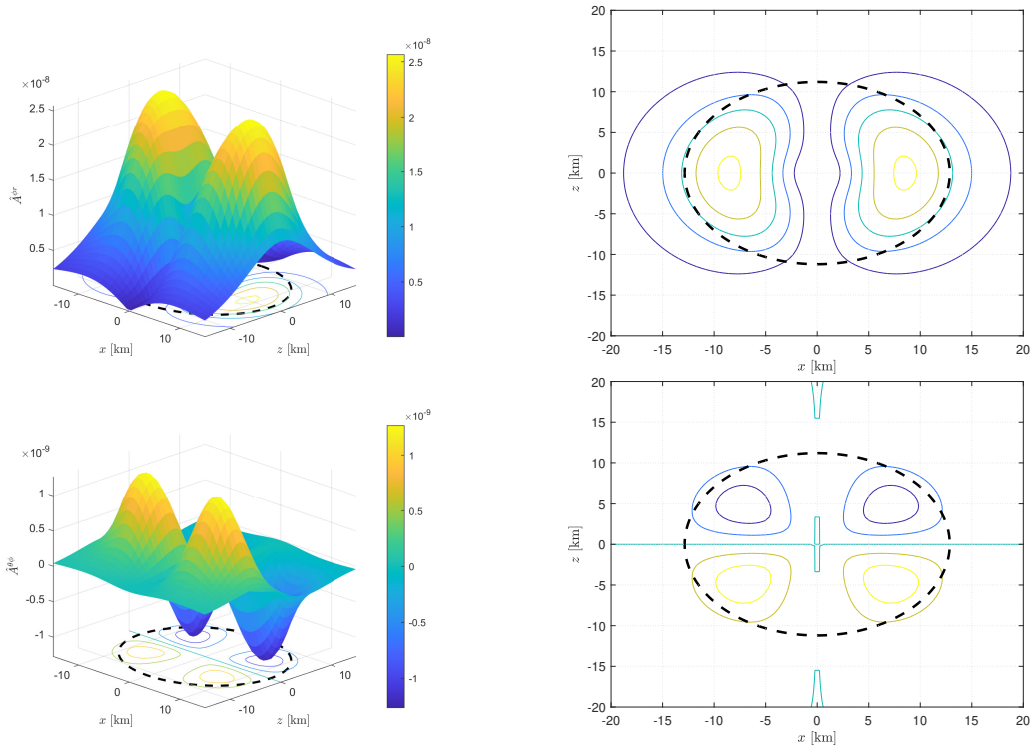

Figure 6.4: Profiles (left) of $\hat{A}^{r\phi}$ (top) and $\hat{A}^{\theta\phi}$ (bottom) in the meridional plane. A contour plot of these components are also displayed (right). The location of the surface of the star is denoted with dashed black lines. The rotation axis is placed at $\theta = 0$.

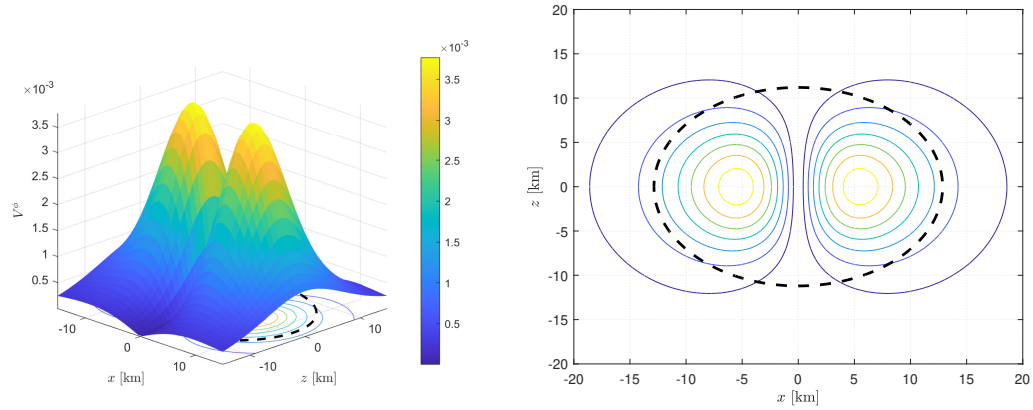

Figure 6.5: Profile (left) of V^{ϕ} in the meridional plane. A contour plot is also displayed (right). The location of the surface of the star is denoted with a dashed black line. The rotation axis is placed at $\theta = 0$.

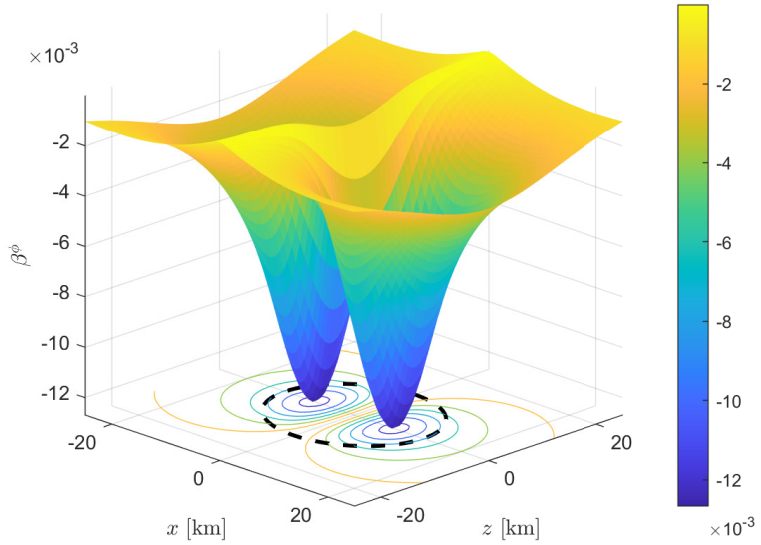

Figure 6.6: Profile of β^ϕ in the meridional plane. A contour plot is also displayed. The location of the surface of the star surface is denoted with a dashed black line. The rotation axis is placed at $\theta = 0$.

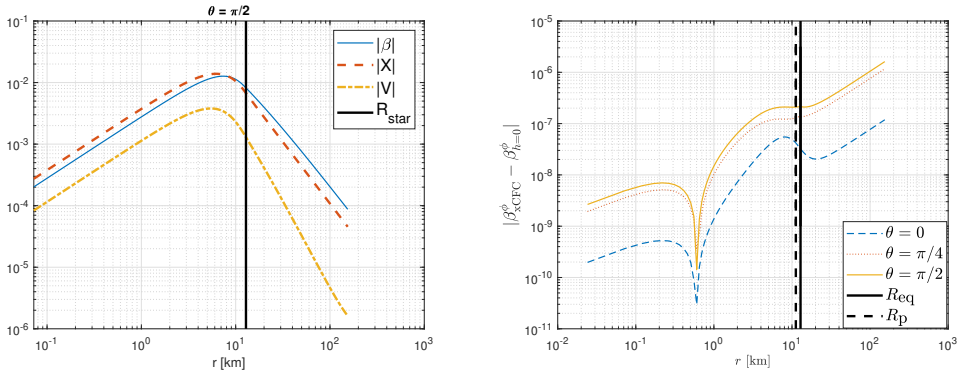

Figure 6.7: Left: radial profiles of β^i (solid blue line), X^i (dashed red line), and V^i (dash-dotted yellow line) in log-log scale at $\theta = \pi/2$. Right: radial profiles of the difference between the computation of β^ϕ in the xCFC formulation, $\beta^\phi_{\rm xCFC}$, and with our approach imposing $h = 0$, $\beta_{h=0}$, in log-log scale at $\theta = 0, \pi/4, \pi/2$. The solid and dashed vertical black lines denote the radius of the star at $\theta = \pi/2$ and $\theta = \pi/4$, respectively.

6.3.5 Numerical resolution of stationary initial data in the FCF

In this Subsection we solve all the metric variables without the restriction $h^{ij} = 0$. We obtain the numerical solution of the Equations (6.4)–(6.8) (without imposing $h^{ij} = 0$) for the variables X^i, ψ, $(N\psi^2 - 1)$ (at this point we can recover N therefore), V^i (at this point we can recover β^i therefore), and $\dot{X}^i$. Moreover, we solve the Equations (6.2) and (6.3) setting to zero the time derivatives, as we are computing a stationary spacetime. On one hand, from the Equation (6.3), we get an elliptic equation for h^{ij}:

$$\begin{aligned}\tilde{\gamma}^{kl}\mathcal{D}_k\mathcal{D}_l h^{ij} \quad &= \left(\frac{N\psi^2}{2}\right)^{-1}\Big(\beta^k\mathcal{D}_k\hat{A}^{ij} - \hat{A}^{kj}\mathcal{D}_k\beta^i - \hat{A}^{ik}\mathcal{D}_k\beta^j + \frac{5}{3}\hat{A}^{ij}\mathcal{D}_k\beta^k \\ &+2N\psi^{-6}\tilde{\gamma}_{kl}\hat{A}^{ik}\hat{A}^{jl} + \frac{3}{4}N\psi^{-6}\tilde{\gamma}^{ij}\tilde{\gamma}_{lk}\tilde{\gamma}_{nm}\hat{A}^{km}\hat{A}^{ln} \\ &+N\psi^2\tilde{R}^{ij}_* - \frac{1}{4}N\psi^2\tilde{R}\tilde{\gamma}^{ij} + \frac{1}{2}(\tilde{\gamma}^{kl}\mathcal{D}_k h^{ij} - \tilde{\gamma}^{ik}\mathcal{D}_k h^{lj} - \tilde{\gamma}^{kj}\mathcal{D}_k h^{il})\mathcal{D}_l(N\psi^2) \\ &+4\psi^{-1}\tilde{\gamma}^{ik}\tilde{\gamma}^{jl}\mathcal{D}_k\psi\mathcal{D}_l(N\psi^2) + 4\psi^{-1}\tilde{\gamma}^{ik}\tilde{\gamma}^{jl}\mathcal{D}_l\psi\mathcal{D}_k(N\psi^2) - 2\psi^{-1}\tilde{\gamma}^{ij}\tilde{\gamma}^{kl}\mathcal{D}_k\psi\mathcal{D}_l(N\psi^2) \\ &-8N\tilde{\gamma}^{ik}\tilde{\gamma}^{jl}\mathcal{D}_l\psi\mathcal{D}_k\psi + 2N\tilde{\gamma}^{ij}\tilde{\gamma}^{kl}\mathcal{D}_k\psi\mathcal{D}_l\psi - \tilde{\gamma}^{ik}\tilde{\gamma}^{jl}\mathcal{D}_k\mathcal{D}_l(N\psi^2) - (L\dot{X})^{ij} \\ &-8\pi N\psi^{10}S^{ij} + 4\pi NS^*\tilde{\gamma}^{ij}\Big),\end{aligned} \tag{6.26}$$

and, on the other hand, from the Equation (6.2), an algebraic equation for $\hat{A}^{ij}_{TT}$:

$$\begin{aligned}\hat{A}^{ij}_{TT} \quad &= -(2N\psi^{-6})^{-1}\left(\beta^k\mathcal{D}_k h^{ij} - h^{ik}\mathcal{D}_k\beta^j - h^{kj}\mathcal{D}_k\beta^i + \frac{2}{3}h^{ij}\mathcal{D}_k\beta^k + (LV)^{ij}\right. \\ &\left.-X^j\mathcal{D}^i(2N\psi^{-6}) - X^i\mathcal{D}^j(2N\psi^{-6}) + \frac{2}{3}f^{ij}X^k\mathcal{D}_k(2N\psi^{-6})\right).\end{aligned} \tag{6.27}$$

The term $(L\dot{X})^{ij}$ in (6.26) can be neglected since we are computing stationary initial data. We can also check the accuracy of our approach by including this vector field, solving it via its elliptic equation and monitoring the values of this quantity. We will discuss the results of both options at the end of this subsection. The Equation (6.2) already had source terms with consistent post-Newtonian order, so the Equation (6.27) too. Moreover, setting the term $\partial_t\hat{A}^{ij}_{TT}$ to zero in the Equation (6.3) makes the elliptic equation (6.26) to also have a consistent post-Newtonian truncation in the source terms for the computation of the h^{ij} tensor.

We overview here the iterative strategy used to solve all the equations in order to get the stationary spacetime metric initial data, based on the hierarchical structure of the equations already commented in Table 6.1:

1. Solve the Equations (6.4)–(6.8) for X^i, ψ, $(N\psi^2 - 1)$ (N can be therefore also computed), V^i (β^i can be therefore computed), and $\dot{X}^i$, imposing $h^{ij} = 0$.

2. Solve the elliptic equation (6.26) for h^{ij} with values computed in the previous step.

3. Compute $\hat{A}^{ij}_{TT}$ from the Equation (6.27).

4. Solve the Equation (6.4) for X^i, now considering the previous obtained values (in general, $h^{ij} \neq 0$).

5. Compute $\hat{A}^{ij}$ from the Equation (4.115) (in general, $h^{ij} \neq 0 \neq \hat{A}^{ij}_{TT}$).

6. Solve the Equations (6.5)–(6.8) for ψ, $(N\psi^2 - 1)$ (N can be therefore also computed), V^i (β^i can be therefore computed), and $\dot{X}^i$ (in general, $h^{ij} \neq 0$).

7. Go to step 2, until a desired level of tolerance is achieved.

After only 5 iterations with the previous strategy, we observe that the absolute values of the differences of the variables in successive iterations are smaller than 1%.

We obtain similar profiles for all variables with respect to the results shown in the previous subsection. A detailed analysis of the expected difference between the values of the variables when $h^{ij} = 0$ (xCFC) or $h^{ij} \neq 0$ (FCF) are considered can be found in the appendix of [31]. There it is established that those differences are expected to be of the order of h^{ij}. We can check this fact numerically in the Figure 6.8 , where we display the differences of N, ψ and β^i when the cases $h^{ij} \neq 0$ and $h^{ij} = 0$ are considered. We notice that these differences are several orders of magnitude smaller than the corresponding variables, and also smaller than the profiles of the non-zero components of h^{ij} (when $h^{ij} \neq 0$ is considered) shown in the Figures 6.9-6.12.

We get similar profiles for $\dot{X}^i$ in comparison with those computed in the previous Subsection considering $h^{ij} = 0$. Results for $\dot{X}^i$ are displayed in the Figure 6.13. Fourth-order interpolation near $r = 0$ for some second derivatives in the source of the Equation (6.8) was required to avoid

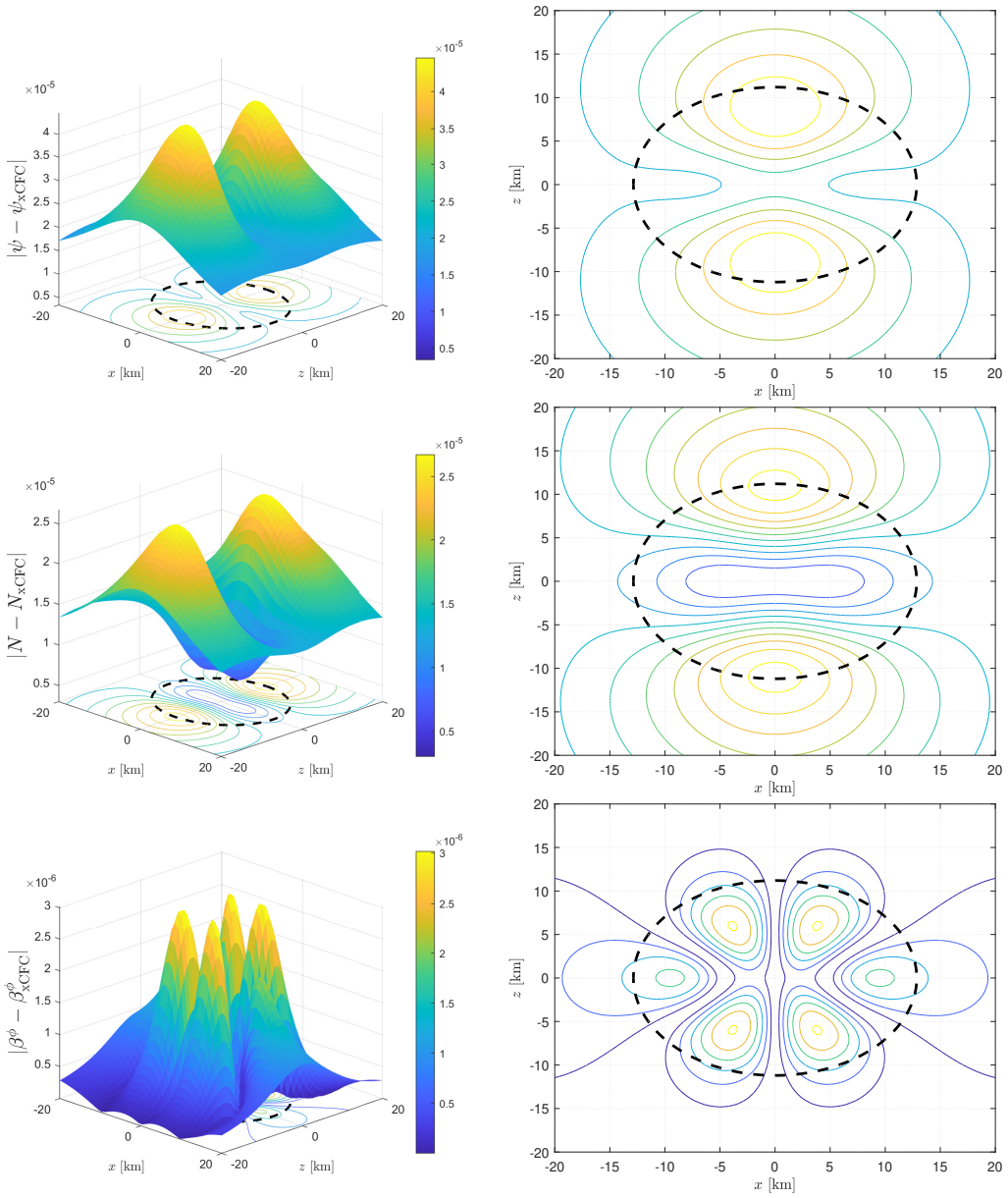

Figure 6.8: Comparison of the conformal factor ψ (top), lapse N (middle) and angular component of the shift β^{ϕ} (bottom) between the corresponding variable obtained using the xCFC and the FCF formulations. A contour plot is also displayed (right). The location of surface of the star is denoted with dashed black lines. The rotation axis is placed at $\theta = 0$.

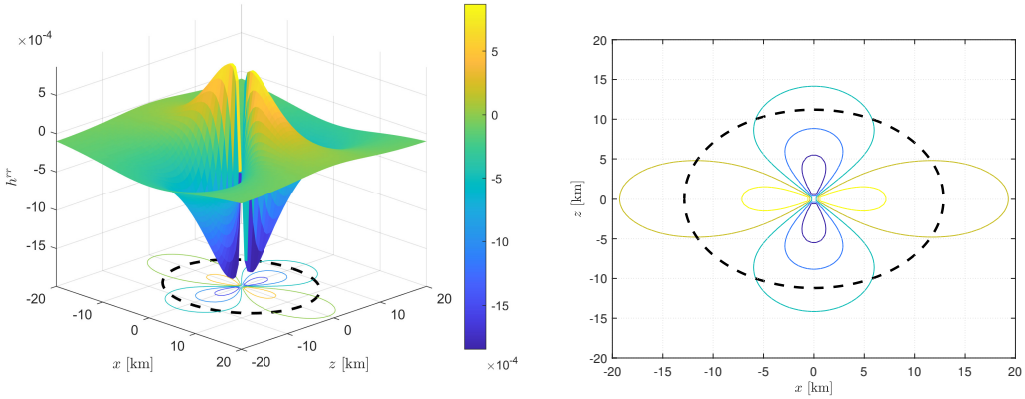

Figure 6.9: Profile (left) of h^{rr} in the meridional plane. A contour plot is also displayed (right). The location of surface of the star is denoted with a dashed black line. The rotation axis is placed at $\theta = 0$.

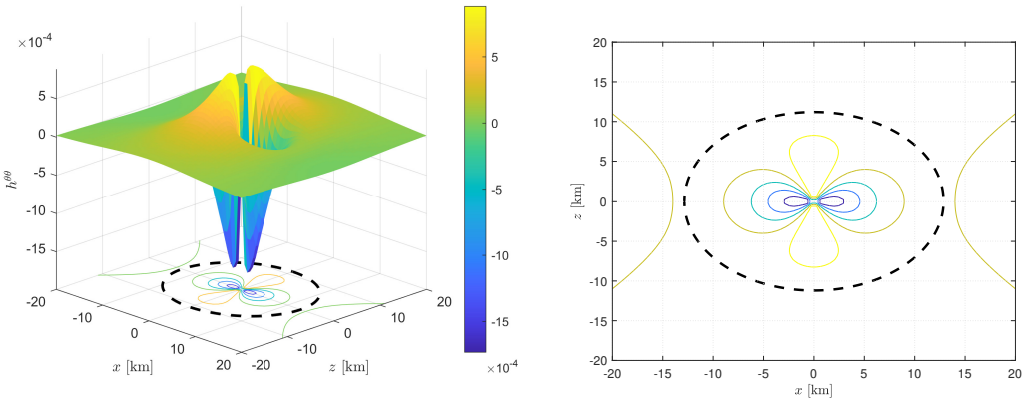

Figure 6.10: Profile (left) of $h^{\theta\theta}$ in the meridional plane. A contour plot is also displayed (right). The location of surface of the star is denoted with a dashed black line. The rotation axis is placed at $\theta = 0$.

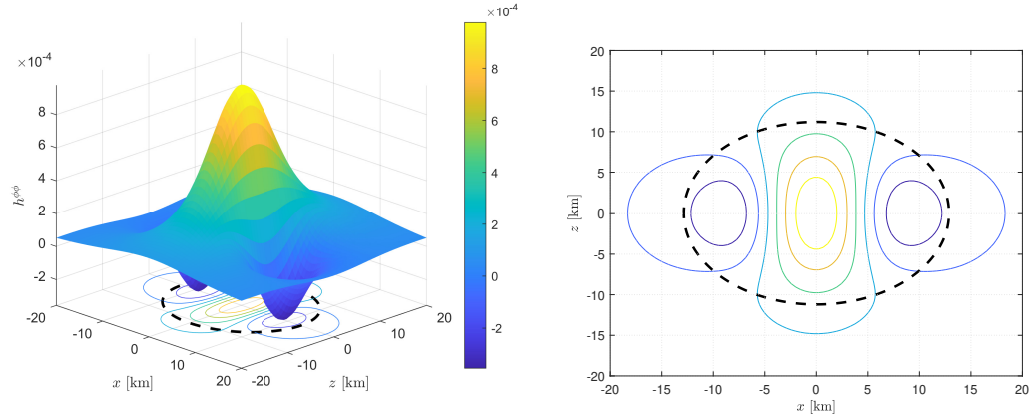

Figure 6.11: Profile (left) of $h^{\phi\phi}$ in the meridional plane. A contour plot is also displayed (right). The location of surface of the star is denoted with a dashed black line. The rotation axis is placed at $\theta = 0$.

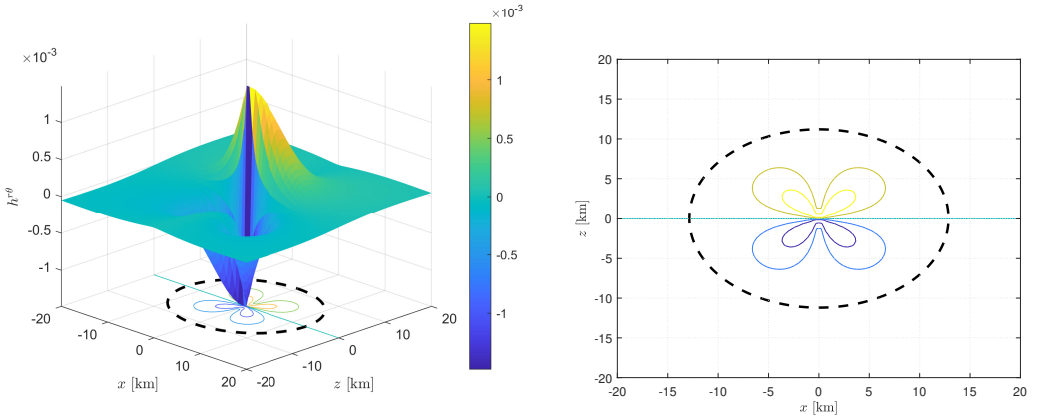

Figure 6.12: Profile (left) of $h^{r\theta}$ in the meridional plane. A contour plot is also displayed (right). The location of surface of the star is denoted with a dashed black line. The rotation axis is placed at $\theta = 0$.

some numerical divergences at the center $r = 0$ (possibly due to the appearance of some numerical errors and their amplification due to the use of orthonormal spherical components). It is interesting to observe that, on one hand, if we neglect the vector $\dot{X}^i$ in general (and in particular the term involving this vector in the Equation (6.26)), we do not need anymore to apply the previously mentioned interpolation and we obtain profiles of h^{ij} which are closer to the reference solution obtained with LORENE [2] close to the center $r = 0$. Remind that LORENE considers $\dot{X}^i = 0$ to compute the initial data. On the other hand, we get profiles closer to the ones from the reference solution from LORENE when $\dot{X}^i$ is included in the whole numerical domain except in the region close to the center. This means that interpolations to avoid the numerical divergences are also introducing a source of error close to $r = 0$. This behaviour can be observed in the Figure 6.14, which will be further commented in the next subsection.

Finally, in the Figure 6.15 we show the profiles for $\hat{A}^{ij}_{TT}$. We check that the components of $\hat{A}^{ij}_{TT}$ are at least two orders of magnitude smaller than the corresponding $\hat{A}^{ij}$ components, in agreement with their expected post-Newtonian orders.

Convergence

We will compare with more detail our results with those computed with LORENE using several resolutions and placing the outer boundary at different radii. LORENE uses spectral methods and an exponential convergence with increasing resolution for smooth variables is expected. In our case, we use finite differences of second-order, so our convergence with increasing resolution is expected to be slower. Then, we use LORENE solutions as reference for testing the convergence and reliability of our approach. We compute the relative error between our numerical solution f and the one derived with LORENE f_L,

$$\varepsilon_r(f) = \frac{||f - f_L||_2}{||f_L||_2},$$

both with the same spatial resolution and numerical domain. We use the discrete 2-norm,

$$||f||_2 = \left(\frac{(\sum_{i=1,j=1}^{i=n_r,j=n_\theta} f(r_i,\theta_j)^2}{n_r n_\theta} \right)^{1/2}.$$

We set a decay of the form r^{-n} at the outer boundary and expect better results as the outer boundary is placed further from the neutron star.

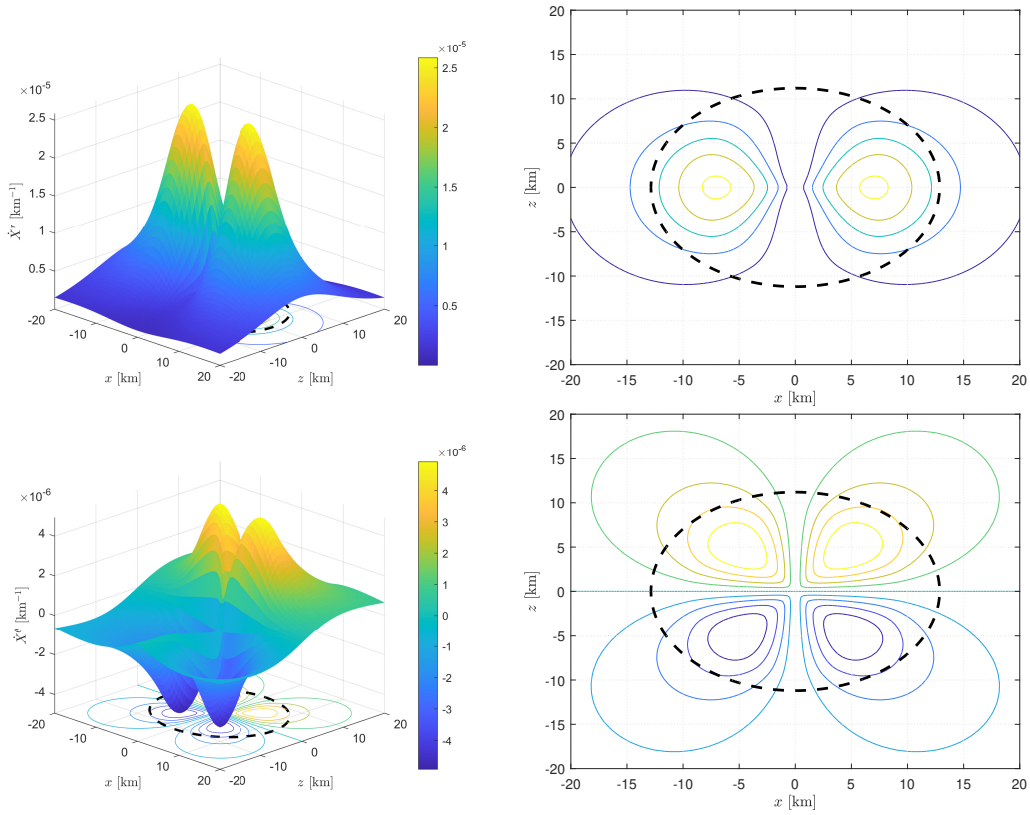

Figure 6.13: Profiles (left) of $\dot{X}^r$ (top) and $\dot{X}^\theta$ (bottom) in the meridional plane. A contour plot is also displayed (right). The location of surface of the star is denoted with dashed black lines. The rotation axis is placed at $\theta = 0$.

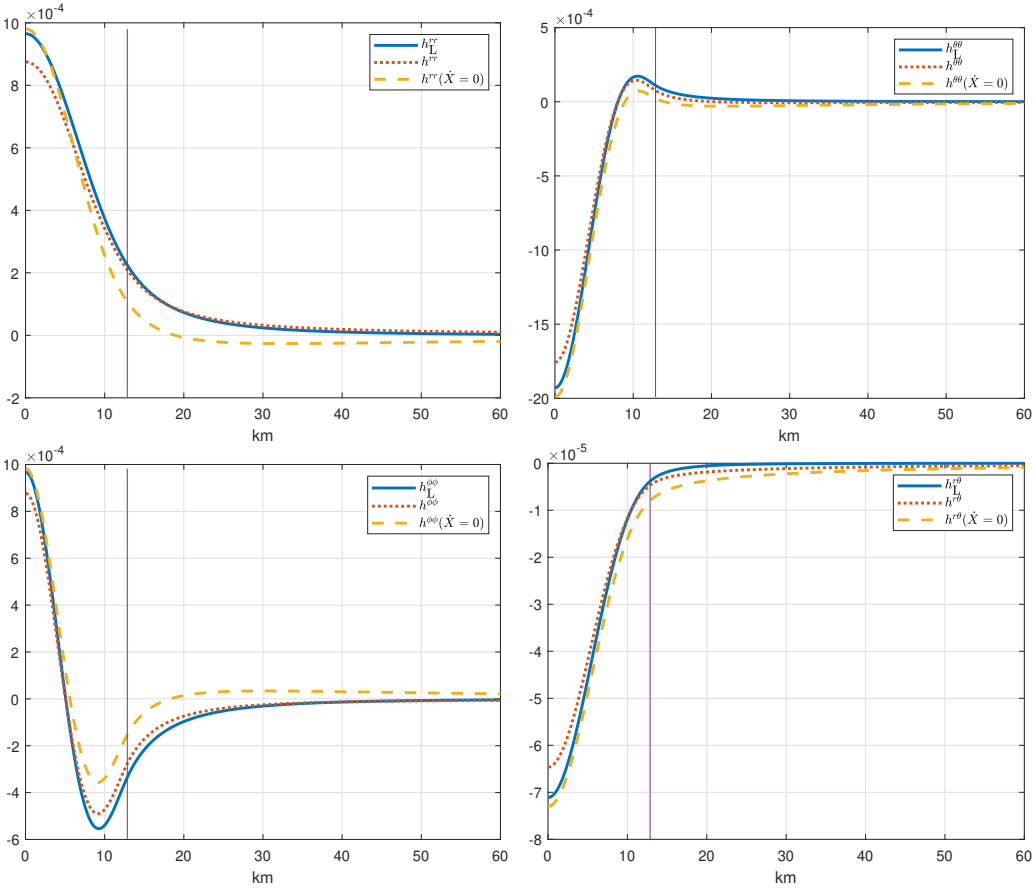

Figure 6.14: Radial profiles of the numerical solution for h^{rr} (top left), $h^{\theta\theta}$ (top right), $h^{\phi\phi}$ (bottom left) and $h^{r\theta}$ (bottom right), imposing $\dot{X}^i = 0$ (dashed yellow lines) and solving the $\dot{X}^i$ vector field (red dotted lines). The reference solution computed with LORENE is also displayed (solid blue lines). $\Delta r = 96$ m.

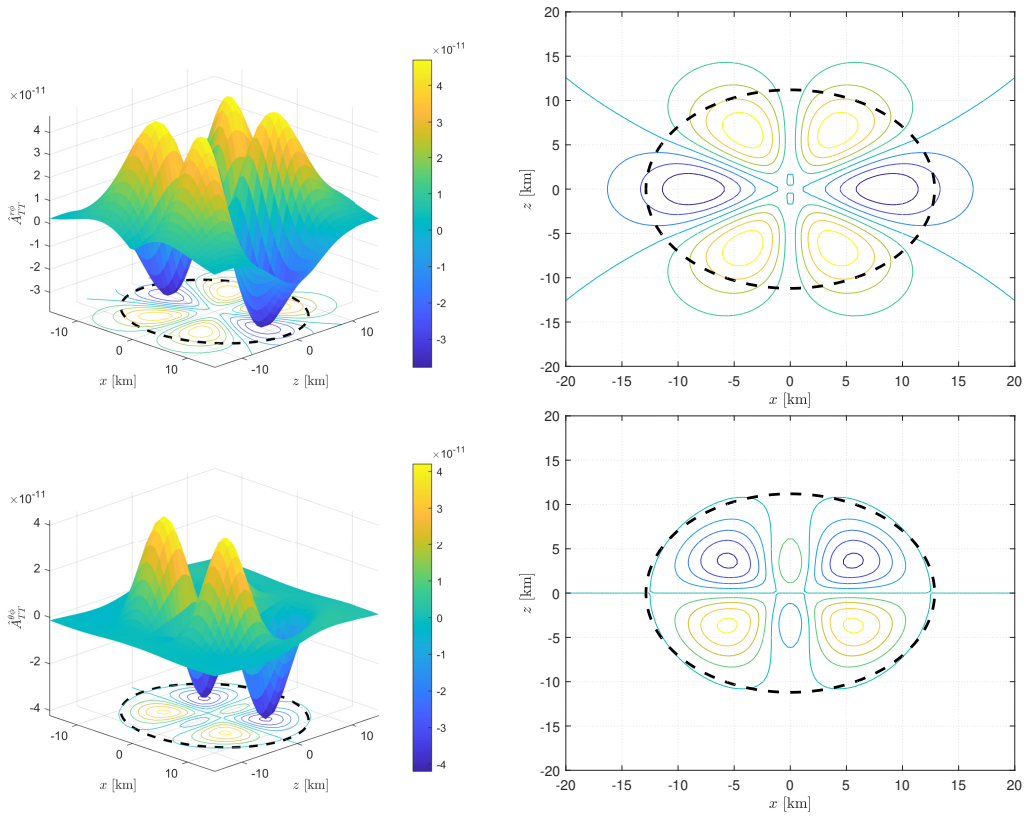

Figure 6.15: Profiles (left) of $\hat{A}^{r\phi}_{TT}$ (top) and $\hat{A}^{\theta\phi}_{TT}$ (bottom) in the meridional plane. A contour plot is also displayed (right). The location of surface of the star is denoted with dashed black lines. The rotation axis is placed at $\theta = 0$.

We will focus on the h^{ij} tensor in this subsection, since the rest of the variables are not computed with LORENE (these variables were just introduced in this work) or we see no significant difference when increasing the resolution or changing the location of the outer boundary. The latter point may be due to other more dominant sources of numerical errors.

We perform some simulations to establish the proper location of the outer boundary. In the Figure 6.16 we show results for the relative errors of all the non-zero components of h^{ij}, including or not the computation of $\dot{X}^i$, respectively, with a fixed spatial resolution of $\Delta r = 386$ m and varying the location of the outer boundary. The error stabilizes once the outer boundary is placed at 3 times the equatorial radius of the star $R_{\rm star}$, or further away. If we are interested in dynamical spacetimes with potential gravitational radiation, the location of the outer boundary should be placed around 100 times the equatorial star radius, according to [27]. From the Figure 6.16, we can quantify the consequences of neglecting $\dot{X}^i$. The errors are considerably higher if $\dot{X}^i = 0$ is imposed. We think that improving the interpolation technique close to the center would decrease even more the relative errors when $\dot{X}$ is not neglected, although this is beyond the scope of this work.

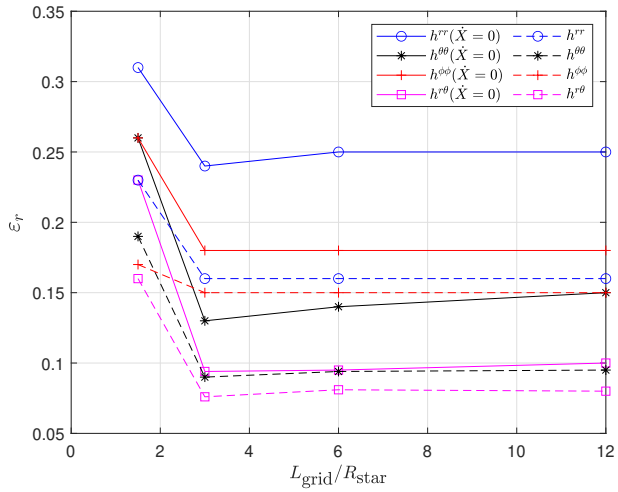

Figure 6.16: Relative errors comparing with LORENE solutions for the non-zero components of h^{ij}, when $\dot{X}^i$ is considered (solid lines) and when is set to zero (dashed lines), for several locations of the outer boundary $L_{\rm grid} = kR_{\rm star}$ with $k = 1.5, 3, 6, 12$. n_r is such that the spatial resolution is fixed to $\Delta r = 386$ m.

Concerning the location of the outer boundary, we see a similar behaviour with other tested resolutions: $\Delta r = 772$ m, 193 m, 96.4 m and 48.2

m. Since we concluded that placing the outer boundary at $r = 3R_{\rm star}$ is enough to guarantee the numerical solution not to be strongly affected by the boundary condition, we fix the outer boundary at $r = 6R_{\rm star}$. In the Figure 6.17 we display the relative errors for several spatial resolutions. All components stabilize its relative error for a spatial resolution of about $\Delta r \lesssim 100$ m.

Notice that the relative errors between the numerical solution of the variables with our approach and using LORENE, shown in the Figure 6.16, are strongly affected by the values of the variables close to the outer boundary, which are several orders of magnitude smaller than those at the center. This fact can be shown in Figures 6.14, where the non-zero components of h^{ij} are displayed.

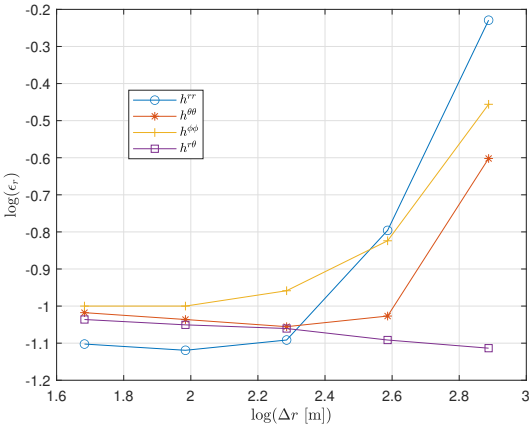

Figure 6.17: Relative errors for the non-zero components of h^{ij} for several radial spatial resolutions.

LORENE results are a very good reference solution. It uses spectral methods which have an exponential order of convergence in N, where N is the number of base functions used in the spectral decompositions. To conclude this subsection, we perform convergence studies with numerical results of our code considering different resolutions. In the Figure 6.18 we plot our numerical solution, close to the center $r = 0$, for the non-zero components of h^{ij} with different resolutions. In Table 6.3 we estimate the order of convergence p at $r = 0$ km and $r = 5$ km, with $\Delta r = 386$ m, according to the following expression

$$p \approx \log_2 \left(\frac{\varepsilon(\Delta r)}{\varepsilon(\Delta r/2)} \right), \tag{6.28}$$

where $\varepsilon(\Delta r) = |u(\Delta r) - u(\Delta r/2)|$ and $u(\Delta r)$ is the numerical value of the variable u at a fixed r when a spatial resolution Δr is used. We obtain in general an order of convergence close to the expected second-order, due to the use of second-order finite differences for the spatial derivatives. We obtain similar but slightly closer to second-order of convergence when we considered the values of the variables at $r = 5$ km, as shown in the Table 6.3.

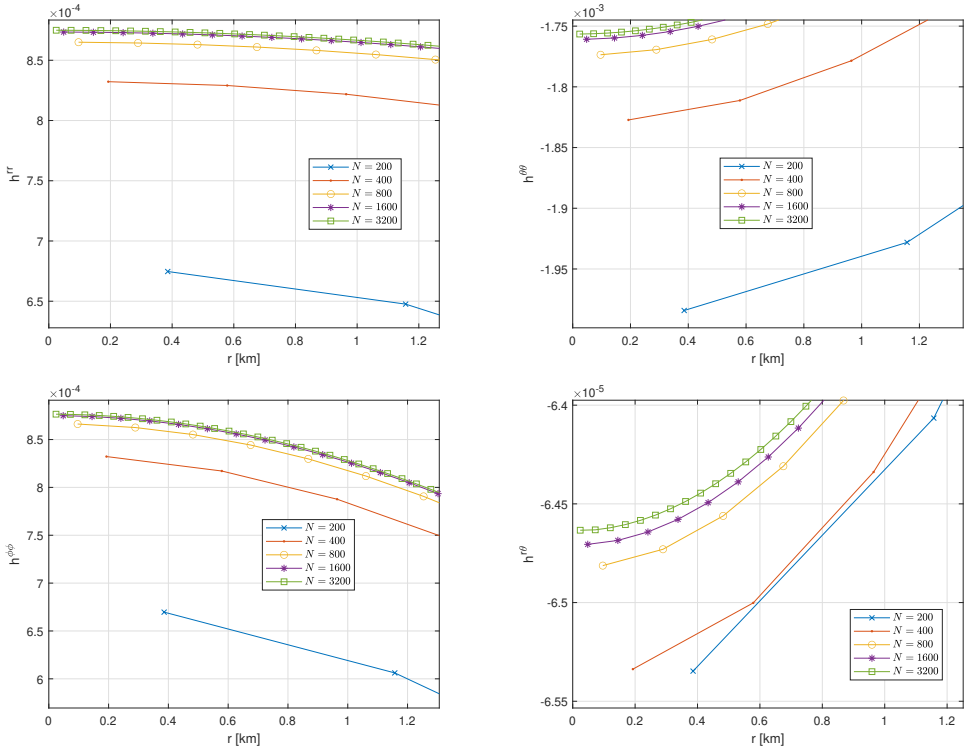

Figure 6.18: Radial profiles for $\theta = \pi/2$ of the numerical solution for h^{rr} (top left), $h^{\theta\theta}$ (top right), $h^{\phi\phi}$ (bottom left) and $h^{r\theta}$ (bottom right) for numerical resolutions $\Delta r = 12R_{\rm eq}/N$ with $N = 200, 400, 800, 1600, 3200$.

r [km]	$p(h^{rr})$	$p(h^{\theta\theta})$	$p(h^{\phi\phi})$	$p(h^{r\theta})$
0	1.9654	2.0646	1.9468	2.2798
5	1.9236	2.1470	2.0655	2.3158

Table 6.3: Estimation of the order of convergence p with the non-zero components of h^{ij} using a spatial resolution $\Delta r = 386$ m in expression (6.28) at $r = 0$ km and $r = 5$ km.

Dirac gauge and determinant condition.

Dirac gauge condition is given by

$$\mathcal{D}_i h^{ij} = 0. \tag{6.29}$$

In axisymmetry the condition $\mathcal{D}_i h^{i\phi} = 0$ is trivially fulfilled. Although we assume the Dirac gauge to be satisfied, we are going to check it numerically computing the following quantities, which we expect to be much smaller than one:

$$Q^i = \left. \frac{|\mathcal{D}_j h^{ji}|}{\max(|\mathcal{D}_r h^{ri}|, |\mathcal{D}_\theta h^{\theta i}|)} \right|_{(r,\theta)=(r_0,\pi/2)}, \quad i = r, \theta, \tag{6.30}$$

where r_0 stands for the radius at which $|\mathcal{D}_j h^{ji}|$ deviates more from zero, i.e., the violation of the Dirac gauge condition is more significant. We choose $r_0 = 7$ km.

The procedure used in LORENE to solve h^{ij} [79], satisfies the Dirac gauge condition by construction. Of course, Q^i is not going to be numerically zero, but one would expect to be tiny compared to 1. In fact, we get $Q^r_{\rm L}, Q^\theta_{\rm L} \sim 10^{-4}$, where the L subscript refers to quantities computed using LORENE data. Notice that our strategy does not impose the Dirac gauge condition directly (although it is applied when the expression in Eq. (6.29) appears explicitly). In our approach, we get $Q^r, Q^\theta \sim 10^{-2}$. In the Figure 6.19 we compare the radial profiles of the Dirac gauge condition for $i = r$ and $i = \theta$ with respect to the individual covariant derivatives involved at $\theta = \pi/2$.

On the other hand, there is another condition that our metric must fulfill, according to Eq. (4.97):

$$\det(f^{ij} + h^{ij}) = 1. \tag{6.31}$$

Reference [79] also imposes this condition in the resolution of the h^{ij} tensor, so the numerical solution derived with LORENE satisfies this algebraic constraint by construction. In our case, we compute the quantity

$$\max(|1 - \det(f^{ij} + h^{ij})|)$$

to check the violation of this algebraic constraint. We get a value of order 10^{-5}, to be compared with zero. Since some variables are solved with a tolerance of 10^{-6}, and taking into account that the absolute value of some

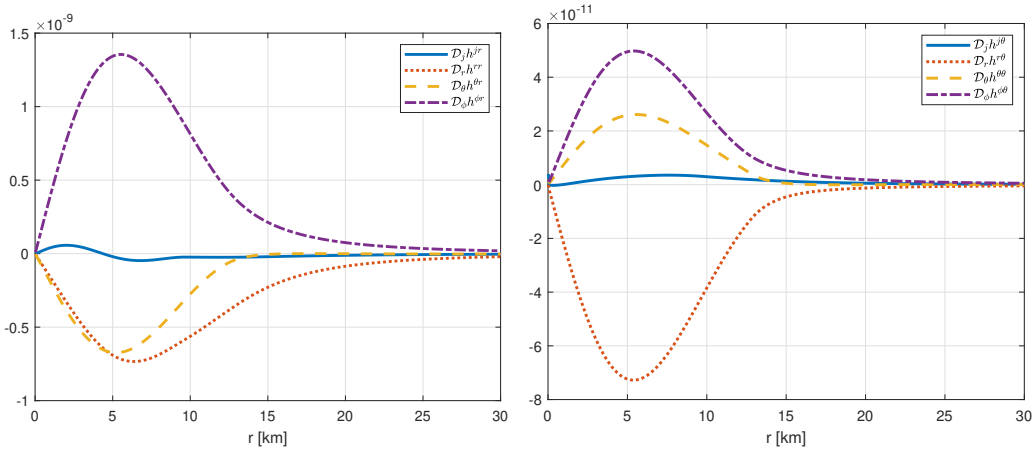

Figure 6.19: Comparison of the gauge condition $\mathcal{D}_j h^{ji}$ (solid blue line) with the covariant derivatives involved $\mathcal{D}_r h^{ri}$ (pointed red line), $\mathcal{D}_\theta h^{\theta i}$ (dashed yellow line) and $\mathcal{D}_\phi h^{\phi i}$ (dash-pointed violet line) for $i = r$ (left) and $i = \theta$ (right).

components $|h^{ij}|$ reach values of order 10^{-3}, we think that the constraint (6.31) is reasonably satisfied.

Indeed, we think that a strategy combining the resolution of the Equation (6.26) with imposing somehow the Dirac gauge and determinant conditions of the Equations (6.29) and (6.31), respectively, is quite important. We can always remove one differential equation for some component of the h^{ij} and then apply the determinant condition to get this remaining component. The Dirac gauge in cylindrical coordinates has only two non-zero components:

$$\frac{\partial h^{\varpi\varpi}}{\partial \varpi} + \frac{1}{\varpi}(h^{\varpi\varpi} - h^{\phi\phi}) + \frac{\partial h^{\varpi z}}{\partial z} = 0, \tag{6.32}$$

$$\frac{\partial h^{\varpi z}}{\partial \varpi} + \frac{h^{\varpi z}}{\varpi} + \frac{\partial h^{zz}}{\partial z} = 0. \tag{6.33}$$

For instance, one can get first $h^{\varpi z}$ from the Equation (6.22). Then, combining the Equations (6.19) and (6.32), an elliptical equation for $h^{\varpi\varpi}$ can be derived:

$$\Delta h^{\varpi\varpi} + \frac{2}{\varpi}\frac{\partial h^{\varpi\varpi}}{\partial \varpi} = S^{\varpi\varpi} - \frac{2}{\varpi}\frac{\partial h^{\varpi z}}{\partial z}. \tag{6.34}$$

h^{zz} can be derived from the Equation (6.21). Finally, $h^{\phi\phi}$ can be deduced from the determinant condition, or the Equation (6.24) for the scalar C_1 or the Equation (6.25) for the scalar C_2, as $h^{\varpi\varpi}$ is known. In this proposal we have only used the first equation of the Dirac gauge.

Another way may be first get h^{zz} from the Equation (6.21). Then, the second Dirac gauge equation (6.33) and the Equation (6.22) provide an elliptic equation for $h^{\varpi z}$:

$$\Delta h^{\varpi z} - \frac{1}{\varpi}\frac{\partial h^{\varpi z}}{\partial \varpi} - \frac{2}{\varpi^2} h^{\varpi z} = S^{\varpi z} + \frac{1}{\varpi}\frac{\partial h^{zz}}{\partial z}. \tag{6.35}$$

Now, if we take into account the Equations (6.24) and (6.25), we get $h^{\varpi\varpi}$ and $h^{\phi\phi}$. We can also consider the Equation (6.34) to get $h^{\varpi\varpi}$, using the first Dirac gauge equation (6.32). Finally, the determinant condition can be used to get $h^{\phi\phi}$, or solve for C_1 or C_2.

A third option, for which all conditions are used, consists in the following steps: solve h^{zz} with the Equation (6.21); solve $h^{\varpi z}$ with the Equation (6.35); solve $h^{\varpi\varpi}$ with the Equation (6.34); and, finally, get $h^{\phi\phi}$ with the Equation (6.31).

These options are beyond the scope of this work, but further investigation is on our future plans.

6.4 Final remarks

In this Chapter we have presented a reformulation of the FCF, including modifications both in the elliptic and the hyperbolic sectors, by introducing two new variables, V^i and $\dot{X}^i$. With this new reformulation, we keep the local uniqueness properties of the elliptic sector, and, moreover, the new set of the equations are presented with a hierarchical structure in terms of PNE. The addition of the new variables also simplifies the source terms of the evolution equations.

In order to numerically test this reformulation, we have computed stationary initial data of a rotating neutron star. We have discretized the spatial derivatives by means of second-order finite-differences. We have compared our results to the numerical solution using the xCFC scheme, and also to the reference solution obtained with the spectral code LORENE. We have also checked the convergence of our numerical solutions, getting the expected second-order. The solution of the reformulation of the FCF deviates from the one using xCFC as expected: the

differences of the variables in the two approaches are of the order of the h^{ij} tensor (or smaller), as it was theoretically established in [31]. Due to the simplification in some equations, some metric variables are solved with more accuracy; in particular, considering the new vector V^i allows one to compute the β^i vector more accurately.

The generalized Dirac gauge and the condition on the determinant for the conformal metric have been checked too. To our knowledge, this is the first time when the condition for the determinant has been checked in any finite-differences code for the resolution of the Einstein Equations in complex non-analytical spacetimes, either in constrained formulations or in free evolution schemes. Although the generalized Dirac gauge is reasonable satisfied (see Figure 6.19 for more details), we plan to check in the future the commented strategies to explicitly imposed these restrictions.

We plan to test the stationarity of the computed initial data for a rotating neutron star. To accomplish this, we will perform its time evolution numerically integrating the hyperbolic sector of the new reformulation. It remains for the future to check the behaviour of the new reformulation in complex and really dynamical numerical simulations, and extract the corresponding gravitational radiation of the system. Also, this new reformulation can be used to compute initial data using finite-differences beyond the xCFC condition, i.e., satisfying all the constraint equations without imposing the conformal metric to be flat. Another potential application of this work is to use a simplified version of our proposed equations in the context of cosmological simulations by considering only the leading terms of the PNE.

7

Resistive relativistic magnetohydrodynamic equations

This Chapter presents the results of the article [29], which applies the Minimally-Implicit Runge-Kutta (MIRK) method to the numerical evolution of the resistive relativistic magnetohydrodynamic (RRMHD) equations.

In the Subsection 4.1.4 we introduced the basic concepts about magnetohydrodynamics (MHD), and we will introduce now the complete system of equations to be solved, accounting for both hydrodynamic and electrodynamic sectors. We will present two simple numerical tests of the RRMHD equations with astrophysical motivations. Significant magnetic fields are present in relevant astrophysical scenarios, like accretion disks, active galactic nuclei, relativistic jets, quasars, or compact objects; see, for example, references [10, 16, 34, 47, 48, 64, 68, 86, 101, 118] for some general reviews. Ideal MHD is recovered in the limit of RRMHD when the resistivity tends to zero (see Equations (4.38) and (4.39)). If we consider numerical simulations solving the ideal MHD equations [96], effects induced by numerical errors and numerical resistivity will ap-

pear. These effects depend on the numerical method and resolutions used, and the physical resistivity is therefore not modeled consistently. A consistent treatment for the resistivity is then necessary.

Here, we follow the approach proposed by [67] of an augmented system of evolution equations to numerically deal with the constraints equations $\nabla \cdot \boldsymbol{E} = q/\varepsilon_0$ and $\nabla \cdot \boldsymbol{B} = 0$. Previous approaches rely on Implicit-Explicit (IMEX) Runge-Kutta schemes. In general, compared to explicit schemes, IMEX methods need to apply the recovery (which can be very expensive computationally) of the primitive variables from the conserved ones (see more details in next section) in numerous additional times. Moreover, the use of an iterative process for the recovery could have potential convergence problems, increased by the additional number of required loops. In addition, the computational cost of the previous IMEX approach in comparison with the standard explicit methods is much higher. The MIRK methods are able to deal with stiff terms (see the end of Subsection 4.1.4) producing stable numerical evolutions, minimize the number of recoveries needed in comparison with IMEX methods, their computational cost is similar to the standard explicit methods and can actually be easily implemented in numerical codes which previously used explicit schemes.

We set the speed of light $c = 1$, the permitivity of vacuum $\varepsilon_0 = 1$ and the permeability of vacuum $\mu_0 = 1$.

7.1 Structure of the evolution system of equations

In the case of the RRMHD equations [67], we have to deal with a hyperbolic system of evolution equations for the mass density ρ, the components of the velocity field measured by the inertial observer V^i, the internal energy density ϵ, the electric charge density q, the components of the electric field E^i and the components of the magnetic field B^i. In addition, we have two constraint equations: the divergence of the magnetic field has to vanish and the divergence of the electric field equals the electric charge density. Shock and rarefaction waves potentially develop

in the evolution of these equations, even when one starts from smooth initial data, and therefore high resolution shock capturing (HRSC) methods [6] must be used in order to properly capture these phenomena. However, in this manuscript we will consider only smooth initial data and smooth data during the evolution, and we will focus on how to deal with the resistive source terms numerically, which become stiff at high conductivities.

In [67], the evolution system of equations was augmented by the addition of two scalar fields, ϕ and ψ, and their corresponding evolution equations. By doing this, the constraint for the divergence of the magnetic field, $\nabla \cdot \boldsymbol{B} = 0$, and its evolution equation, $\partial_t \boldsymbol{B} + \nabla \times \boldsymbol{E} = 0$, were replaced by the following two equations:

$$\partial_t \phi + \nabla \cdot \boldsymbol{B} = -\kappa\, \phi, \tag{7.1}$$

$$\partial_t \boldsymbol{B} + \nabla \times \boldsymbol{E} + \nabla \phi = 0. \tag{7.2}$$

Analogously, the constraint for the divergence of the electric field, $\nabla \cdot \boldsymbol{E} = q$, and its evolution equation, $-\partial_t \boldsymbol{E} + \nabla \times \boldsymbol{B} = \boldsymbol{J}$, were replaced by the following two equations:

$$\partial_t \psi + \nabla \cdot \boldsymbol{E} = q - \kappa\, \psi, \tag{7.3}$$

$$-\partial_t \boldsymbol{E} + \nabla \times \boldsymbol{B} - \nabla \psi = \boldsymbol{J}, \tag{7.4}$$

where $\boldsymbol{J}$ takes the expression

$$\boldsymbol{J} = \Gamma q \boldsymbol{V} + \sigma \Gamma \left(\boldsymbol{E} + \boldsymbol{V} \times \boldsymbol{B} + (\boldsymbol{E} \cdot \boldsymbol{V}) \boldsymbol{V} \right),$$

where $\Gamma = (1 - V^2)^{-1/2}$ is the Lorentz factor and σ is the conductivity. In the definition of $\boldsymbol{J}$ we are assuming Ohm's law for the charge-current density (7.1). With these replacements and for positive κ, the potential constraint violations that may be generated numerically will decay exponentially and propagate at the speed of light. Moreover, after these replacements are applied, one only has to solve a system of evolution equations for the electromagnetic sector, formed by the Equations (7.1)–(7.4), together with charge conservation equation (4.30), which can be written as an evolution equation for $Q = \Gamma\, q$,

$$\partial_t Q + \nabla \cdot \boldsymbol{J} = 0. \tag{7.5}$$

The electromagnetic sector (7.1)-(7.4) and the evolution equation (7.5) have to be evolved together with the hydrodynamic equations (4.33) and (4.22), which can be written as

$$\partial_t D + \nabla \cdot (\rho\, \Gamma\, \boldsymbol{V}) = 0, \tag{7.6}$$

$$\partial_t e + \nabla \cdot (\boldsymbol{E} \times \boldsymbol{B} + \rho\, h\, \Gamma^2\, \boldsymbol{V}) = 0, \tag{7.7}$$

$$\partial_t \boldsymbol{P} + \nabla \cdot \left(-\boldsymbol{E} \otimes \boldsymbol{E} - \boldsymbol{B} \otimes \boldsymbol{B} + \rho\, h\, \Gamma^2\, \boldsymbol{V} \otimes \boldsymbol{V} + \left((E^2 + B^2)/2 + p \right) \boldsymbol{\eta} \right) = 0, \qquad (7.8)$$

where $D = \rho\,\Gamma$, $e = (E^2 + B^2)/2 + \mu$, $\boldsymbol{P} = (\boldsymbol{E} \times \boldsymbol{B}) + \rho\, h\, \Gamma^2\, \boldsymbol{V}$, h is the relativistic enthalpy per unit mass

$$h = \frac{\mu + p}{\rho},$$

p is the pressure and $\boldsymbol{\eta}$ is the Minkowski spacetime metric tensor. $\mu = \rho + \epsilon$ is the total energy density. All the evolution equations can be written as a hyperbolic balance law.

In [67] the same variable κ was introduced in the replacement of both constraint equations, (7.1) and (7.3). However, for the case of the general relativistic force-free electrodynamics, [82] found it more convenient to choose different values for κ in each of the constraint equations, and the optimal values were actually very different (by approximately 3 orders of magnitude). In this manuscript we will follow the approach considered in [67], since our numerical experiments do not require different values for κ.

At this point, it is important to clarify the process of the recovery of the variables. On one hand, the set of physical variables,

$$\{\phi, B^i, \psi, E^i, Q, \rho, \epsilon, V^i\},$$

are called the primitive variables. On the other hand, the set of evolved variables,

$$\{\phi, B^i, \psi, E^i, Q, D, P^i, e\},$$

are called the conserved variables. The determinant of the matrix of change of variables is always different from zero, so a bijective relation between the primitive and conserved variables is always locally guaranteed to exist. Notice that the subset $\{\psi, E^i, \phi, B^i, Q\}$, associated to the Maxwell equations, has elements which are both part of the primitive and the conserved variables. In one direction, the conserved variables can be obtained directly from the primitive ones from their definitions. In the other direction, this process is known as the recovery, and it can be quite difficult to obtain the explicit values of the primitive variables from the conserved ones in a general scenario. Although the set of quantities that we do evolve in time are the conserved variables, we are interested in the explicit values of the primitive and physical ones, and these values are also needed in order to compute the pressure p appearing in the source terms.

Moreover, it is important to highlight that the conductivity σ can be potentially large, so the source term of the evolution equation for the electric field, and therefore the whole system of equations, can be potentially stiff. The ideal regime is defined by the limit $\sigma \to \infty$, and in this case $E^i = -(\boldsymbol{V} \times \boldsymbol{B})^i$. If not taken into account in the numerical resolution, the stiffness of the source term for $\sigma \gg 1$ can lead to the development of numerical instabilities. We can write whole system of evolution equations as follows:

$$\partial_t E^j = S_E^j - \sigma\,\Gamma\left(E^j + (\boldsymbol{V}\times\boldsymbol{B})^j - (V_l E^l)V^j\right) = \tilde{S}_E^j, \tag{7.9}$$

$$\partial_t B^j = S_B^j, \tag{7.10}$$

$$\partial_t Y = S_Y, \tag{7.11}$$

where Y denotes the rest of the evolved variables, $Y = \{\phi, \psi, Q, D, e, P^i\}$. The factor multiplying $\sigma\,\Gamma$ in (7.9) is the one called stiff term. We will not include the set of variables Y in the implicit terms, and this is the reason for considering this structure for the evolution equations. It is remarkable that in relativistic fluids the conductivity σ always appears multiplied by the Lorentz factor Γ, so one could define an effective relativistic conductivity, $\bar{\sigma} = \sigma\,\Gamma$.

7.2 Minimally implicit Runge Kutta method

7.2.1 Previous numerical approaches

As mentioned in the previous section, the presence of stiff source terms requires a specific approach. One option is to implement an implicit treatment of the source term, or part of it. A hyperbolic equation with a relaxation term can be written as follows:

$$\partial_t U = F(U) + \frac{1}{\epsilon} R(U). \tag{7.12}$$

Here, $R(U)$ does not have derivatives with respect to the evolved variable U, and we have stiff source term in case $\epsilon \ll 1$.

In order to numerically solve the RRMHD evolution system of equations presented in the previous section, and taking into account the structure of a hyperbolic equation with a relaxation and stiff source term, some numerical methods have been used in the literature. For example, in [67] the Strang-splitting method was applied. Also, the authors of reference [96] used IMEX Runge-Kutta methods (we refer to this reference for more details about the application of these methods). With this technique, these authors were able to successfully perform several simulations: the evolution of Alfven waves, where high values for the waves amplitude and the conductivity were considered, and the results for the ideal case were properly recovered; the evolution of a self-similar current sheet; the evolution of shock tubes, where a broad range of different values for the conductivity was considered; or the evolution of a neutron star with magnetic field. In their approach, the implicit operator is also applied to the whole source term which contains the conductivity factor; in particular, this source term also contains the Lorentz factor and it is important to notice that it is defined in terms of primitive variables (specifically, in terms of the components of the velocity field), and therefore requires additional recoveries and iterative loops. This implies that the application of IMEX methods is very expensive computationally, and the nested iterative loops for the additional recoveries of primitive variables do not have any guarantee of convergence. This motivates us to design an alternative approach, which is described in the next subsection.

The authors of [37] use local space-time discontinuous Galerkin methods to deal with the stiffness of the source terms of the same RRMHD equations (again, we refer to this reference for more details), in the context of unstructured meshes in multiple space dimensions with an unified framework of one-step finite volume and discontinuous Galerkin schemes. A locally implicit scheme, explicit for the fluxes and implicit (but not minimally implicit as the approach of next subsection) for the source, was used. These authors were able to successfully perform several simulations (some of them similar to the ones presented in [96]): the evolution of Alfven waves, where high values for the waves amplitude and the conductivity were again considered, and the results for the ideal case were properly recovered; the evolution of a self-similar current sheet; the evolution of shock tubes, with different values for the conductivity; the resistive relativistic version of the MHD rotor problem; the cylindrical explosion problem; or the resistive relativistic analogous of the Orszag-Tang vortex problem.

It would be very interesting to compare these results, which include

non-smooth data, with the ones obtained by using a minimally implicit (our new proposal) implementation for the source terms, but this is beyond the scope of this manuscript.

7.2.2 Alternative approach

Let us describe the general idea of the MIRK method before applying it to the RRMHD equations. Consider a hyperbolic system of equations with a stiff source term where a parameter can be potentially very large (like the conductivity in the case of RRMHD equations) of the form

$$\partial_t U + \partial_i F^i(U) = S(U), \tag{7.13}$$

where U is the vector of conserved variables, F^i are the fluxes and the source term $S(U)$ can be written as

$$S(U) = S_E(U) + \sigma S_I(U). \tag{7.14}$$

Here S_E are explicitly evolved source terms, while S_I is evolved by using MIRK-like methods and can be written as

$$S_I^i(U) = H^i + \sum_{j=1}^{n} G_j^i(U)\, U^j, \tag{7.15}$$

where H^i do not depend on the conserved variables. In the previous expression G_j^i can depend on the conserved variables U and are always evaluated explicitly; only the components of the vector of conserved variables, U^i, multiplying the terms G_j^i, are implicitly evaluated. This means that the inversion of the operators can be done analytically and in a very simple way. Moreover, the coefficients appearing when allowing evaluations in different stages of a single time-step (see next sections) should be derived from stability conditions, and the stiff limit can provide key information to select the correct values for these coefficients.

Identifying if the hyperbolic system of equations for a particular case admits such a decomposition is an art; when this is achieved, one has performed a sort of linearization of the system, quite standard in some physical scenarios. Then, one can study if the application of the MIRK method provides stable numerical evolutions.

7.3 MIRK method for RRMHD equations

In the structure introduced in the Equations (7.9)-(7.11), the terms S_Y, S_B^j and S_E^j are evolved explicitly, and we only consider implicit evaluations of the electric and magnetic components, E^j, B^j, appearing in the source term for the evolution of the electric field multiplied by the conductivity σ (i.e., terms E^j and B^j in the source of the Equation (7.9)).

7.3.1 First-order MIRK method

The general proposal in the case of a first-order method can be written as:

$$\begin{aligned} E^j|_{n+1} &= E^j|_n + \Delta t\, S_E^j|_n - \Delta t\, \bar{\sigma}|_n \big(c_1 E^j|_n + (1-c_1)E^j|_{n+1} + c_2(\boldsymbol{V}\times\boldsymbol{B})^j|_n \\ &\quad +(1-c_2)(\boldsymbol{V}|_n \times \boldsymbol{B}|_{n+1})^j - c_3 V^j|_n V_l|_n E^l|_n \\ &\quad -(1-c_3)V^j|_n V_l|_n E^l|_{n+1}\big), \qquad (7.16)\\ B^j|_{n+1} &= B^j|_n + \Delta t\, S_B^j|_n, \qquad (7.17)\\ Y|_{n+1} &= Y|_n + \Delta t\, S_Y|_n, \qquad (7.18) \end{aligned}$$

where c_i are constant coefficients to be determined. We can isolate E^i_{n+1} in the Equation (7.16) having

$$\begin{aligned} E^i|_{n+1} =& M^i_j \Big\{ \Delta t S_E^j|_n + E^l|_n\big(\delta^j{}_l - \Delta t\bar{\sigma}c_1\delta^j{}_l + \Delta t\bar{\sigma}c_3(V^jV_l)|_n\big) \\ & -\Delta t\bar{\sigma}\Big(c_2(\boldsymbol{V}\times\boldsymbol{B})^j|_n + (1-c_2)\big(\boldsymbol{V}|_n\times\boldsymbol{B}|_{n+1}\big)^j\Big)\Big\}, \end{aligned} \qquad (7.19)$$

where

$$M^i_j = \frac{\Big(1+\Delta t\bar{\sigma}\big(1-c_1-V^2|_n(1-c_3)\big)\Big)\delta^i{}_j + \Delta t\bar{\sigma}(1-c_3)(V^iV_j)|_n}{\big(1+\Delta t\bar{\sigma}(1-c_1)\big)\Big(1+\Delta t\bar{\sigma}\big(1-c_1-V^2|_n(1-c_3)\big)\Big)}. \qquad (7.20)$$

Since we want finite values for the computed quantities for very high values of the effective conductivity (i.e., $\bar{\sigma}\gg 1$), we will request

$$\big(1-c_1-V^2|_n(1-c_3)\big) \neq 0 \neq (1-c_1).$$

Taking into account the wave-like behavior of the magnetic and electric fields, we use a first-order Partially Implicit Runge-Kutta (PIRK) method [30, 26], which sets $c_2 = 0$.

We perform a linear stability analysis of the evolution system in the case of infinite conductivity. We can choose $c_3 = 1$ keeping numerical stability of the numerically evolved system, slightly simplifying the proposed method. Moreover, in the ideal limit $\sigma \to \infty$, the electric field E^i is no longer an independent quantity, since $E^i = (\boldsymbol{V} \times \boldsymbol{B})^i$; this means that, independently of the velocity field V^i, we should have a zero eigenvalue of multiplicity at least 3 and we need to impose $c_1 = 0$. With these choices, the other eigenvalue of the system is bounded by 1 in absolute value, independently of the velocity field V^i value considered. In addition,

$$\big(1 - c_1 + V^2|_n(c_3 - 1)\big) = (1 - c_1) = 1 \neq 0,$$

as requested previously, and the ideal limit is recovered for $\Delta t \to 0$.

The numerical integration of the evolution equation for E^i can then be written as:

$$E^i|_{n+1} = E^i|_n + \frac{\Delta t}{1 + \Delta t\, \bar{\sigma}|_n}\big(S^i_E|_n + \bar{\sigma}|_n\, E^l|_n (V^i|_n V_l|_n - \delta^i_l) - \bar{\sigma}|_n (\boldsymbol{V}|_n \times \boldsymbol{B}|_{n+1})^i\big). \quad (7.21)$$

This scheme can be viewed as an explicit scheme for the evolution of the electric field when an effective time-step is considered:

$$\frac{\Delta t}{1 + \Delta t\, \bar{\sigma}|_n}.$$

This effective time step is of the order of Δt, for sufficiently small values of this quantity. In some sense, we are implementing a numerical first-order explicit method for the modified evolution equation

$$\partial_t E^j = \frac{1}{1 + \Delta t\, \bar{\sigma}|_n} \tilde{S}^j_E,$$

where the modification is of order Δt and thus we recover the original evolution equation for the electric field in the limit $\Delta t \to 0$. Adapting explicit schemes to this method is direct.

7.3.2 Second-order MIRK method

The general proposal for a second-order two-stages method can be written as:

$$\begin{aligned} E^j|_{(1)} &= E^j|_n + \Delta t\, S_E^j|_n - \Delta t\, \bar{\sigma}|_n \big(c_1 E^j|_n + (1-c_1)E^j|_{(1)} + c_2(\boldsymbol{V}\times\boldsymbol{B})^j|_n \\ &\quad +(1-c_2)(\boldsymbol{V}|_n \times \boldsymbol{B}|_{(1)})^j - c_3 V^j|_n V_l|_n E^l|_n \\ &\quad -(1-c_3)V^j|_n V_l|_n E^l|_{(1)}\big), \qquad (7.22)\\ B^j|_{(1)} &= B^j|_n + \Delta t\, S_B^j|_n, \qquad (7.23)\\ Y|_{(1)} &= Y|_n + \Delta t\, S_Y|_n. \qquad (7.24) \end{aligned}$$

$$\begin{aligned} E^j|_{n+1} &= \frac{1}{2}\big(E^j|_n + E^j|_{(1)} + \Delta t\, S_E^j|_{(1)}\big) - \Delta t\, \bar{\sigma}|_{(1)} \left\{ \frac{(1-c_1)}{2} E^j|_n + c_4 E^j|_{(1)} \right. \\ &\quad + \left(\frac{c_1}{2} - c_4\right) E^j|_{n+1} + \frac{1-c_2}{2}(\boldsymbol{V}|_{(1)} \times \boldsymbol{B}|_n)^j + c_5(\boldsymbol{V}\times\boldsymbol{B})^j|_{(1)} \\ &\quad + \left(\frac{c_2}{2} - c_5\right)(\boldsymbol{V}|_{(1)} \times \boldsymbol{B}|_{n+1})^j \\ &\quad \left. + V^j|_{(1)} V_l|_{(1)} \left(\frac{(1-c_3)}{2} E^l|_n + c_6 E^l|_{(1)} + \left(\frac{c_3}{2} - c_6\right) E^l|_{n+1} \right) \right\}, \qquad (7.25)\\ B^j|_{n+1} &= \frac{1}{2}\big(B^j|_n + B^j|_{(1)} + \Delta t\, S_B^j|_{(1)}\big), \qquad (7.26)\\ Y|_{n+1} &= \frac{1}{2}\big(Y|_n + Y|_{(1)} + \Delta t\, S_Y|_{(1)}\big). \qquad (7.27) \end{aligned}$$

$E^i|_{(1)}$ can be isolated from (7.22) getting an expression similar to (7.19) and, from (7.25), $E^i|_{n+1}$ can be expressed as

$$\begin{aligned} E^i|_{n+1} =& N^i_{\ j} \left\{ \frac{\Delta t}{2} S_E^j|_{(1)} + \frac{E^l|_n}{2} \left(\delta^j{}_l - \Delta t\bar{\sigma}(1-c_1)\delta^j{}_l + \Delta t\bar{\sigma}(1-c_3)V^j|_{(1)} V_l|_{(1)} \right) \right. \\ &+ E^l|_{(1)} \left(\delta^j{}_l/2 - \Delta t\bar{\sigma} c_4 \delta^j{}_l + \Delta t\bar{\sigma} c_6 V^j|_{(1)} V_l|_{(1)} \right) \\ &- \Delta t\bar{\sigma} \left(\frac{1-c_2}{2} \left(\boldsymbol{V}|_{(1)} \times \boldsymbol{B}|_n\right)^j + c_5(\boldsymbol{V}\times\boldsymbol{B})^j|_{(1)} \right. \\ &\left. \left. + \left(\frac{c_2}{2} - c_5\right) \left(\boldsymbol{V}|_{(1)} \times \boldsymbol{B}|_{n+1}\right)^j \right) \right\}, \end{aligned} \qquad (7.28)$$

where

$$N^i_{\ j} = \frac{\Big(1 + \Delta t\bar{\sigma}\big(c_1/2 - c_4 - V^2|_{(1)}(c_3/2 - c_6)\big)\Big)\delta^i_{\ j} + \Delta t\bar{\sigma}(c_3/2 - c_6)(V^iV_j)|_{(1)}}{\big(1 + \Delta t\bar{\sigma}(c_1/2 - c_4)\big)\Big(1 + \big(c_1/2 - c_4 - V^2|_{(1)}(c_3/2 - c_6)\big)\Big)}. \tag{7.29}$$

Since we want finite values for the computed quantities for very high values of the effective conductivity (i.e., $\bar{\sigma} \gg 1$), we will request

$$\big(1 - c_1 - V^2|_n(1 - c_3)\big) \neq 0 \neq (1 - c_1),$$
$$\big(c_1/2 - c_4 - V^2|_{(1)}(c_3/2 - c_6)\big) \neq 0 \neq (c_1/2 - c_4).$$

Using a second-order PIRK method for the wave-like behavior of the electric and magnetic fields sets

$$c_2 = 1 - \frac{\sqrt{2}}{2}, \quad c_5 = \frac{\sqrt{2} - 1}{2}.$$

As in the first-order method, we perform a linear stability analysis of the evolution system in the case of infinite conductivity. We can choose $c_3 = 1$ and $c_6 = 1/2$, keeping numerical stability of the numerically evolved system, slightly simplifying the proposed method. Moreover, in the ideal limit $\sigma \to \infty$, due to the same reason as in the first-order method, we need to impose

$$c_4 = \frac{(1 - c_1)^2}{2c_1}, \quad c_1 \neq 0,$$

so one eigenvalue of multiplicity at least 3 is set to zero. With these choices, the other eigenvalue of the system is bounded by 1 in absolute value, independently of the velocity field V^i value considered, if $c_1 < 0$; actually the expression for this eigenvalue achieves its minimum in absolute value with respect to the remaining coefficient c_1 for $c_1 = -1/\sqrt{2}$. We will choose this value for the c_1 coefficient. Finally,

$$\big(1 - c_1 + V^2|_n(c_3 - 1)\big) = (1 - c_1) = (1 + 1/\sqrt{2}) \neq 0,$$
$$\big(c_1/2 - c_4 - V^2|_{(1)}(c_3/2 - c_6)\big) = (c_1/2 - c_4) = (1 + \sqrt{2}/2) \neq 0,$$

and the ideal limit is recovered for $\Delta t \to 0$.

The two-stages of the numerical integration of the evolution equation for E^i can then be written as follows:

$$\begin{aligned} E^j|_{(1)} \;=\; & E^j|_n + \Delta t\, S^j_E|_n - \Delta t\, \bar{\sigma}|_n \left(-\frac{1}{\sqrt{2}}E^j|_n + (1 + 1/\sqrt{2})E^j|_{(1)}\right. \\ & \left. +(1 - 1/\sqrt{2})(\boldsymbol{V} \times \boldsymbol{B})^j|_n + \frac{1}{\sqrt{2}}(\boldsymbol{V}|_n \times \boldsymbol{B}|_{(1)})^j - V^j|_n V_l|_n E^l|_n\right) \end{aligned} \tag{7.30}$$

$$
\begin{aligned}
E^j|_{n+1} &= \frac{1}{2}\left(E^j|_n + E^j|_{(1)} + \Delta t\, S^j_E|_{(1)}\right) - \Delta t\,\bar{\sigma}|_{(1)}\Bigg\{\frac{(1+1/\sqrt{2})}{2}E^j|_n \\
&\quad -\frac{\sqrt{2}(1+\sqrt{2})^2}{4}E^j|_{(1)} + (1+\sqrt{2}/2)E^j|_{n+1} + \frac{1}{2\sqrt{2}}(\boldsymbol{V}|_{(1)}\times\boldsymbol{B}|_n)^j \\
&\quad +\frac{(\sqrt{2}-1)}{2}(\boldsymbol{V}\times\boldsymbol{B})^j|_{(1)} + (1-3\sqrt{2}/4)(\boldsymbol{V}|_{(1)}\times\boldsymbol{B}|_{n+1})^j \\
&\quad +\frac{1}{2}V^j|_{(1)}V_l|_{(1)}E^l|_{(1)}\Bigg\}. \qquad (7.31)
\end{aligned}
$$

The Equation (7.30) can be rewritten as:

$$
\begin{aligned}
E^j|_{(1)} &= E^j|_n + \frac{\Delta t}{1+\Delta t\,\bar{\sigma}|_n(1+1/\sqrt{2})}\Big(S^j_E|_n + \bar{\sigma}|_n E^l|_n(V^j|_n V_l|_n - \delta^j_l) \\
&\quad -\bar{\sigma}|_n(1-1/\sqrt{2})(\boldsymbol{V}\times\boldsymbol{B})^j|_n - \frac{\bar{\sigma}|_n}{\sqrt{2}}(\boldsymbol{V}|_n\times\boldsymbol{B}|_{(1)})^j\Big). \qquad (7.32)
\end{aligned}
$$

The Equation (7.31) can be rewritten as:

$$
\begin{aligned}
E^j|_{n+1} &= \frac{1}{2}(E^j|_n + E^j|_{(1)}) + \frac{\Delta t}{1+\Delta t\,\bar{\sigma}|_{(1)}(1+1/\sqrt{2})}\Big\{\frac{1}{2}S^j_E|_{(1)} \\
&\quad -\bar{\sigma}|_{(1)}(1+1/\sqrt{2})E^j|_n + \bar{\sigma}|_{(1)}\frac{(1+\sqrt{2})}{2}E^j|_{(1)} \\
&\quad -\bar{\sigma}|_{(1)}\frac{\sqrt{2}}{4}(\boldsymbol{V}|_{(1)}\times\boldsymbol{B}|_n)^j - \bar{\sigma}|_{(1)}\frac{(\sqrt{2}-1)}{2}(\boldsymbol{V}\times\boldsymbol{B})^j|_{(1)} \\
&\quad -\bar{\sigma}|_{(1)}(1-3\sqrt{2}/4)(\boldsymbol{V}|_{(1)}\times\boldsymbol{B}|_{n+1})^j - \bar{\sigma}|_{(1)}\frac{1}{2}V^j|_{(1)}V_l|_{(1)}E^l|_{(1)}\Big\}. \qquad (7.33)
\end{aligned}
$$

Here, again, an effective time step appears:

$$\frac{\Delta t}{1+\Delta t\,\bar{\sigma}(1+1/\sqrt{2})}.$$

For the first stage, $\bar{\sigma}$ is evaluated in the previous time-step, $\bar{\sigma}|_n$. For the second stage, $\bar{\sigma}$ is evaluated in the first stage, $\bar{\sigma}|_{(1)}$.

7.4 Numerical simulations

We use Cartesian coordinates, equally spaced numerical grid and centered finite differences of second-order for the discretization of the spatial derivatives. We present two different numerical tests, namely the self-similar current sheet test and the large amplitude Alfven wave test; both tests deal with smooth initial data and smooth data during the evolution. They are also discussed in detail in references [96, 37] where it can be checked the success of their numerical codes when dealing with high values for the conductivity.

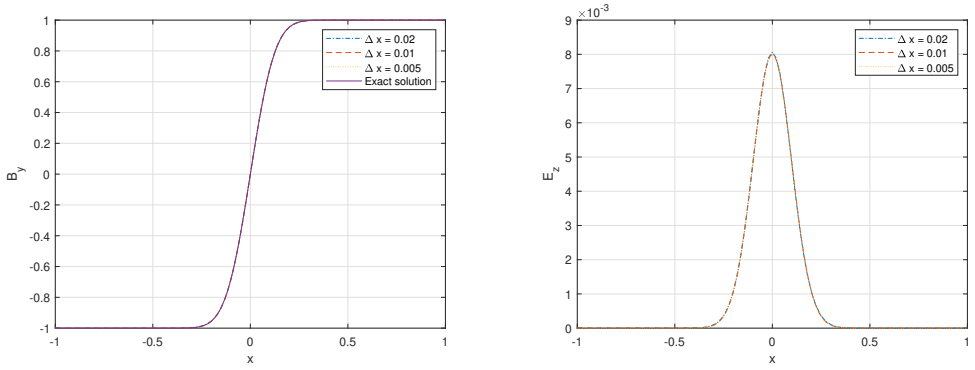

(a) B^y (b) E^z

Figure 7.1: Self similar current sheet test. Numerical values for B^y and E^z at $t = 5$, for three different spatial resolutions, when a first-order MIRK method is used. $V^x = 0$, $\sigma = 10^3$ and CFL=0.8. The exact solution is also included.

In general, the evolution of the magnetic and electric fields are considered, and the charge is computed from its definition as divergence of the electric field. The zero divergence of the magnetic field is conserved through the evolution due to the particular configuration of initial data. We present numerical results using the first and second-order MIRK methods.

7.4.1 Self similar current sheet

This is a simple test in 1D. During the evolution, the only non-zero components of the electric and magnetic fields are $B^y(x,t)$ and $E^z(x,t)$. Vacuum is considered, so we do not evolve the hydrodynamic sector. We keep both the velocity components and the conductivity as constant values. Unless otherwise stated, a Courant-Friedrichs-Lewy (CFL) value of 0.8 is used. The set-up for the initial data is: $\phi = 0$, $\boldsymbol{V} = (V^x, 0, 0)$, $\boldsymbol{E} = (0,0,0)$, $\boldsymbol{B} = (0, B^y(x, t=1), 0)$, being $B^y(x,t=1) = \text{erf}(x\sqrt{\sigma}/2)$. The exact solution of this problem is

$$B^y(x,t) = \text{erf}\left(\frac{x}{2}\sqrt{\frac{\sigma}{t}}\right). \tag{7.34}$$

We consider $t = 1$ for the initial data to avoid singular values of the exact solution. We consider $x \in [-1,1]$. At the spatial boundaries $x = -1$ and $x = 1$, we make use of ghost cells, where the evolved variables are set equal to the the values from the adjacent cells inside our numerical domain. We explore two illustrative examples among the possibilities for this very simple case.

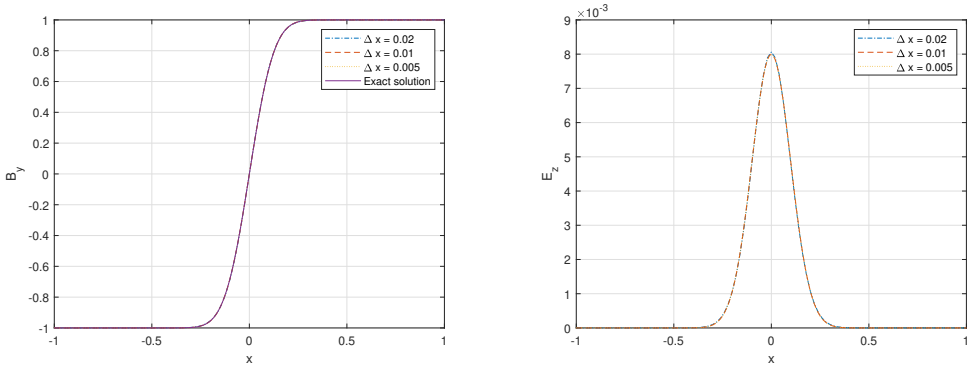

(a) B^y (b) E^z

Figure 7.2: Self similar current sheet test. Numerical values for B^y and E^z at $t = 5$, for three different spatial resolutions, when a second-order MIRK method is used. $V^x = 0$, $\sigma = 10^3$ and CFL=0.8. The exact solution is also included.

On one hand, we consider $V^x = 0$ and $\sigma = 10^3$. The results for B^y and E^z for three different spatial resolutions (namely, $\Delta x = 0.02$, 0.01 and 0.005) when the first-order MIRK method is used, together with the exact

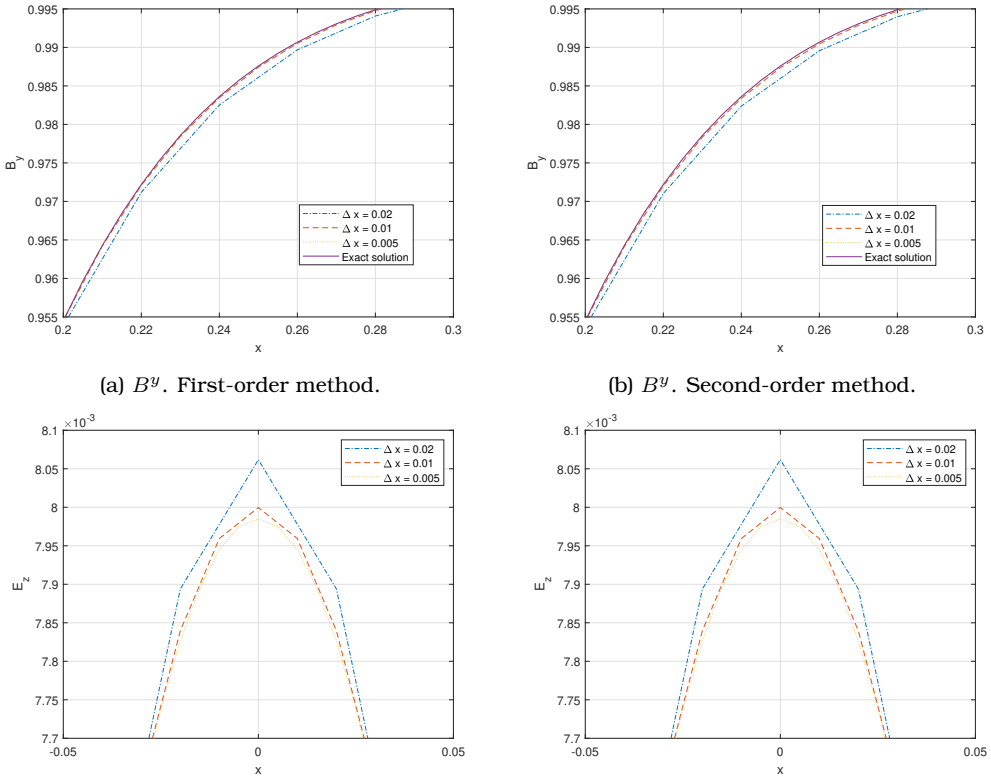

(a) B^y. First-order method.

(b) B^y. Second-order method.

(c) E^z. First-order method.

(d) E^z. Second-order method.

Figure 7.3: Self similar current sheet test. Zoom on the numerical values for B^y and E^z at $t = 5$, for three different spatial resolutions, when a first and second-order MIRK methods are used. $V^x = 0$, $\sigma = 10^3$ and CFL=0.8.

Δx	0.04	0.02	0.01
p for the 1st-order MIRK method	2.1648142	2.0709731	2.0383649
p for the 2nd-order MIRK method	2.1522280	2.0501579	2.0197818

Table 7.1: Estimated convergence orders for the first and second-order MIRK methods applied to the self similar current sheet test at $t = 5$, with $\sigma = 10^3$ and CFL = 0.5, and resolutions $\Delta x = 0.04/2^k$, $k = 0, 1, 2, 3$, according to the formula (7.35).

solution, are displayed in the Figures 7.1a and 7.1b at $t = 5$. The same data are displayed in the Figures 7.2a and 7.2b when a second-order MIRK method is used.

In all cases, the numerical values are on top of the exact solution. We

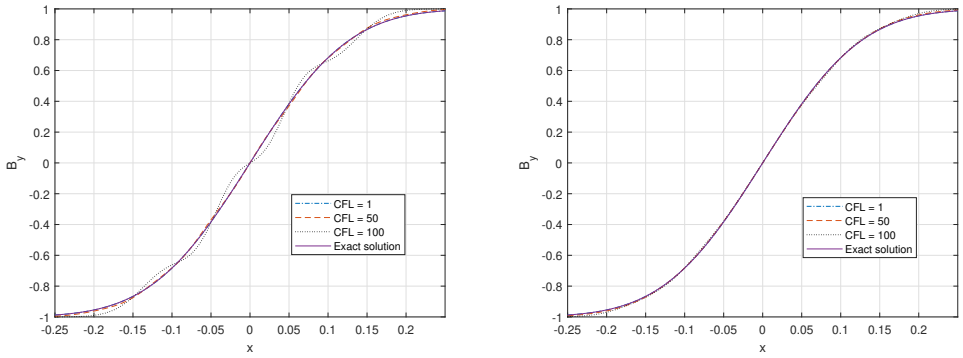

(a) First-order MIRK method.

(b) Second-order MIRK method.

Figure 7.4: Self similar current sheet test. Numerical results for several CFL values when first and second-order MIRK methods are used at $t = 5$. $V^x = 0$, $\sigma = 10^3$ and $\Delta x = 0.005$.

get convergence of the evolved variables, as can be better appreciated in a zoom of the previous Figures, displayed in the Figure 7.3. No significant differences between the results of first and second-order MIRK methods are found. Second-order convergence is obtained when both methods are applied using the L_2 norm of the error between the numerical and the analytical (available for this test) solutions, always using points from the coarsest grid. Specifically, we are considering the following formula:

$$p \approx \log_2 \left(\frac{\varepsilon(\Delta x)}{\varepsilon(\Delta x/2)} \right), \tag{7.35}$$

where p is the estimate of the order of convergence and $\varepsilon(\Delta x)$ is the L_2 norm of the error of a numerical solution with respect to the analytical one for a resolution Δx. In Table 7.1 we show the estimated order of convergence for several resolutions. We get second-order of convergence for both first and second-order MIRK methods. It is remarkable that second-order is achieved also for the first-order MIRK method. This is, most probably, due to the fact that this is indeed a very simple test where the solution is symmetric with respect to $x = 0$.

We explore now several CFL values, even higher than 1, to check the stability of the simulations, using first and second-order MIRK methods. We choose CFL values of 1, 50 and 100. We can observe in the Figures 7.4a and 7.4b the appearance of numerical oscillations for very high CFL values. Increasing the order of the method improves this behaviour, making the numerical simulations for a CFL value of 100 stable at $t = 5$. The appearance of these oscillations is not due to the use of

MIRK methods; for large CFL values and using IMEX methods, we will find a similar behaviour [3]. The reason of these oscillations is the consequence of using a larger CFL than allowed for the source terms included in the purely explicit part in the MIRK methods (S_E^j, S_B^j, S_Y), producing this oscillatory behaviour.

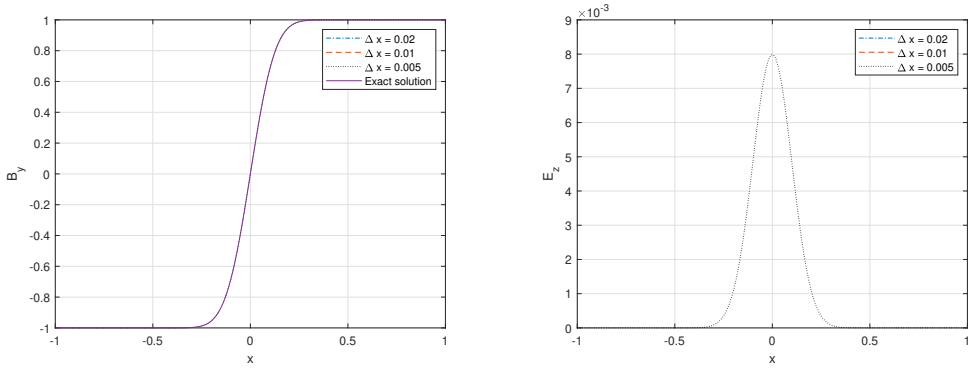

(a) B^y (b) E^z

Figure 7.5: Self similar current sheet test. Numerical values for B^y and E^z at $t = 5$, for three different spatial resolutions, when a first-order explicit method is used. $V^x = 0$, $\sigma = 10^3$ and CFL=0.3. The exact solution is also included.

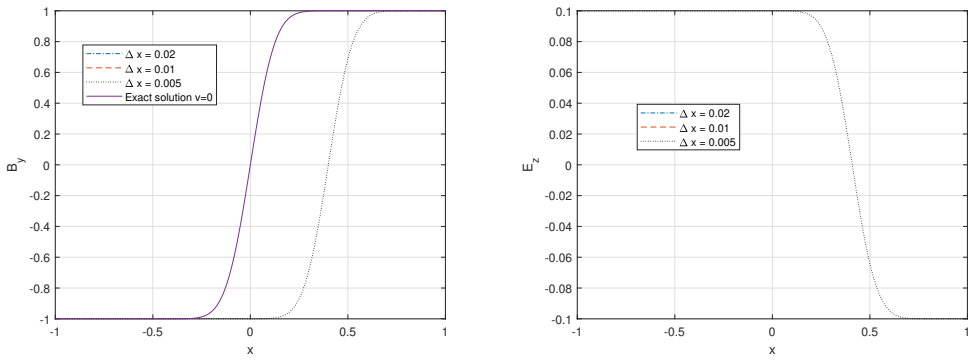

(a) B^y (b) E^z

Figure 7.6: Self similar current sheet test. Numerical values for B^y and E^z at $t = 5$, for three different spatial resolutions, when a first-order explicit method is used. $V^x = 0.1$, $\sigma = 10^3$ and CFL=0.3. The exact solution is also included.

In the case of the first-order (pure) explicit method, $\Delta x = 0.02$ and CFL=0.8, numerical instabilities develop very quickly, the electric and magnetic field components achieving values of 10^{290} at $t = 5$. In order

to get stable and accurate results, we need to consider $\Delta x = 0.005$ and CFL=0.3, as shown in the Figures 7.5a and 7.5b. We find an analogous behaviour for the second-order explicit method.

On the other hand, we consider $V^x = 0.1$ and $\sigma = 10^3$. In the case of the first-order explicit method, $\Delta x = 0.02$ and CFL=0.8, the electric and magnetic field components develop again numerical instabilities very quickly, achieving values of order 10^{291} or higher at $t = 5$. As previously for $V^x = 0$, setting $\Delta x = 0.005$ and CFL=0.3, we obtain good numerical results, as shown in the Figures 7.6a and 7.6b. We find an analogous behaviour for the second-order explicit method.

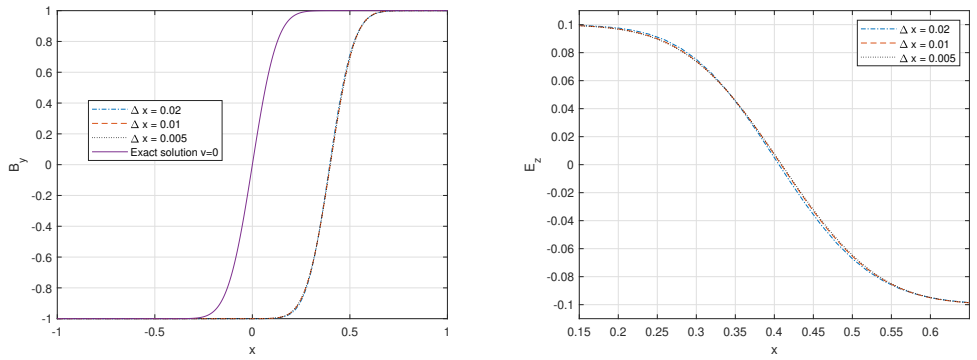

(a) B^y (b) E^z

Figure 7.7: Self similar current sheet test. Numerical values for B^y and E^z at $t = 5$, for three different spatial resolutions, when first and second-order MIRK methods are used. $V^x = 0.1$, $\sigma = 10^3$ and CFL=0.8. The exact solution is also included.

Instead, when the first-order MIRK method is used, the B^y and E^z profiles, shown in the Figures 7.7a and 7.7b, respectively, have the expected behavior for all resolutions: initial profiles are shifted to the right and slightly smoothed with time. All the profiles lie on top of the exact solution.

We also explore several CFL values. We see in the Figures 7.8a and 7.8b that much lower CFL values are allowed; the oscillations begin to appear with CFL=4.5 for the first-order method and with CFL=10 for the second-order one. Again, the reason of these oscillations is associated to the stability of the terms included in the purely explicit part in the MIRK methods (S_E^j, S_B^j, S_Y).

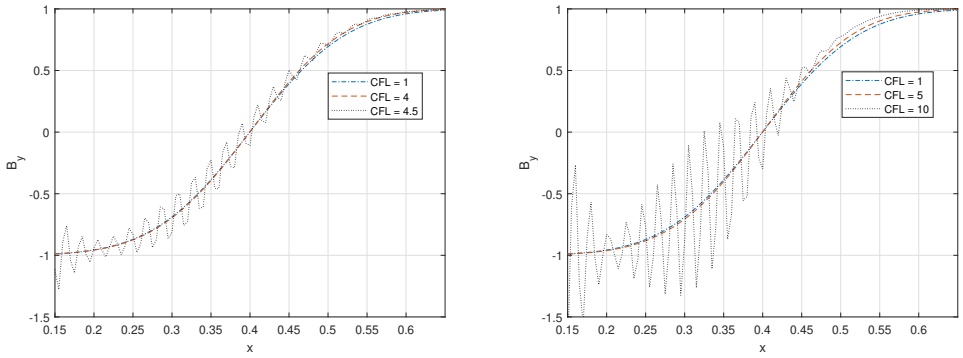

(a) First-order method

(b) Second-order method

Figure 7.8: Self similar current sheet test. Numerical results for several CFL values when first and second-order MIRK methods are used at $t = 5$. $V^x = 0.1$, $\sigma = 10^3$ and $\Delta x = 0.005$.

7.4.2 CP Alfven waves

In this second test we simulate the Circular Polarized (CP) Alfven Waves in 1D. Here the hydrodynamic equations (7.6)–(7.8) need to be solved, as well as the Maxwell Equations. The set-up for the initial data for the electromagnetic field is

$$\boldsymbol{B}(x,0) = B_0\,(1, \cos(k\,x), \sin(k\,x)), \tag{7.36}$$

with $k = 2\pi$ and $B_0 = 1.1547$, and

$$\boldsymbol{E}(x,0) = -\boldsymbol{V}(x,0) \times \boldsymbol{B}(x,0), \tag{7.37}$$

with

$$\boldsymbol{V}(x,0) = \frac{V_A}{B_0}(0, B^y(x,0), B^z(x,0))$$

and V_A the special relativistic Alfven speed, see [96]. Moreover, we consider $\rho(x,0) = p(x,0) = 1$ and the initial values for conserved hydrodynamic variables can be derived from them. We consider a perfect fluid model and an ideal fluid equation of state

$$p = (\Gamma_1 - 1)(\rho + \epsilon),$$

with $\Gamma_1 = 4/3$, being Γ_1 the adiabatic index. With these choices $V_A = 0.423695$. $x \in [0,1]$ defines our numerical domain (one spatial period) and

we impose periodic boundary conditions. Since we want to test if we are able to recover the ideal MHD limit, we consider $\sigma = 10^8$ in all the simulations presented in the manuscript; the numerical solution should be very close to the analytical solution in the ideal limit.

Primitive variables must be computed on each time stage of each iteration; we apply the recovery procedure used in [37]. First, a quartic equation for the Lorentz factor Γ can be derived, with coefficients defined in terms of conserved variables:

$$A_4\Gamma^4 + A_3\Gamma^3 + A_2\Gamma^2 + A_1\Gamma + A_0 = 0, \tag{7.38}$$

where $A_0 = \gamma_1^2\,(C_1 + D^2)$, $A_1 = -2\gamma_1\,C_2\,D$, $A_2 = C_2^2 - 2\gamma_1\,C_1 - \gamma_1^2\,D$, $A_3 = 2\gamma_1\,C_2\,D$, $A_4 = C_1 - C_2^2$, $C_1 = |\boldsymbol{P} - \boldsymbol{E}\times\boldsymbol{B}|^2$, $C_2 = e - (E^2 + B^2)/2$ and $\gamma_1 = (\Gamma_1 - 1)/\Gamma_1$. We use the bisection method to get the solution of the Equation (7.38) with machine precision. Afterwards, we can compute the remaining primitive variables as follows:

$$\rho = \frac{D}{\Gamma}, \tag{7.39}$$

$$h = \frac{e - \frac{1}{2}(E^2 + B^2) - \gamma_1\frac{D}{\Gamma}}{\Gamma^2 - \gamma_1}, \tag{7.40}$$

$$p = \gamma_1\rho(h - 1), \tag{7.41}$$

$$\boldsymbol{V} = \frac{\boldsymbol{P} - \boldsymbol{E}\times\boldsymbol{B}}{e - \frac{1}{2}(E^2 + B^2) + p}. \tag{7.42}$$

We consider CFL=0.3. A Kreiss-Oliger term of the form

$$-\frac{\epsilon_d}{16}(\Delta x)^3\partial_x^4 Y \tag{7.43}$$

has been included in the hydrodynamic sector, in order to guarantee stability by adding a controlled amount of artificial dissipation, with $\epsilon_d = 0.01$.

The time coordinate starts at $t = 0$ and ends after one period, at $t = T = 1/V_A$. In the Figures 7.9a and 7.9b we display the numerical solution of B^y and E^y at $t = T$ for three different resolutions, $\Delta x = 0.02/2^k$, $k = 0, 1, 2$, when a first-order MIRK method is used, together with the exact solution in the ideal MHD limit.

In the case of second-order MIRK method, we use the same set up as before, but removing the Kreiss-Oliger term (similar results are obtained when this term is not removed). The numerical results are shown in the Figures 7.10a and 7.10b for the same variables as for the first-order method. The numerical solution is closer to the exact solution in the

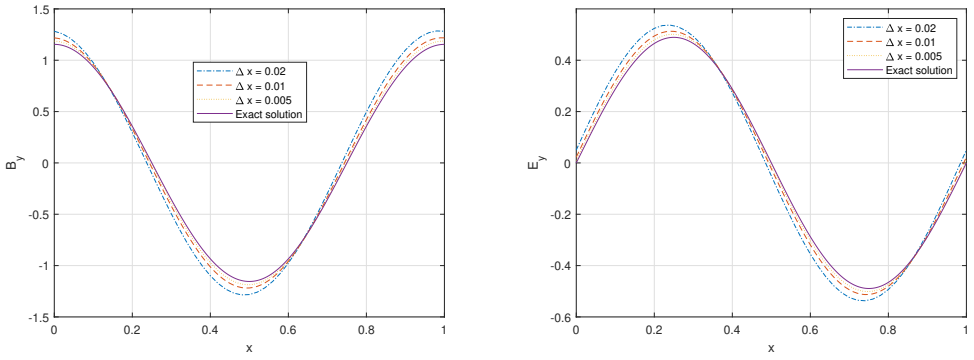

(a) B^y (b) E^z

Figure 7.9: CP Alfven waves test. Numerical values for B^y and E^y at $t = T$, for three different spatial resolutions, when first-order MIRK method is used. $\sigma = 10^8$ and CFL=0.3. The exact solution in the ideal MHD limit is also included.

ideal MHD limit in comparison with the one obtained with the first-order method, as it can be seen clearer in the zoom of the Figures 7.11.

We estimate the convergence order of our methods for this test. We carry out simulations for successive smaller resolutions. We have detected that the Kreiss-Oliger dissipation term (7.43) affects this computation; therefore, we increase in one unit the power of the factor Δx and the coefficient $\epsilon_d = 0.1$ in this term. Moreover, we employ a CFL value of 0.1. We consider, as in the previous test, the L_2 norm of the errors; in this case, however, since we do not have the exact solution (the exact solution in the ideal MHD limit should be considered as a reference), the error is computed based on the difference of numerical solutions S for successive smaller resolutions, always using points from the coarsest grid:

$$\varepsilon(\Delta x) = ||S(\Delta x) - S(\Delta x/2)||_2. \tag{7.44}$$

We get first-order of convergence for the first-order MIRK method as expected, but also first-order of convergence is obtained for the second-order MIRK method. Table 7.2 shows the obtained results. We were not able to find the reason of this reduction in the order of convergence. Nevertheless, for the second-order MIRK method the orders of convergence computed are always bigger than for the first-order MIRK method.

Finally, we explore three different values for the CFL. We obtain interesting results: for CFL=0.3 and 0.7 we have stable numerical results, but for CFL=0.8 this is no longer the case. This effect is more severe if the Kreiss-Oliger dissipation term is neglected. In the Figure 7.12, we

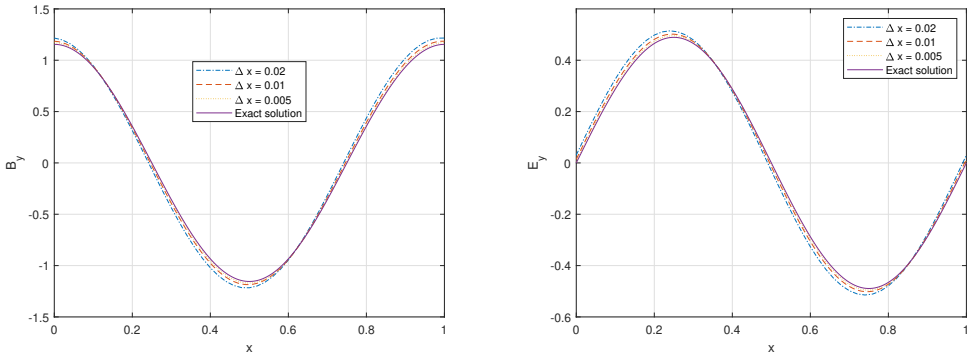

(a) B^y (b) E^z

Figure 7.10: CP Alfven waves test. Numerical values for B^y and E^y at $t = T$, for three different spatial resolutions, when second-order MIRK method is used. $\sigma = 10^8$ and CFL=0.3. The exact solution in the MHD ideal limit is also included.

Δx	0.04	0.02	0.01	0.005	0.0025	0.00125
p for the 1st-order MIRK method	1.38867	0.93344	0.87209	0.92522	0.96129	0.98042
p for the 2nd-order MIRK method	1.63763	1.20525	0.99682	0.96979	0.97859	0.98787

Table 7.2: Estimated convergence orders for the first and second-order MIRK methods applied to the CP Alfvén waves test at $t = T$, with $\sigma = 10^8$ and CFL = 0.1, and resolutions $\Delta x = 0.04/2^k$, $k = 0, 1, \ldots, 6$, according to the Equation (7.44) and the formula (7.35).

show the numerical results obtained using first and second-order MIRK methods for these CFL values. It has been checked that the behaviour with and without artificial dissipation in the second-order MIRK method is quite similar.

7.5 Final remarks

In this work, first and second-order MIRK methods have been presented to numerically integrate the RRMHD equations proposed in [67]. In these MIRK methods, only conserved variables are included in the implicit evaluations. The inversion of the operators can be done analytically

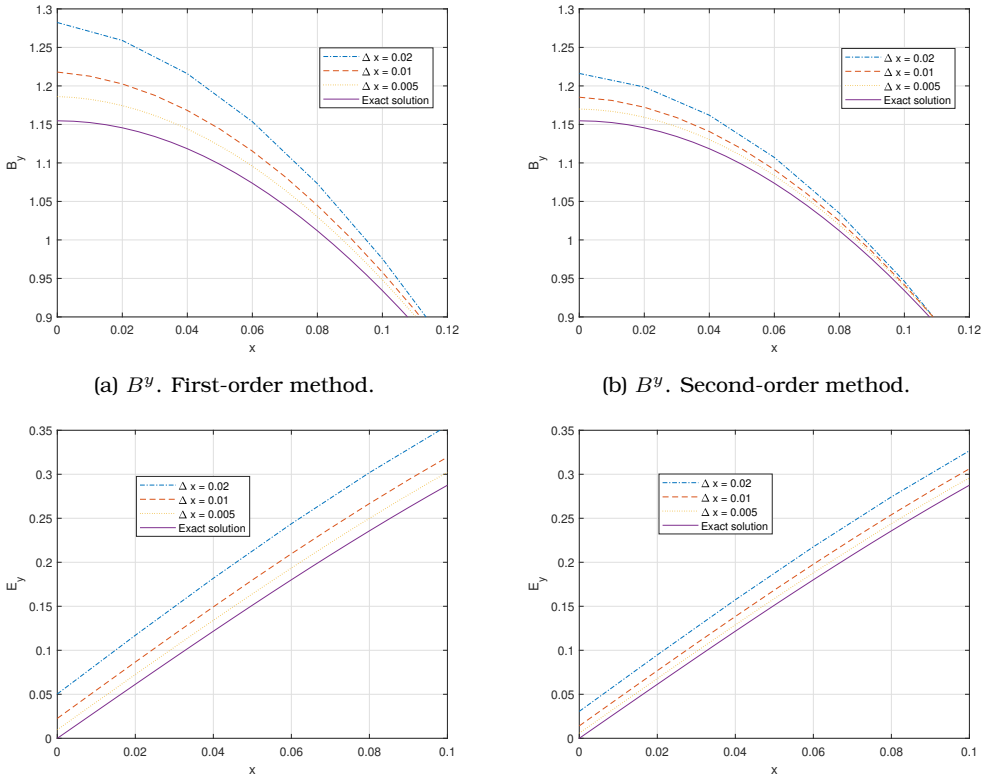

(a) B^y. First-order method.

(b) B^y. Second-order method.

(c) E^y. First-order method.

(d) E^y. Second-order method.

Figure 7.11: CP Alfven waves test. Zoom on the numerical values for B^y and E^y at $t = T$, for three different spatial resolutions, when first and second-order MIRK method are used. $\sigma = 10^8$ and CFL=0.3. The exact solution in the MHD ideal limit is also included.

and is trivial. First and second-order PIRK methods to take into account the wave-like behaviour of the magnetic and electric fields, in addition to linear stability conditions close to the ideal limit, are used to select the values for the c_i coefficients. There is no need of additional iterative steps on each stage with respect to the explicit methods. The potential comparison with IMEX methods strongly depend on the numerical tests carried out: MIRK methods have the same computational cost as explicit ones, while IMEX methods will be more computationally expensive and this cost will depend on the complexity of the equation of state considered (and therefore on the complexity of the recovery process). For both first and second-order MIRK methods, an effective time-step can be defined, making the change of the numerical codes with explicit methods quite direct.

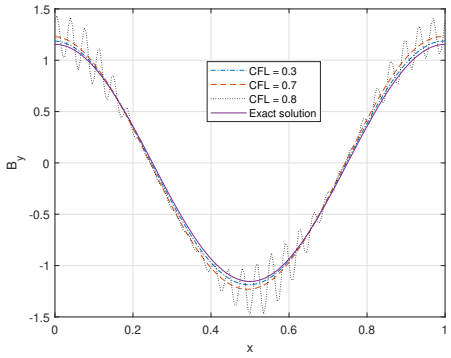

(a) First-order method

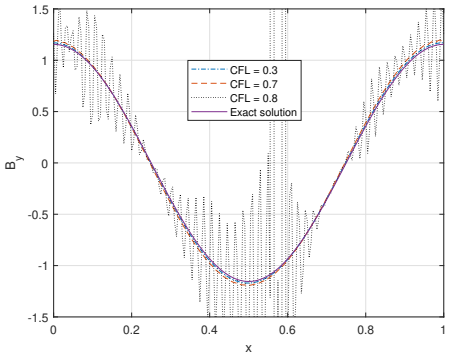

(b) Second-order method without Kreiss-Oliger term

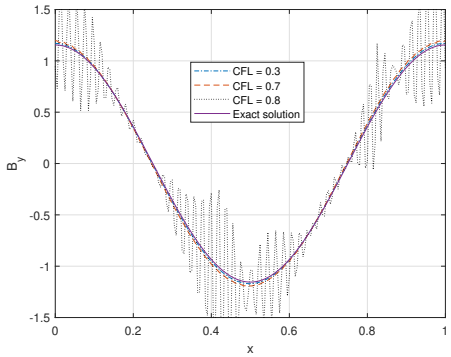

(c) Second-order method with Kreiss-Oliger term

Figure 7.12: CP Alfven waves test. Numerical results for several CFL values when first and second-order MIRK methods are used. $\sigma = 10^8$ and $\Delta x = 0.005$.

We have also shown some simple dynamical numerical simulations with smooth data, namely the self similar current sheet test and the CP Alfven waves test. More complex simulations and also with non-smooth data are needed to really check the potential of the proposed schemes. Also, the comparison with other approaches, like the ones used in [96, 37], would be also addressed in future steps.

The idea behind the MIRK methods can be applied to other kinds of equations. In particular, in the next chapter, we will apply this strategy to the numerical resolution of the Boltzmann Equation to solve the neutrino transport equations in supernovae simulations using the so-called M1 closure approximation. Also, the application to the force-free electrodynamics in its different formulations (see references in [82]) can be

further discussed. Other examples can be found in contexts with rarefied gases [66] and the shallow water equations [65]; there, stiff terms appear in the balance laws coming from the corresponding scenarios. Regarding the future, it is planned to combine the strategy of the MIRK method with a well-balanced method (see [22]) to manage the fluxes in order to preserve stationary solutions.

8

Radiative transport equations

The contents of this Chapter are those of reference [111].
The radiation hydrodynamic equations describe the dynamics of the interaction between matter and radiation such as photons or neutrinos. Its evolution couples the hydrodynamic equations to those of radiative transfer [88, 89], and they appear in many astrophysical scenarios.

Neutrinos are extremely important in core-collapse supernovae (CCSNe) and neutron stars. In usual environments, they can traverse huge amounts of matter without interacting as they only undergo the electroweak interaction and its mass is negligible. We say that the matter is optically thin or transparent. Nonetheless, we find the reverse case when extreme conditions, as nuclear densities, in CCSNe are reached (matter becomes optically thick). Neutrinos are such important that the explosion mechanism of CCSNe cannot be understood without a detailed account of the generation and transport of neutrinos.

With this context in mind, in this Chapter we will apply the MIRK method to numerically integrate the neutrino transport equations in a stable way. In the Chapter 7, we applied the MIRK method to the RRMHD equations, which may become stiff due to the fact that the conductivity σ

may be high. Here the stiff regime will be determined by two scalar functions, the absorption and scattering opacities. The method can also be expressed in an explicit-like form and the inversion of the implicit operator can be done analytically too. We also take into account the physical behavior of the evolved variables in the limit of the stiff regime. We will show the results of applying this method to the reactions between neutrinos and matter in CCSNe simulations.

8.1 Radiation hydrodynamics equations

In this Section we describe the coupling between the radiation and the hydrodynamic sector. Much of the complexity of theoretically modelling the aforementioned systems comes from the equation underlying radiative transfer. At a basic level, the Boltzmann equation, which come from statistical mechanics, describes the evolution of the distribution function, $\mathcal{F}$, of radiation quanta in the phase-space. In the following, we will also describe the Method of Moments to solve Boltzmann Equation. The contents described here are a summary of those in the reference [63].

8.1.1 Statistical mechanics

We introduce now some basic concepts about statistical mechanics which will contextualize the Boltzmann Equation. We address the interested reader to the book [55] for further information about this topic.

Statistical mechanics address the problem of counting the number of possibles microstates given a macroscopic thermodynamic state. It involves results about classical mechanics, thermodynamics or quantum physics. Its natural work space is the phase space where the position $\boldsymbol{X}$ and the momentum $\boldsymbol{P}$ of particles are the independent variables. Statistical mechanics relies on the Heisenberg uncertainty principle which

states that

$$\Delta X \Delta P \geq \frac{\hbar}{2} \tag{8.1}$$

where $\hbar = h/2\pi$, being h the Planck constant and ΔX and ΔP are the standard deviation of the distribution function of position and momentum, respectively, of a particle. For this reason, the volume of a single state of particle in the phase space is assigned to be h^3. Another important result is the Entropy Boltzmann Equation

$$S = k_{\mathrm{B}} \log g, \tag{8.2}$$

where S is the entropy of a macroscopic thermodynamic system, g is the number of possibles microstates (also called statistical weight) and k_{B} is Boltzmann constant. This relation connects microscopic and macroscopic worlds.

On the other hand, a function that plays a crucial role in statistical mechanics is the particle distribution function $\mathcal{F}$ defined in such way the quantity

$$dN = \frac{g}{h^3}\mathcal{F}(t, \boldsymbol{X}, \boldsymbol{P}) dX^3 dP^3 \tag{8.3}$$

is the number of particles in the volume of phase space $dX^3 dP^3$. The statistical weight g must account for the Pauli exclusion principle if the particle under consideration is a fermion.

8.1.2 Boltzmann equation for radiative transfer

The particle distribution function $\mathcal{F}$ is determined by the Boltzmann equation for radiative transfer

$$\frac{1}{c}\frac{\partial \mathcal{F}}{\partial t} + \boldsymbol{N} \cdot \vec{\nabla}\mathcal{F} = \mathcal{B} \tag{8.4}$$

where $\boldsymbol{N} = \boldsymbol{K}/K$, and $\mathcal{B}$ is the collision integral. In the Equation (4.19) we referred as $\boldsymbol{K}$ the momentum of massless particles, notation we follow from now. $\mathcal{B}$ contains terms representing the interaction of one quanta with others or with matter that take the form of integrals over momentum space. Then, the Boltzmann Equation is an integro-partial differential equation, and a rigorous treatment is feasible only in special cases.

The numerical methods that used to model, e.g., CCSNe rely on approximations of the Boltzmann Equation.

In a very common approach, we integrate the specific intensity

$$\mathcal{I} = (K/h)^3 c\mathcal{F} \tag{8.5}$$

multiplied by the tensor product of $n = 0, 1, ...$ unit vectors $\boldsymbol{N}$. Then, yielding a series of moments, now only functions of space and time. The first four moments are

$$\{cE, F^i, cP^{ij}, Q^{ijk}\} = \int d\Omega \mathcal{I}\{1, N^i, N^i N^j, N^i N^j N^k\}. \tag{8.6}$$

where $d\Omega$ is the element of solid angle. The first ones have a direct physical interpretation: $n = 0, 1,$ and 2 correspond to the radiation energy and momentum densities and the radiation pressure, respectively. The resulting infinite series of evolution equations takes the form of conservative form, in which the moment of order $n + 1$ appears as a (spatial) flux of the moment of degree n and source terms, accounting for the reactions, follow from moments of the collision integrals. Truncating the series at a finite degree n and closing the system with a local algebraic relation for the higher moment(s) defines the family of $\boldsymbol{M_n}$ **methods**.

M_0 or (flux-limited) diffusion and M_1 or algebraic Eddington tensor methods offer a good compromise between accuracy and numerical costs, and are thus widely used in relativistic astrophysics. The system for E and F^i (in the comoving frame) can be written for each neutrino species as

$$\partial_t E + \nabla_j F^j + \nabla_j (V^j E) + (\nabla_j V_k) P^{jk} - (\nabla_j V_k) \partial_\omega (\omega P^{jk}) = C^{(0)}, \tag{8.7a}$$

$$\partial_t F^i + c^2 \nabla_j P^{ij} + \nabla_j (V^j F^i) + F^j \nabla_j V^i - (\nabla_j V_k) \partial_\omega (\omega Q^{ijk}) = C^{(1),i}, \tag{8.7b}$$

where terms of order $\mathcal{O}(V^2/c^2)$ have been excluded, $\omega = cK$ (see (4.19)), V^i is the velocity of the fluid and

$$C^{(0)} = \int d\Omega (K/h)^3 c\mathcal{B}, \tag{8.8a}$$

$$C^{(1),i} = \int d\Omega (K/h)^3 c\mathcal{B} N^i. \tag{8.8b}$$

The system (8.7) is the spectral M_1 system of transport equations. The closure relations for the moments of order higher than 1 are too complex to put them here; we refer to [63] instead for more details.

M_1 methods are very good at modelling radiation in the optically thick and the transparent regimes and also work well in the intermediate, semi-transparent regime. Nonetheless, a few difficulties remain. A particularly important one pertains to the time integration in the optically thick regime, in which the typical time scales of interactions between radiation and matter (the inverse of the reaction rates) can be many orders of magnitude smaller than the time scales associated to the radiation propagation or the dynamical time scales: the equations are stiff.

Designing methods for stiff equations requires specific considerations. Explicit time integration is only stable if the numerical time step is reduced to the characteristic time scales of the fastest evolving term, which in this case would be the radiation-matter interaction ones. Implicit methods, on the other hand, allow for a stable evolution even when using the–much larger–time steps set by, e.g., radiation propagation or hydrodynamics. They, however, can be very complicated to implement due to the inversion of the operators involved, in particular for parallel execution, and suffer from low computational efficiency. As a compromise, IMEX Runge-Kutta methods [97] combine an implicit integration of only the stiff terms with an explicit integration of the rest of the equations. This strategy has been used very recently by [57]. Semi-implicit numerical schemes [43] have also been used very recently in neutron star mergers (see for example [104]). Here, we will apply the MIRK method to the system (8.7). This system will be coupled to the hydrodynamics equations which, for completeness, we briefly describe hereunder.

8.1.3

Hydrodynamic sector

The hydrodynamic sector involves the usual mass, energy and momentum conservation equation of the Chapter 4. However, the neutrino interaction give rise to source terms in this case. As usual, we deal with fluid density ρ, momentum density ρV^i and total energy density μ of the

fluid. The system written as a conservation law reads

$$\frac{\partial \rho}{\partial t} + \nabla_j(\rho V^j) = 0, \tag{8.9a}$$

$$\frac{\partial (\rho Y_e)}{\partial t} + \nabla_j(\rho Y_e V^j) = Q_{\rm N}, \tag{8.9b}$$

$$\frac{\partial (\rho \boldsymbol{V})}{\partial t} + \vec{\nabla} \cdot (\rho \boldsymbol{V} \otimes \boldsymbol{V}) = -\vec{\nabla} p + \boldsymbol{Q}_{\rm M}, \tag{8.9c}$$

$$\frac{\partial \mu}{\partial t} + \vec{\nabla} \cdot ((\mu + p)\boldsymbol{V}) = Q_{\rm E} + \boldsymbol{V} \cdot \boldsymbol{Q}^i_{\rm M}, \tag{8.9d}$$

where Y_e is the electron fraction and the source terms are computed as

$$Q_{\rm N} = -\sum_{\rm species} \int_0^\infty C^{(0)} d\omega, \tag{8.10a}$$

$$\boldsymbol{Q}_{\rm M} = -c^{-2} \sum_{\rm species} \int_0^\infty \boldsymbol{C}^{(1)} d\omega, \tag{8.10b}$$

$$Q_{\rm E} = -m_{\rm B} \int_0^\infty \left\{ \left(\frac{C^{(0)}}{\omega} \right)_{\nu_e} + \left(\frac{C^{(0)}}{\omega} \right)_{\bar{\nu}_e} \right\} d\omega, \tag{8.10c}$$

where ν_e and $\bar{\nu}_e$ accounts for electronic neutrino and electronic antineutrino species, respectively.

We present in this manuscript a numerical scheme to solve the M_1 neutrino-hydrodynamics equations to first and second-order in time which, as in the Chapter 7, preserves stability properties of implicit methods and, at the same time, has a computing speed similar to that of an explicit method. We implement the new solver in the neutrino-hydrodynamics code of [63] as an higher order alternative to the IMEX scheme that is already implemented.

Other very different numerical approaches can be considered. For example, Monte Carlo methods can be used to include neutrino transport in the context of CCSNe and this strategy has been implemented in the general relativistic code SpEC [44, 45].

8.2

Equations for neutrino transport in the $\mathrm{M_1}$ closure

The basic variables of M_1 radiative transfer, the energy and momentum density, $E(t, \boldsymbol{X}, \omega)$ and $\vec{F}(t, \boldsymbol{X}, \omega)$, respectively, of the radiation field, are functions of time t, position $\boldsymbol{X}$ and particle angular frequency ω associated to quantum physics [88, 89]. Owing to their conservative character, the corresponding evolution equations take the form of balance laws including the spatial transport and the redistribution across particle energies by differential operators. Exchange of energy and momentum with matter enter the equations via source terms that typically depend only on the local state of radiation field and the matter, but not on their derivatives. Since we will deal with the latter terms, we write the M_1 system in the following simplified way (see also [63]):

$$\partial_t E = S_E + C^{(0)}, \tag{8.11a}$$

$$\partial_t F^i = S_F^i + C^{(1),i}, \tag{8.11b}$$

where the terms with spatial or energy derivatives are included in the S_E and S_F^i terms, and the interaction source terms $C^{(0)}$ and $C^{(1),i}$ are explicitly split from the rest of the source terms. The form of the interaction source terms depends on the choice of interactions and possible approximations used to describe them. We focus on the thermal emission and absorption and isotropic scattering. Then, the rates of energy and momentum exchange are proportional to the absorption opacity κ_{a} and transport opacity κ_{tra}, respectively. The interaction source terms are given by the following expressions:

$$C^{(0)} = c\,\kappa_a(E_{\mathrm{eq}} - E), \tag{8.12a}$$

$$C^{(1),i} = -c\,\kappa_{\mathrm{tra}} F^i. \tag{8.12b}$$

The transport opacity satisfies $\kappa_{\mathrm{tra}} = \kappa_a + \kappa_s$, where κ_s is the scattering opacity. The Equation (8.12a) describes how matter emits radiation thermally with an equilibrium energy density E_{eq} (associated with the Maxwell-Boltzmann distribution for photons or Fermi-Dirac distribution for neutrinos), and how it absorbs the local radiation energy. In the case

of neutrinos E_{eq} is computed as

$$E_{\mathrm{eq}}(\omega, \mu_\nu, T) = \int d\Omega \left(\frac{\omega}{hc}\right) \mathcal{F}_{\mathrm{FD}} = \int d\Omega \left(\frac{\omega}{hc}\right) \left(\exp\left(\frac{\omega - \mu_\nu}{k_{\mathrm{B}} T}\right) + 1\right)^{-1}, \tag{8.13}$$

where T and μ_ν are the fluid temperature and chemical potential of the neutrino species, respectively. The Equation (8.12b) accounts for the transfer of momentum to the gas by means of absorption and scattering reactions. We note that the same terms appear with the opposite sign (and integrated over particle energy) as sources in the hydrodynamic equations for the gas (see the Equations (8.9) and (8.10)).

We do not go deeper into the detailed, potentially very complicated, dependence of the opacities on E and $\vec{F}$, as well as on the composition and thermodynamic state of the gas, because our method is valid for general opacity laws. Our main focus lies on the stiff, optically thick limit, in which the opacities are very high, $\kappa_{\mathrm{a,tra}} \gg 1$, and the interaction terms dominate over S_E and S_F^i in the Equations (8.11). Under these conditions, numerical difficulties arise due to the need to simultaneously follow all the terms with characteristic time scales that can differ by many orders of magnitude.

The physically correct stiff limit consists of E approaching the equilibrium energy density E_{eq}. Furthermore, the Equation (8.12b) indicates that high opacities will reduce $\vec{F}$ to zero. However, the precise manner in which $\vec{F}$ vanishes matters a lot for getting the correct solution. In a non-uniform radiation field, $\vec{F}$ has to approach the diffusion limit satisfying

$$\vec{F} \to \vec{F}_{\mathrm{diff}} = \frac{1}{3\, c\, \kappa_{\mathrm{tra}}} \vec{\nabla} E.$$

While some M_1 methods [59, 103, 60, 9] deal with this requirement by explicitly enforcing the diffusion flux for high optical thickness, others [63] found that an appropriate treatment of the flux terms in S_F is sufficient to reproduce the correct limit. In practise, approaches such as the one of [63] allow us to offload the issue of the correct diffusion limit to the solution of S_F. As long as our method for $C^{(1),i}$ ensures that $\vec{F}$ vanishes in the optically thick limit in the absence of S_F, the coupled solution of S_F and $C^{(1),i}$ will behave correctly.

We focus now on the numerical schemes that can be used to solve the Equations (8.11). The time-integration strategy for the transport equations (8.11) is usually chosen based on a trade-off between stability, accuracy, and numerical costs. These goals are somewhat at odds with each other: the most stable schemes, implicit time integrators, and the

most accurate ones, high-order methods, are also the most expensive ones; furthermore, high-order implicit methods tend to be particularly complex. The difficulties are exacerbated when applying the integrators to terms involving spatial as well as temporal derivatives. For this reason, an operator-splitting approach is common in which the transport terms, $S_{E,F}$, the interaction terms, $C^{0,1}$, and, in the case of coupled radiation hydrodynamics, the flux and source terms of the hydrodynamics equations not connected to neutrino interactions, are treated separately using suitable methods. In the applications we are mostly interested in, CCSNe, we follow the evolution of the system on the hydrodynamical time scales, which leads us to select an explicit time integrator for the latter group of terms. Furthermore, the maximum hydrodynamic flow and sound speeds are similar to the characteristic velocities of the neutrino transport terms, which allows us to use an explicit time integrator for them with roughly the same stability constraint on the time step. On the other hand, their stiffness makes an implicit time integration scheme the only feasible option for the interaction terms.

The IMEX strategy is commonly employed in neutrino-hydrodynamics codes in high-energy astrophysics. Among the proposed methods, we follow the one implemented by [63], whose discretized schematics we briefly summarise in the following. We denote the conserved variables of hydrodynamics (the densities of mass, momentum, energy) and of the neutrino radiation $(E, \boldsymbol{F})$, collectively as $\boldsymbol{U}$ and $\boldsymbol{W}$, respectively, and use superscripts $^{n,n+1}$ to indicate the states at discrete time steps t^n and $t^{n+1} = t^n + \Delta t$, respectively. Then our prescription to update the variables to the next time step is given by

$$(U^{n+1} - U^n)/\Delta t = \mathcal{L}_{\rm hydro}(U^n) + \bar{\mathcal{L}}_{\rm int}(U^n, W^{n+1}), \tag{8.14}$$

$$(W^{n+1} - W^n)/\Delta t = \mathcal{L}_{\rm tr}(W^n) + \mathcal{L}_{\rm int}(U^n, W^{n+1}), \tag{8.15}$$

where we the symbols $\mathcal{L}_{\rm hydro}$ and $\mathcal{L}_{\rm tr}$ stand for the discretized operators including the fluxes and sources of hydrodynamics and the fluxes of neutrino transport, respectively. Without entering into further details, we note that they are evaluated explicitly with data of the previous time step, t^n. The neutrino-matter interactions, represented by the operator $\mathcal{L}_{\rm int}$, i.e., the discretized version of the Equations (8.12), depends on both $\boldsymbol{W}$ and $\boldsymbol{U}$. Its dependence on the hydrodynamic variables is a result of both the opacities and the equilibrium energy density, $E_{\rm eq}$, being functions of the thermodynamic state of the gas. We note its counterpart in the hydrodynamic equations, $\bar{\mathcal{L}}_{\rm int}$, can be computed after $\mathcal{L}_{\rm int}$, and thus presents no further difficulty.

A fully implicit treatment of $\mathcal{L}_{\rm int}$ in (8.15) would imply a fully implicit evaluation of all the variables, $\mathcal{L}_{\rm int}(U^{n+1}, W^{n+1})$. The intricate dependence of $\kappa_{\rm a,tra}$ and $E_{\rm eq}$ on $\boldsymbol{U}$ makes this task computationally costly, which burden the numerical solution. This step would require at multiple times the recovery of the primitive (thermodynamic) variables, in particular the temperature, from $\boldsymbol{U}$, i.e., the inversion of non-linear relations.

The MIRK method will minimize the computation cost of the process of the recovery of variables. Our alternative approach differs in that we evaluate implicitly only the conserved neutrino variables, W^{n+1}, but treat the hydrodynamic variables and the variables derived from them, opacities and equilibrium energy density, explicitly by using U^n. This simple change allows for preserving the stability properties and simultaneously reducing the computational cost to that of an explicit method, as there is no need to apply the recovery multiple additional times. In the following we explain the method in detail. Such an approach has been implemented by [63] without exploring the mathematical framework presented in the next section. Here we go beyond their method, and this mathematical framework also allows for a higher order extension.

8.3 Numerical methods

This Section present the equations of a general MIRK method of first and second-order. The general expressions contain undetermined coefficients that we will choose adequately in order to guarantee a correct behaviour in the stiff limit regime.

8.3.1 First-order method

The equations of a first-order MIRK method for the Equations (8.11) take the form

$$E^{n+1} = E^n + \Delta t \left(S_E^n + ac\kappa_a^n (E_{\rm eq}^n - E^n) + (1-a)c\kappa_a^n (E_{\rm eq}^n - E^{n+1}) \right) \quad (8.16a)$$

$$(F^i)^{n+1} = (F^i)^n + \Delta t \left((S_F^i)^n - bc\kappa_{\rm tra}^n (F^i)^n - (1-b)c\kappa_{\rm tra}^n (F^i)^{n+1} \right), \quad (8.16b)$$

where a, b are arbitrary real coefficients that we will select later according to stability criteria. From previous equations, the explicit expressions for E^{n+1} and $(F^i)^{n+1}$ can be derived easily; they can be cast in matrix form as:

$$\begin{pmatrix} E \\ F^i \end{pmatrix}^{n+1} = \begin{pmatrix} E \\ F^i \end{pmatrix}^{n} + \begin{pmatrix} \frac{\Delta t}{1+\Delta t\,\kappa^n(1-a)} & 0 \\ 0 & \delta^{ij}\frac{\Delta t}{1+\Delta t\,\kappa'^n(1-b)} \end{pmatrix} \begin{pmatrix} c\,\kappa_a(E_{\text{eq}} - E) + S_E \\ -c\,\kappa_{\text{tra}}\,F^i + S_F^i \end{pmatrix}^{n}, \tag{8.17}$$

where $\kappa := c\,\kappa_a$ and $\kappa' := c\,\kappa_{\text{tra}}$. The conditions $a, b < 1$ must be satisfied to force non-zero (and positive) denominators always. Notice that the Equations (8.17) resemble a pure explicit method with effective time steps

$$\Delta t_E = \frac{\Delta t}{1 + \Delta t\,\kappa^n(1-a)}, \quad \Delta t_F = \frac{\Delta t}{1 + \Delta t\,\kappa'^n(1-b)}$$

for the E and F^i evolution equations, respectively. The previous matrix expression has been easily and analytically derived thanks to the fully explicit evaluation of the non conserved variables (e.g., all the variables different from E and F^i). Due to this reason, one would expect to have a computational cost similar to that of applying a fully explicit method. We now analyze the behaviour in the stiff limit regime.

Mathematically speaking, the stiff limit refers to $\kappa_a, \kappa_{\text{tra}} \to \infty$. In that limit, the Equation (8.17) reads

$$\begin{pmatrix} E \\ F^i \end{pmatrix}^{n+1} = \begin{pmatrix} \frac{-a}{1-a} & 0 \\ 0 & \delta^{ij}\frac{-b}{1-b} \end{pmatrix} \begin{pmatrix} E \\ F^i \end{pmatrix}^{n} + \begin{pmatrix} \frac{E^n_{\text{eq}}}{1-a} \\ 0 \end{pmatrix}. \tag{8.18}$$

Thus, the conditions

$$a < 1/2, \quad b < 1/2, \tag{8.19}$$

must be fulfilled for the spectral radius of the updated matrix to be strictly bounded by 1, thus having a stable numerical method. This is a more restrictive condition in comparison with previous conditions $a, b < 1$ (needed to avoid zero values in the denominators). In order to guarantee a correct behaviour of the numerical solution at the stiff limit, and assuming a well-behaved and smooth data for the previous time step, $E^n = E^n_{\text{eq}} + \mathcal{O}(\Delta t)$ and $(F^i)^n = 0 + \mathcal{O}(\Delta t)$, we have that, $\forall\, a, b$,

$$E^{n+1} = E^{n+1}_{\text{eq}} + \mathcal{O}(\Delta t),$$

$$(F^i)^{n+1} = 0 + \mathcal{O}(\Delta t).$$

So, independently on the values of the coefficients a, b we get well-behaved and smooth data in the next time step at first-order. This give us, in principle, full freedom for choosing a and b, as long as conditions (8.19) are satisfied. However, the behaviour of the evolved variables are far from been smooth in CCSNe simulations. Therefore, we should guarantee their correct behaviour at the stiff limit even when we are dealing with non-smooth data, and regardless the possible presence of numerical errors in the previous time steps. The choice $b = 0$ guarantees the correct behaviour for F at the stiff limit, i.e., $(F^i)^{n+1} = 0$. It remains choosing a value for a. By analogy with b, and taking into account the particular case $E_{\rm eq} = 0$, we will simply consider $a = 0$. This means that the behaviour of E at the stiff limit is not controlled by previous values of this quantity, but only by evaluations of $E_{\rm eq} = E_{\rm eq}(\boldsymbol{U})$, which only depends on the hydrodynamic variables $\boldsymbol{U}$. With this choice, it is satisfied that $E^{n+1} = E^n_{\rm eq} = E^{n+1}_{\rm eq} + \mathcal{O}(\Delta t)$. Finally, in the case $a = b = 0$ the method reads:

$$E^{n+1} = E^n + \frac{\Delta t}{1 + \Delta t\, \kappa^n} \left(S^n_E + \kappa^n (E^n_{\rm eq} - E^n) \right), \tag{8.20a}$$

$$(F^i)^{n+1} = (F^i)^n + \frac{\Delta t}{1 + \Delta t\, \kappa'^n} \left((S^i_F)^n - \kappa'^n (F^i)^n \right). \tag{8.20b}$$

8.3.2 Second-order method

Hereafter we follow the same strategy as in the first-order case. Two stages are needed for the second-order method. We denote the intermediate step by a (1) superindex and the final step by $n + 1$. In general, we have four coefficients, a, a', b, b', to be determined based on stability arguments. The first stage reads

$$E^{(1)} = E^n + \Delta t \left(S^n_E + a\, \kappa^n (E^n_{\rm eq} - E^n) + (1 - a)\, \kappa^n (E^n_{\rm eq} - E^{(1)}) \right) \tag{8.21a}$$

$$(F^i)^{(1)} = (F^i)^n + \Delta t \left((S^i_F)^n - b\, \kappa'^n (F^i)^n - (1 - b)\, \kappa'^n (F^i)^{(1)} \right), \tag{8.21b}$$

and the second stage can be written as

$$\begin{aligned} E^{n+1} &= \frac{1}{2}[E^{(1)}+E^n]+\Delta t\left[\frac{1}{2}S_E^{(1)}+a'\,\kappa^{(1)}(E_{\rm eq}^{(1)}-E^{(1)})\right. \\ &+ \left.\frac{1-a}{2}\kappa^{(1)}(E_{\rm eq}^{(1)}-E^n)+\left(\frac{a}{2}-a'\right)\kappa^{(1)}(E_{\rm eq}^{(1)}-E^{n+1})\right], \qquad (8.22a) \\ (F^i)^{n+1} &= \frac{1}{2}[(F^i)^{(1)}+(F^i)^n]+\Delta t\left[\frac{1}{2}(S_F^i)^{(1)}\right. \\ &- \left. b'\kappa'^{(1)}(F^i)^{(1)}-\frac{1-b}{2}\kappa'^{(1)}(F^i)^n-\left(\frac{b}{2}-b'\right)\kappa'^{(1)}(F^i)^{n+1}\right]. \qquad (8.22b) \end{aligned}$$

Isolating $E^{(1)}$ and $(F^i)^{(1)}$, we get similar expressions to those of first-order, just substituting the superindex n by (1):

$$E^{(1)} = E^n+\frac{\Delta t}{1+\Delta t\,\kappa^n(1-a)}\left(S_E^n+\kappa^n(E_{\rm eq}^n-E^n)\right), \qquad (8.23a)$$

$$(F^i)^{(1)} = (F^i)^n+\frac{\Delta t}{1+\Delta t\,\kappa'^n(1-b)}\left((S_F^i)^n-\kappa'^n(F^i)^n\right). \qquad (8.23b)$$

Then, E^{n+1} and $F^{i,n+1}$ can be expressed explicitly in terms of previous evaluations of these quantities as:

$$\begin{aligned} E^{n+1} &= \left[1+\Delta t\,\kappa^{(1)}\left(\frac{a}{2}-a'\right)\right]^{-1}\left\{\left[\frac{1}{2}-\Delta t\,\kappa^{(1)}\left(\frac{1-a}{2}\right)\right]E^n\right. \\ &+ \left.\left[\frac{1}{2}-\Delta t\,\kappa^{(1)}a'\right]E^{(1)}+\frac{\Delta t\,S_E^{(1)}}{2}+\frac{\Delta t\,\kappa^{(1)}E_{\rm eq}^{(1)}}{2}\right\} \\ &= \left[1+\Delta t\,\kappa^{(1)}\left(\frac{a}{2}-a'\right)\right]^{-1}\left\{\left[\frac{1}{2}-\Delta t\,\kappa^{(1)}\left(\frac{1-a}{2}\right)\right]E^n\right. \\ &+ \left.\left[\frac{1}{2}+\Delta t\,\kappa^{(1)}\left(\frac{1}{2}-a'\right)\right]E^{(1)}+\frac{\Delta t}{2}\left[S_E^{(1)}+\kappa^{(1)}(E_{\rm eq}^{(1)}-E^{(1)})\right]\right\}, \end{aligned} \qquad (8.24a)$$

$$\begin{aligned} (F^i)^{n+1} &= \left[1+\Delta t\,\kappa'^{(1)}\left(\frac{b}{2}-b'\right)\right]^{-1}\left\{\left[\frac{1}{2}-\Delta t\,\kappa'^{(1)}\left(\frac{1-b}{2}\right)\right](F^i)^n\right. \\ &+ \left.\left[\frac{1}{2}-\Delta t\,\kappa'^{(1)}b'\right](F^i)^{(1)}+\frac{\Delta t\,(S_F^i)^{(1)}}{2}\right\} \\ &= \left[1+\Delta t\,\kappa'^{(1)}\left(\frac{b}{2}-b'\right)\right]^{-1}\left\{\left[\frac{1}{2}-\Delta t\,\kappa'^{(1)}\left(\frac{1-b}{2}\right)\right](F^i)^n\right. \\ &+ \left.\left[\frac{1}{2}+\Delta t\,\kappa'^{(1)}\left(\frac{1}{2}-b'\right)\right](F^i)^{(1)}+\frac{\Delta t}{2}\left[(S_F^i)^{(1)}-\kappa'^{(1)}(F^i)^{(1)}\right]\right\}. \end{aligned} \qquad (8.24b)$$

The following conditions are necessary for forcing non-zero (positive) denominators always:

$$\frac{a}{2}-a'>0, \quad 1-a>0; \quad \frac{b}{2}-b'>0, \quad 1-b>0. \qquad (8.25)$$

We finally determine the coefficients of the method taking into account previous conditions and the behaviour of the numerical solution at the stiff limit.

The stiff limit refers to $\kappa^n, \kappa^{(1)}, \kappa'^n, \kappa'^{(1)} \to \infty$. In that limit, the Equations (8.24) read

$$E^{n+1} = \lambda_E E^n + \frac{-a'}{\left(\frac{a}{2} - a'\right)(1-a)} E^n_{\text{eq}} + \frac{1/2}{\frac{a}{2} - a'} E^{(1)}_{\text{eq}}, \tag{8.26a}$$

$$(F^i)^{n+1} = \lambda_F (F^i)^n, \tag{8.26b}$$

where

$$\lambda_E = \frac{a'a - \left(\frac{1-a}{2}\right)(1-a)}{\left(\frac{a}{2} - a'\right)(1-a)}, \tag{8.27a}$$

$$\lambda_F = \frac{b'b - \left(\frac{1-b}{2}\right)(1-b)}{\left(\frac{b}{2} - b'\right)(1-b)}. \tag{8.27b}$$

The conditions $|\lambda_E| \leq 1$ and $|\lambda_F| \leq 1$ must be fulfilled to guarantee stability of the numerical method at the stiff limit. If we assume well-behaved and smooth data at second-order in time at $t = t^n$,

$$E^n = E^n_{\text{eq}} + \mathcal{O}(\Delta t^2), \tag{8.28a}$$

$$(F^i)^n = 0 + \mathcal{O}(\Delta t^2), \tag{8.28b}$$

we can get, from the Equation (8.26) the following expressions:

$$E^{n+1} = E^{n+1}_{\text{eq}} + \frac{a' + \frac{1-a}{2}}{\frac{a}{2} - a'} \left(\nabla_X E_{\text{eq}}\right)^n \cdot \tilde{S}^n_X \Delta t + \mathcal{O}(\Delta t^2), \tag{8.29a}$$

$$(F^i)^{n+1} = 0 + \mathcal{O}(\Delta t^2), \tag{8.29b}$$

where we have used a Taylor expansion over $E^{(1)}_{\text{eq}}$, $\boldsymbol{X} = (\boldsymbol{U}, \boldsymbol{W})$ represents the vector of all the evolved variables, $\nabla_X = (\partial_{X_1}, \partial_{X_2}, ...)$ and $\tilde{\boldsymbol{S}}_X$ is the source term in the evolution equation of the form $\partial_t \boldsymbol{X} = \tilde{\boldsymbol{S}}_X$. So in order to satisfy the Equation (8.28) in the next time step t^{n+1}, we need to impose $a' = (a-1)/2$. We could choose b' in resemblance with a',

$$a' = \frac{a-1}{2}, \quad b' = \frac{b-1}{2}. \tag{8.30}$$

This choice for a' preserves the second-order behaviour of our numerical solution in the next time step and at the stiff limit when smooth data are involved. Moreover the condition $a/2 - a' > 0$ is trivially satisfied and

$\lambda_E = -1$. Note that having $\lambda_E = -1$ means consider a value for λ_E at the border of the stability region, which seems to be not very convenient. In addition, as commented for the first-order method, we must take into account that the evolved variables have a non-smooth behaviour in CCSNe simulations.

Our proposal is then to consider $b \neq 0$ and $b' = (b-1)^2/(2b)$ to guarantee $\lambda_F = 0$ (as we did choosing $b = 0$ for the first-order method), preserving the correct behaviour of our numerical solution regardless the possible presence of numerical errors or non-smooth data. By analogy with b', and taking into account the particular case $E_{\text{eq}} = 0$, we will consider $a \neq 0$ and $a' = (a-1)^2/(2a)$, or $\lambda_E = 0$ equivalently. For these choices, the conditions (8.25) result in

$$a' = \frac{(1-a)^2}{2a}, \quad a \in (-\infty, 0) \cup (1/2, 1), \tag{8.31a}$$

$$b' = \frac{(1-b)^2}{2b}, \quad b \in (-\infty, 0) \cup (1/2, 1), \tag{8.31b}$$

and the Equation (8.29a) reads

$$E^{n+1} \quad = \quad E^{n+1}_{\text{eq}} + \frac{1-a}{2a-1} \left(\nabla_X E_{\text{eq}}\right)^n \cdot \tilde{S}^n_X \Delta t + \mathcal{O}(\Delta t^2). \tag{8.32}$$

Second-order for smooth data at the stiff limit would be guaranteed if $a = 1$, but this is incompatible with conditions (8.31a). Restricting ourselves to (8.31a), we only get first-order in time at the stiff limit for E, as seen in (8.32); a price to pay when non-smooth data is considered. Within these constraints, we still have some freedom for the election of the coefficients a, b.

We can write our numerical method in such a way it resembles a pure explicit scheme of the form

$$X^{(1)} = X^n + \Delta t \tilde{S}^n_X, \tag{8.33a}$$

$$X^{n+1} = \frac{X^n}{2} + \frac{X^{(1)}}{2} + \Delta t \frac{\tilde{S}^{(1)}_X}{2}. \tag{8.33b}$$

For the choices (8.30), the Equations (8.23) keep the same form, while

the Equations (8.24) can be written as:

$$\begin{aligned} E^{n+1} &= \frac{1-\Delta t\,\kappa^{(1)}(1-a)}{2+\Delta t\,\kappa^{(1)}}E^n + \frac{1+\Delta t\,\kappa^{(1)}(2-a)}{2+\Delta t\,\kappa^{(1)}}E^{(1)} \\ &+ \frac{\Delta t}{2+\Delta t\,\kappa^{(1)}}\left[S_E^{(1)} + \kappa^{(1)}(E_{\text{eq}}^{(1)} - E^{(1)})\right], \end{aligned} \tag{8.34a}$$

$$\begin{aligned} (F^i)^{n+1} &= \frac{1-\Delta t\,\kappa'^{(1)}(1-b)}{2+\Delta t\,\kappa'^{(1)}}(F^i)^n + \frac{1+\Delta t\,\kappa'^{(1)}(2-b)}{2+\Delta t\,\kappa'^{(1)}}(F^i)^{(1)} \\ &+ \frac{\Delta t}{2+\Delta t\,\kappa'^{(1)}}\left[(S_F^i)^{(1)} - \kappa'^{(1)}(F^i)^{(1)}\right], \end{aligned} \tag{8.34b}$$

where a, b have not been chosen yet. For $\kappa, \kappa' \to 0$, we recover the structure of the previous second-order pure explicit method.

Finally, with conditions (8.31), the Equations (8.23) keep the same form, while the Equations (8.24) can be written as:

$$\begin{aligned} E^{n+1} &= \frac{1-\Delta t\,\kappa^{(1)}(1-a)}{2+\Delta t\,\kappa^{(1)}\left(2-\frac{1}{a}\right)}E^n + \frac{1+\Delta t\,\kappa^{(1)}\left(3-\frac{a^2+1}{a}\right)}{2+\Delta t\,\kappa^{(1)}\left(2-\frac{1}{a}\right)}E^{(1)} \\ &+ \frac{\Delta t}{2+\Delta t\,\kappa^{(1)}\left(2-\frac{1}{a}\right)}\left[S_E^{(1)} + \kappa^{(1)}(E_{\text{eq}}^{(1)} - E^{(1)})\right], \end{aligned} \tag{8.35a}$$

$$\begin{aligned} (F^i)^{n+1} &= \frac{1-\Delta t\,\kappa'^{(1)}(1-b)}{2+\Delta t\,\kappa'^{(1)}\left(2-\frac{1}{b}\right)}(F^i)^n + \frac{1+\Delta t\,\kappa'^{(1)}\left(3-\frac{b^2+1}{b}\right)}{2+\Delta t\,\kappa'^{(1)}\left(2-\frac{1}{b}\right)}(F^i)^{(1)} \\ &+ \frac{\Delta t}{2+\Delta t\,\kappa'^{(1)}\left(2-\frac{1}{b}\right)}\left[(S_F^i)^{(1)} - \kappa'^{(1)}(F^i)^{(1)}\right], \end{aligned} \tag{8.35b}$$

with a, b still to be chosen. Choices to be used in the forecoming simulations are summarized in the Tables 8.1 and 8.2. For $\kappa, \kappa' \to 0$, we recover the structure of the previous second-order pure explicit method.

8.4 Numerical simulations and results

8.4.1 Input physics

To assess its properties, we apply our method to the Radiation Hydrodynamics of stellar CCSNe in spherical symmetry. This setup tests

the scheme in a highly dynamic system including both the optically thin and the optically thick, stiff regimes of neutrino-matter interactions. As such, it represents a demanding problem for numerical codes. While the neglect of non-spherical flows limits the degree of realism, it makes the problem more standardised and controllable. Therefore, our tests follow in the footsteps of many previous studies of new schemes that used similar setups (e.g., [105, 78, 113, 93, 87, 92, 63, 69, 100, 95, 62, 70]).

All simulations presented in the rest of this Section use the neutrino-(magneto-)hydrodynamics code Alcar [63] and, except where explicitly stated, the same input physics, initial conditions, and, except for the time integration, numerical methods and parameters. We solve the equations of special relativistic hydrodynamics including a balance law for the electron fraction of the gas Y_e (see (8.9)). We account for the self-gravity of the star using a pseudo-relativistic gravitational potential (potential A of [85]). The spectral M_1 transport modules evolve the radiation energy and momentum density in a reference frame comoving with the fluid. The coupling between neutrino particle energies via velocity and gravitational terms, e.g., Doppler or gravitational red-/blue-shifts, are included up to first-order in V/c. We describe the thermodynamic properties of the gas using the nuclear equation of state (EoS) SFHo [121]. Strictly speaking, an EoS of this type, assuming that the composition of the gas is given by nuclear statistical equilibrium, is not valid for low temperatures and densities. Nonetheless, we simplify our setup by not including a transition to a sub-nuclear EoS below a threshold density. This choice has no implication for the tests at hand because the neutrino-matter interaction rates are very small at the densities where the transition between EoS regimes would take place.

We employ the spectral M_1 transport methods for the three species of neutrinos (electron ν_e, muon ν_μ, tau ν_τ neutrinos) and their antiparticles. Our set of neutrino-matter reactions contains the important interactions that dominate the dynamics of the collapse (see [63, 62] for implementation details):

- absorption and emission of ν_e and $\bar{\nu_e}$ by β processes of free neutrons and protons and nuclei,
- iso-energetic scattering of neutrinos of all flavours off nucleons and nuclei,
- pair creation of neutrinos of all flavours by electron-positron annihilation and nucleonic bremsstrahlung,

- non-iso-energetic scattering of neutrinos of all flavours off electrons and positrons.

We note that the last process is not written in terms of an opacity and thus our MIRK method does not apply. We treat it in an operator-split manner in the same way as described in [62]. In principle, the same holds for the pair processes. However, the approximate treatment of [92] reformulates the interaction in terms of opacities, which allows us to include them in the MIRK scheme.

8.4.2 Initial data and reference simulation

As a test case, we used the same model as in the comparison of neutrino-hydrodynamics codes of [105], i.e., the core of a star of a zero-age main-sequence mass of $M_{\mathrm{ZAMS}} = 15\,M_{\odot}$. Before presenting results of the new MIRK method implementation, we describe the dynamics of a reference simulation (denoted RK2) computed with the traditional scheme used in [63]. It uses a method similar to our first-order MIRK scheme as a building block in a second-order Runge-Kutta time integrator.

As the central density increases during collapse, electron captures deleptonize the matter and drive the electron fraction at the center to values $Y_{e,\mathrm{c}} \approx 0.28$ and the lepton fraction, including the net lepton number corresponding to ν_e and $\bar{\nu_e}$, to $Y_{l,\mathrm{c}} \approx 0.34$. These quantities assume a roughly constant level once the neutrinos are trapped inside the inner core as densities $\rho \gtrsim 10^{12}\,\mathrm{g\,cm^{-3}}$ render the gas optically thick. The shock wave launched at core bounce (time t_{b}) and the formation of the proto-neutron star (PNS) stalls about 70 ms later after having reached a maximum radius of $r_{\mathrm{sh;max}} \approx 145\,\mathrm{km}$, i.e., still inside the collapsing iron core (see Figure 8.1, second panel). It recedes slowly for another 90 ms to $r_{\mathrm{sh}} \approx 125\,\mathrm{km}$. Matter continues to fall through the shock wave and settles onto the PNS, which gradually contracts from a maximum radius of up to $r_{\mathrm{PNS}} \lesssim 80\,\mathrm{km}$ immediately after bounce to $r_{\mathrm{PNS}} \gtrsim 20\,\mathrm{km}$ at $t_{\mathrm{pb}} = 1\,\mathrm{s}$ (here we use the radius of the ν_e-sphere as a proxy for the PNS radius). By $t_{\mathrm{pb}} = t - t_{\mathrm{b}} \approx 150\,\mathrm{ms}$, the entire iron core has been accreted. Consequently, the density and ram pressure of the accreting matter drops, which causes a brief expansion of the shock by about 10 km. Neutri-

nos heat the post-shock gas, but, as is typical for spherically symmetric CCSNe, the conditions for shock revival and an explosion are never met. Thus, the shock wave gradually contracts to a radius below 50 km over the course of 1 s after bounce. The early neutrino emission is characterized by the intense burst of ν_e emitted in the first few tens of ms after bounce (third panel of the Figure 8.1). After the burst, the ν_e luminosity, L_{ν_e}, and those of the other two flavors reach slowly varying values of several $10^{52}\,\mathrm{erg/s}$. We find the typical ordering with almost equal luminosities of the electronic flavors and a lower emission of the heavy-lepton neutrinos as well as the dependence of the luminosities on the mass accretion rate that leads to the lower levels of L_ν after $t_{\mathrm{pb}} \sim 200\,\mathrm{ms}$. The mean energies (bottom panel) with values in the range of 10–25 MeV reflect the rising temperatures near three neutrinospheres of the three flavors with the sequence $e_{\nu_e} < e_{\bar{\nu_e}} < e_{\nu_X}$ following from the hierarchy of neutrino-matter cross sections.

8.4.3 First-order MIRK numerical simulations

The first-order MIRK scheme has two free parameters, a and b. We compare the four combinations of setting them to zero and to a non-zero value of $1/2$ (see Table 8.1). Simulation M1-1 with $a = b = 0$ satisfies the correct optically thick limit. It produces a stable simulation whose results are very close to those of the reference simulation, both in terms of the global evolution shown in the Figure 8.1 and in terms of the radial profiles of the Figure 8.2. The density profiles at representative epochs during the evolution (top panel) are almost identical to the ones of model RK2. The PNS at the center as well as the surrounding region of decreasing density do not show any notable difference between the two simulations. The only small discrepancies appear right at the shock wave where ρ falls by about an order of magnitude over a few km. The entropy and the electron/lepton fractions (second and third panels) are more sensitive than the density to the details of the neutrino treatment. Nevertheless, there are only minor deviations of model M1-1 from RK2. Apart from the shock wave, we only find small differences in the precise pattern of oscillations in the entropy behind the shock wave at late times ($t_{\mathrm{pb}} = 400\,\mathrm{ms}$). If anything, the MIRK simulations might be able to resolve the shock wave more sharply. Furthermore, there is a minor offset of Y_l

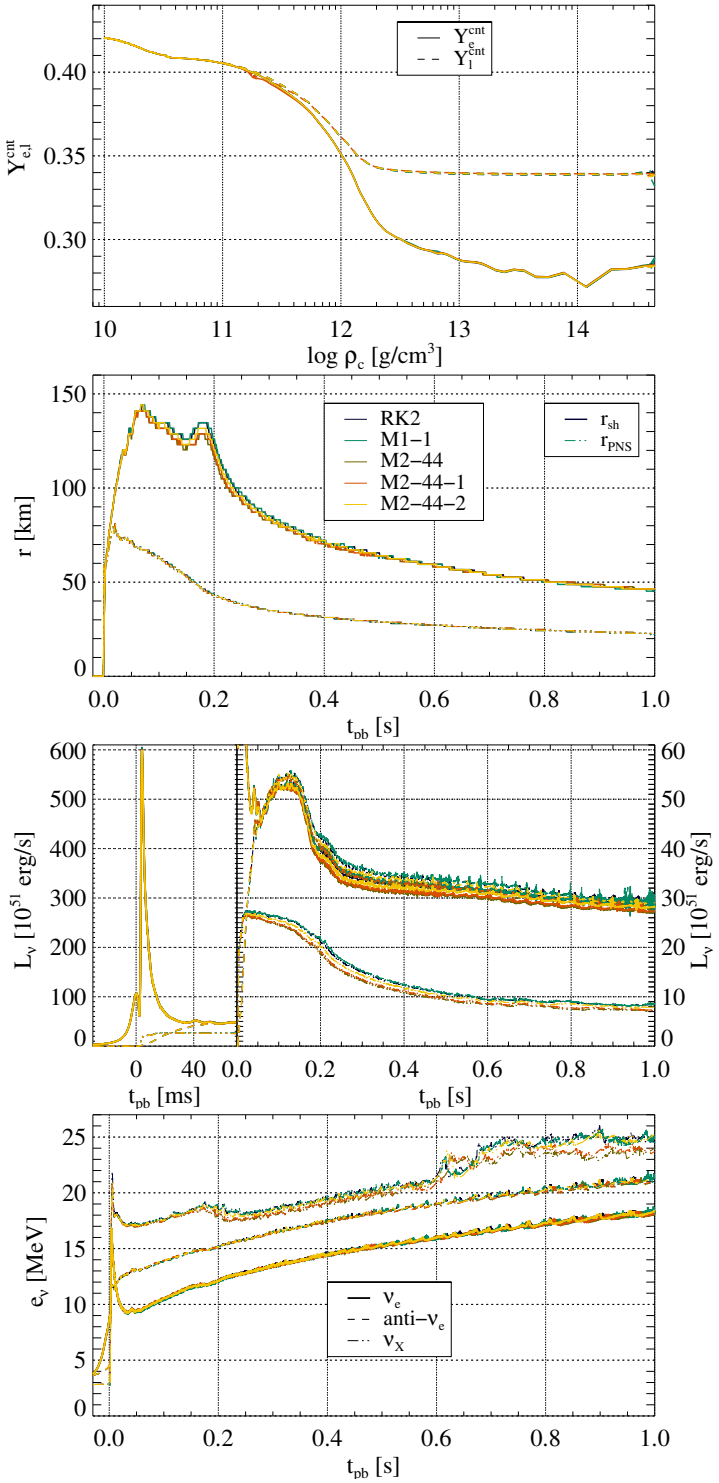

Figure 8.1: From top to bottom, evolution of the following quantities: central electron and lepton fractions as a function of central density during collapse; $r_{\rm sh}$, and $r_{\rm PNS}$, during the first second after bounce; luminosities of the three neutrino flavors, where left part focuses on the ν_e burst and the right part on the evolution until the end of the simulations; mean energy of the three neutrino energies. Models are distinguished by colors, according to the second panel (see the Tables 8.1 and 8.2).

model	a	b	result
M1-1	0	0	✓
M1-2	$1/2$	$1/2$	$\times$
M1-3	0	$1/2$	$\times$
M1-4	$1/2$	0	△

Table 8.1: List of first-order MIRK simulations. The first three columns give the name of the simulation, and the values of the parameters a and b. In the last column, the symbols ✓, △, and $\times$ indicate simulations that ran stably and with correct results, simulations that ran stably into the post-bounce phase, but gave wrong results, and simulations that turned unstable when the core reached optically thick conditions, respectively.

outside of the shock wave. This deviation turns out to be connected to the neutrinos, not the matter, as we find a similar offset in the profiles of the neutrino luminosities (bottom panel) exterior to the shock. Among the neutrinos, we point out the relatively pronounced temporal fluctuations of the heavy lepton species, ν_X, in particular of its mean energy, which we attribute to the fact that these neutrinos are generated and absorbed only via the relatively subdominant pair processes. Thus, they tend to bear the imprint of fluctuations at their production site at larger radii to a higher degree than the electron type neutrinos. In any case, the differences between the first-order MIRK run and the reference solution are entirely within the margins of uncertainty of the latter alone.

The correct limit in the optically thick limit of the momentum equation is a crucial requisite for the stability of the simulations. Models M1-2 and M1-3 with $(a, b) = (1/2, 1/2)$ and $(0, 1/2)$, respectively, which do not satisfy the asymptotically correct behavior (8.20b) for all, smooth and non-smooth, initial data, turn unstable once the core becomes optically thick at a central density $\rho_c \gtrsim 3 \times 10^{12}\,\mathrm{g\,cm^{-3}}$ (see Figure 8.3). The instability appears first in the form of strong fluctuations near the origin that spread outward and lead to a termination of the simulation before the bounce can occur.

Model M1-4 with $(a, b) = (1/2, 0)$ evolves stably and correctly through collapse and until immediately before bounce (Figure 8.4). The evolution of the central electron and lepton fractions agrees well with the reference model. After bounce, however, differences between the two models appear. Most notably, the central values of $Y_{e,l}$ do not stabilize at the levels they reached during neutrino trapping, but decrease further (note the drop of the two green lines in the top panel of the Figure 8.4 for $\rho_c \gtrsim 2 \times 10^{14}\,\mathrm{g\,cm^{-3}}$). After about 30 ms more, they reach a minimum around $Y_{e,l} \approx 0.065$, i.e., far below the correct values. Unlike in the ref-

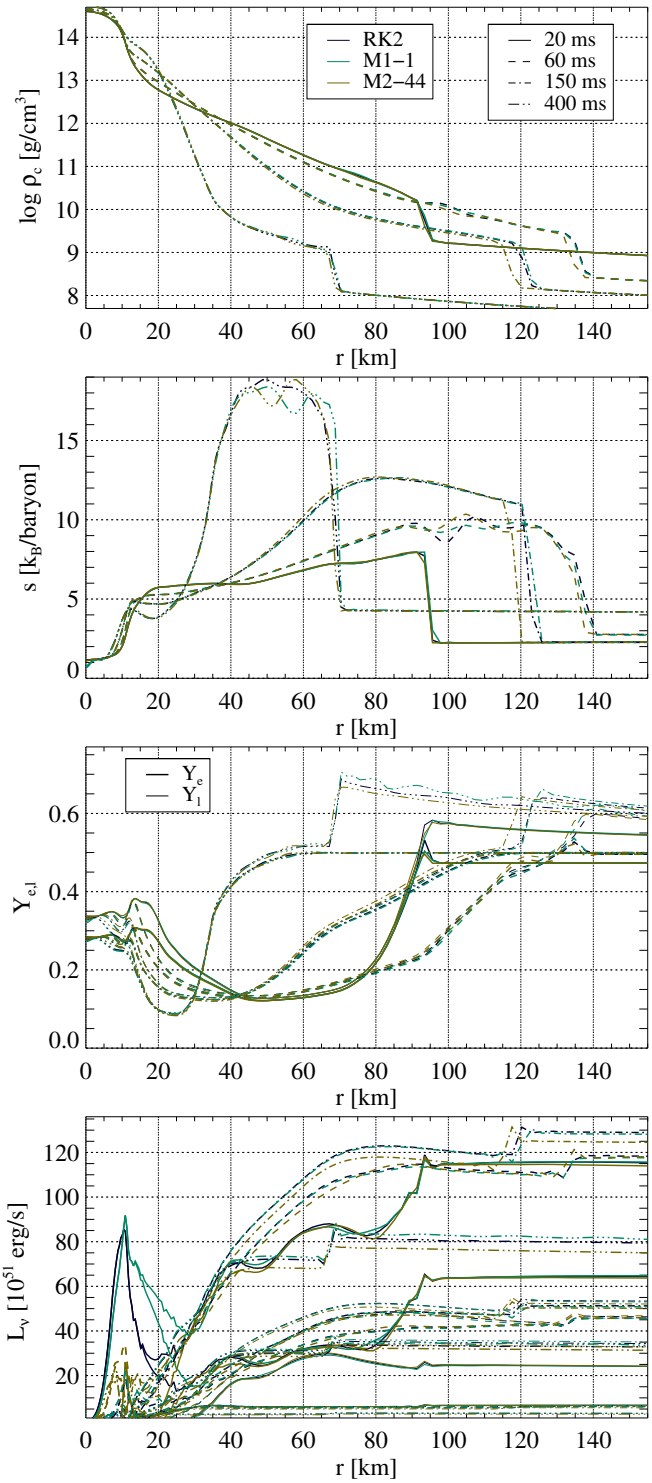

Figure 8.2: Radial profiles of selected models at a few times after bounce, as given in the legend in the top panel. Top panel: mass density. Second panel: specific entropy. Third panel: electron and lepton fractions (distinguished by line thickness, see legend). Bottom panel: total neutrino luminosities of all flavors.

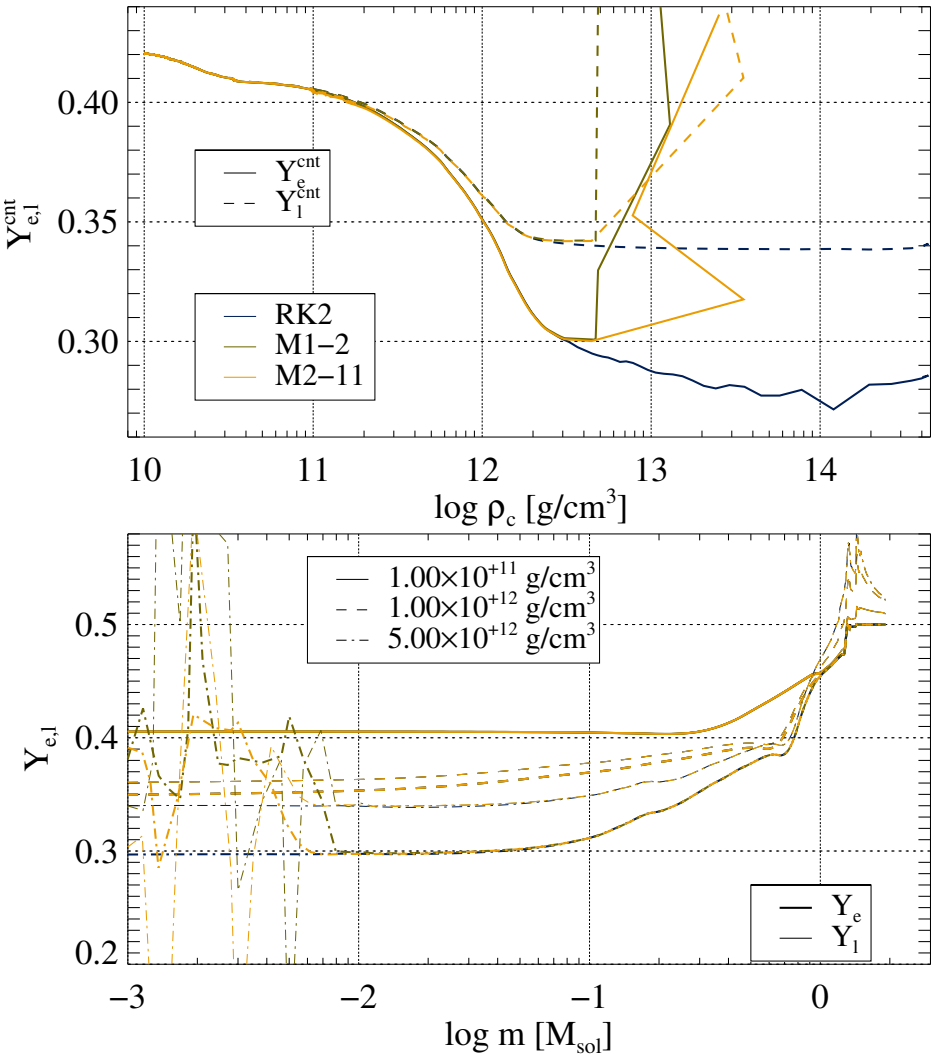

Figure 8.3: Comparison of unstable simulations, as indicated in the legend, to the reference simulation. Top panel: evolution of the central electron and lepton fractions as function of central density during collapse. Bottom panel: profiles of Y_e and Y_l as functions of Lagrangian mass coordinates at the times at which the central density assumes the three values indicated in the legend.

erence case, the two variables are almost equal at $r = 0$ throughout the entire post-bounce evolution (see third panel of the Figure 8.5), i.e., the net neutrino lepton number is close to zero. Additionally, the center of the PNS is hotter at almost twice the entropy of that of RK2 (second panel).

Discrepancies between the models are present in the ν_e burst, mostly in the form of larger fluctuations in all three flavors. Afterwards model M1-4 emits a considerably lower L_{ν_e} and higher $L_{\bar{\nu}_e}$ than RK2. The mean neutrino energies lie below the ones of RK2.

Additional differences appear in the structure of the core. Until $t_{\mathrm{pb}} \approx 20\,\mathrm{ms}$, the shock wave transiently expands faster than in RK2. This phase is characterized by the appearance of a bump in density (see top panel of the Figure 8.5, t_{pb}, at $r \approx 60\,\mathrm{km}$) absent from the reference case and marked differences in the entropy and $Y_{e,l}$ profiles (second and third panels). Whereas the shock wave starts to recede in the reference model after it reached its furthest expansion at $t_{\mathrm{pb}} \approx 70\,\mathrm{ms}$, it stays in M1-4 at the same radius for another 90 ms before expanding up to $r_{\mathrm{sh}} \approx 158\,\mathrm{km}$ and retreating only thereafter. The main differences between the models are found in the PNS, which is less dense with a shallower ρ profile, hotter and neutron-richer in M1-4 than in RK2. In the surrounding hot bubble, the differences are less pronounced, but still far larger than the ones between the reference model and M1-1. Finally, a numerical instability develops in the PNS after almost 400 ms of post-bounce evolution.

To summarize, our MIRK scheme is able to reproduce the results of the reference simulations stably and correctly if the parameters a and b for the energy and momentum equations, respectively, are chosen such that they satisfy the correct limit in the optically thick regime. Using a different parameter in the momentum equation, i.e., $b \neq 0$ makes the simulations unstable once neutrinos are trapped by scattering reactions. The choice $b = 0$, but $a \neq 0$, i.e., obeying the constraints in the momentum, but not the energy equation, cures this instability, but results in incorrect results once, near bounce, the emission/absorption reactions become stiff as well. The simulation can continue for several 100 ms thereafter, but the PNS properties are wrong and eventually a numerical instability ensues.

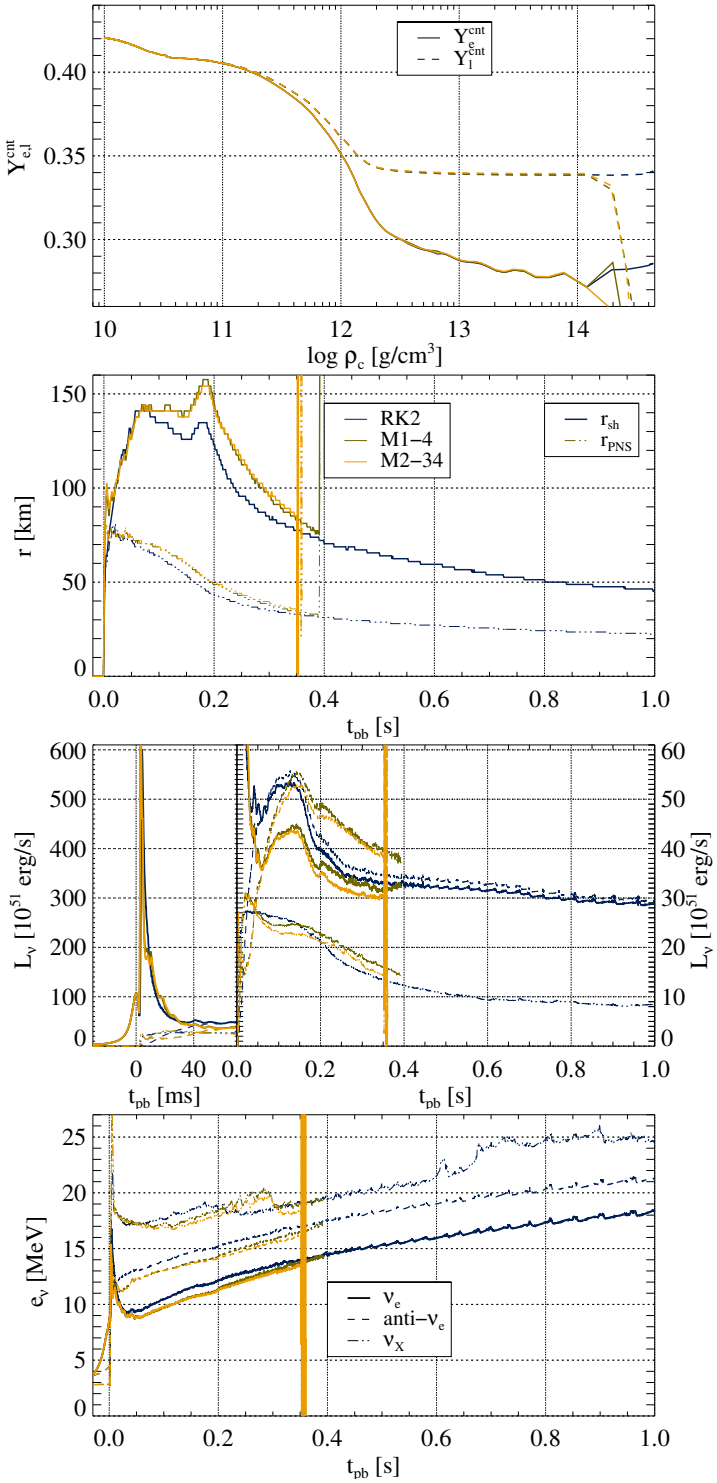

Figure 8.4: Similar plots as in the Figure 8.1, but comparison of simulations that evolve stably beyond bounce but produce incorrect results, as indicated in the legend, to the reference numerical solution.

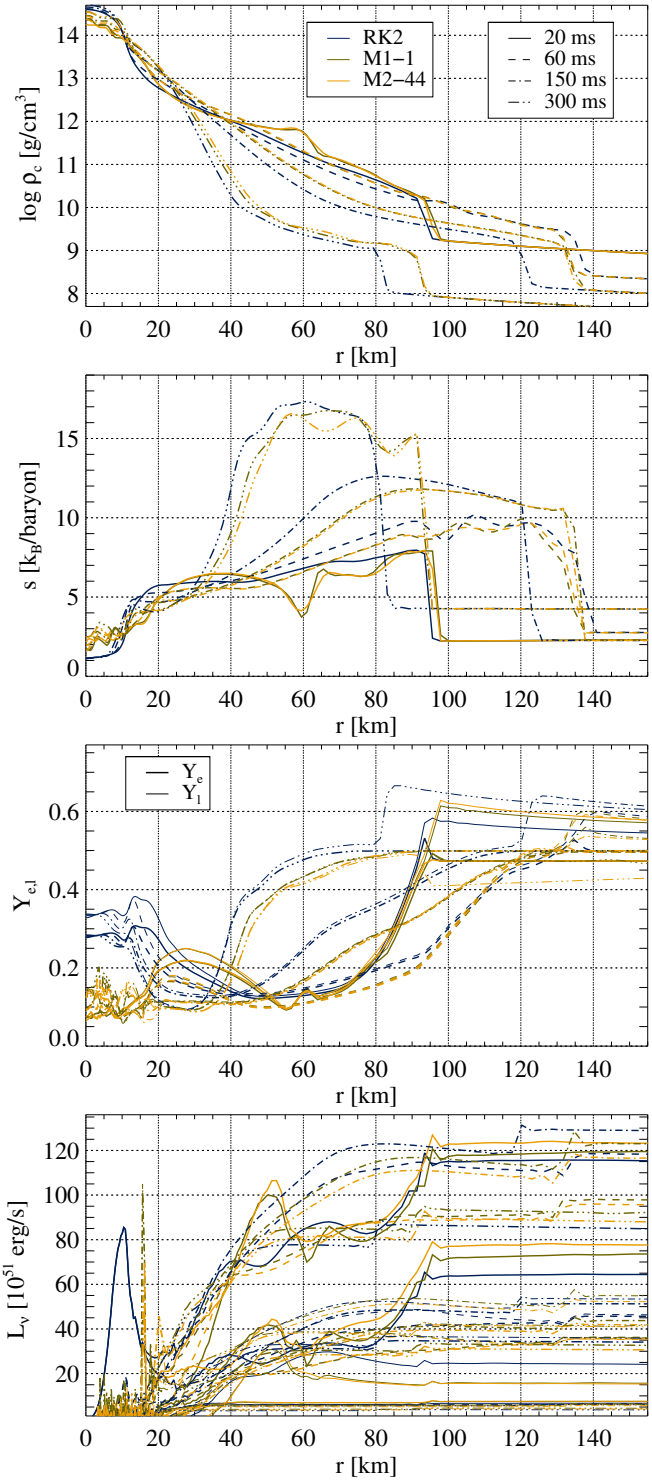

Figure 8.5: Similar plots as in the Figure 8.2, but comparison of simulations that evolve stably beyond bounce but produce incorrect results, as indicated in the legend, to the reference numerical solution.

8.4.4 Second-order MIRK numerical simulations

We performed a series of simulations using the second-order MIRK scheme and explore the evolution for various combinations of the four parameters a, a', b, b' (see Table 8.2). The basic set of simulations consists of the 16 models M2-11, ..., M2-44, in which we set, following the possible choices introduced in the Section 8.3, $a \in \{1/2, -1/2\}$ and $a' = \frac{a-1}{2} \in \{-1/4, -3/4\}$ or $a' = \frac{(1-a)^2}{2a} \in \{1/4, -9/4\}$, and analogously for b and b' (see Table 8.3 for the values of these two functions for all the parameters we have used). The nomenclature of the models is given by the following systematic scheme: the last two digits of the generic model name M2-AB indicate the values of the parameters a and b. Indices $\mathrm{A} = 1, 2, 3, 4$, stand for values $(a, a') = (a, \frac{a-1}{2}) = (1/2, -1/4)$, $(a, a') = (a, \frac{(1-a)^2}{2a}) = (1/2, 1/4)$, $(a, a') = (a, \frac{a-1}{2}) = (-1/2, -3/4)$, and $(a, a') = (a, \frac{(1-a)^2}{2a}) = (-1/2, -9/4)$, respectively, and analogously for index B and parameters (b, b').

We find the same three evolutionary paths as in the first-order case. Most combinations result in a numerical instability at the onset of neutrino trapping, as shown for the example of model M2-11 in the Figure 8.3. As in the unstable first-order runs, the instability develops in the optically thick core and causes catastrophic oscillations in the electron and lepton fractions which quickly lead to a termination of the simulations.

All simulations with $(b, b') = (b, \frac{(1-b)^2}{2b}) = (-1/2, -9/4)$ avoid this instability, irrespective of the values of a and a'. However, within the basic set of the 16 models M2-11 – M2-44 only the choice $a < 0$ and $a' = \frac{(1-a)^2}{2a}$ produces stable and correct results that, like for M1-1, agree very well with the reference simulation both in the evolution of global quantities (Figure 8.1) and in the profiles at specific times (Figure 8.2). The differences with model RK2 are limited to minor details such as the width of the shock wave (second panel of the Figure 8.2) or a small offset in the neutrino luminosity outside the shock wave.

Models M2-41, M2-42, and M2-43 with $(b, b') = (-1/2, -9/4)$ and $(a, a') \neq (-1/2, -9/4)$ show the same behavior as model M1-4 (see Figures 8.4 and Figure 8.5). Until close to the point at which the source terms in the energy equation become stiff, they follow the reference simulation. At that point, however, they yield an incorrect PNS with too low $Y_{e,l}^{\mathrm{cnt}}$, too shallow density profiles, and too low entropy. The luminosities and mean ener-

model	a	a'	b	b'	result
M2-11	$+1/2$	$-1/4$	$+1/2$	$-1/4$	$\times$
M2-12	$+1/2$	$-1/4$	$+1/2$	$+1/4$	$\times$
M2-13	$+1/2$	$-1/4$	$-1/2$	$-3/4$	$\times$
M2-14	$+1/2$	$-1/4$	$-1/2$	$-9/4$	$\triangle$
M2-21	$+1/2$	$+1/4$	$+1/2$	$-1/4$	$\times$
M2-22	$+1/2$	$+1/4$	$+1/2$	$+1/4$	$\times$
M2-23	$+1/2$	$+1/4$	$-1/2$	$-3/4$	$\times$
M2-24	$+1/2$	$+1/4$	$-1/2$	$-9/4$	$\triangle$
M2-31	$-1/2$	$-3/4$	$+1/2$	$-1/4$	$\times$
M2-32	$-1/2$	$-3/4$	$+1/2$	$+1/4$	$\times$
M2-33	$-1/2$	$-3/4$	$-1/2$	$-3/4$	$\times$
M2-34	$-1/2$	$-3/4$	$-1/2$	$-9/4$	$\triangle$
M2-41	$-1/2$	$-9/4$	$+1/2$	$-1/4$	$\times$
M2-42	$-1/2$	$-9/4$	$+1/2$	$+1/4$	$\times$
M2-43	$-1/2$	$-9/4$	$-1/2$	$-3/4$	$\times$
M2-44	$-1/2$	$-9/4$	$-1/2$	$-9/4$	✓
M2-44-1	$-1/4$	$-25/8$	$-1/4$	$-25/8$	✓
M2-44-2	$-1/16$	$-289/32$	$-1/16$	$-289/32$	✓
M2-44-3	$-1/2$	$-9/4$	$-1/4$	$-25/8$	✓
M2-44-4	$-1/4$	$-25/8$	$-1/2$	$-9/4$	✓
M2-51	$-1/2$	$-9/4$	$3/4$	$1/24$	$\times$
M2-52	$-1/2$	$-9/4$	$3/4$	$-1/8$	$\times$
M2-53	$3/4$	$1/24$	$3/4$	$1/24$	$\times$
M2-54	$3/4$	$-1/8$	$-1/2$	$-9/4$	$\triangle$
M2-55	$3/4$	$1/24$	$-1/2$	$-9/4$	✓

Table 8.2: List of second-order MIRK simulations. The first five columns give the name of the simulation, the values of the parameters a, a', b, and b'. The symbols in the last column have the same meaning as in the Table 8.1.

x	$\frac{x-1}{2}$	$\frac{(1-x)^2}{2x}$
$-1/2$	$-3/4$	$-9/4$
$-1/4$	$-5/8$	$-25/8$
$-1/16$	$-17/32$	$-289/32$
$1/2$	$-1/4$	$1/4$
$3/4$	$-1/8$	$1/24$

Table 8.3: Values of $x = (a, b)$ (first column) and the corresponding values of the functions used to compute $x' = (a', b')$ (second and third columns).

gies show the same deviations from RK2 as found in M1-4, and all models suffer the same numerical instabilities after a time of $t_{\rm pb} \sim 300 - 400\,{\rm ms}$.

We added models M2-44-1 – M2-44-4 similar to M2-44. Their results agree well with those of model M2-44, indicating that stability and accuracy do not depend on the specific values as long as $(a', b') = \left(\frac{(1-a)^2}{2a}, \frac{(1-b)^2}{2b}\right)$ and $a, b < 0$.

Another group of simulations, models M2-51 – M2-55, probe positive values of a and b between $1/2$ and 1, which according to the Equations (8.31a) and (8.31b) could also lead to a stable evolution. However, we find that all simulations with $b = 3/4$ are unstable. If we set, as in M2-44, $(b, b') = (-1/2, -9/4)$, we obtain a stable and correct simulation with $(a, a') = (3/4, 1/24)$ and a stable, but incorrect one with $(a, a') = (3/4, -1/8)$.

Hence, we find that, similarly to the first-order schemes, the stability is set by the parameters for integrating the momentum equation: only $b' = \frac{(1-b)^2}{2b}$ and $b < 0$ are stable. Among these, the ones for which the parameters for the energy equation fulfil the constraint $a' = \frac{(1-a)^2}{2a}$ and $a < 0$ or $1/2 < a < 1$ are also correct.

8.5 Final remarks

We have derived a MIRK method for the M_1 equations for neutrino transport. We use it to treat the neutrino matter interaction terms describing reactions such as absorption, emission, and scattering in an operator-split manner separately from the (hyperbolic) transport terms of an M_1 method. In general, the stiffness of the interaction terms in the optically thick regime poses a stability problem for their time integration. The problem can be overcome by fully implicit methods, but these can be very costly because of the complex dependence of the reaction rates on the neutrino fields and the thermodynamic state of the matter. The proposed approach reduces the use of implicit terms to the minimum required for stability by evaluating the opacities and the thermodynamics at the original time step. This choice makes the resulting scheme take a form similar to that of an explicit method. The first-order method is a straightforward modification of an explicit scheme with an effective,

reduced time step that guarantees the stability. This method is similar to the one that has already been used in this context in the neutrino-hydrodynamics code Alcar [63]. Here we give a mathematical framework and a generalization to a second-order method that retains the simplicity of the first-order one.

The second-order method depends on two numerical parameters. We demonstrate that these parameters can be chosen in such a way that they satisfy an algebraic condition that guarantees the correct optically thick limit for the source terms for neutrino energy and momentum. In this case, the new time integrator gives stable and accurate results in simulations of the collapse of stellar cores, as we show by implementing it in the code Alcar and comparing it to its traditional solver. If, on the other hand, these conditions are violated, the simulations become unstable once the core turns optically thick.

Our scheme is simple and efficient and can be used in a wide range of similar applications. We already applied it in [29] for the RRMHD equations, whose contents were presented in the previous Chapter. In future works in supernovae simulations, we will explore more general sets of parameters, the incorporation of more complex reactions such as pair processes, and a combination with a well-balanced method scheme [22] for the fluxes. Other examples, already stated, are rarefied gases contexts [66], shallow water equations [65] or force-free electrodynamics in General Relativity [82].

9

Realistic equation of state for nuclear matter

In the Chapter 4 we introduced the theory of gravitation. We addressed a simple scenario in spherical symmetry in the Chapter 5, where we focused on the hydrodynamic sector and in the Chapter 6 we solved the Einstein Equations numerically in the context of a rotating neutron star. There, we solved a reformulation of the FCF of Einstein Equations. In all these chapters, a polytropic EoS was always the model to describe the fluids involved. However, we know that this simple model does not describe real matter in general. For instance, in the Chapter 8 we used a more realistic EoS called SFHo [121] to describe a CCSNe. Another case which requires a realistic EoS are neutron stars. In black holes all information is kept inside the event horizon. However, a neutron star, the second densest compact object observed in the universe, does not have any horizon. Then, we are able to access to some information about the structure of the matter they are made of. An object of such extreme density is composed of matter which properties are poorly know, and the

determination of the EoS in this case is arduous. Tabulated data computed from particle and nuclear physics are available, from which we can carry out numerical simulations with neutron stars. The simulated results could be compared to observations in order to study the viability of EoS data. Unfortunately, tabulated data add noise in the numerical simulations in such way they may become unstable. A strategy to smooth these data is needed and, in this chapter, we will develop an algorithm to carry out polynomial regression in several variables to address this problem.

9.1 Numerical issues with realistic equations of state

Gravitational waves have become a new way to explore the universe, complementary to the electromagnetic waves. Information about matter of neutron stars is accessible by these channels. Modeling EoS for neutron stars in order to perform numerical simulations is important. If we are able to simulate astrophysical events with any type of EoS, to be compared with observables from detections, one can get constraints about this type of matter. Binary coalescence or oscillations of neutron stars beyond axisymmetry are events subject to emit gravitational waves.

The main problem is the lack of knowledge about the true EoS for these objects. Considering different approaches is possible in numerical simulations. Polytropic EoS are a simple choice, but it is more realistic to consider data from particle and nuclear physics computations which are tabulated in CompOSE [1]. In this Chapter we will study and develop numerical techniques that will help applying realistic EoS. It turns out that the data from CompOSE tables are noisy enough to make simulations unstable. Then, a polynomial fit of these data will be derived to smooth them. The main contribution of this Chapter is to provide an algorithm to carry out this task with EoS of one, two and three independent variables. Data from CompOSE tables provide values of thermodynamic quantities as a function of the number baryon density n_b, the electron fraction Y_e and the temperature T. Realistic matter should be modeled by EoS depending on these three independent variables. Nonetheless, using one

or two variables are the convenient previous steps.

The aim is that the work developed in this Chapter will be applied in simulations with oscillating neutron star, but in this manuscript we will not detail this complex phenomena. To get some knowledge about this topic, we refer the reader to [109]. Simulations will use the software LORENE [2], which relies on the spectral decomposition of functions. The work presented in this Chapter is not focused on the simulations themselves, but in the development of some C++ scripts to be coupled with LORENE and that will manage the EoS sector.

9.2 Thermodynamic relations

Polynomial fits will provide us analytic expressions for the adiabatic index. The thermodynamic relations in this Section will be used to compute some thermodynamic variables from the adiabatic index. The thermodynamic variables describe matter of neutron stars. Some of the expressions of this Section have been derived by the researcher Gaël Servignat from the Observatoire de Paris-Meudon or have been gathered from [115] and [127]. Basic variables under consideration are the total energy density μ, the pressure p, the entropy S and the baryon number density n_b. The definition of the velocity of sound is

$$c_s^2 := \left(\frac{\partial p}{\partial \mu}\right)_{S,\, N_b,\, N_e}, \tag{9.1}$$

where N_b and N_e are the baryon number and the electron number, respectively.

If we suppose zero temperature and β equilibrium, the baryon number density n_b can be used as unique independent variable. In that case, one can arrive to the following expression

$$c_s^2 = \frac{p}{\mu + p}\frac{d\log p}{d\log n_b}. \tag{9.2}$$

and the adiabatic index is defined as

$$\Gamma_1 = \frac{d\log p}{d\log n_b}. \tag{9.3}$$

Let us define the chemical potential of the baryon matter μ_b as $\mu_b = d\mu/dn_b$. On the other hand, we can write the first law of thermodynamics as

$$\mu = \mu_b n_b - p, \tag{9.4}$$

But using n_b as independent variable may be cumbersome as it is not continuous in general, for instance at the surface of the star or in regions where a phase transition happens. Then, it is convenient to work with the enthalpy h defined as

$$h = \frac{\mu + p}{n_b m_b}, \tag{9.5}$$

where m_b is the neutron mass. In fact, we will use the log-enthalpy $H = \log h$. Considering differentials of the first law of thermodynamics (9.4) and using the definition of the chemical potential, one arrives to the expression

$$\frac{dp}{dH} = \mu + p, \tag{9.6}$$

and we also can get the following relation:

$$\Gamma_1 = \frac{p'^2}{p(p'' - p')}, \tag{9.7}$$

with $p' = dp/dH$. In previous Chapters we have mentioned that an EoS is given by an expression of the form $p = p(\mu)$. Another form of giving an EoS is to provide Γ_1 in terms of the rest of variables. Suppose that we have $\Gamma_1 = \Gamma_1(H)$. Now, we define $\Pi = \log p$ and $Y = 1/\Pi'$, where the prime denotes derivative with respect to H. We can derive the following ordinary differential equation (ODE):

$$Y' + Y = \frac{\Gamma_1 - 1}{\Gamma_1}. \tag{9.8}$$

Integrating this ODE, one can obtain the variables Y, Π and p. Once we get $p = p(H)$, other important quantities can be computed easily. The sound velocity is given by

$$c_s^2 = Y\Gamma_1, \tag{9.9}$$

the total energy density is

$$\mu = p\left(\frac{1}{Y} - 1\right), \tag{9.10}$$

and the baryon number density is

$$n_b = \frac{p}{e^H Y m_b}. \tag{9.11}$$

Now, we consider two independent variables by adding the electron fraction Y_e to H. As stated in [127], several definitions for the adiabatic index are used in astrophysics. We will use the following choice:

$$\Gamma_1 := \left(\frac{\partial \log p}{\partial \log n_B}\right)_{Y_e}. \tag{9.12}$$

In that case, we recover a similar expression as for one independent variable (9.7) but substituting p' by $(\partial p/\partial H)_{Y_e}$. A differential equation of the form (9.8) also holds substituting derivative by a partial derivative. Then we can easily extend the procedure of one independent variable to two independent variables. Another reasonable choice could have been

$$\Gamma_1 := \left(\frac{\partial \log p}{\partial \log n_B}\right)_{n_e}, \tag{9.13}$$

in resemblance with the sound speed in several variables. Then, we get the following expression:

$$\Gamma_1 = \frac{\dot{p}^2}{p(\ddot{p} - \dot{p})}, \tag{9.14}$$

with $\dot{p} = (\partial p/\partial H)_{n_e}$. The problem in this case arises when one wants to stick using H and Y_e as independent variables, because from the relation

$$\left(\frac{\partial p}{\partial H}\right)_{n_e} = \left(\frac{\partial p}{\partial H}\right)_{Y_e} - \frac{Y_e \left(\frac{\partial n_B}{\partial H}\right)_{Y_e}}{Y_e \left(\frac{\partial n_B}{\partial Y_e}\right)_H + n_B} \left(\frac{\partial p}{\partial Y_e}\right)_H, \tag{9.15}$$

where we have used Maxwell thermodynamic relations, we find that Γ_1 and p are related by a complex partial differential equation (PDE), making computations trickier.

9.3 EoS and polynomial regression

In this section, we explain how to use a realistic tabulated EoS in Numerical Relativity simulations with the open source C++ library LORENE. We have already stated the numerical problems that arise when using realistic EoS data from CompOSE. A polynomial fit of such data is necessary and this is widely applied in EoS with one free parameter. In this

section, we will describe the procedure and extend the implementation to EoS with two and three free parameters. We will use the relations of the Section 9.2 to compute smooth data from the fitted data. Before doing it, we will describe some important features of LORENE.

9.3.1 Spectral method software: LORENE

We do not plan to give an extensive description of the LORENE library, but just some basic ideas about the file structure. To learn more about LORENE, the reader can consult the manual in [2].

Spectral methods

LORENE is based in the approximation of functions by a finite expansion of the form

$$\sum_{i=0}^{N} c_i \phi_i, \tag{9.16}$$

where ϕ_i is a member of the base of the norm space

$$L^2_\omega(I) := \{f \text{ such that } \int_I f(x)^2 \omega(x) dx < \infty\}, \tag{9.17}$$

being ω a function with integrable square called weight. $L^2_\omega(I)$ is a Hilbert space with the scalar product

$$\langle f, g\rangle = \int_I f(x) g(x) \omega(x) dx \tag{9.18}$$

for $f, g \in L^2_\omega(I)$. Any derivative of a function is again approximated by an expression of the type (9.16). This type of approximation is the main idea of spectral methods to numerically solve PDEs. The order of convergence of spectral methods is exponential in N, much more efficient than finite differences or finite volumes methods. Nonetheless, this rate of convergence is only valid when functions satisfy certain regularity requirements. Chebyshev polynomials are orthogonal base functions for $\omega(x) = 1/\sqrt{1-x^2}$, and they are the ones used by LORENE.

Files structure

LORENE has a lot of directories with pre-established physical cases in the main directory. Inside each one, we find parameter files that settles the physics and the numerical resolution. In the Figure 9.1 we show the structure of the files and directories we are interested in. For example, inside `RotStar/Dirac` we find a parameter file called `parrot.d` to set some parameters about a rotating star case, as the angular velocity or the central density. This case in particular imposes Dirac gauge.

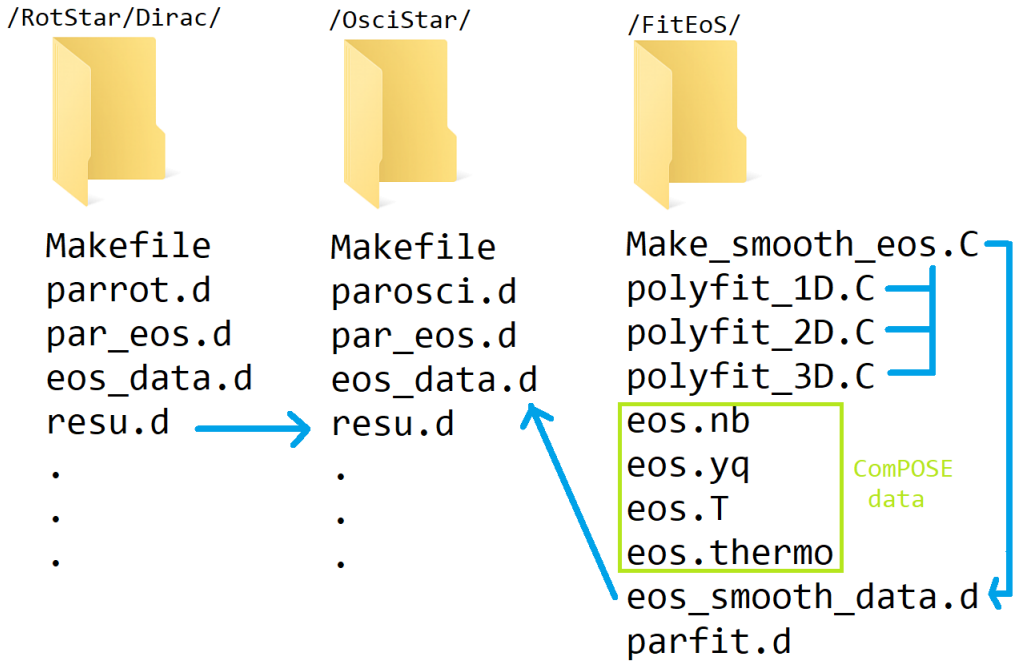

Figure 9.1: Structure of files and directories we are focused on.

Nonetheless, we focus on the file `par_eos.d` which settles the type of EoS. There, we can fix a polytropic EoS or, if we want to set a more complex one, we have the chance to create a file, call it `eos_data.d`, with structured data about density, energy and pressure.

The aim is to implement smooth data of realistic EoS to simulations of oscillating neutron stars. Results (called `resu.d` in the Figure 9.1) from non-oscillating rotating star will serve as initial data.

We will consider realistic EoS given through tabulated data from CompOSE [1]. We will detail how the polynomial regression of these data

have been done and how to create the file `eos_data.d` containing the smoothed data.

9.3.2 Polynomial regression of CompOSE data

In the website of CompOSE one can download different data files with thermodynamical quantities. In particular, in this subsection, we select the type SLy4. We consider a particular version tagged as "one-parameter cold neutron star EoS". We can choose several versions depending on the number of independent variables, but let us schedule the whole procedure for one independent variable first.

One independent variable approach

We download the files `eos.nb` and `eos.thermo`. A detailed description of these files can be found in the manual of CompOSE [127]. The file `eos.nb` is just a list of the values for the baryon number density n_b, and the file `eos.thermo` is a list for several thermodynamic variables of interest.

Once we have the data from CompOSE the fit is managed by a C++ script that we are calling `Make_smooth_eos.C`. We show in the Box 9.1 its structure in pseudo-code.

```
read par_fit.d
read eos.nb, eos.thermo
store nb, p, e
compute H, Gamma
call function polyonomial_fit_1D (H, Gamma, N)
compute Gamma_fit, Y, Pi, p_fit, e_fit, nb_fit
write eos_smooth_data.d
```

Box 9.1: Pseudo-code of the script `Make_smooth_eos.d`, that reads CompOSE data, carries out the one-parameter polynomial fit of the adiabatic, computes thermodynamic quantities and creates `eos_smooth_data.d` with smooth tabulated data to be read with LORENE

After reading a parameter file and CompOSE data, we build arrays to store the information about n_b, p and μ. Then, we are able to compute the log-enthalphy H and the adiabatic index Γ_1 with expressions of the Section 9.2. The polynomial fit is to be done to the adiabatic index Γ_1, taking H as independent variable. For one independent parameter or variable, we will simply use

$$p_N(x) = a_0 + a_1 x + a_2 x^2 + ... + a_N x^N, \tag{9.19}$$

where $N \in \mathbb{N}$. We proceed by applying a previously built C++ function called `polynomial_fit_1D`, which gives the coefficients a_i of the polynomial fit (9.19) using the least squares method. At this point, it is interesting to remark that LORENE deals with expressions of the form (9.16), with ϕ_i being the Chebyshev polynomials:

$$p_N(x) = c_0 T_0(x) + c_1 T_1(x) + c_2 T_2(x) + ... + a_N T_N(x). \tag{9.20}$$

Notice that there is a linear transformation from the coefficients a_i in (9.19) to the coefficients c_i in (9.20). The way LORENE stores the information of the fitted Γ_1 will be by means of the coefficients c_i.

At this stage we have an adiabatic index which is smooth enough to get rid of the noise instability problems. Then, making use of the Equations (9.8),(9.10) and (9.11), we can get the pressure, energy density and baryon number. These variables are also smooth enough to preserve stability. In the last line of the Box 9.1 the file `eos_smooth_data.d` is created from the smooth expressions of the thermodynamic variables. Then, providing "smooth" data.

Two independent variables approach

In general, not only n_b is cast as independent variable but also the electron fraction Y_e and the temperature T. In CompOSE we can select several EoS that depend on these three parameters. In those cases, we need to download files with temperature data `eos.t` and electron fraction data `eos.yq`. In this Subsection we will focus on two independent variables, n_b and Y_e, but the case with three variables can be derived analogously. When the definition 9.12 is considered for the adiabatic index, we can repeat the whole procedure as for one parameter EoS by substituting primes by partial derivatives. The scheme is quite similar to that in the Box 9.1, including also the corresponding data for the new independent variable Y_e, and performing a two-parameter polynomial regression. The Box 9.2 shows the pseudo-code of the modified script

`Make_eos_smooth.C`. The two-parameter polynomial fit is carried out by the previously built C++ function `polyonomial_fit_2D`. The regression is done using the following expression of a polynomial of degree N in two variables:

$$\begin{aligned} p_N(x,y) =& a_0 + a_1 x + a_2 x^2 + ... + a_N x^N + a_{N+1} y + a_{N+2} xy + ... \\ & + a_{k(i,j)} x^i y^j + ... + a_M y^N, \end{aligned} \tag{9.21}$$

where $M = (N+2)(N+1)/2$ is the number of coefficients a_i in this expansion. Note that LORENE only manages one-parameter expansions of the

```
read par_eos.d
read eos.nb, eos.yq, eos.thermo
store nb, yq, p, e
compute H, Gamma
call function polyonomial_fit_2D (H, yq, Gamma, N)
compute Gamma_whole
for each yq
     compute Y, Pi, p, e, nb
end
write eos_smooth_data.d
```

Box 9.2: Pseudo-code of the modified script `Male_eos_smooth.C`, that reads CompOSE data, carries out the two-parameter polynomial fit of the adiabatic index, computes thermodynamic quantities and creates the file `eos_smooth_data.d` with smooth tabulated data ready to be read with LORENE.

form (9.20). However, we would need expansions of the form

$$p_N(x,y) = \sum_{i+j=0}^{N} a_{ij} T_i(x) T_j(y) \tag{9.22}$$

which specifically considers two independent variables. First, we consider the two-parameter polynomial fit of the adiabatic index, $\Gamma_1(x,y) = p_N(x,y)$; second, we evaluate the second parameter of this fit at each Y_e value of our EoS data, $\Gamma_1(x,\hat{y}) = p_N(x,\hat{y})$, where $\hat{y} = (Y_e)$; third, expressions (9.8),(9.10) and (9.11) are used to derive the pressure, energy and number density as one-parameter polynomials evaluated at $(x,\hat{y})$. Then, the rest of the thermodynamic variables are computed from the previous quantities. Doing so, we go from an expression of the form (9.21) to the

following one-parameter expression

$$\begin{aligned} p_N(x,\hat{y}) =& a_0 + a_1 x + a_2 x^2 + ... + a_N x^N + a_{N+1}\hat{y} + a_{N+2} x\hat{y} + ... \\ &+ a_{k(i,j)} x^i \hat{y}^j + ... + a_M \hat{y}^N = b_0 + b_1 x + b_2 x^2 + ... + b_N x^N , \end{aligned} \tag{9.23}$$

where the coefficients $b_i = b_i(a_i, \hat{y})$. In the Figure 9.2 we show the smoothed data for the adiabatic index Γ_1 and the pressure p, obtained with the procedure just described. Data derived from the CompOSE are also plotted.

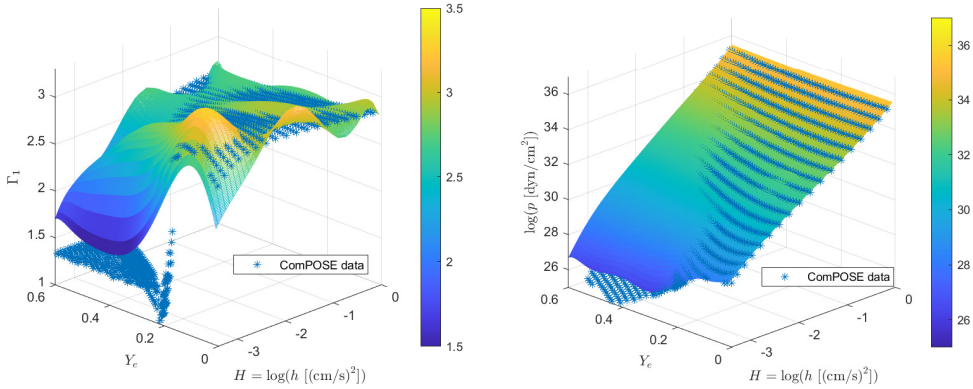

Figure 9.2: Profiles of the smoothed data from polynomial regression with the data from CompOSE, for the adiabatic index Γ_1 (left) and the pressure p (right).

We provide more details of the algorithm that has been developed to carry out the multivariable polynomial fit in the rest of the Chapter. We will derive the explicit form of the dependence $b_i = b_i(a_i, \hat{y})$ in (9.23).

9.3.3 Multivariable polynomial regression

The method of least squares is widely used in science. Let us introduce some expressions in one variable that will serve us to fix some notation for the multivariable case.

One-parameter polynomial regression

We use the arrays x and y (say of length n) representing H and Γ_1

$$\begin{array}{llll} x = (H_1 & H_2 & ... & H_n) \\ y = ((\Gamma_1)_1 & (\Gamma_1)_2 & ... & (\Gamma_1)_n) \end{array} \tag{9.24}$$

to carry out the polynomial fit of the adiabatic index to an expression of the form

$$p_N(H) = a_0 + a_1 H + a_2 H^2 + ... + a_N H^N. \tag{9.25}$$

The number of coefficients a_i in (9.25) is $N+1$. So we need $n \geq N+1$ for the regression to make sense. Let the x-Vandermonde matrix be

$$A^x = \begin{pmatrix} 1 & H_1 & H_1^2 & ... & H_1^N \\ 1 & H_2 & H_2^2 & ... & H_2^N \\ \vdots & \vdots & \vdots & \vdots & \vdots \\ 1 & H_n & H_n^2 & ... & H_n^N \end{pmatrix}. \tag{9.26}$$

A^x is a matrix of dimension $n \times (N+1)$. We define the vector of dimension $N+1$

$$\beta = y A^x, \tag{9.27}$$

and the symmetric matrix $(N+1) \times (N+1)$

$$\alpha = (A^x)^T A^x, \tag{9.28}$$

which has maximum rank if $H_i \neq H_j$ for $i \neq j$. Then the coefficients a_i of the polynomial fit by least squares can be computed as

$$(a_0, a_1, ..., a_N) = \beta \alpha^{-1}. \tag{9.29}$$

We show in Box B.1 in pseudo-code the function `polynomial_fit_1D` that applies the least square method in one variable.

Let us explain now the strategy followed to carry out a polynomial fit in two and three dimensions. In general, the number of coefficients M in a polynomial with k independent variables, $p_N(x^{(1)}, x^{(2)}, ..., x^{(k)})$, is

$$M = \binom{N+k}{k}. \tag{9.30}$$

Then, the number of data n must be equal or greater than this number.

Two-parameter polynomial regression

Suppose that Γ_1 is a function of H and Y_e, $\Gamma_1 = \Gamma_1(H, Y_e)$. Imagine that we have downloaded the proper data from CompOSE and have computed H and Γ_1 in such a way and we have three arrays of n data for H, Y_e and Γ_1:

$$\begin{aligned} x &= (H_1 \quad H_2 \quad ... \quad H_n) \\ y &= ((Y_e)_1 \quad (Y_e)_2 \quad ... \quad (Y_e)_n), \\ z &= ((\Gamma_1)_1 \quad (\Gamma_1)_2 \quad ... \quad (\Gamma_1)_n). \end{aligned} \tag{9.31}$$

We want to fit these data to a polynomial of degree N of two variables for the adiabatic index of the following form:

$$\begin{aligned} p_N(H, Y_e) =& a_0 + a_1 H + a_2 H^2 + ... + a_N H^N + a_{N+1} Y_e + a_{N+2} H Y_e + ... \\ &+ a_{2N} H^{N-1} Y_e + ... + a_{k(i,j)} H^i Y_e^j + ... + a_M Y_e^N. \end{aligned} \tag{9.32}$$

First, powers of H in increasing order from 0 to degree N are considered; then, the same list of considered H powers is multiplied by Y_e; we continue in this way, successively increasing the powers of Y_e. Notice that

$$M = \binom{N+2}{2} \tag{9.33}$$

Now, consider the x-Vandermonde matrix (9.26) and let us define the y-Vandermonde matrix

$$A^y = \begin{pmatrix} 1 & Y_1 & Y_1^2 & ... & Y_1^N \\ 1 & Y_2 & Y_2^2 & ... & Y_2^N \\ \vdots & \vdots & \vdots & \vdots & \vdots \\ 1 & Y_n & Y_n^2 & ... & Y_n^N \end{pmatrix}.. \tag{9.34}$$

We also define a generalized Vandermonde matrix of two set of n data:

$$A^{xy} = \begin{pmatrix} 1 & H_1 & ... & H_1^N & Y_1 & H_1 Y_1 & ... & H_1^{N-1} Y_1 & Y_1^2 & Y_1^2 H_1 & ... & Y_1^N \\ 1 & H_2 & ... & H_2^N & Y_2 & H_2 Y_2 & ... & H_2^{N-1} Y_2 & Y_2^2 & Y_2^2 H_2 & ... & Y_2^N \\ \vdots & \vdots & \vdots & \vdots & \vdots & \vdots & \vdots & \vdots & \vdots & \vdots & \vdots & \vdots \\ 1 & H_n & ... & H_n^N & Y_n & H_n Y_n & ... & H_n^{N-1} Y_n & Y_n^2 & Y_n^2 H_n & ... & Y_n^N \end{pmatrix}. \tag{9.35}$$

The order of the monomials is the one explained before. It turns out that the following relation is satisfied between the coefficients of A^x and A^y and the xy-Vandermonde matrix A^{xy}:

$$A^{xy}_{ij} = A^x_{im_j} A^y_{il_j}, \tag{9.36}$$

where l_j is such that $f_N(l_j - 1) < j \leq f_N(l_j)$, where

$$f_N(l_j) := \binom{N+2}{N} - \binom{N-l_j+2}{N-l_j}. \tag{9.37}$$

The index l_j introduced in this way is unique (given j and N), and we can solve the previous inequations to get the following simpler expression:

$$l_j = \left\lceil \frac{2N+3-\sqrt{(2N+3)^2-8j}}{2} \right\rceil. \tag{9.38}$$

On the other hand, the index m_j is computed as

$$m_j = j, \quad \mod f_N(l_j - 1). \tag{9.39}$$

The case $\mod 0$ is not well defined; in this case, we just assign $m_j = j$. Once, we have A^{xy}, we are able to compute the vector

$$\beta = zA^{xy}, \tag{9.40}$$

which has dimension M, and the symmetric matrix

$$\alpha = (A^{xy})^T A^{xy}, \tag{9.41}$$

which has dimension $M \times M$. The matrix α will be singular if there exist repeated points or the points $(H_i, (Y_e)_i, (\Gamma_1)_i)$ remain in a straight line. Suppose α is invertible. Then, the M coefficients of the polynomial fit p_N of two variables are

$$(a_0,\, a_1,\, ...,\, a_M) = \beta\alpha^{-1}. \tag{9.42}$$

The relation (9.36) provide us an easy algorithm to program the function that will compute such a fit. We have called it `polynomial_fit_2D` in the Box 9.2, and the pseudo-code is shown in the Box B.2.

If we restrict the second independent variable y to a specific $\hat{y} = Y_e$ in the two-parameter polynomial fit we get a one-parameter polynomial:

$$\begin{aligned} p_N(H, \hat{y}) =& a_0 + a_1 H + a_2 H^2 + ... + a_N H^N + a_{N+1}\hat{y} + a_{N+2} H\hat{y} + ... \\ &+ a_{k(i,j)} H^i \hat{y}^j + ... + a_M \hat{y}^N = b_0 + b_1 H + b_2 H^2 + ... + b_N H^N, \end{aligned} \tag{9.43}$$

where the coefficients a_i and b_i are related by the formula

$$b_k = \sum_{j\,/\,m_j = k} a_j\, (\hat{y})^{l_j - 1}. \tag{9.44}$$

The use of this formula has been mentioned before. In the Box B.3, the pseudo-code that applies this formula to compute each b_i can be found. Notice that the coefficient b_i under consideration in each **for** loop, it is not ordered with the counter of the loop.

Three-parameter polynomial regression

Let us add a third independent variable, commonly, the temperature T. Suppose that we have four arrays of n data, being the third ones from the independent variables H, Y_e and T:

$$\begin{array}{llll} x = (H_1 & H_2 & ... & H_n) \\ y = ((Y_e)_1 & (Y_e)_2 & ... & (Y_e)_n), \\ z = (T_1 & T_2 & ... & T_n), \\ u = ((\Gamma_1)_1 & (\Gamma_1)_2 & ... & (\Gamma_1)_n). \end{array} \tag{9.45}$$

We want to find the polynomial of degree N of three variables of the following form

$$\begin{aligned} p_N(H, Y_e, T) &= a_0 + a_1 H + a_2 H^2 + ... + a_N H^N + a_{N+1} Y_e + a_{N+2} H Y_e + ... \\ &+ a_{u(i,j)} H^i Y_e^j + ... + a_{M_2} Y_e^N + a_{M_2+1} T + ... \\ &+ a_{M_2+N} H^{N-1} T + a_{M_2+N+1} Y_e T + a_{M_2+N+2} H Y_e T + ... \\ &+ a_{v(i,j,k)} H^i Y_e^j T^k + ... + a_M T^N. \end{aligned} \tag{9.46}$$

that fit the data for the adiabatic index by using the least squares method. The order of the monomials try to resemble that from the two-parameter case. A way to understand the order is to first build the polynomial (9.32) with Y_e and T as variables, let us say $p_N(Y_e, T)$. Then, take increasing powers of H, and multiply the monomials of $p_N(Y_e, T)$ keeping the same order. Notice that $M_2 = (N+2)(N+1)/2$ and

$$M = \binom{N+3}{3}. \tag{9.47}$$

Consider the x-Vandermonde matrix (9.26) and y-Vandermonde matrix (9.34). Now, we define the z-Vandermonde matrix

$$A^z = \begin{pmatrix} 1 & T_1 & T_1^2 & ... & T_1^N \\ 1 & T_2 & T_2^2 & ... & T_2^N \\ \vdots & \vdots & \vdots & \vdots & \vdots \\ 1 & T_n & T_n^2 & ... & T_n^N \end{pmatrix}. \tag{9.48}$$

The xyz-Vandermonde matrix will be in this case:

$$A^{xyz} = \begin{pmatrix} 1 & ... & H_1^N & ... & Y_1^N & T_1 & ... & H_1^i Y_1^j T_1^k & ... & T_1^N \\ 1 & ... & H_2^N & ... & Y_2^N & T_2 & ... & H_2^i Y_2^j T_2^k & ... & T_2^N \\ \vdots & \vdots & \vdots & \vdots & \vdots & \vdots & \vdots & \vdots & \vdots & \\ 1 & ... & H_n^N & ... & Y_n^N & T_n & ... & H_n^i Y_n^j T_n^k & ... & T_n^N \end{pmatrix}. \tag{9.49}$$

The order of monomials is the same of that in $p_N(H, Y_e, T)$. The following relation holds:

$$A_{ij}^{xyz} = A_{im_j}^{x} A_{il_j}^{y} A_{in_j}^{z}, \tag{9.50}$$

where n_j is such that $f_N(n_j - 1) < j \leq f_N(n_j)$, where

$$f_N(n_j) := \binom{N+3}{N} - \binom{N-n_j+3}{N-n_j}, \tag{9.51}$$

l_j is such that $g_N(l_j - 1) < j \leq g_N(l_j)$, where

$$g_N(l_j) := \binom{N-n_j+3}{N-n_j+1} - \binom{N-n_j-l_j+3}{N-n_j-l_j+1}, \tag{9.52}$$

or equivalently

$$l_j = \left\lceil \frac{2(N-n_j+1)+3-\sqrt{(2(N-n_j+1)+3)^2-8j'}}{2} \right\rceil \tag{9.53}$$

and

$$m_j = j', \quad \text{mod } g_N(l_j - 1) \tag{9.54}$$

where $j' = j - f_N(n_j - 1)$. Remember that we have defined $m_j = j$ for $\text{mod } 0$. From the matrix A^{xyz}, we can build the M-dimensional vector

$$\beta = uA^{xyz}, \tag{9.55}$$

and the symmetric matrix $M \times M$

$$\alpha = (A^{xyz})^T A^{xyz}. \tag{9.56}$$

The matrix α is singular whenever there are repeated points or they all remain in a plane. If α is invertible, the polynomial coefficients are

$$(a_0, a_1, ..., a_M) = \beta\alpha^{-1}. \tag{9.57}$$

The pseudo-code that applies this procedure is shown in the Box B.4.

9.4 Final remarks

The main topic of this Chapter has been polynomial regression in several variables. We have developed numerical techniques to do so in two

and three variables taking advantage of what was widely used in one variable. We applied these techniques to fit the adiabatic index coming from realistic EoS data, taken from CompOSE. EoS can be provided in several ways. For instance giving the pressure in terms of the log-enthalpy, $p = p(H)$ or, if taking H, Y_e and T as independent variables, $p = p(H, Y_e, T)$. EoS can also be given equivalently by an expression of the adiabatic index of the type $\Gamma_1 = \Gamma_1(H)$ or $\Gamma_1 = \Gamma_1(H, Y_e, T)$. It turned out that tabulated data from CompOSE is too noisy and simulations become unstable using them directly. Then, we applied polynomial regression in one and two variables to realistic data, and in particular to the adiabatic index, in order to make them smoother. Simulations of oscillating neutron stars with realistic one-parameter EoS were possible with this strategy [114]. There remains for the future applying it in the case of realistic (two and three)-parameter EoS.

All scripts we built are based on the LORENE library. As LORENE uses expansions of Chebyshev polynomials to describe functions, all thermodynamic variables are described by analytical functions. Nonetheless, only the fitted variable, the adiabatic index, is treated analytically respect the two independent variables H and Y_e. For technical reasons explained before, the other ones are analytical just in one variable, the log-enthalpy H, and discrete in Y_e. It would be interesting having variables described by expressions of the type

$$\sum_{i+j=0}^{N} a_{ij} T_i(x) T_j(y).$$

By doing so, we would have managed all thermodynamic quantities with analytical expressions of H and Y_e. This task would require the development of a new class in the LORENE library which is left for a future work. An extension of the procedure to three or more independent variables can be done analogously.

Other approaches to polynomial regression in several variables use Kronecker product of matrices [35]. For instance, in the two-parameter case consider the polynomial of degree $2N$

$$p_{2N}(x, y) = \sum_{i,j=0}^{N} a_{ij} x^i y^j. \tag{9.58}$$

In that case, the coefficients a_{ij} of the fit to this expression are obtained by means of the Kronecker product $\otimes_K$ of the Vandermonde matrices for

x and y,

$$A^{xy} = A^x \otimes_K A^y.$$

The previous strategy would continue likewise with the xy-Vandermonde matrix A^{xy} computed in this way. Proceeding in this manner is aesthetically simpler but the polynomial expression takes into account powers of x, y from 0 to N, while in our case the sum of the powers of x, y goes from 0 to N. Besides, the degree of the polynomial in the Kronecker case has to be even, $2N$. In k variables the polynomial degree would have to be a multiple of k. Notice that the computational cost of the Kronecker case and our proposed strategy are similar.

10

Summary and perspectives

We finish the manuscript with a summary of the main results, final reflections and perspectives.

We began with a context framed in classical mechanics, where the Navier-Stokes Equations were used to model a fluid mechanics problem: blood flow in aorta. We applied CFD simulation for blood flow in aorta to validate a reconstruction method. This method takes into account key geometrical parameters of aorta geometries. We have seen that the general behaviour observed in real aortas is captured in the reconstructed version. Further improvement is required for the reconstruction algorithm by taking a realistic characterization. For this task it is important to increase the sample of real aortas. The reconstruction of the Sinus of Valsalva and the aorta branches are still to be included. Having a good characterization will permit the generation of synthetic aortas to carry out CFD simulation in order to establish relations between geometrical features and WSS values in the aorta. This is to be done by machine learning techniques and it is ultimate goal of this project.

We have concluded that the SST $k-\omega$ turbulent model is the most ade-

quate to analyze WSS profiles for the study of cardiovascular diseases. A preliminary study on the dependence of the WSS values with respect the inlet boundary condition applied has been conducted. The inlet boundary conditions try to reproduce different aortic valves, a healthy natural valve and two prosthetic valves. We have conclude that the healthy valve produces healthier values of WSS in the ascendant aorta, and that the bileaflet valve works better than the tilting disk valve.

In the next future, time-dependent simulations considering the whole cardiac cycle, are to be carried out. Moreover at some point we will have to take into account fluid-structure interaction models.

This task is not only complex from the mathematical point of view. Nowadays, blood flow and cardiovascular simulations require multidisciplinary research groups composed by mathematicians, physicists, engineers, computer scientists and physicians. Therefore, an effort to understand us all each other is crucial.

Afterwards, we got into astrophysical scenarios framed in the Theory of Relativity. First, the Euler Equation was studied in Newtonian gravity and we made an analysis of characteristic curves. We deducted that the surface of a Newtonian self-gravity star is a contact discontinuity. After that, we address the general relativistic version of the Euler Equation. We restricted to a Schwarzschild spacetime background and used Gullstrand-Painlevé coordinates. Then, we could consider the whole domain $0 < r < \infty$, differently as when Schwarzschild coordinates were used in [73]. We wrote the system as a balance law and studied its hyperbolic type behaviour. We also obtained its stationary solutions which will permit the development of well-balanced methods to solve numerically the general relativistic Euler Equation in its non-steady version.

We reformulated the Fully Constrained Formulation of [31] of the Einstein Equations by introducing the variables V^i and $\dot{X}^i$. The new version preserves the good properties of local uniqueness and hierarchical structure and posses numerical accuracy advantages. We carried out the first preliminary tests with a rotating neutron star, where spacetime is stationary.

It is planned for the future, applying the new formulation to more complex astrophysical scenarios and cosmology.

We have introduced the MIRK method for stiff balance laws. The general a idea comes from IMEX Runge-Kutta methods with a key difference:

only conserved variables are evaluated implicitly in the equations of the method. We have applied it to the equations of the RRMHD and the Radiation Transport equations for neutrinos. In the first case, we saw two academic tests with astrophysical motivation. In the self similar current sheet test no evolution of matter was present. In the circular polarized Alfven waves test we checked that the primitive variables can be recovered in a straightforward manner. This would not have been the case in pure IMEX methods, where iterative fix-point methods had been needed in the recovery process. The Radiation Transport equations for neutrino-matter interaction, present in CCSNe, were also solved numerically in the M_1 closure approximation with the new MIRK approach.

In all cases we did a linear stability analysis at the stiff limit, deducing a stability region, from which we proposed some choices for the coefficients of the method. Imposing a good behaviour of the conserved variables at the stiff limit have guided us determining some of the coefficients. Some choices for coefficients provide stable simulations and reproduce the correct physical behaviour. Of course, a complete analysis would have determined a narrow stability region, and indeed some choices have driven to non-physical or unstable simulations in the case of CCSNe. We were also able to write the equations of the method in a explicit-like form by means of an effective time step. This means that the computational cost of the new approach is that of explicit methods, but preserving the good properties of implicit methods when stiff terms are present in the balance laws.

We let for the future the application of the MIRK method to other contexts where stiff balance laws are present. Some of them could be the force-free electrodynamics [82], rarefied gases [66] or the shallow water equations [65]. Moreover, a combination with well-balanced methods (see [22]) can provide fruitful results managing numerical solutions close to a stationary solution.

We ended the manuscript with a different numerical problem. We developed a polynomial regression algorithm in several variables. We did it for two and three independent variables, and the expressions make one think that it can be generalized to any number of independent variables.

We applied this strategy to the adiabatic index obtained from tabulated data from CompOSE [1] to model realistic EoS for nuclear matter. It is left for the future coupling these modules to simulations with oscillating neutron stars with LORENE [2].

We also commented the benefit of using products of Chebyshev polynomials to describe functions of several variables; this will be explored

deeper in a future work.

Appendices

A

OpenFOAM structure

```
solid Inlet
    facet normal -0.081044 -0.000000 -0.996711
    outer loop
    vertex 0.076150 0.182734 -1.722376
    vertex 0.662153 -0.210114 -1.770025
    vertex 0.270598 -0.798052 -1.738187
    endloop
    endfacet
    facet normal -0.081043 0.000009 -0.996711
...
endsolid Inlet
solid Wall
    facet normal 0.001038 0.995185 -0.098012
    outer loop
    vertex 4.972343 0.201948 3.898096
    vertex 5.148643 0.182733 3.704861
    vertex 4.974410 0.182733 3.703016
    endloop
    endfacet
    facet normal 0.003075 0.956941 -0.290267
...
endsolid Wall
solid Outlet
    facet normal 0.999944 0.000002 0.010590
    outer loop
    vertex 5.136793 -0.415367 4.823768
    vertex 5.139659 -1.068649 4.553185
    vertex 5.146577 -0.798051 3.899940
    endloop
    endfacet
    facet normal 0.999944 0.000000 0.010604
...
    endfacet
endsolid Outlet
```

Figure A.1: STL file defining the triangulated surface to be used by OpenFOAM.

```
castellatedMeshControls
{
    maxLocalCells 1000000;
    maxGlobalCells 8000000;
    minRefinementCells 100;
    nCellsBetweenLevels 1;
    features
    (
        {
            file "aorta_surface.eMesh";
            level 0;
        }
    );
    refinementSurfaces
    {
        aorta_surface
        {
            level (0 0);
            regions
            {
                Outlet
                { level (0 0); patchInfo { type patch; } }

                Wall
                { level (2 2); patchInfo { type patch; } }

                Inlet
                { level (0 0); patchInfo { type patch; } }
            }
        }
    }
    resolveFeatureAngle 20;
    refinementRegions
    {
            Wall
            {

            }
    }
    locationInMesh (0.0 0.0 0.0);
    allowFreeStandingZoneFaces true;
}
```

Figure A.2: Main lines of the file `snappyHexMeshDict` to specify different parameters to the castellation process of `snappyHexMesh` utility.

```
14063
(
(0.0013555307 0.30274852 -1.8986701)
(-0.10568855 0.30133507 -1.800514)
...
)
```

Figure A.3: File `points` with the points that constitute the vertices of the final mesh.

```
34969
(
3(12921 13413 12644)
4(13413 12921 13416 12650)
...
)
```

Figure A.4: File `faces` with the faces that constitute the volumes of the final mesh. The number of vertices and the reference number of them in the file `points` is settled for each face.

```
3
(
    Inlet
    {
        type            patch;
        nFaces          67;
        startFace       30206;
    }
    Wall
    {
        type            patch;
        nFaces          4642;
        startFace       30273;
    }
    Outlet
    {
        type            patch;
        nFaces          54;
        startFace       34915;
    }
)
```

Figure A.5: Structure of the file `boundary`. The tags of each patch of the surface are established and the references to the faces are consistent with order in the file `faces`.

```
simulationType RAS;
RAS
{
    RASModel        kEpsilon;
    turbulence      on;
    printCoeffs     on;
}
```

Figure A.6: Structure of the file `turbulenceProperties`.

```
internalField   uniform 0.0;

boundaryField
{
    Wall
    {
        type        zeroGradient;
    }
    Inlet
    {
        type        zeroGradient;
    }
    Outlet
    {
        type        fixedValue;
        value       uniform 0.0;
    }
}
```

Figure A.7: Structure of the file `0/p`. Boundary conditions for the pressure are settled and, in non-steady simulations, the initial conditions.

```
internalField   uniform (0 0 0);

boundaryField
{
    Wall
    {
        type            noSlip;
    }
    Inlet
    {
        type            fixedValue;
        value           uniform (0.0  0.0  1);

    }
    Outlet
    {
        type            inletOutlet;
        inletValue      uniform (0 0 0);
        value       uniform (0 0 0);
    }
}
```

Figure A.8: Structure of the file `0/U`. Boundary conditions for the velocity are settled and, in non-steady simulations, the initial conditions.

```
    Inlet
    {
        type            fixedValue;
        value           nonuniform List<vector>
548
(
(-0.015192 -0.003396 0.01146)
(-0.014498 -0.003241 0.010937)
...
(-0.010019 -0.00224 0.007558)
)
;
    }
    Outlet
```

Figure A.9: Structure of the file `0/U` when a non-uniform boundary condition is applied in a patch.

```
internalField   uniform 1e-6;

boundaryField
{
    Outlet
    {
        type            zeroGradient;
    }
    Wall
    {
        type            kLowReWallFunction;
value     uniform 1e-6;
    }
    Inlet
    {
        type            fixedValue;
        value           uniform 1e-6;
    }
}
```

Figure A.10: Structure of the file `0/k`. Boundary conditions for the kinetic turbulent energy are settled and, in non-steady simulations, the initial conditions.

```
application     simpleFoam;

startFrom       startTime;

startTime       0;

stopAt          endTime;

endTime         100.0;

deltaT          0.1;
...
```

Figure A.11: Structure of the file `system/controlDict`. Main lines only are shown.

```
ddtSchemes
{
    default         steadyState;
}

gradSchemes
{
    // Limit gradient to improve stability when bad cells encountered
    // (0 = no limiting; 1 = do not exceed surrounding cells)
    default         cellLimited Gauss linear 0.95;
    grad(p)         Gauss linear;
}

divSchemes
{
    default         none;
    // Use second-order accurate convection
    // Bounded schemes for steady-state solution
    div(phi,U)      bounded Gauss linearUpwindV grad(U);
    div((nuEff*dev2(T(grad(U))))) Gauss linear;
}

laplacianSchemes
{
    // Limited explicit correction to the surface normal gradient,
    // for stability in highly non-orthogonal cells.
    // (0 = uncorrected, fully implicit; 1 = full correction)
    default         Gauss linear limited 0.3;
}
...
```

Figure A.12: Structure of the file `system/fvSchemes`. Main lines only are shown

```
SIMPLE
{
    // Non-orthogonal correctors for robustness on tet meshes.
    // Porous baffles require a higher number of corrections.
    nNonOrthogonalCorrectors 5;

    consistent no;  // Setting this impairs stability of porous baffles
    residualControl
    {
        p 0.0001;
        U 0.0001;
        "(k|epsilon|omega|f|v2|nuTilda)" 0.0001;
    }
    pRefValue   0;
    pRefCell    0;
}
...
solvers
{
    "(p|p_rgh|pcorr)"
    {
        solver           GAMG;
        tolerance        1e-7;
        relTol           0.01;
        smoother         GaussSeidel;
        nPreSweeps       0;
        nPostSweeps      2;
        cacheAgglomeration on;
        agglomerator     faceAreaPair;
        nCellsInCoarsestLevel 10;
        mergeLevels      1;
    }
...
    U
    {
        solver           smoothSolver;
        smoother         GaussSeidel;
        tolerance        1e-8;
        relTol           0.1;
        nSweeps          1;
    }
    ...
    }
    ...
```

Figure A.13: Structure of the file `system/fvSolution`. Main lines only are shown.

B

Pseudo-codes for polynomial regression

```
function polynomial_fit_1D (x, y, N)
     asssert length(x)=length(y)
     ndata=length(x)
     A(:,1)=1
     for i=1,..,ndata
          for j=1,..,N
               A(i,j)=A(i,j-1)*x(i)
          end
     end
     compute alpha, b
     return inv_alpha*b
end
```

Box B.1: Pseudo-code of a function computing a one-parameter polynomial fit by the method of least squares.

```
function polynomial_fit_2D (x, y, z, N)
     asssert length(x)=length(y)=length(z)
     ndata=length(x)

     Ax(:,1)=1
     for i=1,..,ndata
          for j=1,..,N
               Ax(i,j)=Ax(i,j-1)*x(j)
          end
     end

     Ay(:,1)=1
     for i=1,..,ndata
          for j=1,..,N
               Ay(i,j)=Ay(i,j-1)*y(j)
          end
     end

     M=(N+2)(N+1)/2

     for j=1,..,M
          l=ceil( (2*N+3-sqrt((2*N+3)^2-8*j))/2 )
          mj = j mod l*(2*N+3-l)/2
          for i=1,..,ndata
               Axy(i,j)=Ay(i,mj)*Ay(i,lj)
          end
     end

     compute alpha, b
     return inv_alpha*b
end
```

Box B.2: Pseudo-code of a function computing a two-parameter polynomial fit by the method of least squares with our algorithm

```
function bcoefs_from_acoefs (acoefs, y, N)

     M=(N+2)(N+1)/2

     for j=1,..,M
          l=ceil( (2*N+3-sqrt((2*N+3)^2-8*j))/2 )
          mj = j mod l*(2*N+3-l)/2
          bcoefs(mj) = bcoefs(mj) + acoefs(j)*y^(l-1)
     end

     return bcoefs
end
```

Box B.3: Pseudo-code of a function computing the coefficients b_i from a_i and $\hat{Y}_e$ by the formula (9.44)

```
function polynomial_fit_3D (x, y, z, u, N)
     assert length(x)=length(y)=length(z)=length(u)
     ndata=length(x)

     compute Ax

     compute Ay

     compute Az

     M=(N+3)(N+2)(N+1)/6

     for j=1,..,M
          compute nj
          m=N-ni+1
          compute jp
          lj=ceil( (2*m+3-sqrt((2*m+3)^2-8*jp))/2 )
          mj = jp mod lj*(2*m+3-lj)/2
          for i=1,..,ndata
               Axyz(i,j)=Ay(i,mj)*Ay(i,lj)*Ay(i,nj)
          end
     end

     compute alpha, b
     return inv_alpha*b
end
```

Box B.4: Pseudo-code of a function computing a three-parameter polynomial fit by the method of least squares with our algorithm

Bibliography

[1] https://compose.obspm.fr.

[2] http://www.lorene.obspm.fr/.

[3] Private discussion with C. Palenzuela.

[4] Benjamin P. Abbott, Rich Abbott, T.D. Abbott, Fausto Acernese, Kendall Ackley, Carl Adams, Thomas Adams, Paolo Addesso, Rana X. Adhikari, Vaishali B. Adya, et al. GW170817: observation of gravitational waves from a binary neutron star inspiral. *Physical review letters*, 119(16):161101, 2017.

[5] Miguel Alcubierre. *Introduction to 3+1 numerical relativity*, volume 140. OUP Oxford, 2008.

[6] Luis Antón, Olindo Zanotti, Juan A. Miralles, José M. Martí, José M. Ibáñez, José A. Font, and José A. Pons. Numerical 3+1 general relativistic magnetohydrodynamics: a local characteristic approach. *The Astrophysical Journal*, 637(1):296, 2006.

[7] Richard Arnowitt, Stanley Deser, and Charles W. Misner. Republication of: The dynamics of general relativity. *General Relativity and Gravitation*, 40:1997–2027, 2008.

[8] Hideki Asada, Masaru Shibata, and Toshifumi Futamase. Post-Newtonian hydrodynamic equations using the 3+1 formalism in general relativity. *Progress of theoretical physics*, 96(1):81–112, 1996.

[9] Edouard Audit, P. Charrier, Jean-Pierre Chieze, and Bruno Dubroca. A radiation-hydrodynamics scheme valid from the transport to the diffusion limit. 2002.

[10] Steven A. Balbus and John F. Hawley. Instability, turbulence, and enhanced transport in accretion disks. *Reviews of modern physics*, 70(1):1, 1998.

[11] Enrico Barausse and Luis Lehner. Post-Newtonian approach to black hole-fluid systems. *Physical Review D*, 88(2):024029, 2013.

[12] Thomas W. Baumgarte, Pedro J. Montero, Isabel Cordero-Carrión, and Ewald Müller. Numerical relativity in spherical polar coordinates: Evolution calculations with the BSSN formulation. *Physical Review D*, 87(4):044026, 2013.

[13] Thomas W. Baumgarte and Stuart L. Shapiro. Numerical integration of Einstein's field equations. *Physical Review D*, 59(2):024007, 1998.

[14] Thomas W. Baumgarte and Stuart L. Shapiro. *Numerical relativity: solving Einstein's equations on the computer*. Cambridge University Press, 2010.

[15] George David Birkhoff and Rudolph Ernest Langer. *Relativity and modern physics*. Harvard University Press, 1923.

[16] Omer M. Blaes and Steven A. Balbus. Local shear instabilities in weakly ionized, weakly magnetized disks. *The Astrophysical Journal*, 421:163–177, 1994.

[17] Luc Blanchet, Thibault Damour, and Gerhard Schäefer. Post-Newtonian hydrodynamics and post-Newtonian gravitational wave generation for numerical relativity. *Monthly Notices of the Royal Astronomical Society*, 242(3):289–305, 1990.

[18] Silvano Bonazzola, Eric Gourgoulhon, Philippe Grandclement, and Jérôme Novak. Constrained scheme for the einstein equations based on the Dirac gauge and spherical coordinates. *Physical Review D*, 70(10):104007, 2004.

[19] David Brizuela and Gerhard Schaefer. Fourth-post-Newtonian exact approximation to general relativity. *Physical Review D*, 81(8):084014, 2010.

[20] Colin Gerald Caro, Timothy J. Pedley, R.C. Schroter, and W.A. Seed. *The mechanics of the circulation*. Cambridge University Press, 2012.

[21] Jordi Casacuberta Puig, Eduardo Soudah Prieto, Pedro Javier Gámez Montero, Gustavo Adolfo Raush Alviach, Roberto Castilla López, and Jorge Suit Pérez Ronda. *Hemodynamics in the Thoracic Aorta using OpenFOAM: 4D PCMRI versus CFD*. 2015.

[22] Manuel J. Castro and Carlos Parés. Well-balanced high-order finite volume methods for systems of balance laws. *Journal of Scientific Computing*, 82(2):48, 2020.

[23] Pablo Cerdá-Durán, Guillaume Faye, Harald Dimmelmeier, José A. Font, José M. Ibáñez, Ewald Müller, and Gerhard Schäfer. CFC+: improved dynamics and gravitational waveforms from relativistic core collapse simulations. *Astronomy & Astrophysics*, 439(3):1033–1055, 2005.

[24] The LIGO Scientific Collaboration, the Virgo Collaboration, and the KAGRA Collaboration *et al.* GWTC-3: Compact binary coalescences observed by LIGO and Virgo during the second part of the third observing run, 2021.

[25] Isabel Cordero Carrión. *Evolution formalisms of Einstein equations: numerical and geometrical issues*. 2009.

[26] Isabel Cordero-Carrión and Pablo Cerdá-Durán. Partially implicit Runge-Kutta methods for wave-like equations. *Advances in Differential Equations and Applications*, pages 267–278, 2014.

[27] Isabel Cordero-Carrión, Pablo Cerdá-Durán, and José M. Ibáñez. Gravitational waves in dynamical spacetimes with matter content in the fully constrained formulation. *Physical Review D*, 85(4):044023, 2012.

[28] Isabel Cordero-Carrion, José M. Ibáñez, and Juan A. Morales-Lladosa. Maximal slicings in spherical symmetry: local existence and construction. *Journal of mathematical physics*, 52(11):112501, 2011.

[29] Isabel Cordero-Carrión, Samuel Santos-Pérez, and Clara Martínez-Vidallach. Numerical evolution of the resistive relativistic magnetohydrodynamic equations: A minimally implicit Runge-Kutta scheme. *Applied Mathematics and Computation*, 443:127774, 2023.

[30] Isabel Cordero-Carrión and Pablo Cerdá-Durán. Partially implicit Runge-Kutta methods for wave-like equations. 2016.

[31] Isabel Cordero-Carrión, Pablo Cerdá-Durán, Harald Dimmelmeier, José Luis Jaramillo, Jérôme Novak, and Eric Gourgoulhon. Improved constrained scheme for the Einstein equations: An ap-

proach to the uniqueness issue. *Physical Review D*, 79(2):024017, 2009.

[32] Isabel Cordero-Carrión, Jose M. Ibañez, Eric Gourgoulhon, José Luis Jaramillo, and Jérôme Novak. Mathematical issues in a fully constrained formulation of the Einstein equations. *Physical Review D*, 77(8):084007, 2008.

[33] Marwan Darwish and Fadl Moukalled. *The finite volume method in computational fluid dynamics: an advanced introduction with OpenFOAM® and Matlab®*. Springer, 2016.

[34] Jean-Pierre De Villiers, John F. Hawley, and Julian H. Krolik. Magnetically driven accretion flows in the kerr metric. I. models and overall structure. *The Astrophysical Journal*, 599(2):1238, 2003.

[35] Huaian Diao, Zhao Song, Wen Sun, and David Woodruff. Sketching for kronecker product regression and p-splines. In *International Conference on Artificial Intelligence and Statistics*, pages 1299–1308. PMLR, 2018.

[36] Donald B. Doty, Anne Cafferty, Paul Cartier, Hans A. Huysmans, Neal D. Kon, Albert H. Krause, Roger C. Millar, Colleen F. Sintek, and Stephen Westaby. Aortic valve replacement with Medtronic Freestyle bioprosthesis: 5-year results. In *Seminars in thoracic and cardiovascular surgery*, volume 11, pages 35–41, 1999.

[37] Michael Dumbser and Olindo Zanotti. Very high order $p_n p_m$ schemes on unstructured meshes for the resistive relativistic MHD equations. *Journal of Computational Physics*, 228(18):6991–7006, 2009.

[38] Albert Einstein. Die feldgleichungen der gravitation. *Sitzungsberichte der Königlich Preußischen Akademie der Wissenschaften (Berlin*, pages 844–847, 1915.

[39] David Elad and Shmuel Einav. Physical and flow properties of blood. *Standard handbook of biomedical engineering and design*, pages 3–1, 2003.

[40] Instituto Nacional De Estadística. Defunciones según la causa de muerte. *Notas de prensa*, 2022.

[41] Joshua A. Faber and Frederic A. Rasio. Binary neutron star mergers. *Living Reviews in Relativity*, 15(1):1–83, 2012.

[42] Judith A. Finegold, Perviz Asaria, and Darrel P. Francis. Mortality from ischaemic heart disease by country, region, and age: statistics from world health organisation and united nations. *International journal of cardiology*, 168(2):934–945, 2013.

[43] Francois Foucart, Evan O'Connor, Luke Roberts, Lawrence E. Kidder, Harald P. Pfeiffer, and Mark A. Scheel. Impact of an improved neutrino energy estimate on outflows in neutron star merger simulations. *Physical Review D*, 94(12):123016, 2016.

[44] François Foucart. Monte carlo closure for moment-based transport schemes in general relativistic radiation hydrodynamic simulations. *Monthly Notices of the Royal Astronomical Society*, 475:4186–4207, 2018.

[45] François Foucart, Matthew D. Duez, François Hébert, Lawrence E. Kidder, Phillip Kovarik, Harald P. Pfeiffer, and Mark A. Scheel. Implementation of montecarlo transport in the general relativistic SpEC code. *The Astrophysical Journal*, 920(2):82, 2021.

[46] Yvonne Foures-Bruhat and Yvonne Choquet-Bruhat. Sur l'intégration des équations d'einstein. *CR Acad. Sci. Paris*, 226:1071, 1948.

[47] P. Chris Fragile, Omer M. Blaes, Peter Anninos, and Jay D. Salmonson. Global general relativistic magnetohydrodynamic simulation of a tilted black hole accretion disk. *The Astrophysical Journal*, 668(1):417, 2007.

[48] Michael Gabler, Pablo Cerdá-Durán, José A. Font, Ewald Müller, and Nikolaos Stergioulas. Magneto-elastic oscillations and the damping of crustal shear modes in magnetars. *Monthly Notices of the Royal Astronomical Society: Letters*, 410(1):L37–L41, 2011.

[49] John T. Giblin Jr, James B. Mertens, and Glenn D. Starkman. Departures from the Friedmann-Lemaitre-Robertston-walker cosmological model in an inhomogeneous universe: A numerical examination. *Physical Review Letters*, 116(25):251301, 2016.

[50] Éric Gourgoulhon. *3+1 formalism in general relativity: bases of numerical relativity*, volume 846. Springer Science & Business Media, 2012.

[51] Éric Gourgoulhon. *Special relativity in general frames*. Springer, 2016.

[52] Philippe Grandclément, Silvano Bonazzola, Eric Gourgoulhon, and J.A. Marck. A multidomain spectral method for scalar and vectorial Poisson equations with noncompact sources. *Journal of Computational Physics*, 170(1):231–260, 2001.

[53] Christopher Greenshields. *OpenFOAM v8 User Guide*. The OpenFOAM Foundation, London, UK, 2020.

[54] Utku Gülan, Beat Lüthi, Markus Holzner, Alex Liberzon, Arkady Tsinober, and Wolfgang Kinzelbach. Experimental study of aortic flow in the ascending aorta via particle tracking velocimetry. *Experiments in fluids*, 53:1469–1485, 2012.

[55] Haiping Huang. *Statistical mechanics of neural networks*. Springer, 2021.

[56] James A. Isenberg. Waveless approximation theories of gravity. *International Journal of Modern Physics D*, 17(02):265–273, 2008.

[57] Manuel R. Izquierdo, Lorenzo Pareschi, Borja Miñano, Joan Massó, and Carlos Palenzuela Luque. Global high-order numerical schemes for the time evolution of the general relativistic radiation magneto-hydrodynamics equations. *Classical and Quantum Gravity*, 2022.

[58] Marcelo Biscegli Jatene, Rosangela Monteiro, Maria Helena Guimarães, Siomara Christina Veronezi, Márcia Kyiomi Koike, Fabio Biscegli Jatene, and Adib Domingos Jatene. Aortic valve assessment. anatomical study of 100 healthy human hearts. *Arquivos brasileiros de cardiologia*, 73:81–86, 1999.

[59] Shi Jin and C. David Levermore. Numerical schemes for hyperbolic conservation laws with stiff relaxation terms. *Journal of computational physics*, 126(2):449–467, 1996.

[60] Shi Jin, Lorenzo Pareschi, and Giuseppe Toscani. Uniformly accurate diffusive relaxation schemes for multiscale transport equations. *SIAM Journal on Numerical Analysis*, 38(3):913–936, 2000.

[61] Barbara M. Johnston, Peter R. Johnston, Stuart Corney, and David Kilpatrick. Non-Newtonian blood flow in human right coronary arteries: steady state simulations. *Journal of biomechanics*, 37(5):709–720, 2004.

[62] Oliver Just, Robert Bollig, Hans-Thomas Janka, Martin Obergaulinger, Robert Glas, and Shigehiro Nagataki. Core-collapse supernova simulations in one and two dimensions: comparison of codes and approximations. *Monthly Notices of the Royal Astronomical Society*, 481(4):4786–4814, 2018.

[63] Oliver Just, Martin Obergaulinger, and Hans-Thomas Janka. A new multidimensional, energy-dependent two-moment transport code for neutrino-hydrodynamics. *Monthly Notices of the Royal Astronomical Society*, 453(4):3386–3413, 2015.

[64] Victoria M. Kaspi and Andrei M. Beloborodov. Magnetars. *Annual Review of Astronomy and Astrophysics*, 55:261–301, 2017.

[65] Julian Koellermeier and Ernesto Pimentel-García. Steady states and well-balanced schemes for shallow water moment equations with topography. *Applied Mathematics and Computation*, 427:127166, 2022.

[66] Julian Koellermeier and Giovanni Samaey. Spatially adaptive projective integration schemes for stiff hyperbolic balance laws with spectral gaps. *Journal of Computational Mathematics*, 8:295–325, 2022.

[67] Serguei S. Komissarov. Multidimensional numerical scheme for resistive relativistic magnetohydrodynamics. *Monthly Notices of the Royal Astronomical Society*, 382(3):995–1004, 2007.

[68] Serguei S. Komissarov and Oliver Porth. Numerical simulations of jets. *New Astronomy Reviews*, 92:101610, 2021.

[69] Takami Kuroda, Tomoya Takiwaki, and Kei Kotake. A new multienergy neutrino radiation-hydrodynamics code in full general relativity and its application to the gravitational collapse of massive stars. *The Astrophysical Journal Supplement Series*, 222(2):20, 2016.

[70] M Paul Laiu, Eirik Endeve, Ran Chu, J Austin Harris, and OE Bronson Messer. A DG-IMEX method for two-moment neutrino transport: Nonlinear solvers for neutrino-matter coupling. *The Astrophysical Journal Supplement Series*, 253(2):52, 2021.

[71] Lev Davidovich Landau and Evgenii Mikhailovich Lifshitz. *Fluid Mechanics: Landau and Lifshitz: Course of Theoretical Physics, Volume 6*, volume 6. Elsevier, 2013.

[72] Philippe G. LeFloch, Carlos Parés, and Ernesto Pimentel-García. A class of well-balanced algorithms for relativistic fluids on a Schwarzschild background. *Journal of Scientific Computing*, 89(1):3, 2021.

[73] Philippe G. LeFloch and Shuyang Xiang. Weakly regular fluid flows with bounded variation on the domain of outer communication of a Schwarzschild black hole spacetime. *Journal de Mathématiques Pures et Appliquées*, 106(6):1038–1090, 2016.

[74] Luis Lehner and Frans Pretorius. Numerical relativity and astrophysics. *Annual Review of Astronomy and Astrophysics*, 52:661–694, 2014.

[75] Randall J. LeVeque. *Numerical methods for conservation laws*, volume 214. Springer, 1992.

[76] Liang Liang, Minliang Liu, Caitlin Martin, and Wei Sun. A deep learning approach to estimate stress distribution: a fast and accurate surrogate of finite-element analysis. *Journal of The Royal Society Interface*, 15(138):20170844, 2018.

[77] André Lichnerowicz. Sur certains problèmes globaux relatifs au système des équations d'einstein. 1939.

[78] Matthias Liebendörfer, OE Bronson Messer, Anthony Mezzacappa, Stephen W. Bruenn, Christian Y. Cardall, and F.K. Thielemann. A finite difference representation of neutrino radiation hydrodynamics in spherically symmetric general relativistic spacetime. *The Astrophysical Journal Supplement Series*, 150(1):263, 2004.

[79] Lap-Ming Lin and Jérôme Novak. Rotating star initial data for a constrained scheme in numerical relativity. *Classical and Quantum Gravity*, 23(14):4545, 2006.

[80] Daniel Lindblad, Adam Jareteg, and Olivier Petit. Implementation and run-time mesh refinement for the k- ω SST DES turbulence model when applied to airfoils. *Project work. Chalmers University of Technology*, 2014.

[81] Hayley J. Macpherson, Paul D. Lasky, and Daniel J. Price. Inhomogeneous cosmology with numerical relativity. *Physical Review D*, 95(6):064028, 2017.

[82] Jens F. Mahlmann, Miguel A. Aloy, Vassilios Mewes, and Pablo Cerda-Duran. Computational general relativistic force-free electrodynamics-ii. characterization of numerical diffusivity. *Astronomy & Astrophysics*, 647:A58, 2021.

[83] Adel M. Malek, Seth L. Alper, and Seigo Izumo. Hemodynamic shear stress and its role in atherosclerosis. *Jama*, 282(21):2035–2042, 1999.

[84] Ganesh Manoharan, Mark S. Spence, Joseph Rodés-Cabau, and John G. Webb. St Jude Medical Portico valve. *EuroIntervention: journal of EuroPCR in collaboration with the Working Group on Interventional Cardiology of the European Society of Cardiology*, 8:Q97–101, 2012.

[85] Andreas Marek, Harald Dimmelmeier, Hans-Thomas Janka, Ewald Müller, and Robert Buras. Exploring the relativistic regime with newtonian hydrodynamics: an improved effective gravitational potential for supernova simulations. *Astronomy & Astrophysics*, 445(1):273–289, 2006.

[86] José M. Martí. Numerical simulations of jets from active galactic nuclei. *Galaxies*, 7(1):24, 2019.

[87] Bernhard Müller, Hans-Thomas Janka, and Harald Dimmelmeier. A new multi-dimensional general relativistic neutrino hydrodynamic code for core-collapse supernovae. I. method and code tests in spherical symmetry. *The Astrophysical Journal Supplement Series*, 189(1):104, 2010.

[88] Alain Munier and Robert Weaver. Radiation transfer in the fluid frame: A covariant formulation: Part i: Radiation hydrodynamics. *Comput. Phys. Rep.*, 3(3):127–164, 1986.

[89] Alain Munier and Robert Weaver. Radiation transfer in the fluid frame: A covariant formulation: Part ii: The radiation transfer equation. *Comput. Phys. Rep.*, 3(3):165–208, 1986.

[90] Takashi Nakamura, Kenichi Oohara, and Yasufumi Kojima. General relativistic collapse to black holes and gravitational waves from black holes. *Progress of Theoretical Physics Supplement*, 90:1–218, 1987.

[91] Alexandra N. Nowbar, Mauro Gitto, James P. Howard, Darrel P. Francis, and Rasha Al-Lamee. Mortality from ischemic heart disease: Analysis of data from the world health organization and coronary artery disease risk factors from ncd risk factor collaboration. *Circulation: cardiovascular quality and outcomes*, 12(6):e005375, 2019.

[92] Evan O'Connor. An open-source neutrino radiation hydrodynamics code for core-collapse supernovae. *The Astrophysical Journal Supplement Series*, 219:24, 2015.

[93] Evan O'Connor and Christian D. Ott. A new open-source code for spherically symmetric stellar collapse to neutron stars and black holes. *Classical and Quantum Gravity*, 27(11):114103, 2010.

[94] J. Robert Oppenheimer and Hartland Snyder. On continued gravitational contraction. *Physical Review*, 56(5):455, 1939.

[95] Evan O'Connor, Robert Bollig, Adam Burrows, Sean Couch, Tobias Fischer, Hans-Thomas Janka, Kei Kotake, Eric J Lentz, Matthias Liebendörfer, OE Bronson Messer, et al. Global comparison of core-collapse supernova simulations in spherical symmetry. *Journal of Physics G: Nuclear and Particle Physics*, 45(10):104001, 2018.

[96] Carlos Palenzuela, Luis Lehner, Oscar Reula, and Luciano Rezzolla. Beyond ideal MHD: towards a more realistic modelling of relativistic astrophysical plasmas. *Monthly Notices of the Royal Astronomical Society*, 394(4):1727–1740, 2009.

[97] Lorenzo Pareschi and Giovanni Russo. Implicit-explicit Runge-Kutta schemes and applications to hyperbolic systems with relaxation. *Journal of Scientific Computing*, 25(1):129–155, 2005.

[98] Suhas V. Patankar and D. Brian Spalding. A calculation procedure for heat, mass and momentum transfer in three-dimensional parabolic flows. In *Numerical prediction of flow, heat transfer, turbulence and combustion*, pages 54–73. Elsevier, 1983.

[99] Roger Penrose. Gravitational collapse and space-time singularities. *Physical Review Letters*, 14(3):57, 1965.

[100] Albino Perego, RM Cabezón, and Roger Käppeli. An advanced leakage scheme for neutrino treatment in astrophysical simulations. *The Astrophysical Journal Supplement Series*, 223(2):22, 2016.

[101] Manel Perucho. Dissipative processes and their role in the evolution of radio galaxies. *Galaxies*, 7(3):70, 2019.

[102] Eric Poisson and Clifford M. Will. *Gravity: Newtonian, post-Newtonian, relativistic*. Cambridge University Press, 2014.

[103] Jose A. Pons, Jose M. Ibáñez, and Juan A. Miralles. Hyperbolic character of the angular moment equations of radiative transfer and numerical methods. *Monthly Notices of the Royal Astronomical Society*, 317:550–562, #sep# 2000.

[104] David Radice, Sebastiano Bernuzzi, Albino Perego, and Roland Haas. A new moment-based general-relativistic neutrino-radiation transport code: Methods and first applications to neutron star mergers. *Monthly Notices of the Royal Astronomical Society*, 512(1):1499–1521, 2022.

[105] Markus Rampp and Hans-Thomas Janka. Radiation hydrodynamics with neutrinos-variable Eddington factor method for core-collapse supernova simulations. *Astronomy & Astrophysics*, 396(1):361–392, 2002.

[106] José Manuel Rojas Artuñedo. Influencia del tipo de válvula en el flujo sanguíneo de la aorta torácica: zonas en riesgo de arterioesclerosis. 2020.

[107] Pau Romero, Samuel Santos, Rafael Sebastian, Francisco Martínez-Gil, Dolors Serra, Pilar Calvillo, Alejandro Rodríguez, Rebeca Maldonado Puig, Luis Martí-Bonmatí, Ángel Alberich-Bayarri, Miguel Lozano, and Ignacio García-Fernández. Reconstruction of the aorta geometry using canal surfaces. volume 2 of *CMBE*, pages 801–804, Tohoku, Japan, 2019.

[108] Pau Romero, Dolors Serra, Miguel Lozano, Rafael Sebastián, and Ignacio García-Fernández. Assessment of geometric models for the approximation of aorta cross-sections. In *Functional Imaging and Modeling of the Heart: 11th International Conference, FIMH 2021, Stanford, CA, USA, June 21-25, 2021, Proceedings*, pages 84–92. Springer, 2021.

[109] Johannes Ruoff. The numerical evolution of neutron star oscillations. *Arxiv preprint gr-qc/0010041*, 2000.

[110] Samuel Santos, Jose Manuel Rojas, Pau Romero, Miguel Lozano, J Alberto Conejero, Ignacio García Fernández, et al. Analysis of turbulence models for flow simulation in the aorta. In *Proceedings of the XXVI Congreso de Ecuaciones Diferenciales y Aplicaciones. XVI Congreso de Matemática Aplicada*. Servicio de Publicaciones de la Universidad de Oviedo, 2021.

[111] Samuel Santos-Pérez, Martin Obergaulinger, and Isabel Cordero-Carrión. Minimally implicit methods for the numerical integration of the neutrino transport equations. *arXiv preprint arXiv:2302.12089*, 2023.

[112] Gerhard Schaefer and Achamveedu Gopakumar. Minimal no-radiation approximation to Einstein's field equations. *Physical Review D*, 69(2):021501, 2004.

[113] Yuichiro Sekiguchi. Stellar core collapse in full general relativity with microphysics: —formulation and spherical collapse test—. *Progress of Theoretical Physics*, 124(2):331–379, 2010.

[114] Gaël Servignat. Signature des propriétés de la matière nucléaire sur les spectres en ondes gravitationnelles des étoiles à neutrons: étude numérique préliminaire. 2021.

[115] Gaël Servignat, Jérôme Novak, and Isabel Cordero-Carrión. A new formulation of general-relativistic hydrodynamic equations using primitive variables. *arXiv preprint arXiv:2212.10853*, 2022.

[116] Masaru Shibata, Sho Fujibayashi, Kenta Hotokezaka, Kenta Kiuchi, Koutarou Kyutoku, Yuichiro Sekiguchi, and Masaomi Tanaka. Modeling GW170817 based on numerical relativity and its implications. *Physical Review D*, 96(12):123012, 2017.

[117] Masaru Shibata and Takashi Nakamura. Evolution of three-dimensional gravitational waves: Harmonic slicing case. *Physical Review D*, 52(10):5428, 1995.

[118] Henk C. Spruit. Dynamo action by differential rotation in a stably stratified stellar interior. *Astronomy & Astrophysics*, 381(3):923–932, 2002.

[119] K.N. Srinivasa Rao. The motion of a falling particle in a Schwarzschild field. In *Annales de l'IHP Physique théorique*, volume 5, pages 227–233, 1966.

[120] Ronald Starke and Giulio Albert Heinrich Schober. Relativistic covariance of Ohm's law. *International Journal of Modern Physics D*, 25(11):1640010, 2016.

[121] Andrew W. Steiner, Matthias Hempel, and Tobias Fischer. Core-collapse supernova equations of state based on neutron star observations. *The Astrophysical Journal*, 774(1):17, 2013.

[122] Hiroshi Suito, Kenji Takizawa, Viet QH Huynh, Daniel Sze, and Takuya Ueda. FSI analysis of the blood flow and geometrical characteristics in the thoracic aorta. *Computational mechanics*, 54:1035–1045, 2014.

[123] Kannan Sundaravadivelu and Rafik Absi. Turbulent kinetic energy estimate in the near wall region of smooth turbulent channel flows. *Meccanica*, 56(10):2533–2545, 2021.

[124] Bailey Sykes, Bernhard Mueller, Isabel Cordero-Carrión, Pablo Cerdá-Durán, and Jérôme Novak. Black-hole excision scheme for general relativistic core-collapse supernova simulations. *Physical Review D*, 107(10):103010, 2023.

[125] Kip S. Thorne, John Archibald Wheeler, and Charles W. Misner. *Gravitation*. Freeman San Francisco, CA, 2000.

[126] Wolfgang Tichy. Long term black hole evolution with the BSSN system by pseudospectral methods. *Physical Review D*, 80(10):104034, 2009.

[127] Stefan Typel, Micaela Oertel, Thomas Klähn, Deep Chatterjee, Veronica Dexheimer, Chikako Ishizuka, Marco Mancini, Jérôme Novak, et al. CompOSE reference manual. *The European Physical Journal A*, 58(11):1–41, 2022.

[128] Henk Kaarle Versteeg and Weeratunge Malalasekera. *An introduction to computational fluid dynamics: the finite volume method*. Pearson education, 2007.

[129] Matt Visser. The Kerr spacetime: A brief introduction. *arXiv preprint arXiv:0706.0622*, 2007.

[130] Robert M. Wald. *General relativity*. University of Chicago press, 2010.

[131] Haifeng Wang, Daniel Balzani, Vijay Vedula, Klemens Uhlmann, and Fathollah Varnik. On the potential self-amplification of aneurysms due to tissue degradation and blood flow revealed from FSI simulations. *Frontiers in Physiology*, 12:785780, 2021.

[132] James R. Wilson, Grant J. Mathews, and Pedro Marronetti. Relativistic numerical model for close neutron-star binaries. *Physical Review D*, 54(2):1317, 1996.

[133] Wei Yin, Yared Alemu, Klaus Affeld, Jolyon Jesty, and Danny Bluestein. Flow-induced platelet activation in bileaflet and monoleaflet mechanical heart valves. *Annals of biomedical engineering*, 32:1058–1066, 2004.

[134] James W. York Jr. Conformally invariant orthogonal decomposition of symmetric tensors on Riemannian manifolds and the initial-value problem of general relativity. *Journal of Mathematical Physics*, 14(4):456–464, 1973.

[135] James W. York Jr. Kinematics and dynamics of general relativity. *Sources of gravitational radiation*, pages 83–126, 1979.